The Effect of Laser Shock Peening on the Material Properties of Additively Manufactured Steel

Veronica Helen Marquez Over

Submitted in partial fulfillment of the
requirements for the degree of
Doctor of Philosophy
under the Executive Committee
of the Graduate School of Arts and Sciences

COLUMBIA UNIVERSITY

2024

Abstract

Veronica Helen Marquez Over

This thesis investigates the use of laser shock peening (LSP) to improve mechanical properties, electrochemical behavior, and stress corrosion cracking (SCC) resistance in laser powder bed fusion (LPBF) stainless steel. The thesis begins by introducing metal additive manufacturing and reviews the current technological frontiers of LSP before elucidating the fundamentals behind the imaging, experimental, and theoretical frameworks used in the subsequent chapters. The experimental work is roughly divided into two parts; the first half is dedicated to study of the plasticity response augmentation by LSP in anisotropic stainless steel. The prevalence of back stress hardening occurring in anisotropic metal parts causes reduced fatigue life under random loading. LSP is known to improve fatigue life by inducing compressive residual stress and has been applied with promising results to AM metal parts. It is here demonstrated that LSP may also be used as a tool for mitigating tensile back-stress hardening. This discussion is initially applied to rolled and annealed 304L stainless steel which is shown to exhibit material anisotropy. Back stress is extracted from hysteresis tensile testing for treated and untreated samples. Analysis of plasticity response by orientation imaging microscopy (OIM) and finite element analysis (FEA) describes back stress and residual stress development during tensile testing and LSP treatment. The research indicates LSP's potential to address manufacturing design challenges caused by yield asymmetry due to back stress and is thus next applied to additively manufactured 316L. The microstructure and texture in additively manufactured metal lead to anisotropic hardening behavior. Comparison of LSPed and as-built

LPBF samples shows LSPed samples processed along the build direction demonstrate significant back-stress reduction. Electron backscatter diffraction (EBSD) illuminates grain morphologies' role, while crystal plasticity finite element (CPFE) modeling reveals mechanisms underlying back-stress reduction across different build orientations and crystal planes.

In the second half of the thesis, LSP's effect upon LPBF 316L material performance in corrosive environments is investigated. This effort begins with analysis of LSP's improvement to electrochemical and wetting behavior of as-built LPBF surfaces. The corrosion performance of LPBF stainless steel varies between studies and build parameters, thus motivating the search for postprocessing methods that enable wetted surface applications. The study examines electrochemical properties before and after LSP, measuring pitting potential, electrochemical impedance, contact angle, surface free energy, and surface finish. LSP imparts surface improvement which is attributed to morphology and chemistry alterations as well as compressive residual stress. LPBF stainless steel is also particularly susceptible to SCC due to surface-level tensile residual stress. The final study demonstrates LSP's ability to enhance SCC behavior in LPBF stainless steel by increasing time to crack initiation. Analyses of residual stress, texture, dislocation distribution, hardness, microstructure, and fracture surfaces are conducted to understand the mechanisms underlying SCC improvement. Dynamic crack modeling supports observed outcomes, linking residual stress and failure modes to LSP's effects.

This work highlights LSP's potential as a versatile tool for enhancing the performance and reliability of LPBF stainless steel components in demanding engineering applications. Further, it identifies the key relevance of the anisotropy of LPBF material structure to mechanical behavior and also to the effectiveness of LSP surface processing.

Table of Contents

List of Figures

Chapter 1: Introduction

Chapter 2: Laser Shock Peening Induced Back Stress Mitigation in Rolled Stainless Steel

bulk-averaged back stress as compared with the as-received sample, which is discussed below.

Figure 7. Cross-section of simulation results in an LSPed sample showing uniaxial applied stress (s_{33}) and back stress (α_{33}) a) before tension and b) after 3% strain. As seen in c) the back stress is reduced by LSP in a layer up to 250 μm deep directly under the cite of peening. This reduction near the LSPed surface is lessened after pulling but the depth of the affected area remains the same. The residual stress reduction penetrates to 350 μm but the depth of the residual stress diminishes after strain.

Figure 8. Inverse pole figures (IPF) of top surface in the as-received samples in a) unstrained and b) 4% strained conditions and LSPed samples in c) unstrained and d) 4% strained conditions. Moderate grain refinement and an increase of equiaxed grains can be observed in the LSPed samples both before and after plastic strain.

Figure 9. GND density maps of the top surface in the as-received samples in a) unstrained and b) 4% strained conditions and LSPed samples in c) unstrained and d) 4% strained conditions. The color bar range is between 0-100 $10^{12}/m^2$. White areas are above this range and are excluded to reduce overestimation noise as recommended in the TSL OIM manual. The grain boundaries are defined as 15° misorientation. The as received and strained material (Fig. 9 b) exhibits higher GND density accumulation near grain boundaries than in the LSPed and strained material (Figure 9 d)).

Figure 10. Average GND density vs distance from grain boundary in the top surface (a) and in the cross section (b) at 0% and 4% strain provided for both LSPed and as-received materials. Cross section images taken before tensile strain (c-d) show a

Chapter 4: Effect of Laser Shock Peening on Electrochemistry and Wettability of Additively Manufactured Stainless Steel

Chapter 5: Mitigation of Stress Corrosion Cracking in Additively Manufactured Stainless Steel by Laser Shock Peening

List of Tables

Chapter 3: Laser Shock Peening Induced Back Stress Mitigation in Rolled Stainless Steel

Chapter 4: Effect of Laser Shock Peening on Electrochemistry and Wettability of Additively Manufactured Stainless Steel

Acknowledgments

I am thankful for the guidance, support, and open-mindedness of Dr. Y. Lawrence Yao without whom I would never have considered, let alone accomplished, the research presented in this thesis. I am grateful to the entire Mechanical Engineering Department at Columbia University; together its members helped me to discover my love for engineering as an undergraduate and graduate student. Dr. Kristin Myers and Dr. Arvind Narayanaswamy in particular helped me to envision my path forward as a researcher. I am also grateful for the learning opportunities afforded to me by the GE Research Center, Thomas Jefferson National Research Center, and my mentors there who opened my eyes to applications far beyond my initial experience. I thank my committee members Dr. James Im, Dr. Jeffery Kysar, Dr. Hongqiang Chen and Dr. Sinisa Vukelic for reviewing my research and serving for my dissertation defense. I am grateful for the efforts of the anonymous reviewers and the editors at the Journal of Manufacturing Science and Engineering for providing useful feedback to improve my submissions. I express my deepest gratitude to my mom, dad, and Ate, whose sharp analytical minds and unconditional support shaped my ability to pursue engineering in the first place. Finally, I thank my best friend and fiancé Joey. His unwavering confidence in me and willingness to learn a thing or two about material science and laser processing made even pursuing an experimental PhD during the challenges of the 2020 Pandemic a joyful experience.

Financial funding for this research from the NSF under grant #1761344 and the NSF Graduate Research Fellowship is much appreciated.

Publications under Candidature

[1] **Over, V.** and Yao, Y.L., 2022, "Laser Shock Peening Induced Back Stress Mitigation in Rolled Stainless Steel," ASME Trans. J. of Manufacturing Science and Engineering, **144**(6), pp. 061010, DOI: 0.1115/1.4052909. (also presented at MSEC 2022 conference)

[2] **Over, V.**, Donovan, J., and Yao, Y.L., 2023, "The Effect of Laser Shock Peening on Back Stress of Additively Manufactured Stainless Steel Parts," ASME Trans. J. of Manufacturing Science and Engineering, **145**(4), pp. 041005, DOI: 10.1115/1.4056571. (also presented at ICALEO 2022 conference)

[3] **Over, V.** and Yao, Y.L., 2024, "Effect of Laser Shock Peening on Electrochemistry and Wettability of Additively Manufactured Stainless Steel," ASME Trans. J. of Manufacturing Science and Engineering, pp. 1-31, DOI: 10.1115/1.4065022. (also presented at ILAS 2023 conference)

[4] **Over, V.** and Yao, Y.L., "Mitigation of Stress Corrosion Cracking in Additively Manufactured Stainless Steel by Laser Shock Peening," ASME Trans. J. of Manufacturing Science and Engineering, (under peer review)

Chapter 1: Introduction

1.1 Additive Manufacturing of Metals

Metal additive manufacturing or 3D printing may be taxonomized into three primary types: direct energy deposition (DED), binder jet technology (BJT), and powder bed fusion (PBF). All of these methods involve the fusion of metal layer-by-layer to form a final product and they each involve complex thermal processes whose nuances affect the final material structure. Metal 3D printing, while originally conceived for use in prototyping and small-batch manufacturing, is now being actualized for its ability to achieve complex geometries with all of the beneficial material properties of metal [1]. This allows the reduction in the number of parts in some aviation assemblies [1]. Further applications include use for creating complex fluidic features and for biomedical environments in which the customizability of the part shape is used to create patient-specific features [1]. Steel additive manufacturing, while currently amounting to $21 billion at the end of 2020 is still in its adolescence, requiring more repeatability and material control for the technology to reach its full potential [2]. A form of metal additive manufacturing, wire arc additive manufacturing, was first patented in 1920 as a “method of making decorative articles” involving subsequent layers of welded metal to comprise a net shape [3]. This process now falls under the category of DED. DED uses an energy source to fuse a continuous feed of metal material to previous layers to form the final part. This continuous feed may be in the form of wire, as in the originally conceived idea, or metal powder. BJT is meanwhile more similar to inkjet printing. A binder agent is selectively injected into a bed of metal powder to form a base layer. This process is followed by a roller or blade sweeping another layer of metal powder across the surface of the first layer to be selectively bound by yet another layer of binder agent. After the net shape is produced, the loose powder is removed and the material is fused in a

furnace, melting out the binding agent which has a lower melting point and increasing the part density. PBF, which is currently the most pervasive and researched of all of these technologies [4] employs an energy source to selectively heat and fuse layers of metal powder that is swept onto the build surface to the previous one. Each of these technologies have pros and cons. The cyclic heating processes in PBF and DED results in challenges such as residual stress and anisotropic microstructures and mechanical properties. These effects occur to varying degrees depending on the DED and PBF selected properties and may be mitigated. Meanwhile, BJT is plagued by low part density and weakened mechanical properties with deleterious ramifications for structural applications. While DED has advantages for manufacturing large parts due to high through-put, it cannot achieve the fine part resolution nor the complex shapes that PBF can. The subsequent sections will specifically introduce PBF technologies, highlighting their relevance for stainless steel manufacturing.

1.1.1 Powder Bed Fusion Technology

PBF technology joins powder through either fusion or melting via a moving energy source. Fusion of powder occurs below the melting point of the metal powder and requires application of a lower energy heat source. Fusion specifically employs the tendency of metal powder to minimize surface energy by reducing its surface area to volume ratio, causing the metal powder to adhere together [1]. Thus, the energy source must only supply enough energy for the metal powder to fuse without changing state. If energy costs are a concern or if the powder chemistry precludes melting, this may be an advantageous manufacturing technique. However, due to the limited penetration of this fusion effect, fusion achieves only lesser part density and strength in comparison to melting processes thereby placing the part at risk of delamination. Melting additive manufacturing processes entail complete state change of the build

layer and also the surface of the previous layer as well. The melting and re-solidification of the two layers causes epitaxial grain growth along the build direction allowing strong layer cohesion and resulting in elongated grains. PBF heat sources that may be used for melting or fusion are bifurcated between electron beam and lasers.

Electron beam powder bed fusion (EPBF) comprises a minority of the current additive metal production and research, with systems chiefly manufactured by Arcam EBM, a GE Additive owned company [4] [1]. In general, the process is less popular due to certain material limitations as well as lack of knowledge and prevalence of the technology. EPBF applies a high acceleration electron beam from a tungsten electron source. Due to the high interference of particles with the beam, the process must be performed in vacuum. This has some advantages due to the elimination of the need for shielding gases, however it also causes stripping of some lighter alloying elements such as Mn [4]. The powder must be heavier than in laser processes because of the effect of static electricity [5]. Furthermore, the electron beam spot size tends to be large. Both of these limitations result in a reduction to part resolution. The manufacturing process occurs at elevated temperatures (300-1100°C) and requires a long cooling period after finishing [6]. The result of the high temperature of EPBF is that residual stress is less of a concern, thereby requiring fewer supports, and allowing part nesting. In addition, the magnetic coils that are used to direct the electron beam do not require mechanical maneuvering of a mass such as a mirror to perform scanning processes and can thus respond to altered input conditions quickly. This mechanism results in faster scanning and build rate [1]. Furthermore, electrons penetrate more deeply into the material than light radiation and thus can develop deeper fusion of layers. However, perhaps the largest limitation for EPBF is that the process may only be applied

to conductive materials because nonconductive materials will experience charging with the bombardment of the electron beam, eventually resulting in beam deflection [1].

Laser powder bed fusion (LPBF) has experienced several developments that now make it the most highly used metal additive manufacturing process, especially favored for stainless steel. The process is described by Figure 1, showing the laser source, the powder bed, and part.

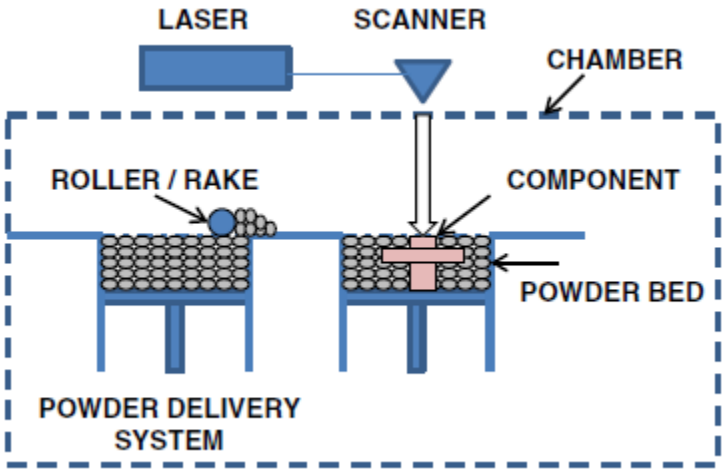

Figure 1. Illustration of a typical LPBF system [7].

LPBF, especially when full melting is used, requires an inert shielding gas to protect the melt-pool from oxidation. It is evident also that the LPBF process is significantly affected by the light absorption properties of the powder material and this presents a significant limitation for the additive manufacturing of certain metals. Originally, the laser intensity was too low such that the process struggled with balling, a phenomena of metal beading in which the fusion was not significant with the previous layer and inconsistency in the deposited layer caused low part density [8]. However, as laser absorption and power improved, better fusion was achieved. Build efficiency was further advanced by transitioning the LPBF lasers from CO_2 lasers to fiber YAG lasers, allowing the percentage of laser light absorption to increase from 20% to 80% [1]. The

absorption ratio (A), transmission ratio (T), and reflectance ratio (R) of light for a given material is given by the following equation:

$$A + T + R = 1. \quad \textbf{(1)}$$

For optimal buildability of a specific material, there must be an adequate balance between A and T with minimization of R. With reflectivity minimized, the material may be built with greatest efficiency and absorption and transmissivity must be balanced such that significant energy is delivered both to the build layer and enough is transmitted to the previous layer thereby allowing good depth of fusion [1]. These optical properties may be somewhat adjusted for materials with powder additives that improve adsorption, though this has limited effectiveness. As a result, certain materials are precluded from being built well by LPBF including copper. These materials are thus better suited for EPBF or BJT building depending on the suitability of their other properties. The chief advantages of LPBF are set in contrast with EPBF, allowing for finer surface finish, improved material flexibility, shorter cooling times, and based in a significantly greater knowledge base. However, the material artefacts of LPBF make it a complex manufacturing technique for structural design. In stainless steel the layer-by-layer process and continual reheating of previous layers results in unusual structures, primarily heterogeneous microstructure, residual stress, epitaxial grain growth along the build direction, oxide inclusions, and phase and alloy separation at melt pool boundaries. Each of these unique properties are described in subsequent chapters (Chapters 3-5). This material heterogeneity is of significant interest especially for plasticity and the interplay between micro and meso-scale stresses [9]. In-depth study of stainless steel built by LPBF reveals 6^{th} order scalable structures which lead to significant mechanical consequences [10]. Current challenges for the build process include repeatability of mechanical properties, with additively built stainless steel exhibiting a wide

range of strength and ductility, and anisotropy [8]. Significant parameter refinement of the build process has been performed to achieve optimal density and part properties.

Input variables into LPBF build processes are various with complex interactions. These input parameters include: I) laser parameters such as beam spot size, wavelength, and power, II) material properties such as substrate geometry, chemical composition, particle size, and III) printing properties such as scan speed, preheating, shield gas velocity, layer height, and hatch rotation between layers [4]. Work has been done to narrow the feasible combinations of parameters by using aggregate variables. The goal is to finely tune the parameters to achieve, not only complete fusion of layers, but also minimal voids that may occur due to keyhole mode welding, spatter, or balling. One of the preferred variables for determining desired parameter spaces is volumetric energy density (VED) which quantifies the energy added to the material per unit volume. There are various methods of defining this quantity:

$$VED_{hatch} = \frac{P}{v \cdot s \cdot l} \quad \textbf{(2)}$$

$$VED_{spot} = \frac{P}{v \cdot d \cdot l} \quad \textbf{(3)}$$

where VED_{hatch} corresponds to the hatch volumetric energy density and VED_{spot} is the spot volumetric energy density. Let P be the laser power, v be the scan speed, l be the layer thickness, and d be the laser spot diameter [4]. Both definitions have relevance for determining parameter range, especially as hatch-spacing and spot size are also interrelated. Generally, it is determined that the ratio of hatch spacing to spot size (s/d) must fall within 0.6 to 1.5 [4]. When normalized by material enthalpy as in equation *(4)*, VED_{spot} may be used to define a specific range for a given material. Given β is the absorption factor of the material to the laser energy, $C_{p,100°C}$ is the

heat capacity of the material at 100°C, T_m is the material melting point, and T_0 is the material room temperature, we find this ratio by calculating:

$$\frac{VED_{spot}}{\Delta H} = VED_{spot} \cdot \frac{\beta}{C_{p,100°C}(T_m - T_0)}. \quad \textbf{(4)}$$

Review of current research determined that, with some exceptions, the value derived in equation (4) must be ≤ 30 to achieve adequate part density [4]. Further parameter insight is formed by using conventional transient models formulated for laser welding processes. The one-dimensional transient model for spatially resolved temperature rise in the welded material is:

$$\Delta T(z,t) = T(z,t) - T_0 = \frac{P\beta}{Ak}\sqrt{4\alpha t}\; iefc\left[\frac{z}{\sqrt{4\alpha t}}\right] \quad \textbf{(5)}$$

where T is the absolute temperature, z is surface depth, t is time, α is thermal diffusivity of the material, A is laser spot area, and k is the thermal conductivity [11]. By setting equation *(5)* to zero, solving for z, and dividing by layer thickness, the maximum depth of heating divided by the layer thickness may be found, also known as the heating depth ratio (HDR):

$$HDR = \frac{\sqrt{4\alpha\frac{d}{v}}}{l}. \quad \textbf{(6)}$$

Due to the necessity for deeply penetrating fusion between layers while also avoiding key-hole mode welding which produces voids, this value may be used to determine an approximate range of layer thickness, scan velocity, and laser diameter for viable LPBF. Literature identifies that typical successful HDR ranges fall near 1.5 for stainless steel [4]. These rough rule-of-thumb quantities are helpful for producing high density parts; however, they may not necessarily guide users to high throughput recipes and thus there is further need to explore the limits of build speed. Innovations such as multi-spot scanning strategies are pushing this aspect of the technology forward [12]. Even with these improved process parameter selections, there are limitations to the microstructures and mechanical attributes that can be achieved. To bridge this

gap, hybrid processes have been introduced to further augment the material properties of additively built metal.

1.1.2 Hybrid Metal Additive Manufacturing Techniques

Hybrid additive techniques range from in-situ process additions, to post-processing steps, to surface augmentation methods that are used in tandem with the generic additive methods to benefit material characteristics after the build. The most common forms of hybrid techniques are post-build heat treatments including hot isostatic pressing (HIP) and annealing. These processes are used to relieve stress and can do so to varying degrees while also often reducing hardness and yield strength. At high temperatures the stress relieve process will also cause grain recrystallization, which, while resulting in more equiaxed and less textured structures, coincides with significant softening [13]. In-situ processes that are favored for tailoring microstructure and also for improving part density for unfavorable process parameters include layer remelting. Layer remelting is advantageous because the same laser for printing may be used to apply remelting at a significantly lower power. This process may be performed after multiple layers are printed and has evidenced improved residual stress profile and significantly improved porosity [14]. However, as with HIP and annealing, the recrystallization due to this hybrid process results in softening [15]. Similar layer-by-layer adjustments are performed through other hybrid techniques including by plasma deposition, ultrasonic peening, laser shock peening, rolling, burnishing, and friction stir deposition [14]. These additions were originally oriented towards improving density and are now chiefly aimed at limiting mechanical residual stress and tailoring microstructure. Such hybrid processes take advantage of the additive manufacturing process to impart beneficial mechanical properties such as compressive residual stress throughout the final part. The use of laser shock peening (LSP) for this end is especially promising due to its

comparatively improved penetration and level of compressive residual stress that it is capable of imparting [16]. This integration of in-situ LSP is limited due to the requirement for a confinement layer and is currently achieved by removing the build plate from the LPBF chamber which poses great risk to feature accuracy [17]. However, with the proliferation of femtosecond laser technology, no-confinement LSP may be possible and it may be more possible to integrate LSP into the build without removing the part to peen the surface. For further details see the following review of LSP technology.

1.2 Laser Shock Peening (LSP)

LSP processing is used chiefly to induce beneficial compressive residual stresses that improve the fatigue life of metal components [16]. However, since its inception, LSP technology has developed beyond this usage and is being investigated for other applications. LSP was first discovered by researchers studying confined laser ablation, identifying that with the application of transparent overlays over ablative targets, significant shock waves are induced into ductile materials that are used as a substrate [18]. The measurement of laser ablative pressure was originally performed with synthetic x-cut quartz crystals to develop a relationship between incident laser intensity and applied pressure [18] [19]. This study produces the coupled differential equation discussed in Chapter 2 that relates peak pressure with plasma thickness. The required laser power densities to achieve LSP are within 10^8 -10^9 W/cm^2 [18]. The propagation of a shockwave throughout the substrate is highly dependent upon the material properties and the applied pressure. A crucial material property for evaluating the response for a ductile solid is the Hugoniot limit (Ph) which describes the yield strength of a material under a uniaxial shock condition [16]. The Hugoniot limit is determined by the following equation:

$$Ph = \frac{1+\lambda}{2\mu} \cdot YS \tag{7}$$

where YS is the material's yield strength and λ and μ are the Lamé constants. This value also determines the greatest shock pressure that will be capable of achieving beneficial stress reduction in the metal target, beyond which only surface roughening occurs [16]. In general, applying a pressure beyond $2Ph$ results in no further material benefit to the surface stress. The material response may also vary greatly with adjustments to sample thickness. In a thin surface, shock wave refection may occur, which, upon the wave rebound can remove surface stress improvement as seen in Figure 2 modelled for a stainless steel solid in ABAQUS with the applied peak stress set at $4Ph$. The center of the peened material where the laser intensity is highest exhibits a stress "hole" where the compressive residual stress is less than in the surrounding material due to shock-wave rebound.

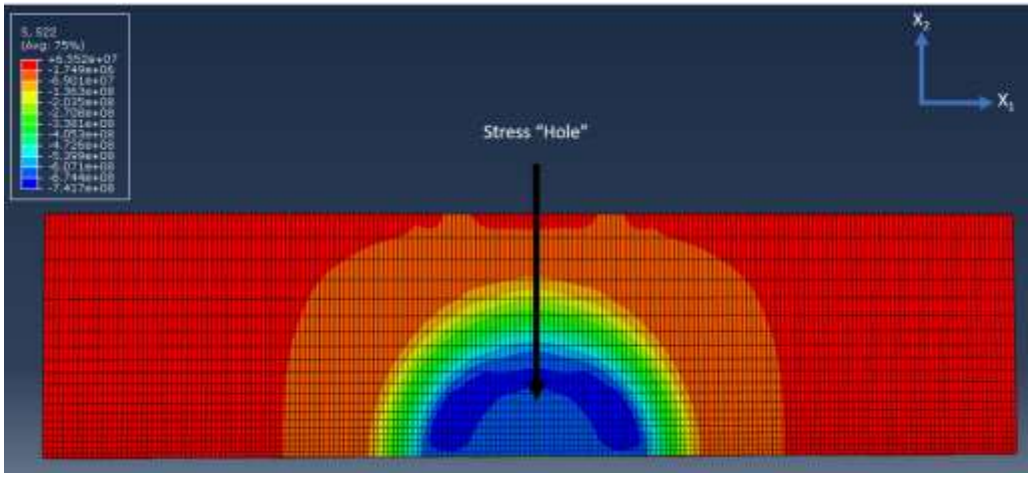

Figure 2. ABAQUS simulation displaying the reduction of compressive stress that occurs at the center of an LSP indent with 300 μm diameter laser pulse with peak pressure set above the Hugoniot limit at 4Ph for a substrate of 150 μm thickness.

The dynamics of propagation of an LSP-induced shockwave within a substrate is likewise determined by shockwave theory and complicated by plastic stress-strain relationships. From momentum and mass conservation principles, the shock wave velocity may be evaluated:

$$U(\epsilon) = \frac{1}{\rho_0 \frac{\delta u}{\delta \sigma}} = \sqrt{\frac{1}{\rho_0}\frac{\delta \sigma}{\delta \epsilon}} \quad \textbf{(8)}$$

such that ρ_0 is the initial material density [20]. Inputting an elastic-plastic material model that encompasses hardening such as the Johnson-Cook law into equation (8) allows solution of dynamic strain velocities as shown in Figure 3. The shockwave produced by LSP within a ductile material creates both an elastic and plastic material response that is unlike the response caused by other forms of peening. The microstructural and plastic augmentation by LSP is discussed in Chapters 2-5.

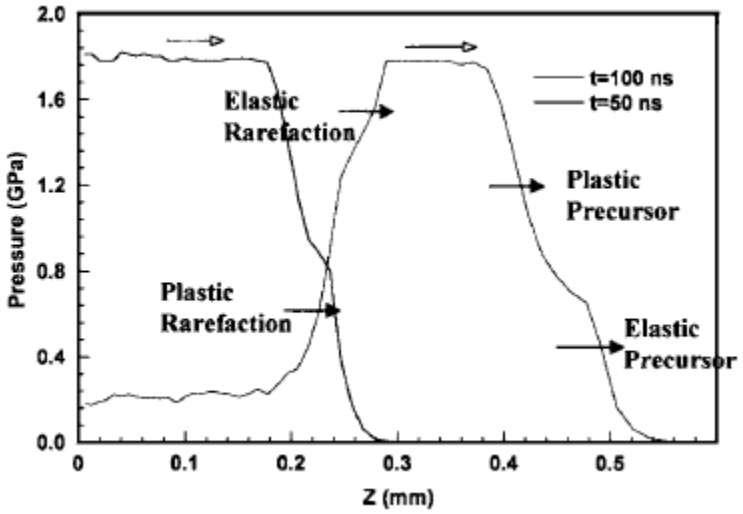

Figure 3. A numeric solution for shock wave resulting form a 50ns pulse duration exemplifying the plastic and elastic reactions within a solid [20].

The current frontier of LSP technology has expanded the use of LSP beyond the original treatment. Microscale LSP has been identified as a technique to manipulate residual stress in metal film structures and single crystals [21] [22]. These studies are applicable to micro-electro-mechanical systems (MEMS) for components with improved mechanical life. LSP is ideal for this usage due to its capacity for high precision and process control. LSP application is also of expanding interest in augmentation of brittle materials such as silicon and ceramic. Silicon

crystal wafers that are LSPed in heat-assisted processing present significant dislocation activity and improvement to compressive residual stress [23]. For ceramic materials, failure modes typically originate at the surface of the material and thus beneficial surface augmentation of ceramic parts is attractive for improving part life. LSP is shown to create a micro-plastic response within ceramic materials with shown improvements to surface hardness and surface residual stress [24]. This expanded application may have implications for ceramic additive manufacturing, a technology that is in its infancy [25]. Beyond ceramics, other brittle materials that are shown to have improved properties due to LSP include bulk Zr-based metallic glass which is used in biomedical applications. This material is plagued by poor ductility, limiting its design use. Thus, LSP has been employed to increase the ductility of this material with additional improvement to residual stress [26]. LSP processing has also developed beyond traditional methodology. Warm LSP, the application of LSP at elevated temperatures, is shown to allow additional LSP improvement by softening the material to increased dislocation mobility and plasticity [27]. This effect directly results in increased fatigue life as compared with conventionally LSPed metal [27]. As laser technology has also progressed to allow ultrafast lasers to become more accessible, the applications of shorter-pulse laser types are shown to widen the possibilities for LSP application. The challenge of introducing transparent confining medium to affect LSP is currently limiting. However, by applying LSP with a femtosecond laser, the high intensity of the beam allows LSP to be applied without a confining medium and potentially even without an ablative layer given the reduced heat affected zone [28]. Femtosecond LSP is shown to affect a 45% improvement to hardness in metal substrates which is comparative with those created by conventional nanosecond LSP processing [28]. Furthermore, it is not only more convenient but also recommended that femtosecond LSP be

applied without a confining medium. Comparative study shows that applying femtosecond LSP with a confining medium such as water produces a reduction in surface hardness as compared to without [28]. This is modelled as being due to the high absorption of the laser energy by the water confining medium [28]. While both hardness and residual stress results appear promising, the fatigue life improvement by femtosecond LSP has not yet been studied. Meanwhile, other confining medium solutions are being investigated as well. Fluid confining mediums such as water contribute lower interface stiffness to LSP processes and must therefore be paired with high laser intensity to produce the same magnitude of beneficial effects as rigid confining mediums in high-yield materials. However, rigid confining mediums present additional issues for rough surfaces as it is challenging to achieve significant contact between the textured surface and a flat transparent medium such as glass or acrylic. To solve this issue, alginate gel is being explored to supply a slightly stiffer interface while also allowing better coherence to rough surfaces [29]. These advancements in LSP technology could expand its versatility significantly.

LSP application is currently primarily of interest for critical high fatigue parts. GE Aircraft Engines have treated the leading edge of military use turbine blades since 1997 and also civilian aircrafts since 2004 [30]. These uses allow focused improvement for a high fatigue, high temperature components. They further protect from damage to foreign objects such as debris or dust. Expanded uses in the aeronautic industry include treatment of fastener holes in aircraft skins, reshaping of aircraft wings, and labelling of tear-sensitive parts [30]. Increasingly LSP is being expanded to use in other industries including for the prevention of stress corrosion cracking. This usage is discussed in depth in Chapter 5. Toshiba has been using LSP to improve the stress profiles and durability of the welded joints of pressurized water vessels in reactors since 1995 [30]. The application of a water confinement medium during LSP has the added

benefit of also cooling welded joints. LSP is also of interest for the treatment of orthopedic implants and is shown to improve the fatigue performance and reduce wear in surfaces of knee, hip, and spinal implants [30]. It is shown that in the applications described above, LSP provides cost-effective industrial benefit. However, there are still barriers when applying LSP as a solution for mechanical problems. LSP requires a high level of precision, automation, and significant process exploration for different materials and structures. For example, for non-flat surfaces, the angle of incidence of LSP on the surface can affect the degree of compressive residual stress that may be achieved with the same laser parameters [31]. Thus, if applied to a complex multifaceted surface, a minimal requirement would be the capacity to orient the interface accordingly, as with a multi-axis beam delivery system. Functionally, for large areas, other surface processing methods may be more ideal as a large beam spot size and thus a large capital cost investment would be required. However, as laser technology progresses and with improved dissemination of the technology, LSP continues to provide industrial solutions to a wide variety of problems. Relevant to the subsequent discussion of LSP's improvement to material properties is the concept of internal stresses as introduced in the following sections.

1.3 Material Investigation Methods of Micro and Meso-scale Stresses

The concept of micro and meso-scale stresses has been advanced by improved microscopy techniques such as synchrotron x-ray diffraction (sXRD) which resolves internal material stresses at grain-scales. Dye et al [32] describes three levels of internal stresses in polycrystals that are shown graphically in Figure 4: type-I stresses are macroscale stresses, type-II are intergranular stresses that occur at the scale of the microstructure, and type-III are intragranular stresses that act within the grain.

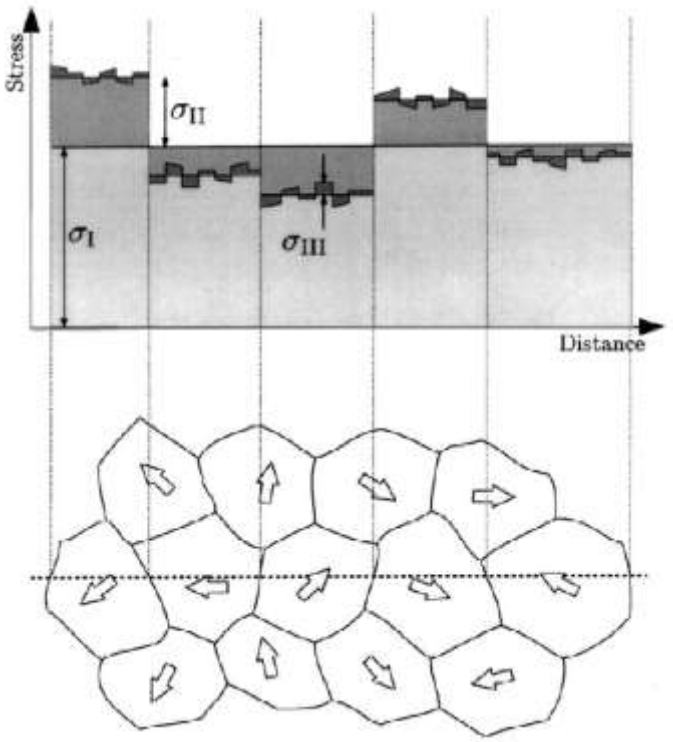

Figure 4. Illustration of type-I (σ_I), type-II (σ_{II}), and type-III (σ_{III}) stresses acting at macro and microscale within a material as sourced from Ref [32]. The material is shown to be randomly oriented by crystal arrows.

Type-I stresses are averaged over a large volume of material and may result in observable deformation such as when the residual stress of LPBF parts caused by cyclic heating causes significant part deflection after release from the build plate. Type-II stresses may occur at high-angle grain boundaries resulting from mismatch in texture and adjacent grains with high or low Schmid factor. The Schmid factor (m) describes the degree to which the applied stress is resolved along the slip direction of the glide plane. The critically resolved shear stress upon the glide plane is defined as:

$$\tau = m\sigma \tag{9}$$

where σ is the applied stress and the Schmid factor is $m = \cos(\phi)\cos(\lambda)$, letting ϕ be the angle between the normal to the slip plane and the applied stress direction and λ be the angle between the slip and stress directions. As stress is applied to an isotropic polycrystal with randomly

oriented grains, adjacent crystals will have different Schmid factors resulting in intergranular stress as one grain is stiffer and the other softer. This stress may be exacerbated when the polycrystal exhibits texture and the grains are non-equiaxed as in LPBF stainless steel. Type-III stress within grains are caused by internal lattice phenomenon such as dislocations or inclusions. These stresses develop with plastic strain and may react to externally applied forces by the surrounding material. Texture is crucially relevant to internal stresses as the prominence of specific grain orientations will result in anisotropic material response. In subsequent chapters pole-figures are employed to describe material texture.

1.3.1 Pole Figure Texture Analysis

Pole figures are a method of showing grain orientations of a polycrystal through a 2-D histogram. While it is considered a basic method of representation in crystallography, it is atypical for mechanical engineering education, thus motivating an introduction here. Austenitic stainless steel, which is the material here studied, has a face centered cubic (FCC) lattice structure with lattice planes defined by Miller indices. A pole figure for a given FCC lattice plane in a single crystal is created by creating a stereogram of the plane normal. Figure 5 shows the construction of a stereogram. A stereogram is formed by projecting the lattice plane normal onto the surface of a sphere. This sphere is then flattened into a 2-D representation of the 3-D plane orientation by drawing a line from the projected point through the opposite pole; the point that intersects the primitive plane or the sphere's equatorial plane is used to describe the lattice plane orientation in 2-D. Note that crystals have symmetry with more than a single plane normal definition for each miller index, thus resulting in multiple points mirrored about the stereogram for the same miller index definition. A scatter plot characterizing a polycrystal's texture is produced by performing this procedure for the same lattice plane of every grain in the

polycrystal and merging the stereograms together. If the polycrystal is randomly oriented, there will be no observed clustering with a large enough sample of grains. However, if the polycrystal exhibits a texture, there will be clusters of points in the stereogram and areas of the stereogram devoid of points. If a harmonic series expansion is performed to create a 2D histogram distribution, it produces a pole figure that may be useful in identifying preferred texture orientations.

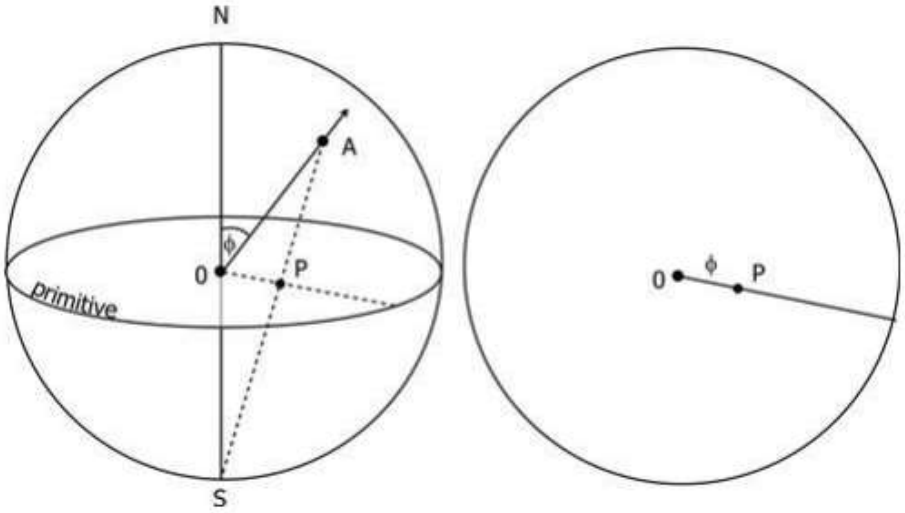

Figure 5. An illustration of a stereogram with A signifying the point projected onto the sphere from the lattice plane normal which is at attitude defined by ϕ and P is the point that is the intersection of the primitive plane and the ray drawn between A and the opposite pole S [33] .

A scanning electron microscopy (SEM) tool called electron backscatter diffraction (EBSD) allows orientation imaging microscopy (OIM) to establish the orientations of each grain within a metal sample. These microscopy tools have proliferated due to improved cost and are thus increasingly common in academic study of crystallography. At Columbia University, the Columbia Nano-Initiative is host to multiple imaging tools, including a Zeiss SEM which is outfitted with electron dispersive spectroscopy (EDS) and EBSD detectors and software. This SEM uses a Schottky thermal field emission source and a Gemini lens allowing improved

focusing using both magnetic and optical beam adjustment. EBSD is performed by first achieving a flat, smooth, clean sample surface through mechanical and electropolishing techniques such that surface roughness is <0.5 μm and without visible scratches. Stainless steel electropolishing is performed with a recipe of 100 mL of H_3PO_4, 50 mL of H_2SO_4, and 50 mL of H_2O. This polishing allows the electron beam to penetrate the surface and prevents the beam from being diffracted off of rough surface features. The sample is then angled within the machine via an angled stub at 70° to the electron beam and a fluorescent puck detector is inserted into the vacuum chamber orthogonally to the electron beam so that it intersects with the diffraction patterns. This set up is shown in Figure 6.

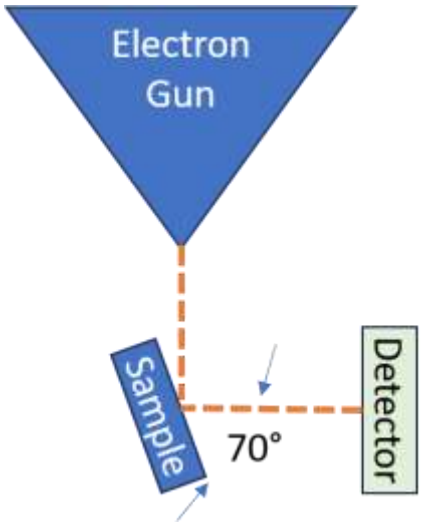

Figure 6. Depicting the in-vacuum layout of the electron gun, sample, and detector used for EBSD. The electron gun irradiates the sample at a 70 tilt and the detector is angled orthogonally to the incident electron beam.

A beam acceleration of 20 kV is used to achieve the required surface penetration of the sample. Kikuchi lines are Bragg diffraction patterns produced by diffusely scattering electrons using a focused electron beam from the lattice planes of the crystal structure. From this elastic and inelastic collision comprising of both diffraction and absorption events, Bragg coherence occurs resulting in a detectable signal of electrons emitted from the surface [34]. The detector fluoresces

upon the interference with the cone of diffracted electrons producing a Kikuchi pattern of intersecting bright lines that correspond to different lattice planes. A camera behind the fluorescent detector images this pattern and computer vision processing sharpens the image. The EBSD software produces a simulation of a chosen crystal lattice to reproduce the diffracted planes and is capable of matching the detected pattern with a specific lattice orientation and lattice strain thus making pole figure construction and other forms of material analysis possible [35]. Pole figure evaluation of each crystal orientation is one method of texture analysis. Another more macroscopic technique that can also be used to discover residual stresses is x-ray diffraction (XRD).

1.3.2 X-Ray Diffraction Residual Stress Measurement

XRD is used in subsequent chapters to analyze residual stress and the method and theory behind XRD analysis is thus introduced. XRD uses the Bragg angle diffraction of x-ray beams from lattice planes within the sample. An x-ray source is used to emit x-rays at the surface of the sample and a detector rotating around the sample counts the number of incident x-ray photons diffracted from the surface at a given angle. Both the angles of the emitter and the angle of the detector may be adjusted to create different measurements. The device used in subsequent chapters is the Panalytical X'Pert PRO MPD Theta-Theta System which is outfitted with a parafocus goniometer that can control both the emitter angle and the detector angle. The beam is produced with a Cu-$K\alpha$ source and emitted through a Ni-$K\beta$ filter with a PIXcel 1D detector. The slits are adjustable. The angles of the machine Ω, ψ, and θ are defined as in Figure 7. For a given Ω angle, the diffractor angle will be swept through a range of values, thus determining the angle of diffraction θ. By then varying the Ω angle, the ψ angle may be varied.

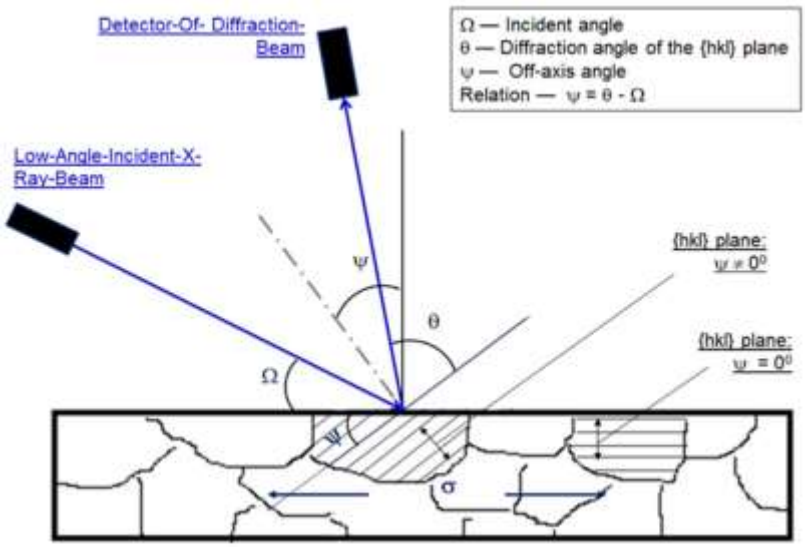

Figure 7. The x-ray beam geometry for a Bragg-Brentano goniometer. The angle ψ describes the angle between the {hkl} lattice plane and the sample surface. The angle θ describes the angle between the diffracted radiation and the {hkl} lattice plane. The angle between the emitter and the sample surface is given as Ω [7].

For austenitic stainless steel under Cu-$K\alpha$ radiation with $K\alpha_1$ wavelength of 1.5406 Å and a Ni-$K\beta$ filter, $K\alpha_1$ peaks will be measurable at angles $2\theta = 43.50 - 146.22°$ diffracted from lattice planes with miller indices [111],[200],[220], [311],[222],[400],[331], and [420] [36]. The incidence of these peaks at identifiable corresponding 2θ is indicative of the presence of randomly oriented austenitic steel. The absence of some of the corresponding peaks may either indicate texture or, if occurring in tandem with new unexpected peaks, a phase change. It is possible to take multiple 2θ measurements of the same lattice planes at multiple detector positioning angles (ψ) to determine lattice strain given a known lattice spacing for each lattice plane type. For residual stress analysis via the $sin\psi^2$ method, it is desirable to analyze the diffraction peak at the highest 2θ angle possible because Bragg's law is most accurate with θ close to 90°. To illustrate, Bragg's law is given by:

$$\lambda = 2dsin(\theta) \quad \textbf{(10)}$$

where λ is the incident wavelength, d is the lattice spacing, and θ is the incident diffraction angle. As seen in **Error! Reference source not found.**, imprecise values of θ correspond to less v ariation of $sin(\theta)$ which creates more accurate measurement of lattice spacing from Bragg's Law despite low angle accuracy.

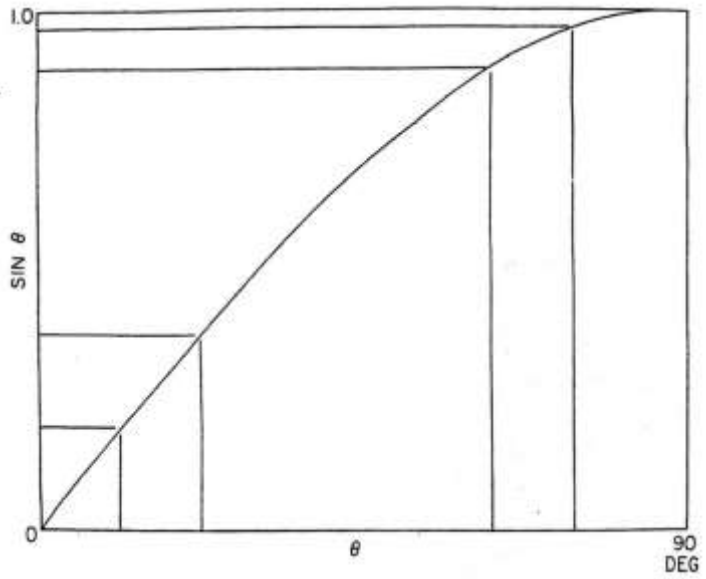

Figure 8. Illustration of how choice of θ close to 90° corresponds to reduced variation in $sin(\theta)$ [36].

However, some constraints due to goniometer positioning and also relative signal strength led to choosing the [311] peak at $2\theta = 90.41°$ corresponding to a d-spacing of 1.085 Å [36]. The computation of residual stress from a spectrum produced by XRD can be done in many ways and may vary in accuracy according to the XRD machine used, specimen geometry and type, and resulting data. The following provides background for only the specific procedure deemed most applicable. Further information such as phase, depth of X-ray penetration, crystallographic structure, etc. can be found from such a spectrum but this discussion is limited only to those methods directly relevant for stress evaluation.

The goal of this method is to use the observable lattice strain at a point in the sample and known constitutive relationships to find the stress along a desired direction. Note that this analysis is only applicable to microstrain calculations. Solving the following equation evaluates the strain along a direction defined by the elliptical coordinates ϕ and ψ as seen in **Error! R eference source not found.**:

$$\epsilon_{\phi\psi} = \frac{1+v}{E}[\sigma_1 cos\phi^2 sin\psi^2 + \sigma_2 sin\phi^2 sin\psi^2 + \sigma_3 cos\psi] - \frac{v}{E}(\sigma_1 + \sigma_2 + \sigma_3) \quad \textbf{(11)}$$

$\sigma_1, \sigma_2, \sigma_3$ are principal stresses and v and E are the Poisson ratio and Young's modulus respectively.

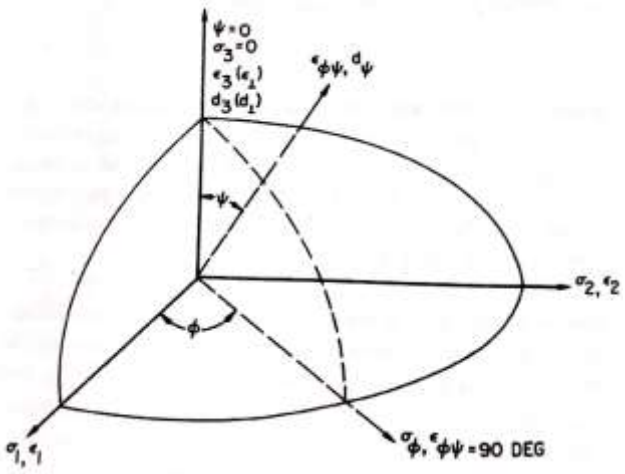

Figure 9. Sample stress and strain shown in terms of elliptical coordinates ϕ and ψ which are defined off of principle axes x_1, x_2, x_3 [36].

This method assumes bi-axial stress with no out-of-plane stress. Given that the primary interest is tensile and compressive residual stress in LPBF samples this is a reasonable assumption. This can be corroborated by other XRD studies of residual stresses in welds. [37] [38] Thus, equation (11) may be simplified to the following:

$$\epsilon_{\phi\psi} = \frac{1+v}{E}(\sigma_1 cos\phi^2 + \sigma_2 sin\phi^2)sin\psi^2 - \frac{v}{E}(\sigma_1 + \sigma_2) \quad \textbf{(12)}$$

When $\psi = \frac{\pi}{2}$, the surface stress component is given by $\sigma_\phi = \sigma_1 cos\phi^2 + \sigma_2 sin\phi^2$ and therefore strain can again be re-expressed as such:

$$\epsilon_{\phi\psi} = \frac{1+v}{E}\sigma_\phi sin\psi^2 - \frac{v}{E}(\sigma_1 + \sigma_2) \quad \textbf{(13)}$$

From equation (13), it can be seen that if strains can be measured at multiple $sin\psi^2$ values and the Young's modulus and Poisson's ratio of a lattice are known, simple linear regression will allow solution of the stress along the azimuth ϕ. Expressing this strain in terms of the lattice spacing: $\epsilon_{\phi\psi} = \frac{d_\psi - d_o}{d_o}$, where d_o is the unstressed lattice spacing and d_ψ is the stressed lattice spacing. It has been observed that there is negligible error by assuming $d_o = d_\perp$ where $d_\perp$ is the lattice spacing evaluated at $\psi = 0$ and thus strain can be re-expressed as in equation (14).

$$\epsilon_{\phi\psi} = \frac{d_\psi - d_\perp}{d_\perp} \quad \textbf{(14)}$$

Identifying the exact incident angle at which a plane of diffraction causes a peak intensity (θ_{pk}) is necessary to discover the lattice spacing from the diffraction-intensity spectrum. There are many methods of calculating this angle θ_{pk}; one of the most robust methods uses the Pearson VII distribution function. [36] This technique requires only seven data points to accurately describe a peak and furthermore correction for linear background intensity and superimposed K_α doublets are built in. A collection of data points around and near a peak profile are used to fit the following equation:

$$I = f(2\theta) + \alpha f(2\theta - \delta) + C * 2\theta + D \quad \textbf{(15)}$$

$$f(2\theta) = A\left(1 + \frac{B^2}{M}(2\theta - 2\theta_0)^2\right)^{-M} \quad \textbf{(16)}$$

Where the fit coefficients are $A =$ the maximum net intensity of the $K_{\alpha 1}$ peak, $B =$ a peak width parameter, $M =$a decay rate parameter, $2\theta_0$= the $K_{\alpha 1}$ peak position, $\alpha =$the fixed $K_{\alpha 1}/K_{\alpha 2}$ ratio (0.5), $C =$ the linear background slope, and $D =$ the linear background intercept. [36] A nonlinear least squares regression evaluates a statistical fit for these parameters and their standard errors. Letting the discovered $2\theta_0 = 2\theta_{pk}$ allows substitution of θ_{pk} into equation (10) and solution of the d-spacing.

Once the d-spacing is calculated for several ψ orientations of the emitter, notably including $\psi = 0$ for evaluation of d_0, linear regression of the $\sin\psi^2$ values against the strains may be performed. The discovered slope coefficient, m, is then used in calculation of the stress value assuming known material properties:

$$\mathrm{m} = \left(\frac{1 + \mathrm{v}}{\mathrm{E}}\right)\sigma_\phi. \quad \textbf{(17)}$$

A sample evaluation of residual stress is provided in Figure 10.

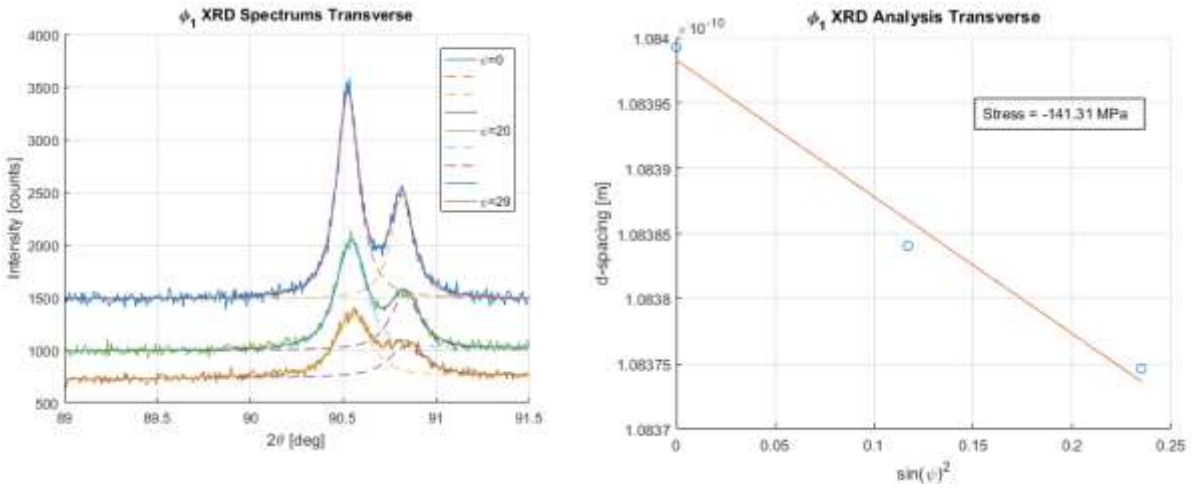

a) b)

Figure 10. Sample XRD evaluation of 316L rolled stainless steel, a) exhibiting the curve fitting of signals taken at a given ϕ orientation for three different Ω source positions and b) the residual stress $sin^2(\psi)$ curve fitting from these same spectrums.

1.3.4 Eshelby Inclusion Solution for Micro and Macro-scale Stress Modelling

To model the effects of intergranular (type-II) and macroscale (type-I) stress upon the internal grain stress, various techniques may be used. In Chapter 3, a crystal plasticity finite element (CPFE) model was used that employed the Eshelby solution for resolving external stress to each grain (element) within a model. The boundary conditions for this model are defined for uniaxial loading however for extension to a bulk continuum, periodic boundary conditions may be used. The Eshelby solution is generally solved to find the internal stresses in continuous medium [39]. This is applied to a polycrystal by averaging the material properties and solving for the surface stresses. The procedure for solving for the deformation of the inclusion is as follows:

Step I. Remove the inclusion from the solid continuum allowing it to undergo strain such that the stress in the inclusion is defined by [39]:

$$p_{ij}^{T} = \lambda e^{T} \delta_{ij} + 2\mu e_{ij}^{T}. \quad \textbf{(18)}$$

Note that e^T is the inclusion strain, λ and μ are the Lamé constants, and δ_{ij} is the identity matrix.

Step II. Apply the surface traction to the isolated inclusion as $-p_{ij}^T n_j$ thus restoring its shape to the original form. Reinsert the inclusion into the continuum body.

Step III. Assert the equal and opposite force $+p_{ij}^T n_j$ to the material continuum thereby allowing solution of the forces in the continuum.

These processes when applied to finite element modelling allow grain-by-grain solution of stress-strain response to external displacement.

1.4 Yield Surface Characterization and Plastic Flow Theory

From internal meso and micro-scale stresses aggregate material properties arise that characterize mechanical response in a material. Once of such responses is the Bauschinger effect which describes the interaction of dislocations to slip barriers. This phenomenon, expanded upon in Chapter 2, causes internal stress to increase like a spring within materials that are under load so that upon unloading, recoil of dislocations assists reverse yield. From a bulk material perspective, this behavior describes a development of continuum mechanics plasticity, namely the transformation of yield surface under load. The yield surface is a smooth continuous six-dimensional surface that exists in stress space and can be described by $f(\boldsymbol{\sigma}, T, \boldsymbol{\xi}) = 0$ [40]. This function is dependent upon temperature (T) , the Cauchy stress tensor (**$\boldsymbol{\sigma}$**), and an array of internal variables (**$\boldsymbol{\xi}$**) with components $\xi_1, \ldots, \xi_n$. The yield function is defined such that there exists a region $f(\boldsymbol{\sigma}, T, \boldsymbol{\xi}) < 0$ where the material exhibits only elastic material response such that the inelastic strain-rate tensor $\dot{\epsilon}^p$ is zero. Under this definition, the transformation of a yield surface must adhere to the restricted work-hardening postulate given by Drucker. Noted that for single stress and strain components σ and ϵ, hardening is defined by the following conditions:

$$\dot{\sigma}\dot{\epsilon}^p \begin{cases} \geq 0, hardening, \\ = 0, perfectly\ plastic\ material, \\ \leq 0, softening\ material. \end{cases} \quad \textbf{(19)}$$

Drucker's postulate states that for a material to be stable under stress control, the yield surface must transform from an initial stress state $\boldsymbol{\sigma}^*$ such that hardening occurs or:

$$\left(\sigma_{ij} - \sigma_{ij}^*\right)\dot{\epsilon}_{ij}^p \geq 0. \quad \textbf{(20)}$$

The consequence of this postulate, as illustrated in Figure 11, results in the following: for a hardening material to be stable under stress control, yield-surface convexity, continuity, and smoothness is required [40].

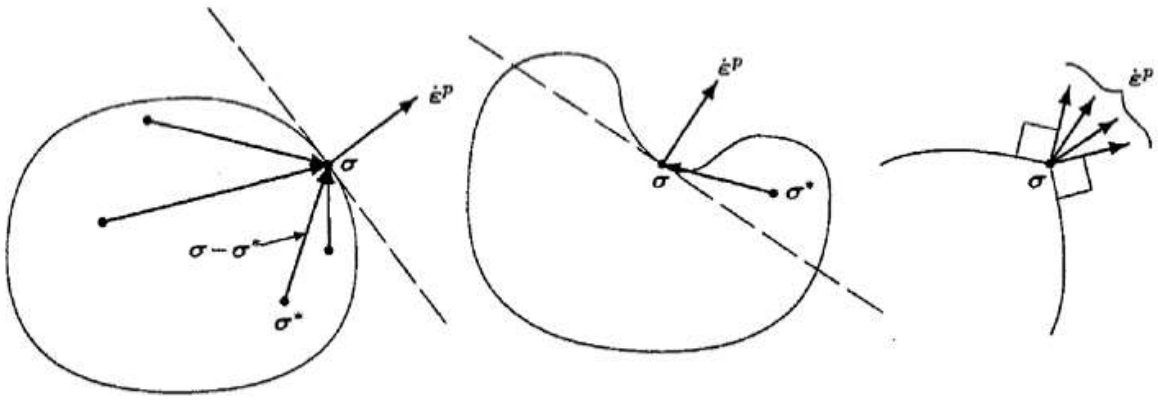

Figure 11. The consequences of Drucker's postulate require for $\dot{\epsilon}^p$ to be directed along the outward normal of the yield surface (left), the yield surface must be convex such that the illustrated condition is prohibited (middle) and the yield surface must be continuous and smooth (right) [40].

It may therefore be desirable to plot the stress surface as it is transformed during work hardening. Two points of each yield surface may be plotted with the hysteresis tensile testing presented in Chapter 2. However, these points are not sufficient to prescribe the surface and determine adherence to Drucker's postulate. Combined axial-torsion loading is capable of plotting yield surfaces before and after yield surface transformation which may then be used to determine convexity, normality, and approximate smoothness. Figure 12 demonstrates one such

test such that the expansion of the yield surface can be shown to satisfy stability. Such tests are of heightened importance for novel ductile materials such as additively manufactured metal, though they have yet to be adequately be performed. This work aims to further the advancement of plasticity modelling of LSPed LPBF stainless steel by quantifying uniaxial yield surface transformation.

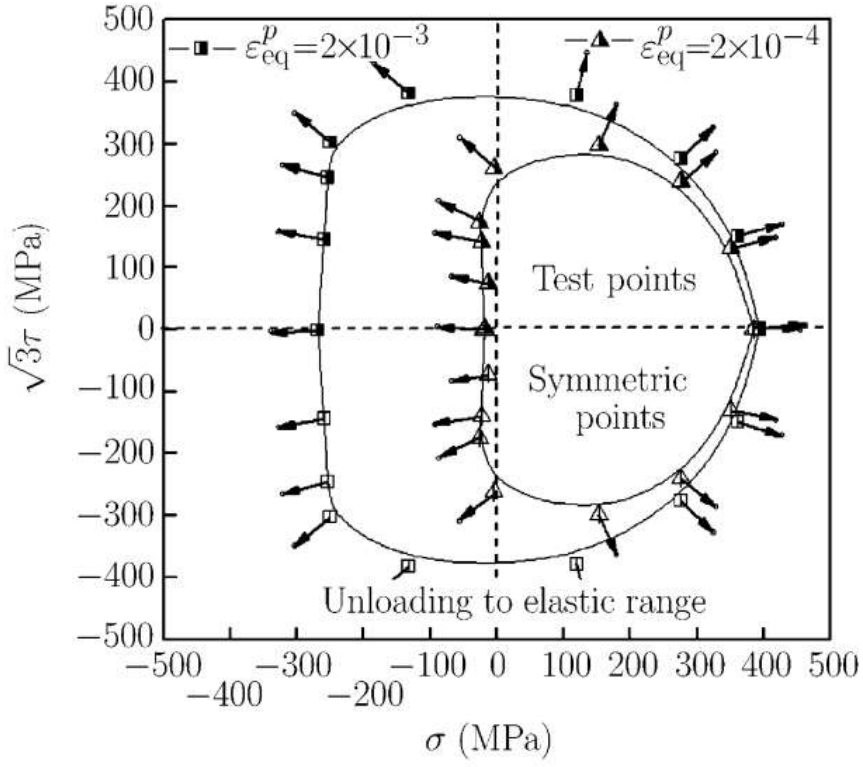

Figure 12.Yield surface measurement performed in axial torsion testing demonstrating adherence to Drucker's postulate with arrows identifying surface normal vectors [41].

1.5 Chemical Reactions in Corrosive Environments

In the absence of passivity, two types of reactions may occur when a reactive metal is immersed in a corrosive environment: anodic and cathodic. Anodic reaction results in active dissolutive corrosion as the work piece is slightly negatively charged, thus causing the metal cations to be released in solution. Cathodic reaction transpires due to the workpiece being

positively charged and thus leading to hydrogen absorption, diffusion, and embrittlement. Passivity occurs when an electrode develops a passive film that is thermodynamically stable in a reactive environment, resulting in the reduction of the anodic reaction rate. Stainless steel is passive due to a high level of chromium alloying (>10.5%) which contributes formation of a densely packed chromium oxide layer (CrO_3) on the surface of the metal [42]. This surface layer prevents the interaction of the corrosive environment with iron, thereby preventing anodic dissolution. The stability of oxidized surface films may be described by the Nernst equation which is derived from the standard thermodynamics of an electrochemical reaction cell with a pH and species A, B, C, and D with their corresponding coefficients:

$$aA + bB + mH^+ + ne^- \rightleftharpoons cC + dD. \quad \textbf{(21)}$$

The equilibrium solution between the components on the left and right side is thus given by:

$$E(V_{SHE}) = E^0 + \frac{RT}{nF} \ln\left(\frac{[A]^a[B]^b[H^+]^m}{[C]^c[D]^d}\right). \quad \textbf{(22)}$$

where [ ] denotes activity of the species, R is the standard gas constant, and F is Faraday's constants [43]. From this equation, equilibrium lines and Pourbaix diagrams, such as those shown in Chapter 4, may be used to determine the pH and breakdown voltage of relevant oxides into solution. The Nernst solution for water is stability as dependent on pH and Voltage is:

$$0.00V - 0.059V\ pH < E < 1.229V - 0.59V\ pH. \quad \textbf{(23)}$$

If the stable region of the Pourbaix diagram for the oxide in question falls within this inequality, then it is stable in water [44]. For example, CrO_3 is stable in water. However, despite the thermodynamic stability of protective oxide films on their surface, passive metals such as steel are still susceptible to local forms of corrosion. When immersed in sufficiently ionizing solution or with sufficient electrical charge, the surface films will develop holes near impurities or defects which allows ion exchange to occur. This phenomenon results in pitting if the material is locally

anodic or hydrogen absorption if it is locally cathodic. Pitting and hydrogen absorption may occur concurrently as pitting causes local pockets of acidified solution that leads to higher regional hydrogen concentrations to be absorbed by the material. This absorption process is described in greater detail in Chapter 5 but simply put is due to increased hydrogen solubility of the metal due to factors that include internal and applied stresses.

1.6 Organization and Objectives of Dissertation

In this thesis, the application of LSP for improvement of 316L stainless steel manufactured with LPBF is investigated from multiple studies. The investigation of LSP application for mitigation of back stress in rolled stainless steel (304L) in Chapter 2 develops the capability of LSP to interact with anisotropic plastic properties to great effect. Hysteresis tensile testing demonstrates a reduction to back stress in LSP-treated specimens compared to untreated ones. EBSD and OIM are employed to analyze the geometrically necessary dislocation GND density distribution in both un-peened and peened conditions, revealing a decrease in GND density on the surface of LSP-treated parts, correlating with the observed reduction in back stress. Grain morphology analysis indicates evidence of recrystallization, which contributes to the reduction of dislocations and alleviates residual morphological anisotropy due to rolling. Finite element analysis (FEA) simulations model the back stress and residual stress development, showing that LSP induces surface-level compressive back stress and residual stress, effectively countering tensile loading and potentially addressing yield asymmetry challenges in rolled steel sheets. These benefits are applied to LPBF 316L stainless steel in Chapter 3. Chapter 3 demonstrates the application of LSP to enhance back stress in additively manufactured 316L parts, addressing unique challenges arising from unusual hardening behavior and anisotropic mechanical properties of LPBF metal. LSP is demonstrated to mitigate tensile back-stress

hardening in additively manufactured parts, improving design utility and fatigue life. The method of LSP application to LPBF parts significantly influences back stress reduction, with analysis revealing insights into grain morphologies, texture, and plastic behavior through EBSD and CPFE modeling. After this initial investigation it is evident that the anisotropy of the additively manufactured metal interacted significantly with LSP. Furthermore, LSP benefitted the material properties of LPBF metal both at the surface and microstructural level, thus motivating further study of other possible improvements achievable by LSP postprocessing and their dependence on build orientation.

Chapter 4 explores the potential of LSP to modify the electrochemical and wetting characteristics of 316L stainless steel fabricated LPBF. As LPBF expands into fluidic applications and with the known application of LSP to high pressure welds, this study contributes to understanding of a ripened technological application that has not yet been explored. Given the variability in corrosion performance of LPBF stainless steel, postprocessing methods like LSP are sought to enable wetted surface applications. LSP has been shown to induce compressive surface stress, reducing corrosion rates in additively manufactured metal, while also enhancing hydrophobicity. Through various analyses including electrochemical impedance spectroscopy, potentiokinetic measurements, contact angle assessments, and surface characterization techniques, Chapter 4 demonstrates that LSP increases the pitting potential and electrochemical impedance, as well as enhances contact angle, suggesting its effectiveness in improving the corrosion behavior of LPBF stainless steel. This study of LSP affected corrosion behavior improvement is complemented by the Chapter 5 which explores the use of LSP postprocessing for stress corrosion cracking improvement. Chapter 5 showcases that LSP not only improves the time to crack initiation in LPBF 316L stainless steel during SCC testing but

also alters SCC behavior differently based on the treated surface. Analyzing factors like residual stress, texture, and microstructure alongside dynamic crack modeling provides insights into the mechanisms underlying these enhancements.

Chapter 2: Laser Shock Peening Induced Back Stress Mitigation in Rolled Stainless Steel

2.1 Introduction

Strain history in rolled steel sheets causes there to be a standard tension-compression yield asymmetry along the material's rolling direction [1]. This yield asymmetry results from residual back stress or a displacement of the material's yield surface due to the Bauschinger effect [2]. Back stress describes the internal frictional stress that resists loading as dislocations pile up at obstacles to glide such as grain boundaries. Residual back stress in as-received material introduces challenges in the design of forming and drawing manufacturing processes and also reduces fatigue life under loading at high strain amplitudes [3]. In forming and drawing manufacturing, yield asymmetry in as-received material exacerbates the disparity between the levels of hardness and fatigue strength in different areas of a subsequent part [4]. These disparities dictate failure-modes and anisotropic behavior corresponding to the shape and method of deformation. Metal spring-back behavior is also of concern during forming, as Bauschinger hardening causes erratic residual plastic strain dependent on the material's loading history [5]. The presence of back stress and kinematic hardening also requires that the design of forming and drawing techniques must be adjusted in order to achieve a desired structure, factoring in an increased number of hardening parameters [6]. As a result, parts such as those used in automotive engines often suffer from misregistry in manufacturing assemblage as strain softening induced by rolling and subsequent metal stamping produces unpredictable final shapes [7]. Further, back stress complicates analyzing fatigue life and requires modified models for failure estimation, standard methods having a tendency to overestimate the life of the part [8-9]. Due to these design challenges, it is of interest to reduce yield asymmetry and general anisotropy

in manufacturing rolled-sheet material, especially in materials such as 304L stainless steel whose low corrosive sensitivity and ductility make it attractive for mechanical design.

Annealing heat treatment may eliminate residual anisotropy and strain history in steel, but it also significantly reduces the material's yield strength and alters its design use. Thus, it may be desirable to modify the back stress of a material without reducing its yield. Other methods of reducing yield asymmetry, especially due to strong texture and tortuous grain morphology, are affected through four primary mechanisms: anisotropic strengthening, weakening of texture and grain-size control. Magnesium alloys and other hexagonal-cubic planed (HCP) metals tend to undergo different modes of plastic deformation in tension and compression, being harder in the direction that is most prone to twinning or according to texture orientations [10-12]. In HCP alloys, unlike FCC metals, precipitates and solid-solution strengthening have uniquely anisotropic hardening modes that can be used to combat characteristic asymmetry [13]. Equal channel angular pressing, multi-directional forging, pre-torsion and hot extrusion achieve grain refinement and texture weakening through recrystallization [14-17]. These microstructure-control methods tend to be unreasonable for application to rolled steel sheets. The development of a predominant bainite phase reduces the Bauschinger effect in chro-molly steel but this is unachievable in austenitic steel [18]. Laser shock peening (LSP) presents a method of back-stress reduction that does not significantly alter the grain morphology or phase composition of the material and is therefore attractive for reducing yield asymmetry in stainless steel sheets.

LSP observably affects microstructure and residual stress in metal targets, making it a potentially promising tool for mitigating tensile back stress along with its more well-known benefits to fatigue and strength performance. LSP is a surface treatment used to improve fatigue

life and corrosion resistance of metal parts [19]. LSP directs a high-powered pulsed laser through a transparent confining medium to strike a metal target which is covered in an ablative coating. The ablative layer absorbs the thermal energy of the laser pulse and turns to plasma, rapidly expanding into the ductile surface of the metal due to the constraint of the confining medium. The impact creates shockwaves that emanate through the metal part causing permanent plastic deformation. Several studies report that this process improves texture and refines grain structure, outcomes known to alleviate microstructural anisotropy [19-21]. Compressive residual stress is the most salient feature of LSP that is primarily responsible for arresting crack growth [22] . Similar compressive stress in the surface of gradient nanograined copper induces compressive back stress [23]. It is thus reasonable that investigating applying such a residual stress field to rolled steel may mitigate unwanted tensile back stress by moving the locus of the yield surface in the compressive direction.

This paper shows that LSP indeed reduces the back stress of rolled steel through both microstructural changes and yield surface changes. The back stress of LSPed and as-received samples is compared through hysteresis tensile testing. Electron back-scatter diffraction (EBSD) and orientation imaging microscopy (OIM) analysis examine both control and experimental sample microstructures as well as dislocation distributions before and after strain. Finite element analysis (FEA) of LSP and uniaxial strain employing non-linear kinematic hardening laws shows peening offsets the yield surface of the material in the compressive direction, measurably reducing the material’s bulk back-stress.

2.2 Background

2.2.1 Kinematic Hardening and Back Stress

Ductile metal kinematically hardens under loading when the central locus of its yield surface offsets in stress space, also known as the Bauschinger effect [24]. The underpinning causes for back stress development have been well discussed in and are widely attributed to the pile-up of dislocations at obstacles and grain boundaries [25]. These pile-ups generate internal friction stress, impeding dislocation glide and increasing the yield stress in the direction of the applied load. After back stress develops in either tension or compression, the material becomes softer when the load is reversed. This softening is due to repelling stresses between dislocations which cause the pile-ups to rapidly dissipate when loading is reversed, thereby assisting reverse yield. Figure 1 demonstrates the transformation of the yield surface during forward and reverse loading. After initial tensile yield, the material flows in compression at a much lower applied stress due to movement of the yield locus in the tensile direction.

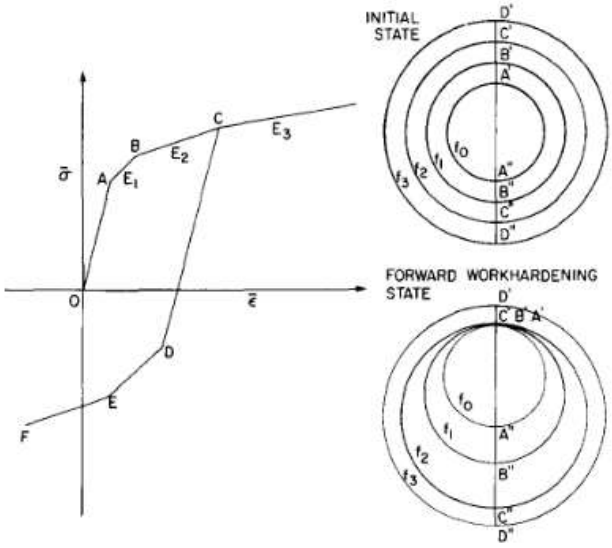

Figure 1. A loading and reverse loading curve illustrating the Bauschinger effect and the translation and expansion of the yield surface. The initial state shows isotropic expansion

of the yield surface and the forward work hardening state depicts the translation of the yield locus under kinematic hardening [26].

When significant back stress has developed, the displacement of the yield surface due to kinematic hardening may be measured without a full load reversal and can be extracted from tensile loading and unloading hysteresis testing [27]. After undergoing plastic strain followed by unloading, material with substantial back stress will experience unloading yielding. Unloading yield occurs at the point in unloading when the applied load is equal to the residual back stress due to dislocation pile-ups. As the applied load further diminishes, the dislocations run back towards their sources away from the obstacles at which they were pinned. The result is a noticeable nonlinearity in the stress-strain curve towards the end of unloading from which it is possible to extract a yield point. It is then assumed that the back stress established before unloading redevelops to the same level through reloading. Extracting reloading and unloading yields from tensile hysteresis enables calculation of the back stress at a given plastic strain. It is then possible to correlate measured back stress with microstructure and dislocation distribution within a material.

2.2.2 Geometrically Necessary Dislocations

Given that kinematic hardening results from dislocation pile-ups, observation of dislocation distribution gives insight into how back stress develops. Approaches for measuring dislocation density differ according to the type of dislocation. Ashby was first to distinguish between geometrically necessary and statistically stored dislocations (GNDs and SSDs), explaining the residual increase of dislocation density after plastic strain [28]. He established that though dislocation glide is the source of permanent deformation, non-mobile dislocations may be generated under plastic strain either from dislocation sources such as Frank-Reade sources or in order to accommodate strain gradients within grains. The former is the origin of SSDs while the

latter is the origin of GNDs. The presence of GNDs within grains results in lattice curvature which can be detected using EBSD and OIM analysis [29-30]. OIM analysis calculates the orientation gradient of each data point taken in an EBSD image. This gradient then correlates directly with GND density, factoring in Burgers vector and the slip systems according to phase. The SSD type is excluded from this analysis because such dislocations do not result from curvature and thus must be observed through direct visual observation such as through transmission electron microscopy. High GND density gradients near grain boundaries in the unloaded state correlate with back stress measurements in large grained tantalum [31]. Dislocations within pile ups are spaced increasingly far apart the further from a pinning obstacle they are, resulting in the creation of dislocation gradients. This behavior allows us to extrapolate back stress from the intensity of GND density gradients near barriers to glide. Ex-situ measurement complicates this analysis, but even in the unloaded state, a residual dislocation gradient is evident near obstacles such as grain boundaries. SSDs' contribution to back stress has yet to be quantified because they are invisible to OIM. By observing the microstructure and GND density distribution within the LSPed and as-received specimens before and after straining, we can observe the mechanics by which back stress may have been altered between the two groups.

2.2.3 Laser Shock Peening

LSP increases the fatigue life of metal parts through creating localized plastic deformation in the surface of metal targets. The impact of the expanding plasma generates high strain rates ($\sim 10^6 s^{-1}$) under the surface of the peened material, creating first elastic then dislocation shock waves emanating from the site of impact [20]. The shock waves dissipate the deeper into the target they penetrate until the waves of applied stress reduces below the

material's Hugoniot limit and no further plastic deformation occurs [22]. The plasma expansion forced into the target by the confining medium causes the metal to try to expand outwards, but the surrounding material restrains its expansion. This process leaves a profile of compressive residual stress extending typically 0.5-1.2 mm under the surface of the peened part [19]. The compressive force acts to hold closed hairline fractures and cracks, thereby increasing the parts fatigue life. LSP has even been used to heal fissures after they have formed [32]. Compressive residual stress has the effect of resisting tensile applied stress and also assisting reverse yielding. The result is to displace the yield surface of the material in the compressive direction, thereby diminishing tensile back stress. This effect is aided by alterations made to the material's microstructure.

The shock waves produced by LSP create several dislocation fronts which transform from dislocation cells into nano-grains, new grain boundaries and residual dislocations as the shock wave expands. The resulting grain refinement, dislocation structure and plastic lattice rotation has been widely observed through TEM and EBSD [33-36]. Application of a high enough LSP pressure to 304 stainless steel causes recrystallization, achieving grain refinement producing more equiaxed grains [33]. Below this pressure threshold the stored strain energy within residual dislocations is such that upon annealing, significant grain refinement and recrystallization can be produced, a tool that has been used to tailor the microstructure of additively manufactured parts [37]. Residual dislocations are also associated with a measured hardness increase local to the LSPed surface [36]. It may be counter intuitive that a process known to create hardening dislocations reduces the back stress of a material given that increased GND density gradient corresponds to increased back stress. However, as detailed by Ashby [28], dislocations in a polycrystalline material have many sources and only generate back stress when

they contribute to resisting the applied load. The dislocations created by LSP harden in compression, which is the mode of yield tested by standard hardness tests. However, by kinematically hardening the material in compression these dislocations assist yield in the material in tension by developing compressive back stress. This effect combined with the compressive residual stress profile, recrystallization, and dislocation annihilation produced by LSP is here shown to contribute to creating a bulk back-stress reduction in material with pre-strain tensile back stress.

2.3 Experimental Procedure

The samples come from 3.175-mm-thick rolled and annealed 304L stainless steel manufactured to the AMS 5511 standard. Wire electrical discharge machining (EDM) cut both control and experimental tensile specimens to a standardized ASTM E8 geometry. Four dog bones were prepared for LSP treatment while four were left as-received; all were cut such that the rolling direction is the same direction as the applied tensile load. A Quanta-Ray Lab Series, Q-switched Nd:YAG Spectra Physics laser was applied LSP to the front and back surfaces of the experimental samples' gauge length. Directed through an acrylic confining medium and set at a 100 Hz rep rate, 10 ns pulse width, and 150 mJ pulse energy the laser ablated a layer of Polyester 3M tape on the surface of the tensile sample below. The two groups of resulting samples are shown representatively in Figure 2. The diameter of the spot size applied to the surface of the sample is around 400 μm. The stage holding the sample moved at a 40 mm/s and each peen center is located 400 μm from the next in the same row. The resulting plastically deformed peen indentations are smaller than the laser spot size as visualized in Figure 3 through optical profilometry. An MTS 7k electromechanical machine strained each sample to 3% before unloading to zero load and reloading to 4% total strain (Figure 4). For EBSD observation, both

strained and unstrained samples were cut using wire EDM to maintain the existing stress distribution. Electropolishing with phosphoric acid, sulfuric acid, and glycerin solution at 0.167 A/mm^2 for ten minutes prepared samples for microscopy, using Teflon tape to mask the sides. The polishing removed approximately 100 μm of material. Lin et al [38] provides the solution chemistry for polishing. EBSD was performed using a Zeiss Sigma VP scanning electron microscope an EDAX Hikari Plus EBSD camera and EDAX TEAM analysis software.

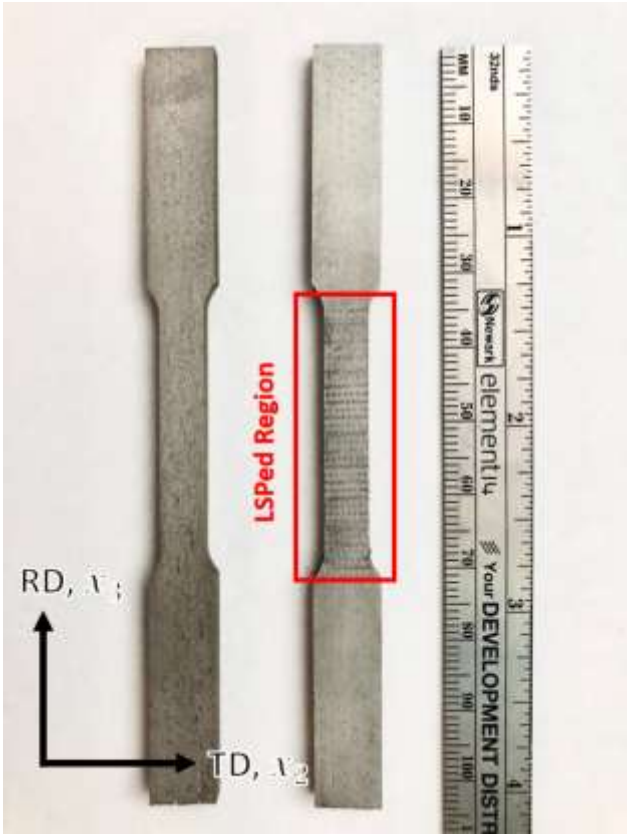

Figure 2. a) As-received sample, b) LSPed sample. The gauge length has LSP applied to both front and back. The laser ran across the transverse direction at a 40 mm/s speed. Each row is spaced approximately 400 μm apart. The x_2 and x_3 directions identify the axes of the simulation.

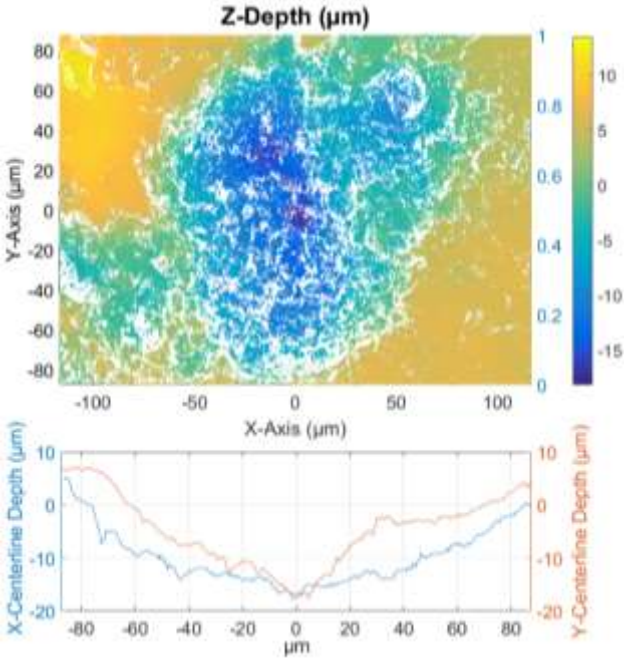

Figure 3. Representative depth profile of an LSP indent as measured by optical profilometry. The diameter of the observable plastic deformation is approximately 180 μm in both x and y directions and reaches a depth of 17 μm.

2.4 Numerical Modeling

LSP pressure loading and continuum kinematic hardening as modelled by Abaqus simulates experimental results. LSP impacts are applied to the surface of a quarter model of the experimental specimen's gauge length with dimensions 3 mm × 1.5 mm × 3 mm. Twenty pulses are applied to the x_2-axis surface (Figure 2): five per row and four per column as produced by the 40 mm/s stage speed in the experiment. After peening, a ramped surface load gradually applies 422 MPa in the x_{33} direction to simulate uniaxial tension. Boundary conditions enforce symmetry on three sides for both LSP and uniaxial tensile loading.

It is standard to assume that LSP has minimal thermal effect on the surface of the metal target, given that the ablative layer absorbs the majority of the laser's thermal energy and converts it into an expanding plasma [39]. The estimation used here assumes the pressure profile to be gaussian and the laser pulse intensity develops as a triangle wave with a ten-nanosecond

pulse width. Solving the coupled differential equations below calculates peak pressure development:

$$P(t) = \frac{Z}{2}\frac{dL}{dt} \quad \textbf{(1)}$$

$$I_{peak}(t) = \frac{Z}{2}\left(1 + \frac{3}{2\alpha}\right)\left(\frac{dL}{dt}\right)^2 + \frac{3}{4}\frac{Z}{\alpha}\left(\frac{d^2L}{dt^2}\right)L \quad \textbf{(2)}$$

where $P(t) =$ peak pressure at the LSP interface as a function of time t, $Z = \frac{2Z_1Z_2}{Z_1+Z_2} =$ combined impedance of the LSP interface ($Z_1 = \ 3{,}960\frac{kg}{cm^2}$ impedance of steel, $Z_2 = 320\ \frac{kg}{cm^2}$ impedance of Acrylic), $L(t) =$ peak plasma thickness, $\alpha =$ parametric fraction of internal energy that increases the thermal energy of the plasma, and $I_{peak}(t) =$ peak laser intensity [39-40]. Given the laser intensity, the maximum peak pressure is found to be 6 GPa and $P(t)$ develops approximately according to a triangle wave. A user subroutine supplies the pressure input into the simulation, developing peak pressure as a triangle wave with the same pulse width as the laser.

A standard Hooke's law describes elastic behavior with a Young's modulus of E= 155.44 GPa as derived from regression fitting to experimental stress-strain. After von Mises yield, the material undergoes combined kinematic and isotropic hardening. A nonlinear iteration of Ziegler's linear kinematic hardening law models the back stress development after LSP and due to uniaxial tension:

$$\dot{\boldsymbol{\alpha}}_k = \frac{C}{\sigma^0}(\boldsymbol{\sigma} - \boldsymbol{\alpha})\dot{\bar{\epsilon}}^{pl} - \gamma_k \boldsymbol{\alpha}_k \dot{\bar{\epsilon}}^{pl} \quad \textbf{(3)}$$

where $\boldsymbol{\sigma}$ = the stress tensor, $\boldsymbol{\alpha} =$ the back stress tensor, $\boldsymbol{\alpha}_k =$ the k^{th} back stress tensor component, $C =$ kinematic hardening modulus, $\dot{\bar{\epsilon}}^{pl} = \sqrt{\frac{2}{3}\dot{\boldsymbol{\epsilon}}^{pl}:\dot{\boldsymbol{\epsilon}}^{pl}} =$ the equivalent plastic strain rate ($\boldsymbol{\epsilon}^{pl} =$ plastic strain), $\gamma =$ an exponential hardening parameter, and $\sigma^0 = \sqrt{\frac{3}{2}(\boldsymbol{S}-\boldsymbol{\alpha}^{dev}):(\boldsymbol{S}-\boldsymbol{\alpha}^{dev})} =$ the size of the yield surface ($\boldsymbol{S} =$ deviatoric stress tensor, $\boldsymbol{\alpha}^{dev} =$ deviatoric component of the back stress tensor) [41]. Assuming only one additive back stress tensor component and uniaxial tension along the x_{33}, $(\boldsymbol{\sigma}-\boldsymbol{\alpha})$ reduces to $(\boldsymbol{\sigma}-\boldsymbol{\alpha})_{33} = \sigma^0$. Thus, the back stress along the loading direction changes as:

$$\dot{\alpha} = (\,C - \gamma\alpha)\dot{\bar{\epsilon}}^{pl} \tag{4}$$

Integration over half of a loading cycle with an initial pre-strain and back stress yields the following:

$$\alpha = \frac{C}{\gamma}\left(1 - e^{-\gamma(\bar{\epsilon}^{pl}-\bar{\epsilon}_0^{pl})}\right) + \alpha_0 e^{-\gamma(\bar{\epsilon}^{pl}-\bar{\epsilon}_0^{pl})} \tag{5}$$

given $\alpha_0 =$ the initial back stress and $\bar{\epsilon}_0^{pl} =$ the initial equivalent plastic strain. With combined isotropic and kinematic hardening, the yield surface size increases exponentially so that the applied stress is given by:

$$\sigma = \sigma|_0 + Q_\infty\left(1 - e^{-b\bar{\epsilon}_0^{pl}}\right) + \alpha \tag{6}$$

where $\sigma|_0 =$ yield stress without strain, $Q_\infty =$ maximum size of the yield surface, and $b =$ the exponential rate of increase of the yield surface size up to the maximum. To model the as-received material, the hardening equation parameters are fit in STATA to measured back stress

and experimental stress-strain curves with. Further parameter exploration finds the closest match with the LSPed experimental data. Firstly, the back-stress hardening Eq. (5) is fit to the measured back-stress and strain, yielding $\alpha_0 = 150$ MPa, $\bar{\epsilon}_0^{pl} = 0.022$, $\gamma = 50$, and $C = 1.19$ GPa (R^2=0.97). The back-stress hardening equation with fit parameters is then input into isotropic hardening Eq. (6) whose parameters are fit using stress-strain data. The resulting fit parameters are $\sigma|_0 = 256$ MPa, b = 300, and Q_∞ = -0.593 MPa (R^2=0.77). This initial yield and initial equivalent plastic yield indicate that the material is indeed pre-strained. The Q_∞ value indicates a moderate contraction of the yield surface. Contraction has been observed to be a feature of a flattening of the yield surface due to kinematic hardening [42]. To model LSP, high-strain rate material properties are also required as an input into the model. The high strain-rate yield ratio up to 10^4 is taken from the literature [43]. Both the LSP and tensile loading were implemented in ABAQUS Explicit.

2.5 Results and Discussion

2.5.1 Back Stress Determination

Tensile testing conducted on as-received and LSPed specimens allowed comparison of stress-strain and back stress development. Each specimen was strained to 3% before unloading to zero load and reloading to 4% total strain. The testing was repeated on four specimens of each group. A typical stress-strain curve may be seen in Figure 4 for an as-received specimen and LSPed specimens show similar patterns. The average 2%-offset initial plastic yield is measured as 343.3 MPa and 360.9 MPa for as-received and LSPed groups respectively. The LSPed samples demonstrate a compressive yield-surface offset upon both tensile and hysteresis loading. Softening of the tensile yield in the shock treated group supports findings from unloading-

reloading analysis showing back stress was reduced in the LSPed samples as compared to the control specimens.

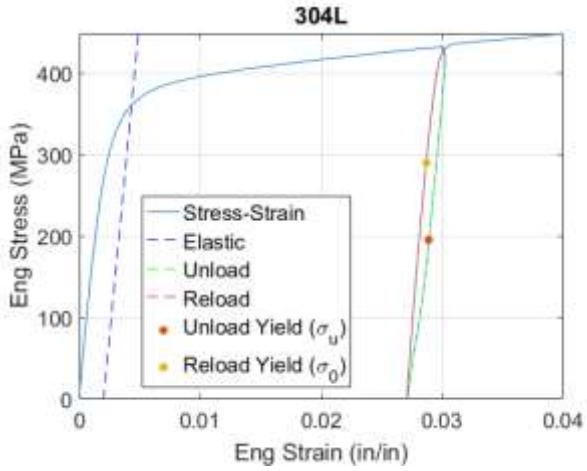

Figure 4. Typical tensile stress-strain curve in as-received specimens. LSPed specimens showed comparable behavior. The initial plastic yield occurs at the intersection of the dashed-blue elastic line marking a 2%-offset from zero elastic strain. The average of the unloading yield and reloading yield is near the measured back stress given that the thermal stress is small.

To derive back stress from stress-strain hysteresis, plastic and elastic responses must be individuated. Unloading and reloading yield are used in calculating back stress:

$$\sigma_b = \frac{\sigma_u + \sigma_0}{2} - \frac{\sigma^*}{2} \quad \textbf{(7)}$$

where $\sigma_u =$ unloading yield stress, $\sigma_0 =$ reloading yield stress, and $\sigma^* =$ thermal relaxation component of plastic flow [27]. The thermal flow adjustment (σ^*) factors in creep relaxation at the start of unloading. In the original formulation of deriving back stress from unloading-reloading hysteresis, Yang et al (2016) identifies unloading yield as a 5%-15% deviation from elastic behavior [27]. As seen in Figure 5 the unloading stress-strain has a distinct elastic regime as demonstrated by the flattened portion of the tangent modulus. The tangent modulus is evaluated by calculating the regression slope of a neighborhood of 65 points at each point of the

unloading curve. This number of points allows a sufficient amount of smoothing to reduce noise. The slope of the tangent modulus curve is then calculated using 20 neighboring points and the minimum point of the second-derivative of the unloading curve is considered the center of the elastic response. The tangent modulus at the center of elastic unloading is the adjusted elastic modulus or the unloading elastic modulus (E_u). The unloading yield (σ_u) is marked as the lowest stress during unloading that has a 5%-15% deviation from E_u. The highest stress of the reloading curve that has a 5%-15% deviation from the E_u marks the reloading yield point (σ_r). Thermal relaxation stress (σ^*) is calculated as the difference between the stress at the beginning of unloading and the stress at the beginning of the unloading elastic regime.

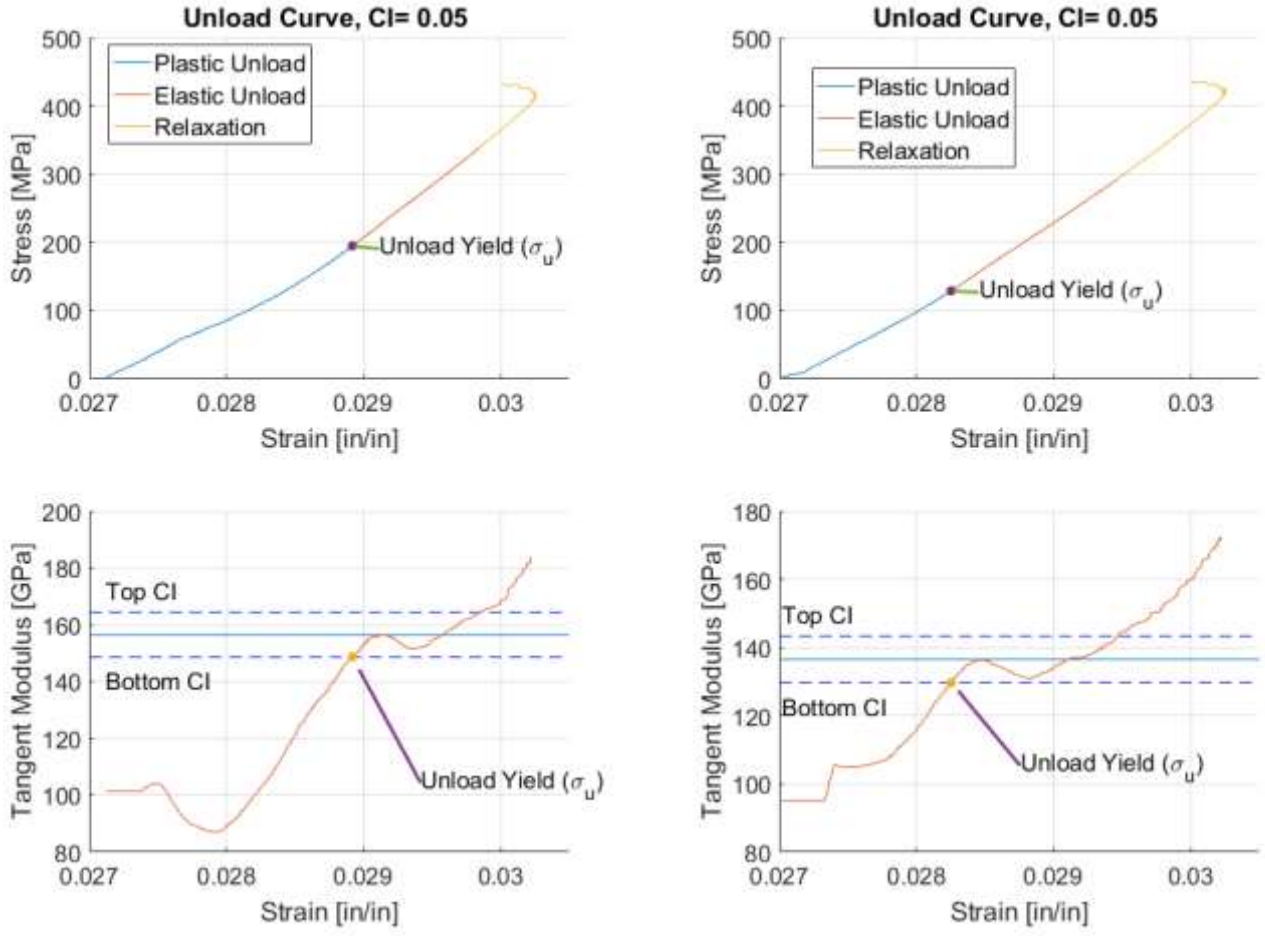

a) b)

Figure 5. Unloading curve and unloading yield definition at 3% strain for an a) as-received sample and a b) LSPed sample. The elastic response is defined as occurring between the top and bottom confidence interval (CI) which is ±5% of the elastic unloading modulus. The LSPed sample exhibits a longer elastic response with a lower unloading yield, therefore indicating a lower back stress.

The average back stress of the LSPed materials at 5%, 10%, and 15% unloading yield definitions are 131.1 MPa, 152.0 MPa, and 170.1 MPa respectively. The back stress of the as-received samples at 5%, 10%, and 15% unloading yield definitions are 194.5 MPa, 196.9 MPa, and 202.0 MPa respectively. Figure 6 shows the distribution of back stress calculations according to each definition and compares the result with simulation. The difference between the LSPed and as-received samples is most prominent at the 5% yield definition. As seen in Figure 5 the as-received material has an elastic regime that ends at a higher stress and that is also shorter than in the LSPed material, indicating a higher back stress. On average, the back stress reduction under these three definitions is 23.7%, which is not insignificant and indicative of the effectiveness of LSP in reducing back stress under the conditions investigated.

2.5.2 Numerical Simulation

Although the simulation also shows a back stress reduction by LSP, the model underestimates the bulk-averaged reduction to back stress after strain, compared with experimental results in Figure 6. However, this is likely because it does not factor in microstructural changes such as recrystallization. Furthermore, the material response modelled by implicit Abaqus rate-dependent plasticity is a simplification of the true hydrodynamic fluid-like behavior of the material at high strain [44]. Simulation also assumes only a single component of the back stress tensor to refrain from over fitting the data; a larger data set fit with multiple back stress components may create a more accurate reduction. Simulation shows that with increased pressure and or with multiple LSP applications the reduction improves. It is

feasible that with increased LSP density and increased laser power, back stress could be reduced further. The modest reduction to the bulk back stress within the simulation model shows that microstructural changes that are not accounted for in the numerical simulation play a dominant role in adjusting the sample's yield surface.

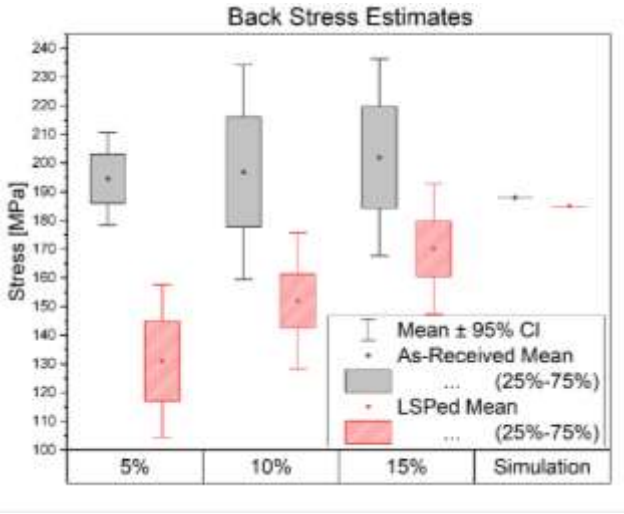

Figure 6. Back stress in the as-received and LSPed samples at all unloading yield definitions and from simulation. The bars represent standard deviation. Back stress results are calculated with the unloading yield evaluated at 5%, 10%, and 15% deviation from elastic behavior, demonstrating a reduction in LSPed samples for all three definitions. The simulation results after pulling show only a 3.5 MPa reduction in bulk-averaged back stress as compared with the as-received sample, which is discussed below.

To further explore the simulation results, spatially resolved back stress distributions are investigated. Simulation identifies that LSP treatment locally reduces the pre-existing back stress near the surface, an effect that lasts through uniaxial tension. Figure 7 demonstrates that the maximum reduction to the back stress occurs at the surface at the point on the material that experiences the highest pressure due to LSP. The decrease is extremely local to the region of plastic strain region due to LSP and decays exponentially outward from the point of impact up to a depth of 250 μm. At the point of peak applied pressure the reduction changes the back stress 180 MPa to -16.7 MPa. The back stress profile after LSP is unlike the residual stress profile

which shows the maximum reduction after peening occurs at a depth of 130 μm with a compressive residual stress of -94.5 MPa but the depth of compressive stress extends to 350 μm. Evidently the compressive plastic flow nearest the point of peening relaxes the residual stress while maximally reducing the back stress. After strain the back stress increases according to Eq. (3), and the difference between the surface and center of the material reduces. If uniaxial tension were to continue, the difference would eventually diminish entirely. The residual stress reduction decays by an even greater extent after strain and the depth of affect is also reduced.

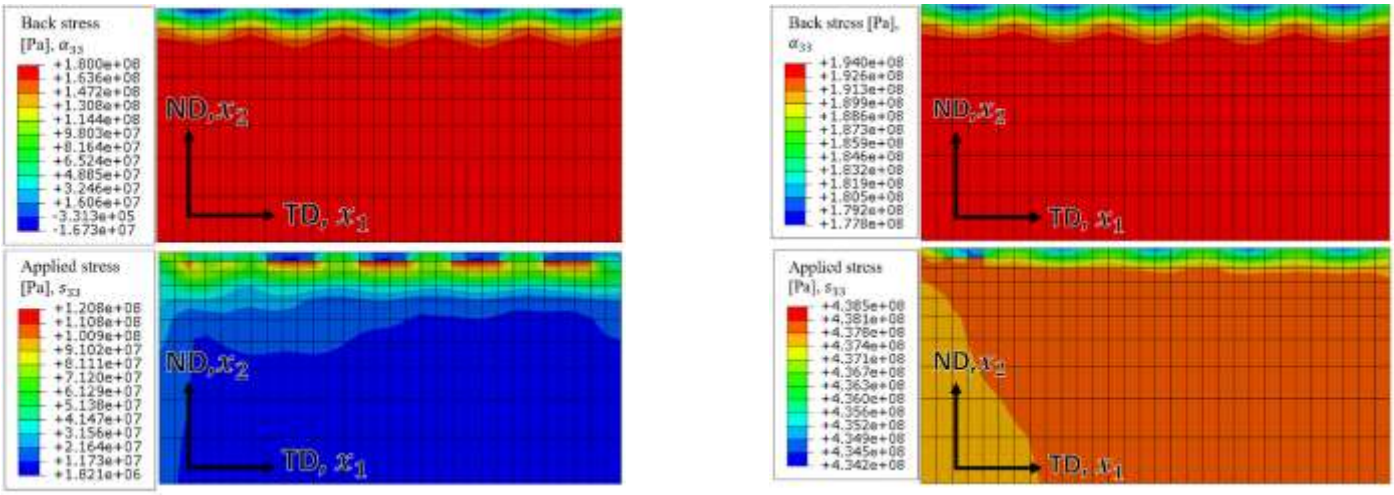

a) b)

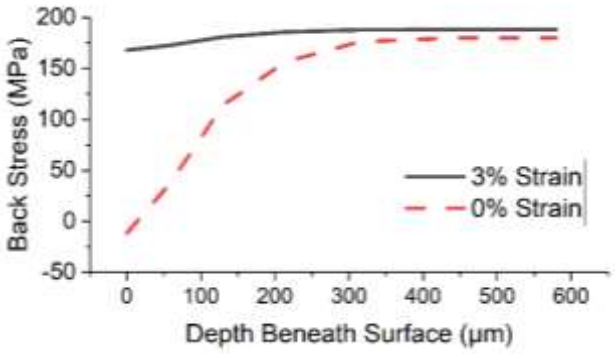

c)

Figure 7. Cross-section of simulation results in an LSPed sample showing uniaxial applied stress (s_{33}) and back stress (α_{33}) a) before tension and b) after 3% strain. As seen in c) the back stress is reduced by LSP in a layer up to 250 μm deep directly under the cite of peening. This reduction near the LSPed surface is lessened after pulling but the depth of the affected area remains the same. The residual stress reduction penetrates to 350 μm but the depth of the residual stress diminishes after strain.

2.5.3 EBSD Analysis

EBSD imaging and TSL OIM analysis of the microstructures of control and experimental samples construes the yield surface displacement made due to grain morphology and dislocation distribution changes. The majority of the microstructure in both LSPed and as-received samples is austenite. EBSD phase identification reveals the as-received composition was 90.5% austenite, 8.7% cementite, 0.2% martensite, 0.5% iron epsilon and 0.1% iron alpha. The LSP composition was nearly the same showing 90.5% austenite, 8.6% cementite, 0.1% martensite, 0.6% iron epsilon and 0.1% iron alpha. Multiple images were taken of the top surface (rolling direction (RD) × transverse direction (TD)) as well as of the cross-section (normal direction (ND) × (TD)) though only a representative four images are presented here with different analysis processing.

2.5.3.1 IPF and Texture

Inverse pole figure (IPF) images (Figure 8 a)) of the as-received unstrained material show weak texture and identifiable orientation gradients within large grains especially near grain boundaries. Residual effects of rolling manufacturing are observable. Several grains are slightly elongated along the RD and also contain mechanical twins primarily sheared along the RD. Clusters of small grains and annealing twins likely resulted from recrystallization due to heat treatment but it is evident that the temperature increase was not held long enough to sustain complete stress relief and grain renewal. The average grain size is 10.82 μm in diameter. After LSP (Figure 8 c)), the microstructure has fewer long thin grains with an increase in the fraction of equiaxed grains free of twins or else with lenticular recrystallization twins. This has been previously noted to evidence the creation of new grains due to dislocation shock wave expansion [33]. There is still some residual mechanical twinning along the RD in large grains. After straining to 4% total strain, both the as-received samples and LSPed samples (Figure 8 b) & d))

have much more pronounced orientation gradients within both large and small grains, as well as significantly more twinning and a larger representation of small grains which is typical of plastic strain.

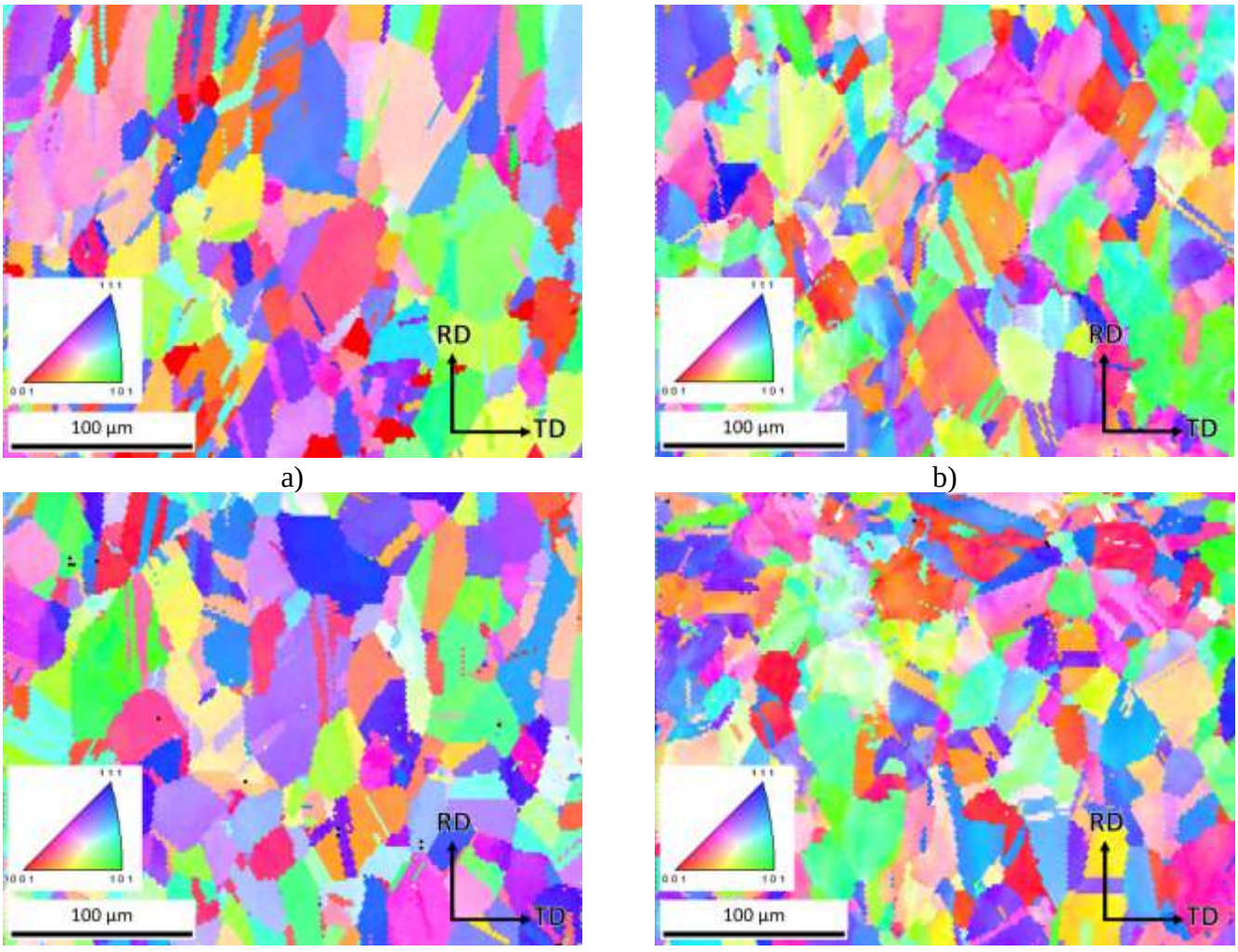

Figure 8. Inverse pole figures (IPF) of top surface in the as-received samples in a) unstrained and b) 4% strained conditions and LSPed samples in c) unstrained and d) 4% strained conditions. Moderate grain refinement and an increase of equiaxed grains can be observed in the LSPed samples both before and after plastic strain.

2.5.3.2 GND Distribution

The lack of a strong texture and very large grains in the as-received sample along with the evident high unloading yield measured in tensile testing indicates dislocation pile-ups are dominant in contributing to yield asymmetry in rolled and annealed 304L steel. TSL OIM

analysis directly observes GND distribution, using the austenite FCC $\{111\}[1\bar{1}1]$ slip system for calculation. As seen in Figure 9 a), the as-received material shows a level of GND density of pileups near grain boundaries and near twins, as a result of rolling. Within around 50 μm of the LSPed surface, there is observed a moderate increase in level of GND density as compared with the as-received samples (Figure 10 c)). However, at 100 μm deep, the LSPed sample exhibits a slightly lower intensity of such dislocation pileups with a distinctly lower peak density near grain boundaries (Figure 10 c)). After straining, both LSPed and as-received samples show significant increase in GND density in general, GND pileups occurring along planes that are close to twinning shear and near the end of lenticular twins in particular. It is important to note such GND dislocation pileups are more severe in as-received sample than the LSPed sample under strained condition. Thus, LSP reduces back stress. Pileups are also most intense within small grains showing maximum GND density near grain boundaries.

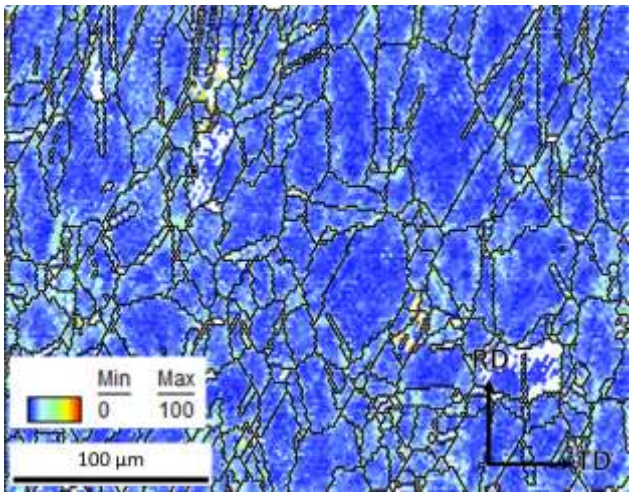

a)

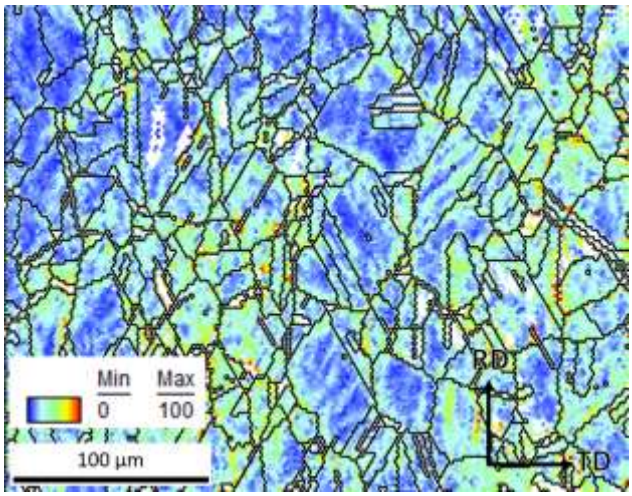

b)

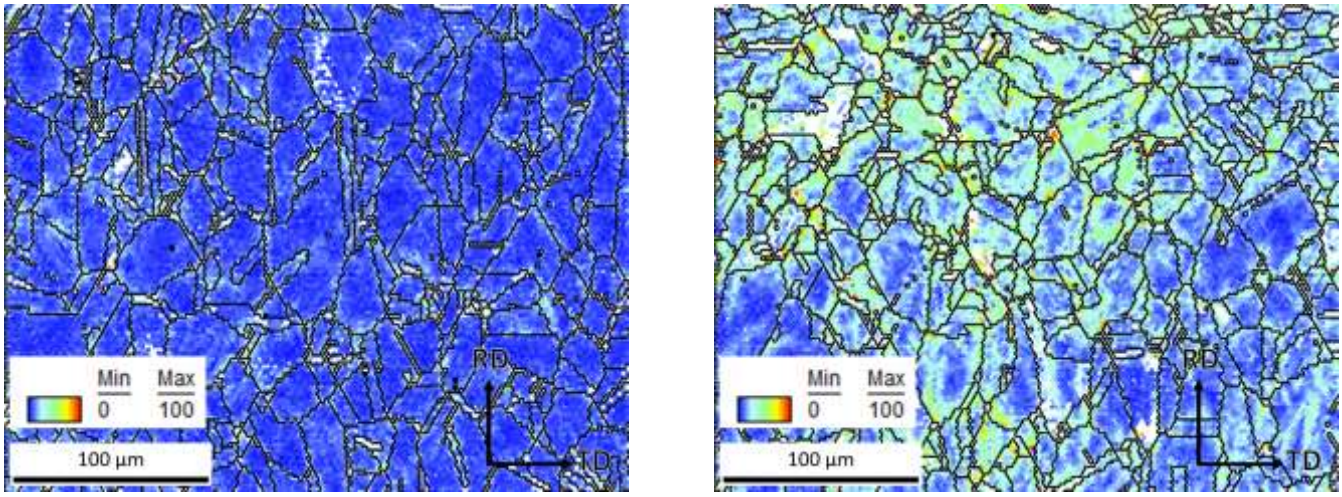

c) d)

Figure 9. GND density maps of the top surface in the as-received samples in a) unstrained and b) 4% strained conditions and LSPed samples in c) unstrained and d) 4% strained conditions. The color bar range is between 0-100 1012/m2. White areas are above this range and are excluded to reduce overestimation noise as recommended in the TSL OIM manual. The grain boundaries are defined as 15° misorientation. The as received and strained material (Fig. 9 b) exhibits higher GND density accumulation near grain boundaries than in the LSPed and strained material (Figure 9 d)).

Plotting the GND density against their distance to the nearest grain boundary quantifies the GND-density gradient near obstacles to glide which illuminates the mechanism by which LSP reduces back stress. To reduce noise, data points with higher than a 100 $10^{12}/m^2$ GND density were omitted from this qualification. In this calculation, the grain boundary is defined as a scan point that contains a boundary with at least a 15° misorientation relative to its neighbor. Each EBSD point has a set of coordinates in µm within the EBSD scan. Dependent on the EBSD step size, the scan records data at either 1 µm, 1.5 µm, or 2 µm increments in x and y. The distance between a given data point and all grain boundary points is calculated and the minimum of these distances is taken as the distance of that point to the nearest grain boundary. Due to the discrete step size of the EBSD scans, the nearest distance calculation is discrete, with the minimum distance being 0 µm the next distance being 1 µm. Thus, average GND density is

calculated by binning each scan point into a rounded-down distance bin and taking the average of each bin.

From the plots in Figure 10 a), it is evident that at depth of 100 μm the level of GNDs is slightly reduced after LSP and this result is sustained through uniaxial tension, especially as seen in the top surface. Before straining, the GND density and gradient is slightly higher in the as-received sample. The gradient difference is small but still distinct. A regression analysis finds that the slope of the as-received GND-distance data is -0.77 while the slope of the LSPed GND-distance data is -0.68. After straining, the GND density level increases in both the as-received and LSPed samples. The level of GNDs in as-received samples after strain is higher than in the LSPed and strained samples. However, the GND density gradient is increased in the LSPed sample after strain with a slope of -1.18 compared to the -0.87 slope in the as-received sample. Noted also is that the magnitudes of both of these slopes are increased along with the level of GND density as compared with the unstrained samples.

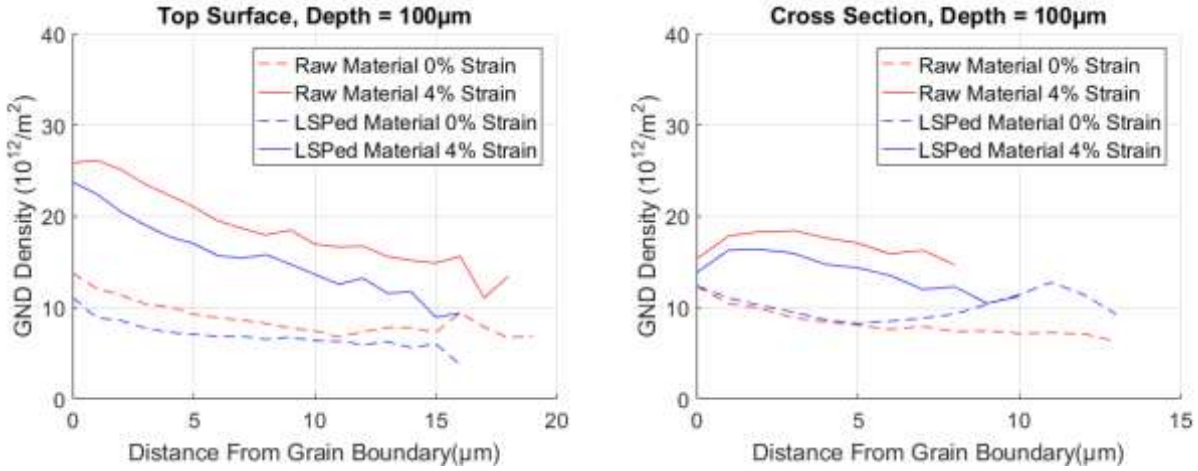

a) b)

Figure 10. Average GND density vs distance from grain boundary in the top surface (a) and in the cross section (b) at 0% and 4% strain provided for both LSPed and as-received materials. Cross section images taken before tensile strain (c-d) show a marginal increase of GNDs near the peened surface as compared with the untreated sample. The cross-section

measurements in (b) are taken at 100 μm beneath the top surface. The top surface images are taken at 100 μm deep due to the depth of polishing show a higher GND density level in the as-received material in both strained and unstrained material. The GND density gradient is higher in the as-received material before strain but not after. The cross section shows no GND density gradient in either sample.

Evaluating dislocation pile-ups ex-situ is a challenge because upon unloading, dislocations run back to their sources, thus homogenizing the distribution of GND density and softening in reverse loading. In a loaded state, a high GND density gradient near grain boundaries is indicative of dislocation pileups which contribute to back stress and assist reverse loading when they flow away from their pinning barriers. However, in an unloaded state an increased level of homogenous GNDs may still indicate high back stress because once loading begins, these evenly distributed dislocations are likely to run back towards pinning barriers, redeveloping dislocation gradients and arresting dislocation glide. From this understanding coupled with the parameters discovered in the non-linear fit of the continuum back-stress laws, it is possible to construct a narrative. In the as-received material, back-stress was predeveloped to 150 MPa (according to the nonlinear fit of Eq. (5)) with pre-existing GND pile-ups. LSP reduced the dislocation pileups and thus back stress. Tension and subsequent unloading caused the as-received sample to experience more reverse plastic strain than the LSPed sample going through the same loading-unloading regime. This is due to the higher back stress initially present in the as-received material which increased the unloading yield so that reverse yielding occurs for longer than in the LSPed sample. This longer regime of reverse yield decreases the number of GND pile-ups at the grain boundaries while still maintaining a higher level of GND density overall. In cross-section images, neither the raw nor the LSPed samples exhibit significantly high GND density gradient. This is a logical result because the TD and ND directions do not have

known yield asymmetry or back stress. It must now be answered how LSP could have reduced GND density gradient and thus back stress in the rolled specimens.

Reduction in GND density gradient due to LSP beneath a marginal GND density increase near the treated surface may be attributed to dislocation annihilation and recrystallization caused by compressive shock. In annealed materials the dislocation motion due to LSP causes grain refinement as dislocation wave fronts expand from the cite of impact, forming cells and subsequently sub-grain and grain boundaries [20]. This expansion of dislocations typically induces a marked increase in dislocations near the surface of the material [35]. In rolled steel with dislocation structures that contribute to characteristic anisotropic back stress, the expanding cells created by LSP may break apart sessile tangles deeper under the surface and show a reduction in GND density, especially in newly formed grains. Recrystallization is known to reduce GNDs and high-power LSP induces grain-refinement in 304 steel [33,45,46]. It is therefore reasonable to construe that recrystallization due to LSP is a driving force in the observed dislocation reduction. Dislocation annihilation may also result from a similar mechanism to GND density reduction observed in load reversal. Dislocation cells made by tensile pre-stain at low and high temperatures can be unstable upon compression, such that immediately after small amounts of compressive plastic strain the material also shows a reduction in GNDs [47] [48]. Dislocation annihilation has been observed in unloading and load reversal during metal-forming spring-back as well [49-50]. Compressive stress caused by LSP acts similarly to this load reversal, neutralizing obstacles prevalent in the material's microstructure.

2.5.3.3 Subsurface Recrystallization

Recrystallization as a source of dislocation reduction can be evinced by multiple forms of EBSD analysis. The misorientation-angle histograms are given in Figure 11. These histograms also make evident an increase in the high-angle grain boundaries above 25°. Such an increase in high-angle boundaries indicates recrystallization [33]. High-angle grain boundaries (HAGBs) have been characterized as misorientation exceeding 15° which also matches the IPF imaging. HAGBs may result from recrystallization under plastic strain and correlate with recrystallization in LSPed 304L [33, 51]. While this increased representation of HAGBs in the LSPed sample is not sustained through tensile testing, the effects of the reduction to back stress is lasting.

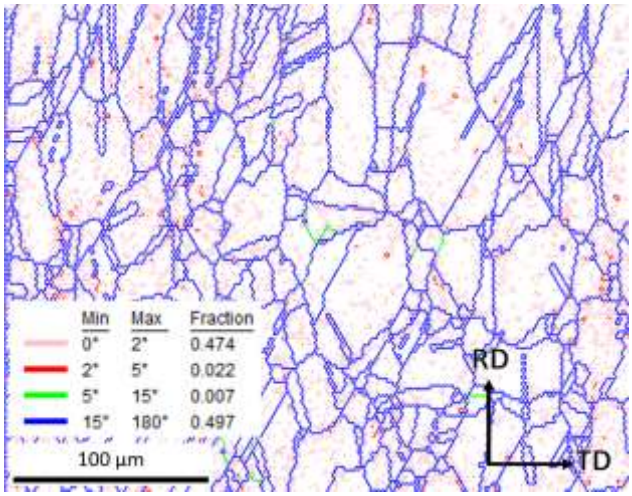

a)

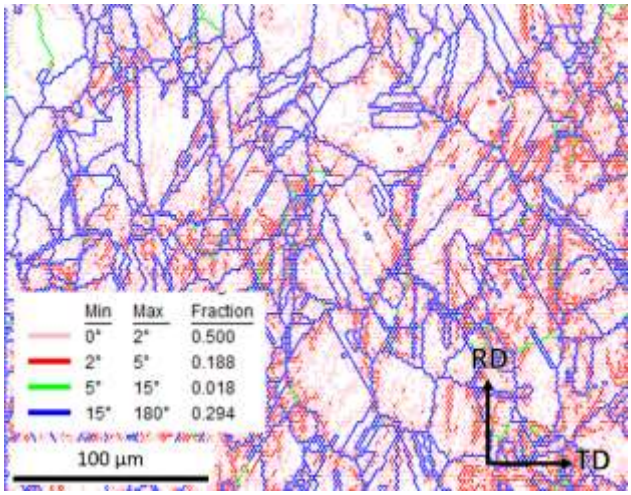

b)

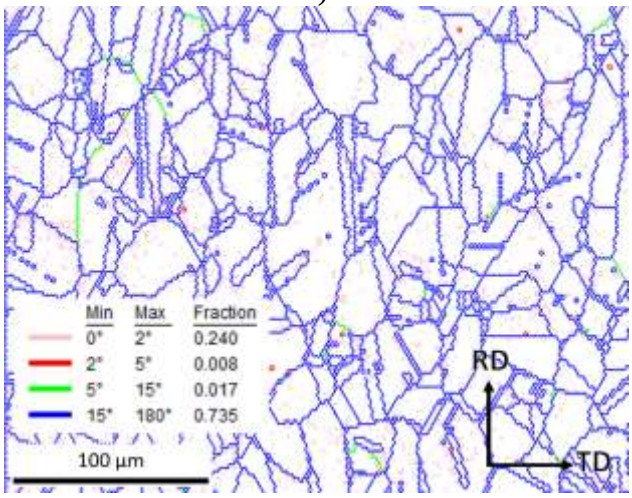

c)

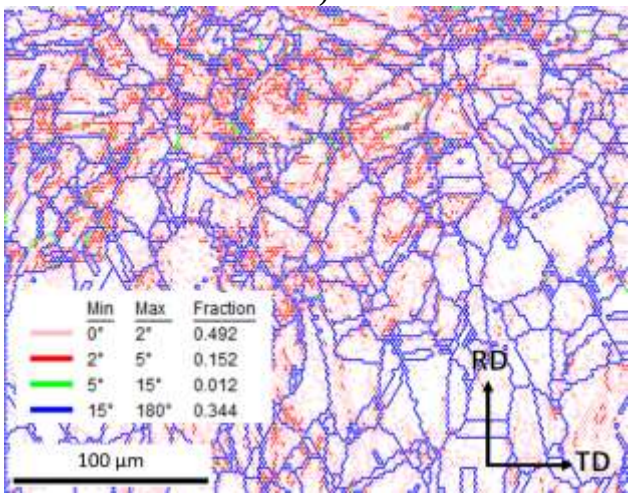

d)

Figure 11. Misorientation-angle histogram of the grains on the unstrained top surface of a) the as-received sample and b) the LSPed sample. Misorientation above 15° is considered a high-angle grain boundary (HAGB). The LSPed sample shows a distinctly higher representation of HAGBs which indicates recrystallization by dislocation annihilation.

Recrystallization twinning due to LSP can be directly observed through characterization within the EDAX TSL OIM software. The primary recrystallization twinning mode of FCC is identified as a 60° rotation about the <111> axis [52]. This identification can be used to show parent-daughter recrystallization in the as-received and LSPed scans. Figure 12 presents two representative scans. The original grain boundaries are given in black. The LSPed material has a larger area-fraction occupied by twinning daughter grains which, when compared with the IPF image of the same scans in Figure 9, are shown to be many of the more equiaxed grains. This form of twinning occurs during primary recrystallization as a low fault-energy mis-stack of newly formed lattice planes [45]. Dislocation cells grow and form boundaries, creating new grains with low dislocation density and as the lattice planes stack, recrystallization twins occur. Recrystallization likely also generates a more equiaxed grain morphology which further may cause a decrease in bulk back stress.

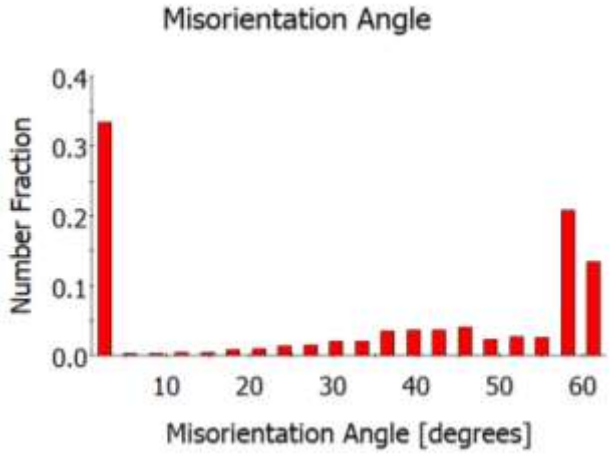

a)

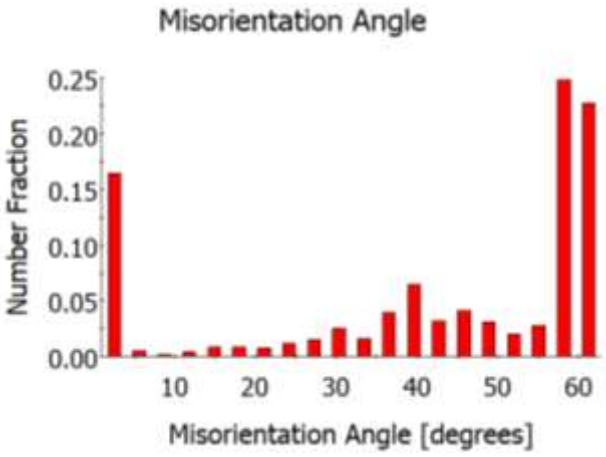

b)

Figure 12. Representative parent-daughter images of the unstrained top surface of a) the as-received sample and b) the LSPed sample. The white regions are non-twinned grains and the total fractions of parent and daughter twins are out of total twinned area. Recrystallization twinning is identified as a 60° rotation about the <111> axis in austenite. LSPed scans show a greater representation of daughter grains than in the as-received samples indicating recrystallization due to dislocation shock wave expansion.

2.5.3.4 Aspect Ratio

Grain morphology is known to be a fundamental factor in the inter and intra-granular stress state of a polycrystalline material. As viewed in Figure 13, the microstructure is significantly more equiaxed after LSP. A single-tailed student t-test of the aspect ratios for the grains of the unstrained samples reveals a statistically significant difference between LSPed and as-received conditions at a 95% confidence interval. The mean aspect ratio of the LSPed grains is 0.454 with a sample size of 525 grains and a standard deviation of 0.141. The mean aspect ratio of the as-received sample is 0.429 with 586 grains and a standard deviation of 0.144. Furthermore, as seen in Figure 13 a) & c) the equiaxed grains in the LSPed sample dominate a larger proportion of the area fraction. The strained LSPed sample has a higher average aspect ratio than the strained as-received sample with a mean of 0.422 as compared with 0.415. The grain population is 412 in the LSPed strained sample and 426 in the as-received strained sample;

the standard deviations are 0.147 and 0.155 respectively. At a 95% confidence this difference does not prove statistically significant. After uniaxial tension, plastic strain along the pulling direction dominates the samples grain structure.

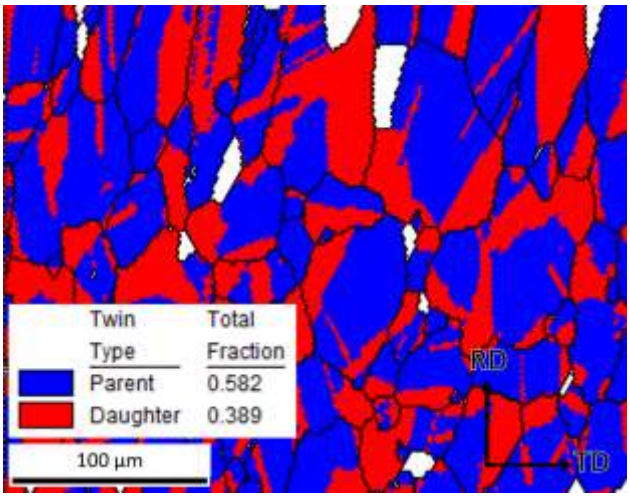

a)

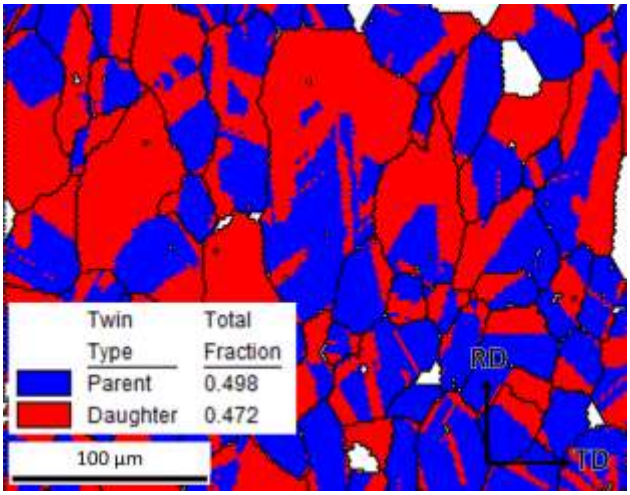

b)

Figure 13. Aspect ratio images of the top surface in the as-received samples in a) unstrained and b) 4% strained conditions and LSPed samples in c) unstrained and d) 4% strained conditions. An increase in the area occupied by equiaxed grains in the LSPed samples directly results in a decrease of bulk-averaged back stress as derived analytically using the Eshelby inclusion solution.

The increase in the aspect ratio in the LSPed material independently reduces long-range back stress. This is because higher aspect ratio inherently reduces the back stress within a grain all else equal. Back stress along an axis of a grain is equal to the shear stress resisting twinning. The Eshelby inclusion solution for shear stress within a penny-shaped grain in an elastic continuum is known [53]. From this derivation, back stress can be calculated as the following:

$$\alpha = \frac{\nu - 2}{4(1-\nu)} \pi \frac{a_2}{a_1} s \quad \textbf{(8)}$$

where $\nu =$ Poisson's ratio, $a_2 =$ the transverse grain diameter, $a_1 =$ the grain diameter along the axis of tension, and $s =$ the twinning shear. The elongated grains in the as-received material are seen to have their largest diameter along the tension direction. Thus, an increase in the aspect ratio decreases the $\frac{a_2}{a_1}$ component of the back stress. The tendency of the recrystallized grains in the LSPed material to be more equiaxed therefore inherently reduces back stress.

2.6 Conclusion

LSP reduces back stress by primarily creating compressive plastic strain in the surface of the material which is a well-known result in literature. This effect causes dislocations to pile up at obstacles to compressive yield, causing the yield surface to shift or elongate in the compressive direction. Upon tensile loading, the dislocations run away from these compressive obstacles and cause tensile yield at a lower stress than compressive yield. Isotropic hardening combined with kinematic hardening may occur, however the yield asymmetry of a sample with tensile back stress is reduced. An improved aspect ratio due to grain shape changes also contributes to reducing back stress. More broadly, LSP mitigates yield asymmetry in rolled stainless steel by augmenting the surface characteristics of the part through three mechanisms: 1) compressive residual stress, 2) compressive back stress, and 3) recrystallization. LSP-induced

compressive residual stress has been established by others as the primary mode of fatigue life improvement. This compressive stress also resists tensile loading, causing the yield surface of the metal to be displaced in the compressive direction. LSP also causes surface-level compressive back stress as shown by experiments and FEA modelling established non-linear hardening theory. The compressive back stress neutralizes existing tensile back stress when bulk averaged and reduces the back stress developed during tensile load. Beneath the surface hardened layer of the LSP-treated parts, the GND density is less before and after plastic straining, correlating with the measured back stress reduction. Grain morphology analysis shows evidence of recrystallization which both alleviates residual morphological anisotropy due to rolling and also likely contributes to the reduction of dislocations. This paper demonstrates LSP may be applied to rolled stainless steel to overcome the problems presented by yield asymmetry in addition to the already well-known effect of fatigue life improvement.

Chapter 3: The Effect of Laser Shock Peening on Back Stress of Additively Manufactured Stainless Steel Parts

3.1 Introduction

Laser shock peening (LSP) is typically used to process metal for fatigue life improvements in traditionally manufactured parts. [1] This process has been studied in detail for inducing compressive residual stress, which is responsible for arresting hairline fractures during fatigue loading and delaying stress corrosion cracking. [2, 3] LSP also has a strong effect on dislocation structure and distribution causing a distinctive increase in geometrically necessary dislocation (GND) density in metal targets near the peened surface as well as a noticeable grain refinement and increased misorientation. [4, 5, 6, 7] The dislocation shock waves produced by LSP have been observed to mitigate the tensile back stress of rolled stainless steel. [8] These authors have published finite element simulation results showing LSP processing causes bulk back-stress reduction via a highly localized compressive layer of back stress that overlaps with the compressive residual stress profile which LSP is known for introducing. [8]

LSP is being investigated as a post-processing tool for additively manufactured (AM). [9] The effect of LSP on the measured tensile back stress of metal AM parts is as yet unstudied and is of particular interest due to the tortuous grain morphologies and dislocation distribution within 3D printed metal. The presence of back stress, also known as the Bauschinger effect, in AM steels is heightened due to both the high number of GNDs and dislocation cells in the as-built state and due to the heterogenous microstructure. [10] Parts with increased back stress display a lower resistance to random fatigue. [11] This is attributed to materials with high back stress developing a smaller plastically strained “shielding” volume which precedes ahead of cracks. [12] Therefore, materials with a high back stress have more catastrophic crack propagation and

are thus more susceptible to weakening due to overloading and underloading. [12] Back stress also complicates analysis of fatigue life and spring-back causing challenges for failure design. [13, 14, 15] It is therefore desirable to investigate post-processing techniques such as LSP for the reduction of back stress.

Metal AM is poised to disrupt industry and in recent years both the public and private sector have increasingly been investing in progressing relevant technology. [16] Metal AM has the potential to radically reduce manufacturing waste and environmental impact as well as improve rapid prototyping processes and low-volume production. [17] Selective laser melting (SLM) or laser powder-bed fusion (LPBF) is hailed as one of the most promising forms of metal AM due to its high dimensional accuracy among other benefits. [18] However, this form of AM is still plagued by complications that act as stipulations for design. Artifacts of the build process include unique microstructural and mechanical characteristics that are introduced by the complex thermal history and temperature gradients occurring during fusion. In particular, dislocations are mired within unusual texture and microstructures to cause anisotropic properties.

The SLM build process produces both a high density of dislocations and directionally-dependent internal structure, which causes back-stress hardening and subsequent challenges when fabricating for structural use. The primary form of dislocation generation in 316L AM stainless steel has been attributed to thermal strain history and is affected by the rate of cooling, temperature gradient, and scanning strategy of printing. [19, 20] Dislocation density is high within 3D printed steel—typically around 10^{13}-$10^{14}m^{-2}$, imparting both micro-scale and long-range stresses. [19, 21] Grains near the melt-pool undergo plastic strain due to thermal expansion stresses and thus accumulate GNDs as they are forcibly confined by the surrounding material. Gradient microstructures, which have been linked to back-stress hardening, also occur inherently

in AM steel. [22, 23] Grain structure depends on the ratio of solidification rate to temperature gradient, causing either cellular or dendritic growth. [24, 25] Grains tend to grow towards the centerline of the melt-pool, forming new grain boundaries at the surface. Cooling influences dendritic separation which also coincides with dislocation cell spacing in SLM metal. [26] Mosaic or "checker-board" macrostructures are often observed due to rotation of the scanning pattern between layers. [27, 28] In builds with rotation between layers, the surface remelting of the previous layer causes epitaxial growth in the current build layer along the melt-pool boundaries of the previous layer. [29] The result is a pattern of rhomboid grain structures the size of the melt-pool with larger central grains surrounded by smaller sub-grains. This variance of grain-size based on location is characteristic of gradient microstructures and poses barriers to slip that encourage back-stress hardening. The prevalence of low-angle grain boundaries and solute segregation in AM stainless steel are also observed as providing significant obstacles to slip. [30] In-situ observation of dislocations in loading-unloading-loading cycles of AM metal shows that GNDs tend to be annihilated upon unloading in a manner that is heightened at greater strains. [31] This behavior indicates the development of back stress during forward loading with mobile dislocations rebounding upon unloading to assist reverse yield. Strong crystallographic texture and grain elongation along the build direction further contribute to mechanical anisotropy. [32] Cubic crystal cells tend to grow either in a [100] or a [110] texture depending on the energy density used. [33, 22] As a result of these properties, yielding and fatigue life vary according to the alignment of the loading direction to the building direction. [34] In particular, the back stress in SLM 316L is characterized as being distinctly tensile due to the metal's yield being stronger in tension than compression. [21] The presence of yield asymmetry due to back stress is a detriment to a part's fatigue behavior under selected loading conditions.

High residual stress is also prevalent and its distribution within 3D printed parts is contingent on the build orientation and parameter specification. [21, 36, 37] Residual stress forms in AM due to the temperature gradient mechanism (TGM) in which the plastic expansion of a heated zone is confined by the surrounding material so that upon cooling there is a region of compressive residual stress surrounded by a zone of tensile residual stress. [38] This effect occurs when layers underneath the build layer are heated and cooled, resulting in a part with a core of compressive residual stress surrounded by an outer layer of tensile stress. [38, 39] Residual stress profile and magnitude is dependent on scanning strategy and process parameters. [37, 40] This residual stress can cause large part distortions, brittle fracture, a reduction in fatigue life, and susceptibility to stress corrosion cracking. [41] Stress can be alleviated by in-situ heating of the build as well as various forms of post-processing such as hot-isostatic pressing, annealing, surface remelting and LSP. [36, 42, 43]

Solving the issues of residual stress, mechanical asymmetry and anisotropy improves the applicability of metal 3D printing technology to structural design. While many of these features are mitigated effectively by forms of annealing and hot isostatic pressing, the side-effect is softening and it does not also induce beneficial properties. [21, 43, 44] LSP processing of AM metal has the potential to create advantageous compressive residual stress, improve fatigue life, and, as studied here, reduce tensile back stress. LSP has been investigated as both an in-situ and post-processing technique for improving mechanical properties of AM parts. [45, 46] The effects of the in-situ process have been studied experimentally and through simulation, resulting in a beneficial compressive residual stress three-dimensional profile, deeply penetrating into the part. [42, 47] It has also been shown to have promise in healing cracks during the build as well as closing pores. [48, 49] As a post-processing mechanism for AM parts, many varied applications

have been studied. It is shown that LSP induces a surface of refined grains and increased dislocation density as observed in traditionally manufactured parts. [50] It also has been shown to improve fatigue behavior of additively manufactured parts in a similar fashion to traditionally manufactured parts, namely by producing compressive residual stress. [51, 52] In one study, Lu et al [53] found that LSP post-processing hardened and strengthened the specimens according to their build direction: in particular, horizontally built specimens were hardened and strengthened more than specimens built vertically. Lu et al hypothesized that this is due to LSP increasing inter-layer diffusion in horizontally built samples and decreasing the interlayer bonding in vertically built samples. [53] However, this analysis is currently untested and lacks observation of the interlayer micro-mechanics. Another effect produced by LSP post processing has been observed upon annealing the AM and LSPed samples and examining the microstructure under the processed surface. [54] An investigation of the surface-level microstructure under the LSPed surface shows significant grain recrystallization after annealing with the dislocation cells produced by LSP serving as seeds for more equiaxed grain growth during heat treatment. [54] There is also some interest in using the residual stress produced by LSP to shape parts, allowing the deeply penetrating strain to curve metal parts back into their desired form. [45] The application of LSP to mitigate back stress in AM parts has potential as demonstrated by its previously studied effect on rolled stainless steel. [8] Due to the unique influences of microstructure and texture in AM metal, to further understand the effect of LSP, it is crucial to complement experiments with simulation methods that takes these defining mechanisms into account.

The effect of LSP on back stress in AM parts is here quantified through hysteresis tensile testing and simulation. Of particular interest is the interaction of build orientation with the

direction of LSP. Texture and microstructure are examined using electron back-scatter diffraction (EBSD) before and after LSP as well as before and after 4% strain. Statistical regression shows that LSP only reduces back stress in samples aligned with the build direction. The cause of this reduction is examined through a multi-crystal rate-dependent CPFE simulation which factors in grain orientation, residual strain, and initial back stress.

3.2 Crystal Plasticity Modelling

Crystal plasticity finite element (CPFE) models assess the influence of texture and microstructure upon the mechanical properties of a material and has been applied to AM structures. Given that so many aspects of the resultant AM part are dictated by build process, simulation allows parameter investigation which can provide insight into how to tailor the build for design use. Sub-grain formation and crystallization simulations articulate how process parameters directly affect the texture and structure. [58, 59] CPFE simulation shows how this texture and structure affect bulk material properties. The mechanical effect of phase content and distribution within parts has been studied. [60] Polycrystalline CPFE has been used to quantify the effects of residual stress, back stress, microstructure morphology, and texture upon fatigue life, yielding, and stress-strain response. [21, 60, 61, 62, 63] These models tend to adhere to the basic form of CPFE in which grains are defined as either individual elements or groups of elements with an assigned crystal structure and orientation that reflects experimentally measured microstructure and texture. To model texture development, grain-specific strain, and back stress hardening, this paper largely follows the crystal plasticity modeling by Chen et al [6], which builds upon the work of Kalidindi et al [64] and Asaro and Needleman [65]. Key relations and steps are briefly summarized here. A representative volume of 8000 elements is used. Each element in the model is an individual FCC crystal and the resolved stress upon the element is

solved using the Eshelby inclusion solution and therefore assumes equiaxed grains. [66] The use of equiaxed grains causes an underestimation of the back-stress hardening behavior because it would not capture the effect of aspect ratio on material properties. See the section on "Texture and Microstructural Effects" for more details. The use of equal-sized equiaxed grains is inherent to the solution mechanism due to volume averaging. The solution for translating the polycrystalline aggregate strain to slip-system strain within each individual crystal follows Taylor's solution. [68] The FCC crystals are defined as having 12 {111}[110] slip systems each of which follow a rate-dependent hardening model. The plastic shearing rate follows a power law:

$$\dot{\gamma}_i^{\,p} = \dot{\gamma}_0^{\,p} \left| \frac{\tau_i - b_i}{s_i} \right|^{\frac{1}{m}} sgn(\tau_i - b_i) \tag{1}$$

in which $\tau_i =$ the resolved shear stress, m = strain rate sensitivity, s_i = shear rate resistance, and $b_i = \boldsymbol{B}: sym(\boldsymbol{m_i} \otimes \boldsymbol{n_i})$ a measure of back stress. The shear-rate resistance evolves continuously and is conditional on the rate of slip causing the hardening law to be rate dependent:

$$\dot{s} = \sum\nolimits_j h_{ij} \left| \dot{\gamma}_j^{\,p} \right| \tag{2}$$

where

$$h_{ij} = q_{ij} h_0 \left(1 - \frac{s_j}{s_s} \right)^a \tag{3}$$

with $q_{ij} =$ the symmetric latent hardening matrix. The diagonal elements of q_{ij} are 1 while the off-diagonal elements are 1.4. The off-diagonal elements are the ratio of the latent hardening rate to the self-hardening rate. The hardening values are defined as the initial hardening rate $h_0 = 250\ MPa$ and the saturation resistance $s_s = 447\ MPa$ while $a = 0.023$. The measure of back

stress is dependent on the slip system direction and normal vectors $\boldsymbol{m_i}$ and $\boldsymbol{n_i}$ as well as the back-stress tensor **B.** The back-stress tensor is calculated through integrating:

$$\dot{\boldsymbol{B}} = \sum_{j=1}^{12} h_b e^{-k\gamma_j^p} \dot{\gamma}_j{}^p sym\left(\boldsymbol{m_j} \otimes \boldsymbol{n_j}\right). \quad \textbf{(4)}$$

In equation (4), h_b and k are material constants. Texture and residual strains are introduced into the model by assigning each grain of the representative volume a grain orientation and residual strain from measurements. While this model is unable to take into account the unusual grain shapes present in AM parts, assigning the model texture from EBSD scans enables simulation of the influence texture has upon the hardening behavior of the material, particularly the back stress. The back stress, strain and texture can be extracted from each element according to grain family which allows comparison with EBSD results. Given that texture and grain rotation is a key method of plastic strain analysis, we must be able to identify typical modes of grain rotation using EBSD.

3.3 Experimental Methods

The effects of build orientation and LSP on the back stress, texture, and dislocation distribution of AM stainless steel were characterized by using tensile testing, EBSD, and CPFE. Thirteen standard ASTM E8 dog-bone samples were built using LPBF and 316L stainless steel powder. All dog-bones had the same dimensions with outside dimensions 101.5mm × 9.5mm×3.2mm. 6 samples were built in the XY orientation with the build direction (BD) oriented along the axis of peening and 7 samples were built in the XZ direction with the transverse direction (TD) oriented along the axis of peening (see Figure 5). The loading direction (LD) is perpendicular to the TD and BD in both orientations. These build orientations will from now on be referred to as XY and XZ. The build parameters: 0.04-mm layer thickness, energy densities of 57.7, 90° rotation between scan direction between layers, and 21-50 µm powder size.

The front and back of the gauge length of all samples were mechanically polished followed by electropolishing. LSP was applied to the front and back of the gauge lengths of the test specimens. The test group comprised of 4 of the XY-built and 3 of the XZ-built dog bones while 3 of the XY-built dog bones and 3 of the XZ-built dog bones were left untreated as control samples. The sample-size asymmetry is due to laser availability for processing. A Spectra Physics Q-switched laser was used to peen the parts with a 700-μm diameter spot size set at 9.5 GW/cm^2 laser intensity. The pulse width is 10 ns and the repetition rate is 100 Hz. The LSP was applied with 75% overlap. The ablative coating used was 3M Polyester tape and the confining medium was 0.25-inch-thick clear acrylic. A method of hysteresis tensile loading developed by Yang et al [23] and detailed in a previous study [8] was used to evaluate back stress. The unloading yield of the samples was defined as the point where the tangent modulus deviated from the unloading elastic modulus by 5%. The samples were pulled to 3% strain, unloaded, and reloaded to 4% strain. This range of loading captures the back stress at low plastic strain therefore best capturing the immediate hardening effects due to LSP. This range is also most relevant to low cycle fatigue. EBSD was performed before and after LSP and also before and after strain on the same grains.

3.4 Results and Discussion

3.4.1 Back Stress Characterization

The LSPed samples exhibited a plastically deformed peen approximately 500 μm in diameter and 4 μm deep as measured by stylus profilometer. The polished surface of the material after peening shows uneven deformation along the indent boundaries. Tensile testing revealed that LSP consistently created a lower back stress in XY samples but did not do so consistently in XZ

samples. The average back stress across all 13 samples is 149.81±80.74 MPa. To ascertain such a difference is statistically significant, the regression table shown in Table 1 is presented to show statistically significant differences in back stress between the XZ and XY builds. Two dummy variables are defined for build orientation (XY=1), whether the sample has been LSPed (LSPed=1) and an interaction term between the build orientation and whether the sample has been processed (XY*LSPed = 1). The table demonstrates that when considering a single variable at a time, the result seems to suggest that the effect of build direction is not significant enough (p=0.026) nor the effect of LSP (p=0.251). When these two variables are considered together, however, the XY*LSPed interaction term shows that LSPed samples built in the XY orientation have an effect on back stress at a high significance (p<0.01).

Table 1. Regression table of ANOVA analysis showing the effect of build direction and LSP processing on the back stress measured by tensile testing. Dummy variables are defined as "XY"=1 denotes the build is the XY orientation, "LSPed"=1 indicates the sample is LSPed, and "XY*LSP"=1 is an interaction term where the build orientation is XY and it is LSPed.

Variables	Coef.	95% Conf. Interval		p-value	Sig.
XY	128.75	19.39	238.1	0.026	**
LSPed	58.75	-50.61	168.1	0.251	
XY *LSPed	-247.61	-403.2	-92.00	0.006	***
Constant	127.66	43.98	211.3	0.008	***
Mean dependent var		149.81	SD dependent var		80.74
R-squared		0.68	Number of obs		13

****p<0.01, **p<0.05*

Figure 1 depicts these results by showing the predicted means and 95% confidence interval of LSPed and as-built samples for both build orientations. As seen, there is significant overlap of the mean confidence intervals for LSPed and as-built samples built in the XZ orientation but not in the XY orientation. In the XY orientation, the lack of confidence interval overlap between

processed and unprocessed means shows that there is a significant difference between the two. Furthermore, performing an F-test rejects the null hypothesis that the LSP dummy variables (LSPed and XY*LSPed) have no effect upon the data at a 99% confidence. This reinforces that LSP statistically significantly affects back stress overall. As such, LSP is shown to significantly reduce the back stress of AM metal in the XY-build orientation but has no significant effect upon the XZ-built samples.

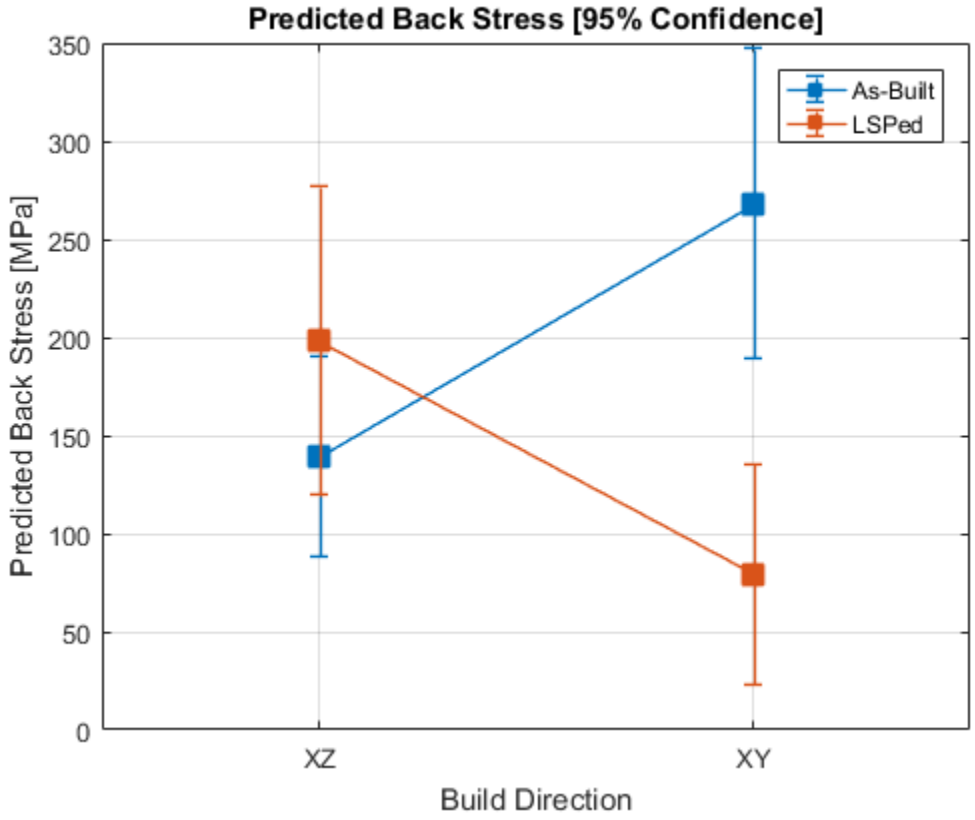

Figure 1. Predicted average back stress for as-built and LSPed samples for both build directions holding manufacturer constant (Manufacturer 2 = 0.62). The 95% confidence intervals of the LSPed and As-Built samples overlap significantly for the XZ samples but do not overlap for the XY samples. This shows that the build-direction effects the ability of LSP to reduce back-stress in additively manufactured parts.

From this analysis, the effect that LSP has upon back stress is dictated by the orientation of the build with respect to loading and peening. LSP evidently only is able to achieve a significant

back stress reduction in XY-built samples and there is an interaction between the direction of peening, the direction of build, and the direction of loading. As previously discussed, Lu et al [53] also noted that LSP had a stronger hardening and strengthening effect on tensile samples built in the XY orientation and peened in the BD than those built in the XZ orientation and peened in the TD. It is therefore unsurprising that the effect of LSP on back stress is also more pronounced for the XY orientation. While Lu et al [53] theorizes that this is due to layer bonding, they do not consider textural effects, nor do they examine the microstructural effects of different build orientations. To understand further the effect of build orientation on LSP-induced back stress mitigation, EBSD is performed upon samples before and after LSP as well as before and after loading.

3.4.2 Texture and Microstructural Effects

The difference in response to LSP between the build orientations is rooted in the alignment of the direction of processing and tensile loading with the sample's internal anisotropy. The directionality of the microstructure is one of these contributing factors. Characteristic three-dimensional grain maps for the two build directions are shown in Figure 2 a) and b). As shown in Figure 2, a distinct mosaic morphology dominates the samples and grains have an elongated structure along the BD. This morphology is oriented differently in the part according to build orientation so that in the XY build, the plane with mosaic structure is normal to the axis of peening, while in the XZ build it is perpendicular. The effect of elongated grains upon tensile back stress development has been studied as the "aspect-ratio effect." [67] It has been shown that the higher the aspect ratio of a grain, the more back stress develops in transverse loading because of an increase in the number of obstacles to slip causing dislocation tangles. In the tested samples, the axis of tensile loading is oriented transversely to the elongated grain structure and

contributes to heightened back stress development. The orientation of the grain direction also affects the impact of LSP on the back stress of the different builds. The XZ samples have a larger number of grain boundaries acting as barriers to the plastic strain induced by LSP and thus should show less plastic strain after LSP than the XY samples.

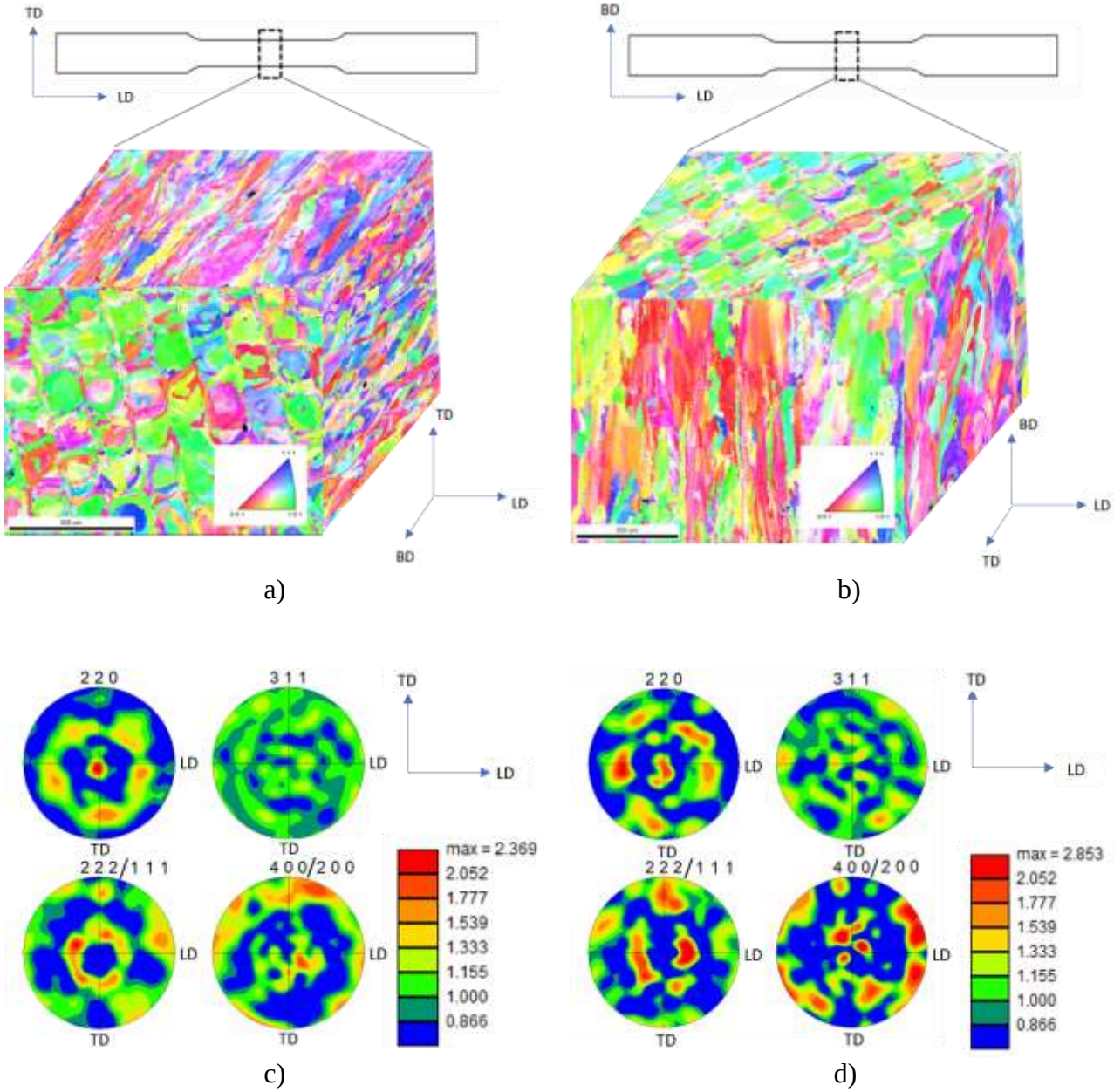

Figure 2. Typical IPF maps of a) the XY-build direction sample microstructure and b) the XZ-build direction sample microstructure. Pole figures for grain families from EBSD in the c) XY-build orientation and d) XZ-build orientation. A strong [110] texture is evident along the build direction.

The texture of the two build orientations, while similar along the BD, differ somewhat as shown in the pole figures in Figure 2c) and d). While both samples demonstrate a moderate [220]/[110] texture along the BD, it is stronger in the XZ oriented samples than in the XY samples. A weaker [100] texture is identified along the TD for both builds. This texture makes the samples softest along the BD. The strongest texture is along the BD due to the columnar grains. The processing window used, specifically the energy density does not create strong texture. The Schmid factor (m) for the texture is as follows: along the LD m=0.447±0.043, along the BD m=0.465±0.030, and along the TD m=0.454±0.041. The Schmid factor is calculated using the primary slip mode for FCC crystals namely $\{111\}[1\bar{1}1]$. Orientation imaging microscopy (OIM) analysis is used to calculate the average Schmid factors for stress application along different sample directions. For all scans, the BD axis of loading has a higher Schmid factor than the TD with the lowest Schmid factor along LD. We can thus expect more plastic rotation in the samples LSPed along the BD than those LSPed along the TD because the planes of slip are oriented to experience the most stress for loading along the BD. This hypothesis is tested to be correct by taking EBSD scans of the samples before and after LSP. IPF analysis shows that in both samples, the grains are oriented such that their planes of slip are clustered in a roughly stable configuration for tensile rotation of FCC crystals along the LD. These orientations are key for distribution of observable lattice rotation after loading especially at low strain.

The same grains were then scanned before and after LSP for both sample orientations, revealing differences in plastic response between XY and XZ samples. A difference pole figure demonstrating the change in texture due to LSP for the XY build is shown in Figure 3 a). The XY texture shows greater plastic grain rotation due to LSP. The grain rotation is most pronounced in the [400]/[200] planes and then the [222]/[111] planes for both build orientations.

However, the [220]/[110] planes also show some rotation. The plastic slip occurring in the XY build is observed to be more pronounced than in the XZ build. This is determined to be due to a combination of texture, microstructure and anisotropy inherent to the build.

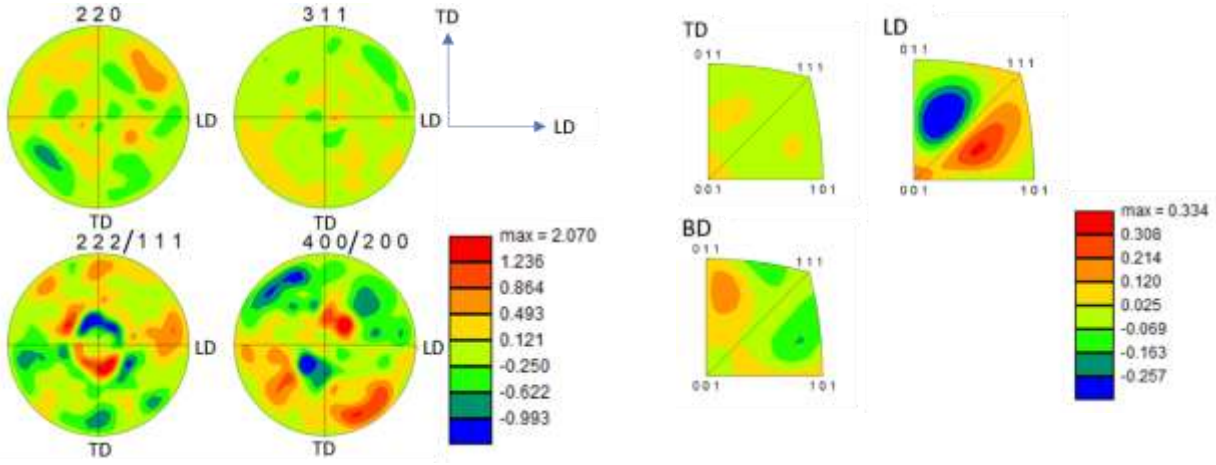

a) b)

Figure 3. A difference between textures is taken for the same group of grains and thus is able to show texture changes due to plastic deformation in a single plot. A higher intensity (red/blue) signifies a higher difference. This figure shows the change before and after LSP processing in the XY-build orientation shown with a) difference pole figure and b) difference IPF.

In addition, inverse pole figures (IPFs) show the crystal planes that are oriented along a given direction and demonstrate key aspects of grain rotation in crystalline structures during tensile and compressive strain. Figure 4 illustrates the modes of rotation for FCC crystals. Under tension loading (Figure 4 a)), the tensile axis of FCC crystals rotates towards the [101] direction until reaching the [001]-[111] line. Then a secondary mode of rotation occurs during which grains will rotate towards the [112] orientation. [68] During the initial mode of compression (Figure 4 b)), the slip plane normal within FCC crystals will rotate to align with the compression axis, causing grains to rotate into the [001]-[110] symmetry line. The grains then enter the duplex slipping mode to rotate toward the [011] direction [68]. Deviations from these modes of slip for tension and compression loading imply additional microscale stresses that warp plastic strain behavior. These effects are to be observed in relation to build direction and LSP direction.

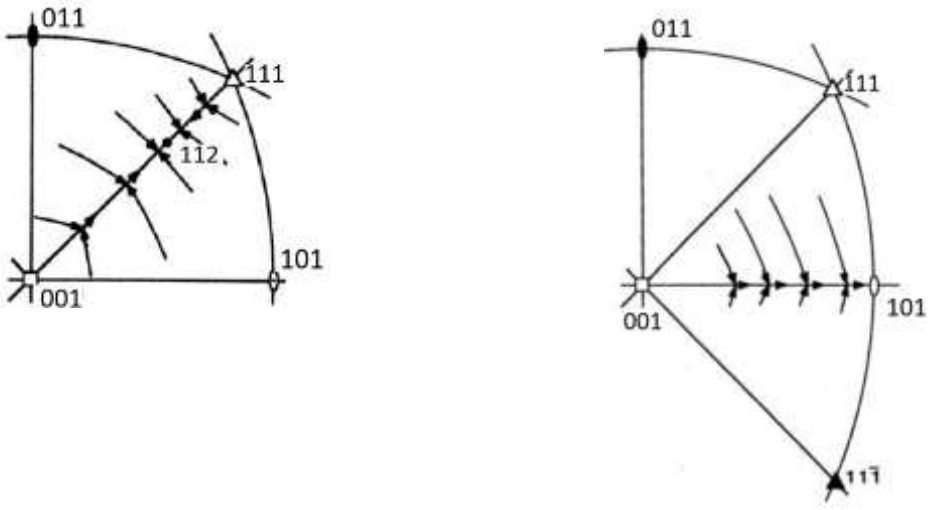

a) b)

Figure 4. a) Tension IPF rotation in an FCC crystal. b) Compression IPF rotation in an FCC crystal. Images adapted from Hosford. [69]

Figure 3 b) shows the IPF rotation after LSP in the XY build. The XY build showed a distinctively different response to LSP in the LD in comparison with the XZ build. The difference IPF along the LD shows that the XY samples exhibited a high rotation towards and across the [001]-[111] boundary line which has implication for subsequent tensile plastic deformation along the LD. Movement out of the [011]-[111]-[001] triangle reduces the Schmid factor for the primary slip mode [11-1](101) so that other modes of slip are more likely. [69] Meanwhile the XZ build demonstrated characteristic compression grain rotation along the TD which is the axis of applied pressure after LSP with some smaller magnitude rotations in the LD and BD axes. It can be inferred that, due to the compression-stable orientation of the grains along the BD, applying pressure to the XY build samples along the BD caused the most detectable grain rotation to be by modes of compression plastic strain beyond the secondary compression rotation mode which contributed to the high rotation in the LD. As studied by Chen et al [70], LSP causes different rotation in grains according to their orientation. It is likely that the anisotropic intragranular features and grain morphology present in 3D printed samples will

exacerbate these effects. Figure 3 shows that this strong tensile rotation of [222]/[111] and [400]/[200] planes in the LD primarily accounts for the larger magnitude of LSP-induced plastic rotation in the XY build as compared with the XZ build.

Comparison of the texture of LSPed and as-built samples before and after tensile loading demonstrate how LSP changes the mode of deformation in these samples. Samples experienced different grain rotation after 4% strain according to whether they had been LSPed or not. Characteristic difference IPFs as shown in Figure 5 illustrate the different modes of grain rotation each of the samples experienced. The non-LSPed samples in both the XY and XZ build orientations display similar modes of grain rotation after tensile strain. Along the LD, the grains undergo the primary mode of FCC tensile grain rotation with rotation towards the [001]-[111] symmetry line. In the axes perpendicular to loading, the grains rotate along compression modes towards the [011] and [101] corners. The LSPed samples exhibit noticeably different grain rotation as exhibited in Figure 5 b). The LSPed XY samples show compressive grain rotation in the LD. This is likely due to the compressive back stress and residual stress induced in the surface of the XY builds. The compressive back stress within the part is due to dislocation pile-ups at barriers to compressive strain. The compressive residual stress pins these dislocation pile-ups in place and as it is relaxed during loading, the compressive dislocations already formed encourage modes of grain rotation typically seen in compressive loading. LSP induced fewer pinned dislocations in the XZ build due to the texture's inherent hardness along the TD. As a result, the compressive rotation mode that is induced in the XY samples is not as pronounced in the XZ build.

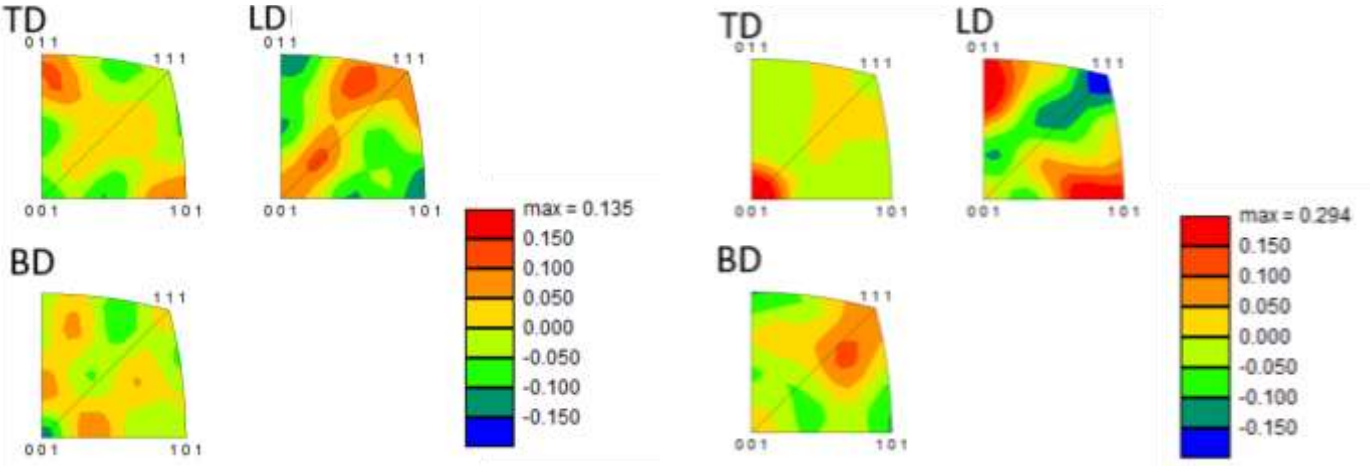

a) b)

Figure 5. Characteristic difference IPFs showing the change before and after 4% strain for the a) as-built XY-build orientation and b) LSPed XY-build orientation.

This analysis is supported by the dislocations viewed in the XY and XZ build orientations before and after LSP. Dislocation density can be extracted from the EBSD images by using OIM analysis to detect lattice curvature. Lattice curvature is directly proportional to GNDs and thus, given a known FCC primary slip system, we may extrapolate GND density. Figure 6 show an increase in dislocation pile-ups near the grain boundaries after LSP for the same grains. It is evident from many such analyses of all sample conditions that LSP increases both the level and density gradient near the grain boundaries in the XY build by more than in the XZ build. The observed dislocation pile-ups contribute to a surface layer of compressive back stress that mitigates the field of tensile back stress developed during loading. These results support that the texture and microstructure of the metal interact with the direction of LSP and loading to produce significant back stress reduction in the XY build and no observable effect in the XZ build. CPFE simulation of the texture is capable of demonstrating how back stress is developed for each orientation.

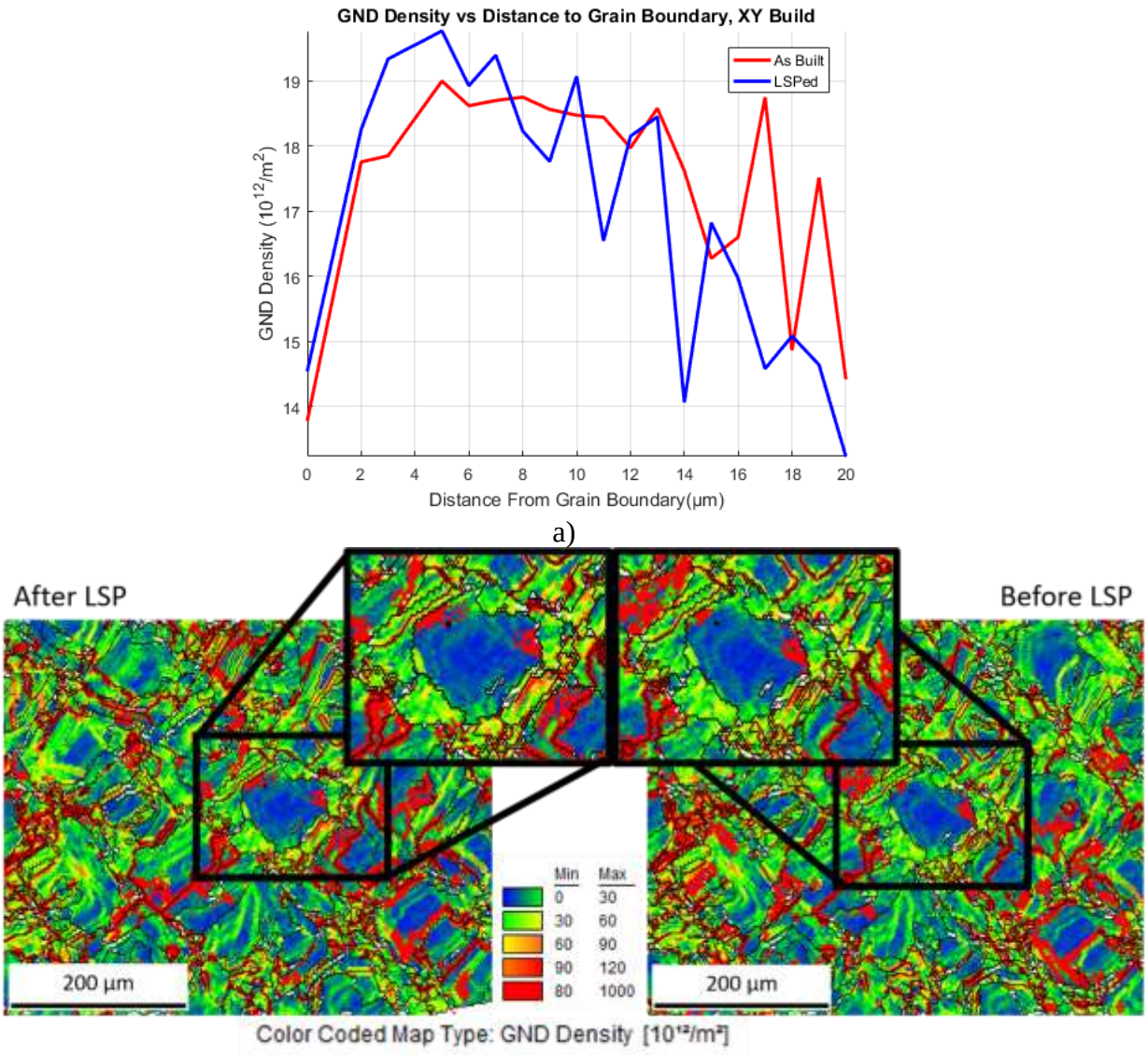

Figure 6. a) GND density vs distance to grain boundary before and after LSP for the same grains viewed in the TD-LD plane of the XY-build sample. b) A sample scan showing the same grains before and after LSP highlighting the increased GND density gradient near the grain boundaries in the LSPed condition.

3.4.3 CPFE Simulation

For CPFE simulation, each grain of the representative volume was assigned Bunge Euler angles randomly sampled from the grains of EBSD images. Figure 7 shows the orientation distribution of [110] planes as experimentally measured and compares it with the randomly

sampled texture used in the representative volume. Though there is not an exact match of distribution, the strong [220]/[110] texture along the BD is still evident.

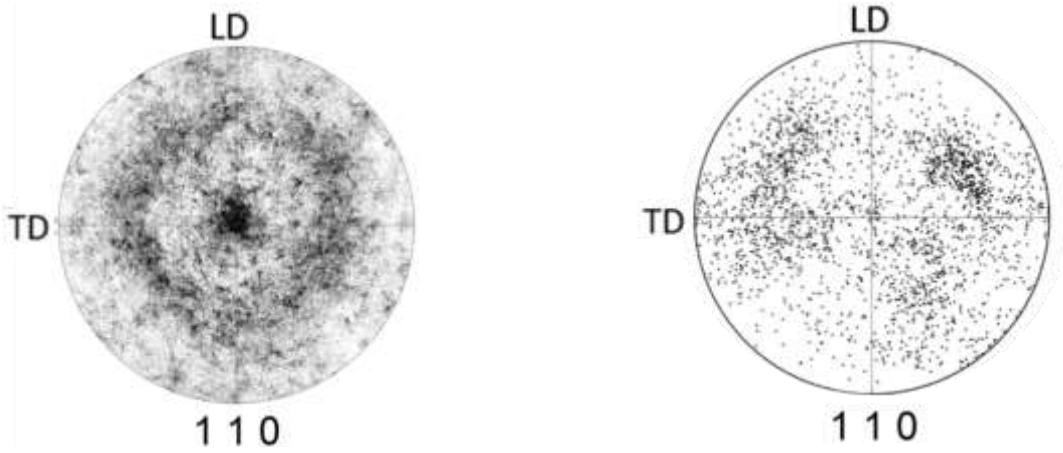

a) b)

Figure 7. The experimentally measured texture in a) compared with the texture used in simulation as shown in b).

X-ray diffraction (XRD) was used to extract residual strains from the as-built samples to input by grain family into the simulation as well. A regression of the $sin\psi^2$ vs the d-spacing with correction for the out-of-plane stresses allowed for residual stress and strain to be evaluated for all of the grain families in each build. Figure 8 shows a representative stress analysis. These residual strains are allocated to each grain family in the simulation grain by grain. To model the effect of texture on back stress development, all representative volumes inherit the same back-stress tensor as was originally defined by Chet et al [21].A positive back stress of 30 MPa is applied in the LD and TD direction with a back stress of -60 MPa along the BD. Note that this initial back stress is applied across both build orientations to analyze the sole effect of texture and residual stress on back stress hardening. To simulate back stress development during tensile loading, a set velocity of 4 mm/s is defined on one plane of the representative volume while the opposite plane experiences a static boundary condition. The elastic strain of each grain family is extracted during this loading and the back stress of each grain family is evaluated as well. To

simulate LSP, a gaussian spatial distribution of pressure with 2 GPa peak load is applied perpendicularly to the tensile loading direction. The pressure is applied so that it is ramped up to peak load at 5 ns and linearly decays to zero at 10 ns. The simulation is allowed to run so that the dislocations and stresses reach steady state before applying tensile loading.

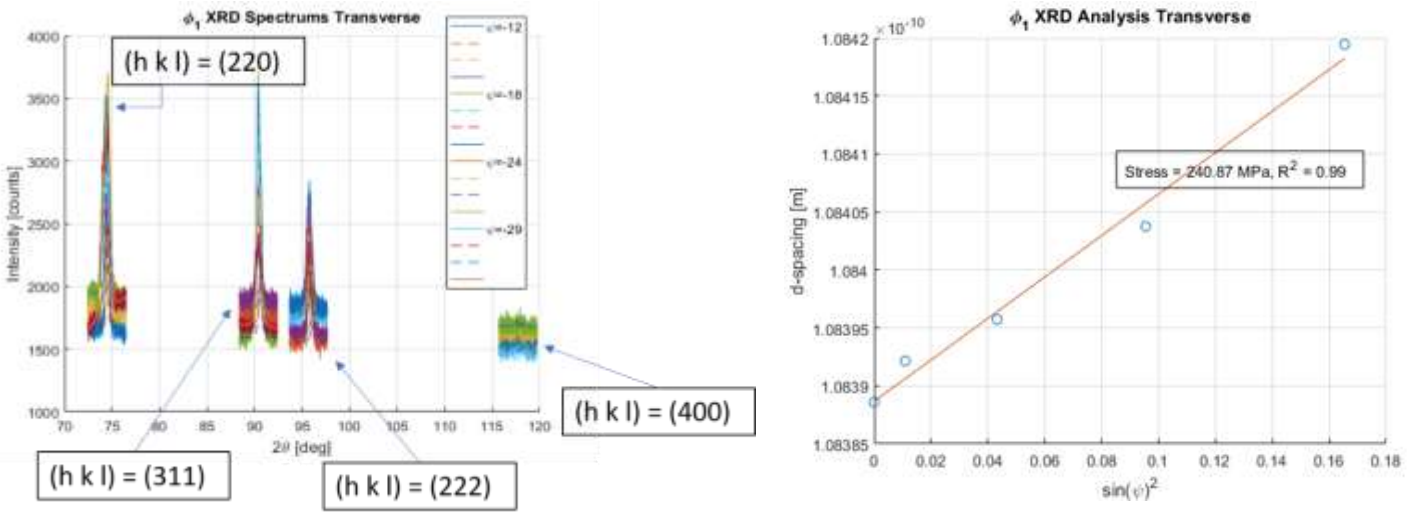

a) b)

Figure 8. a) Plot of a representative sweep of XRD count intensity vs. 2θ for different ψ angles. b) The resultant stress analysis for the [222] lattice plane using linear regression of $\sin^2(\psi)$ vs. d-spacing data.

Applying the sample texture measured by EBSD to CPFE enables simulation to approximate the hardening behavior of differently textured build orientations. Figure 9 shows the calculated CPFE effect of 4% tensile strain in the different build orientations alongside the experimentally measured difference pole figure demonstrating plastic grain rotation after 4% strain and unloading. CPFE accurately predicts the relative hardness of each of the grain families. Grain families are defined by the crystal plane normal that is most parallel with the peening direction. The CPFE reports that in both the XY and XZ orientations, the hardest grain family is the [311] grain family. The experimentally measured EBSD difference pole figure also identifies that the [311] planes are those that experience the least rotation. In the XY build orientation, the next hardest grain family according to the CPFE is the [220] grain family which

is corroborated by the EBSD results. The two softest grain families in the XY build orientation are the [400]/[200] and the [222]/[111] grains. These planes are also the planes that yield the most according to the EBSD analysis. Difference pole figure analysis shows that the XY-build grain families experience texture difference before and after 4% strain of 1.51, 1.14, 0.60, 0.51 for the [400]/[200] , [222]/[111], [220], and [311] grain families respectively. The XZ build orientation simulation exhibits the same hierarchy of material softness showing more plastic rotation in the [400]/[200] grain families than any of the other grain families. The XZ-built sample is also simulated to be significantly softer overall demonstrating that the stronger [220]/[110] texture contributes to the material's hardening behavior. Experimental EBSD confirms this fact with the texture difference before and after 4% strain of XZ samples being 12.02, 6.38, 2.96, and 2.45 for the [400]/[200] , [222]/[111], [220], and [311] grain families respectively. The hierarchy of grain rotation is again reflected well in the CPFE analysis. The [400]/[200] grain family shows the greatest strain followed by the [222]/[111] family. The [220] and [311] families show the least amount of strain. As can be seen from Figure 9 d) the CPFE shows a wide strain difference between the [400]/[200] and [222]/[111] grain families which is mirrored by difference in the residual plastic rotation of the two grain families as shown by the EBSD difference pole figure: an intensity change of 12.02 is nearly twice as high as 6.38. Similarly, the [220] and [311] grain families are most similar in their CPFE cumulative strain and the change in the two families' textures are only different by 0.51 intensity. This method of comparison is a mode of validation of the hardening modelling of the CPFE.

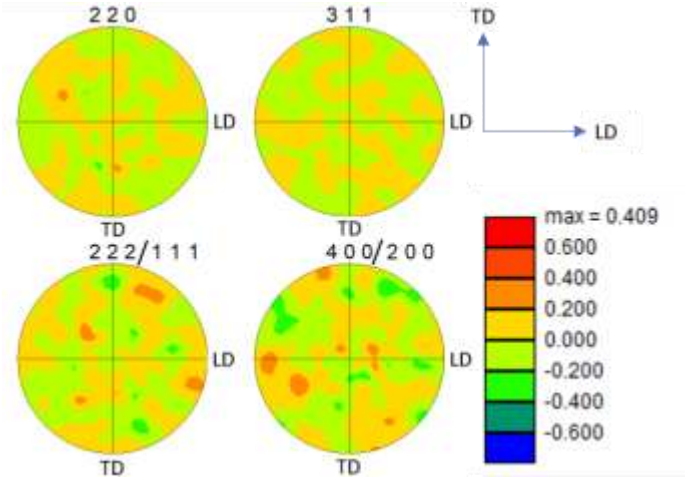

a)

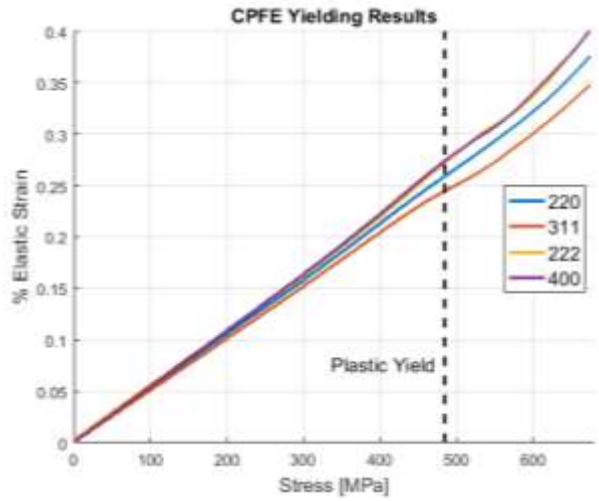

b)

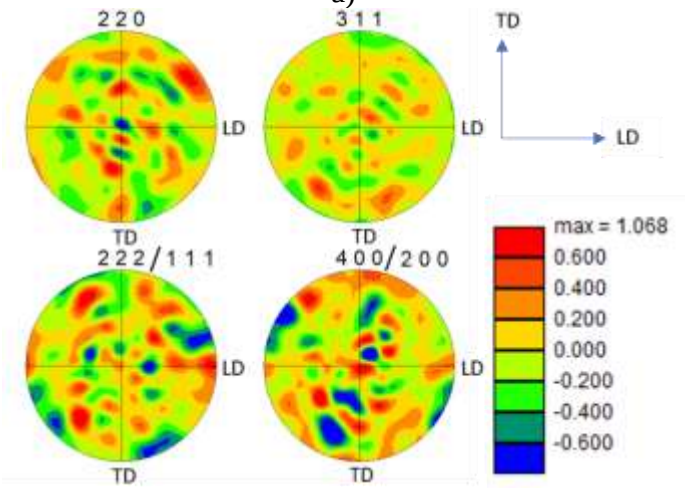

c)

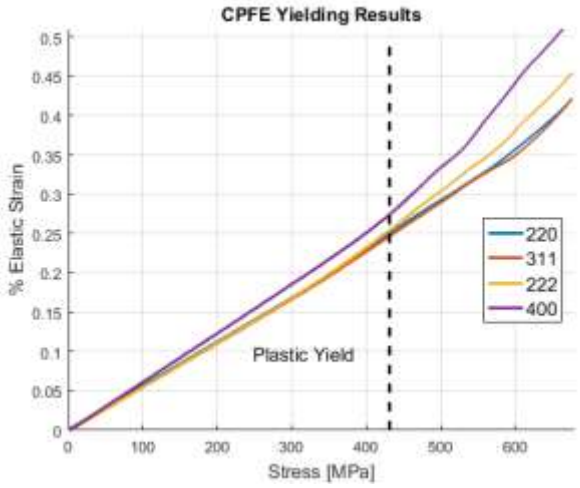

d)

Figure 9. EBSD results showing the difference pole figure change before and after 4% strain for the a) as-built XY-build orientation and c) as-built XZ-build orientation. CPFE elastic strain according to grain family after strain in b) the XY build orientation and d) the XZ build orientation.

CPFE back stress analysis shows that the greater plastic strain exhibited by the XZ build resulted in an on average faster rate of back-stress development. The average back stress across all elements develops to 44.4 MPa in the XZ build after 4% strain compared with 38.4 MPa in the XY build. The higher rate of slip as exhibited by the [400]/[200] and [222]/[111] grain families in the XZ build drives higher back stress development as shown with equation (4). On

the other hand, in the XY build, the slip rate is roughly similar across all grain families. This effect has consequences for the interaction between LSP and build direction.

The LSPed simulation results show how the difference in hardening behavior of the [400]/[200] and [222]/[111] grain families between build directions contributes to the diminished effects of LSP on the XZ build as compared with the XY build. After LSP the back stress along the loading direction is reduced significantly from 30 MPa to an average of -62.5 MPa and -75.0 MPa in the XZ build and XY build orientations respectively. As seen experimentally in the EBSD analysis, the XY texture was softer to LSP resulting in greater compressive hardening. The increase in magnitude of compressive back stress due to LSP causes both orientations to begin yielding below 300 MPa of applied stress as compared with the un-processed yielding behavior above 400 MPa as shown in Figure 9 b) and d). However, the XZ build back-stress hardens more quickly than the XY-built samples. The average back stress after 4% strain is 8.55 MPa in the XZ build as compared with -11.9 MPa in the XY build. The XY build direction retains a measure of compressive back stress through 4% loading which contributes towards an overall reduction of bulk back stress. As can be seen in Table 2 this is because of the unique hardening behavior of the [400]/[200] and [222]/[111] grain families in the XZ build orientation. The texture of the XZ build favors a high rate of tensile plastic yield in these grain families and thus more rapidly hardens the overall build. This causes the effects of the LSP to be dissipated in the XZ build at a faster rate resulting in an experimentally non-observable difference between the LSPed and non-LSPed samples.

Table 1. The average back stress from the LSPed CPFE simulation according to grain family after 4% tensile strain.

	(220)	(311)	(222)	(400)
XY-Build Back Stress	-12.0 MPa	-12.6MPa	-16.2 MPa	-10.0 MPa

XZ-Build Back Stress	5.72 MPa	0.38 MPa	6.91 MPa	16.6 MPa

3.5 Conclusion

This work indicates that it is possible to induce lasting tensile back-stress reduction with LSP in additively manufactured stainless steel, given the build orientation and texture is chosen to be favorable. The XZ and XY built samples show statistically significant differences in measured back-stress after LSP. While LSP does not have a significant effect on the XZ built samples, it produces on average -247.61 MPa difference in XY-built samples all else equal. This study shows that the disparity in effect of LSP between build orientations is due to the following:

- **Aligning the axis of peening along the BD causes LSP to compressively harden the surface material more, thereby reducing overall tensile back stress.** Experimentally measured texture differences before and after LSP as well as CPFE simulation analysis show that LSP induces compressive hardening in XY-built samples due to the yielding of [400]/[200] and [222]/[111] planes which are positioned so as to be softer to peening along the build direction. Greater compressive plastic strain due to LSP causes heightened compressive back-stress hardening in the surface of the sample, resulting in an observable reduction to bulk tensile back stress.
- **The texture of the XZ-built samples is softer to tensile loading along the pulling direction than that of the XY-built samples, causing tensile hardening to negate back stress reduction in the LSPed XZ samples.** EBSD analysis shows that [400]/[200] and [222]/[111] grain families are especially soft to tensile hardening in XZ-built samples. This is shown by the greater texture difference in these grain families before and after strain. The rapid hardening of the [400]/[200] and [222]/[111] grain families in the

XZ samples dissipates the compressive back stress induced by LSP, leaving no observable difference between LSPed and non-LSPed samples.

Build orientation is therefore shown to interact with LSP to alter back stress and tensile hardening behavior in additively manufactured stainless steel parts. In particular, the metal's texture and the orientation of its texture with respect to loading and peening may either nullify the back-stress reduction due to LSP or sustain it through tensile strain.

Chapter 4: The Effect of Laser Shock Peening on Electrochemistry and Wettability of Additively Manufactured Stainless Steel

4.1 Introduction

Additively manufactured stainless steel offers unique design solutions for fluid mechanical applications. Laser powder bed fusion (LPBF) in particular is of interest for use in nuclear reactor cells and other corrosive wet environments due to its ability to achieve complex internal fluidic features and high-resolution designs [1, 2]. For these applications to reach their full potential, the risk of corrosion failure must be minimized. The molybdenum content and reduced carbon content in 316L allows for increased pitting resistance and reduced susceptibility to sensitization. Thus, it is a common choice for corrosive environments. The corrosion behavior of additively manufactured 316L is therefore of heightened manufacturing interest.

Process parameters profoundly affect corrosion resistance of additively manufactured steel. High porosity encourages anodic dissolution and therefore choosing build conditions that minimize lack-of-fusion errors, keyhole defects, and balling is vital [3, 4, 5]. Studies of the corrosion performance of LPBF steel have produced varied results, some observing increased sensitization and susceptibility to intergranular corrosion in comparison with wrought and others reporting reduced [6, 7]. These properties are tied to the chemistry of the steel. Carbide precipitation along grain boundaries in stainless steel causes the area near the precipitates to be leached of chromium, thereby reducing the corrosion resistance near these grain boundaries [8]. During welding, regions of the heat affected zone is prone to sensitization. The complex thermal history introduced by the LPBF process similarly may cause some sensitization with certain build parameters. Microstructure and parameter control of the LPBF process is therefore critical

to corrosion performance. Studies of LPBF with small grains and high density of mechanical twins show that by keeping the carbide precipitation below a critical size, it is possible to have good corrosion behavior in LPBF parts [7]. However, without access to mature in-situ monitoring technology, it may be desirable to enhance corrosion behavior of LPBF stainless steel without altering build parameters. In this circumstance, postprocessing of the material's surface passivity is a possible solution.

Corrosion behavior of stainless steel is dependent on the material's surface passive film stability, which is affected by surface stress. As-built LPBF stainless steel is characterized by an exterior layer of tensile residual stress which has been shown to be detrimental to passivity and increase the corrosion rate [9, 10]. Compressive residual stress meanwhile correlates with improved passive film creation, its effects isolated from other influences through studies that control for surface finish [11, 12, 13]. Poteniokinetic investigation finds compressive residual stress to both increase pitting potential and reduce corrosion rate [14, 15]. The mechanism by which compressive residual stress improves passivity is theorized to be due to alterations to the metal's inclusion-steel interfaces, the tightening of interatomic spacing, an increased chromium density, and the creation of an improved barrier to charge transfer by anion absorption [16]. These effects increase the work function by which electrons are ejected from the material, thereby reducing dissolution [17]. Inducing compressive residual stress in additively manufactured steel with postprocessing methods such as low plastic burnishing and annealing have shown improved corrosion behavior [11, 18]. However, annealing softens the material and burnishing requires inconvenient tooling. Laser shock peening (LSP) is identified as an advantageous alternative. LSP has been applied to wrought and additively manufactured metal to induce compressive residual stress for fatigue life improvement and mechanical behavior

modification [19, 20, 21]. Studies also show that application of LSP improves corrosion and stress corrosion cracking behavior [13, 10, 17]. Recently LSP has been applied to LPBF AlSi10Mg and wire additive 308L steel, demonstrating corrosion improvement for additively made metals as well [22, 23]. However, the effects are not studied for LPBF steel nor have the corrosion and surface mechanisms been exposited.

Wettability also affects the corrosion behavior of a material. Hydrophobicity has been shown to improve the corrosion resistance of metals due to reduced invasion of the material's surface with the corrosive medium, thereby reducing ion exchange. By introducing hydrophobicity via surface patterning, studies have been able to improve stainless steels corrosion behavior [24]. Surface morphology is key for inducing this effect. Additively manufactured steel is characterized by unique surface topology and chemistry due to the build procedure with surface features such as scan tracks and spatter. The faces normal to the build direction have different structures than walls and down-skin features. Surface roughness modification of additively manufactured metal to induce the desired wettability characteristic has been achieved with polishing, laser texturing, and altering the surface properties with chemical cleaning [25]. These methods however do not also deliver beneficial compressive residual stress. LSP not only applies compressive stress but it also alters the wettability of metal by inducing plastic deformation to surface features [26]. LSP is shown by some studies to consistently increase surface roughness with effects varying according to initial surface roughness [27]. However, the precise surface modifications have also been shown to be nuanced, sometimes reducing surface roughness [28, 29]. LSP is shown to reduce surface wettability in wrought material [26]. The interaction of laser shock peening with additive scan morphology is therefore likely to adjust the wettability behavior in favor of improved corrosion resistance. However, the

relationship between LSP-induced surface morphology alterations and wettability in LPBF metal is yet to be explored.

The many applications of LPBF stainless steel in corrosive wet environments motivates searching for tools that may be used to improve the material's surface passivation. LSP has already been identified as being able to reduce corrosion rate and improve pitting potential in wrought metal and is preliminarily investigated for application to additive manufacturing. However, the relevant interactions between LSP and LPBF stainless steel remain unexplained. This paper seeks to illuminate these mechanisms by quantifying passivation improvement due to LSP with electrochemical impedance spectroscopy (EIS) studies and potentiokinetic measurements. Residual stress, surface roughness, and corrosion chemistry are compared before and after LSP with x-ray diffraction (XRD) complemented by simulation, profilometry and energy-dispersive X-ray spectroscopy (EDS). Wettability measurements, compared with modeling results, describe surface energy changes due to laser processing. All experiments and analysis are performed to both wall and top (i.e. build plane) surfaces to identify how build orientation may affect corrosion behavior and interaction with LSP.

4.2 Background

4.2.1 Corrosion in Additively Manufactured Stainless Steel

Stainless steel is comprised of chemically reactive elements that remain inert in corrosive environments due to a bi-layer passive film covering the metal's surface [30]. The creation and maintenance of this passive film is dictated by ionic exchanges as described by the point defect model [31]. The electrochemical nature of a steel-water interface may be characterized by a complex impedance using EIS. This impedance can be modelled by an equivalent circuit of the electrolyte resistance (R_s) in series with the passive film which is described as a polarization

resistance (R_p) in parallel with a constant phase element (CPE) [11]. The impedance of the CPE is shown for stainless steel to be $Z_{CPE} = 1/(Q(\omega i)^{\alpha}$ where $\omega =$ frequency in rad/s and Q and α are constants [11]. From this model, the combined impedance is separated into real and imaginary parts as shown in equation 24 where $x_{re} = \cos(\frac{\pi}{2}\alpha)$ and $x_{im} = \sin(\frac{\pi}{2}\alpha)$.

$$Z_{real}(\omega) = \frac{R_s + R_p(1 + Q\omega^{\alpha}x_{re})}{\left(1 + R_pQ\omega^{\alpha}x_{re}\right)^2 - \left(R_pQ\omega^{\alpha}x_{im}\right)^2}$$
$$Z_{im}(\omega) = \frac{R_p^2Q\omega^{\alpha}x_{im}}{\left(1 + R_pQ\omega^{\alpha}x_{re}\right)^2 - \left(R_pQ\omega^{\alpha}x_{im}\right)^2} \quad \textbf{(24)}$$

The polarization resistance (R_p) reflects the passivated film's resistance to charge transfer across the material's surface while the CPE (Z_{CPE}) describes diffusion of molecules [32]. This electrochemical behavior may be altered by changes in surface chemistry, wettability or residual stress. Increased compressive residual stress by annealing has been shown to coincide with increased surface resistance as evidenced by an impedance phase shift [11].

Additively manufactured stainless steels have a unique chemical composition due to powder chemistry and complex thermal and chemical reactions occurring during the build process. Investigation of LPBF 316L stainless steel that is solidified in low-oxygen environments show that (Mn, Cr) Cr_2O_4 spinel, SiO_2, and Cr_2O_3 corundum oxides form at the material's surface [33]. These oxides preferentially occur at the edges of the scan track melt pools [3]. Silicon-rich oxides in particular are found to form in cracks and on the surface of pores [34]. The stability of these components must be examined under corrosive conditions to analyze their role in the metal's wetted passivation chemistry. The stability of each chemical component in aqueous environment is identified by Pourbaix diagrams, which show the stable dominant chemical components in equilibrium at a given voltage and pH. The divisions within Pourbaix

diagrams are drawn using Nernst equations. As shown in **Error! Reference source not found.**, g enerated using codes [35],SiO_2, Fe_2O_3, and Cr_2O_3 surface oxides are stable at neutral pH for the majority of the water-stable voltage-range as indicated by the region between dotted lines. These oxides will therefore contribute towards surface passivation in neutral pH environments. In acidic media it can be seen that chromium and silicon oxides are far more stable than iron oxide. Chromium oxide has been observed to create an outer layer protecting the iron oxide layer on additively manufactured 316L steel in acidic media [36]. In silicon-rich steels, the silicon oxide is also highly protective at high acidity [37]. These elements together therefore contribute to protecting the steel from corrosion at a large range of acidities.

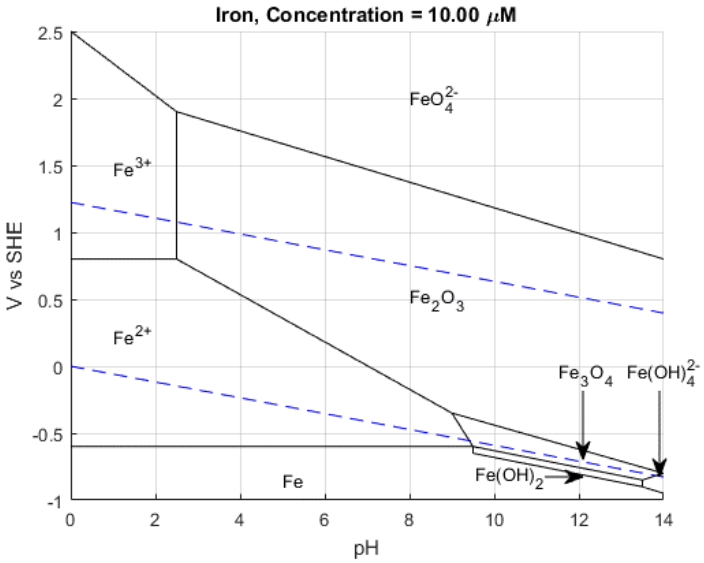

a)

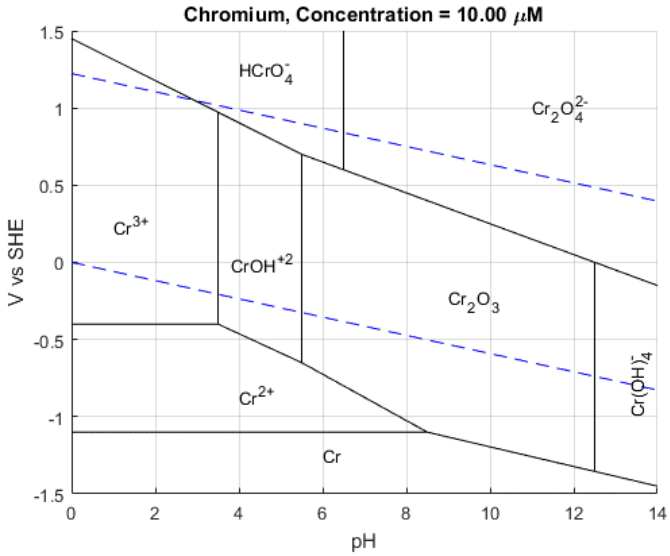

b)

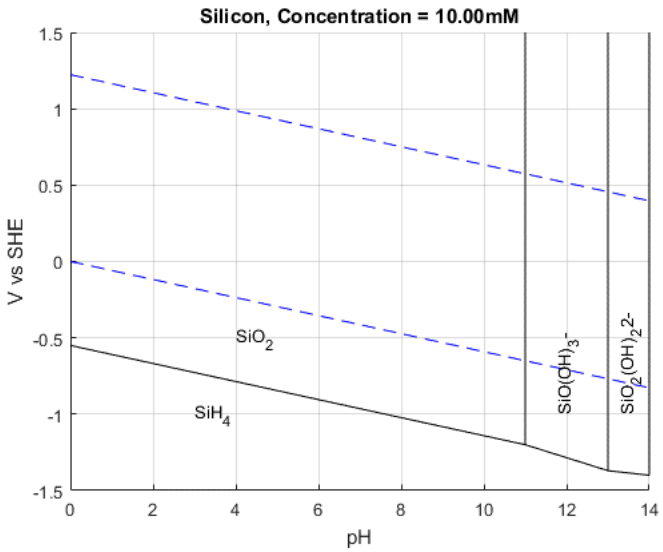

c)

Figure 1. Pourbaix diagrams for iron (a), chromium (b), and silicon (c). The Pourbaix diagram of water is super imposed in dotted lines.

At neutral pH, sweeping the voltage across a negative-to-positive range, as is done in potentiokinetic tests, will show metal to exhibit the following: 1) a region of metal dissolution where there is no passive film as characterized by a high current, 2) a region where the anodic and cathodic reactions balance to create a passive film with low current, and 3) a region where the passive film breaks down exhibiting high current once more [38]. These regimes may identify both the pitting potential of the material as well as the corrosion rate. Studies show that while LPBF 316L stainless steel consistently has higher pitting potential, its repassivation potential is lower than that of wrought stainless steel [39]. This is believed to be due to the increased surface porosity of the LPBF material as compared to wrought. The unusually porous surface of additively manufactured metal also allows regions of higher corrosion current density which dissolves protective oxides and then attacks the metal via crevice dissolution [3]. In wrought 316L steel, LSP increases the pitting potential of a material without significantly altering the surface chemistry [13]. Therefore, the improved surface passivation is attributed to surface morphology changes and compressive residual stress. LSP has also been shown to reduce

surface porosity in additively manufactured metal [40]. LSP therefore further has potential to raise surface repassivation voltage in LPBF steel which would improve the material's long term corrosion behavior. The different surfaces produced by LPBF are also shown to have different corrosion characteristics [34]. The top build-plane surface of the build (i.e. the surface whose normal is along the build direction) is shown to have a lower pitting potential than the wall (i.e. the surface whose normal is transverse to the build direction) [34]. The corrosion properties are strongly influenced by surface roughness and morphology, showing that increased surface roughness directly affects the material's pitting potential [34]. It is therefore crucial to identify the interaction between the as-built morphology with postprocessing.

4.2.2 Wettability and Surface Free Energy

Wettability has been identified to strongly influence corrosion behavior in aqueous environments [24, 25]. Wettability of a solid in contact with any liquid is dictated by the solid surface's surface free energy (γ). This energy quantifies the difference between the energy of an atom at the surface of the solid versus that of an atom in the interior. When a solid surface is wettable by a liquid, the system's energy is reduced by the solid being in greater contact with the liquid, therefore making the wetted state more favorable. Thus, non-wettable surfaces have a lower surface-free energy than wettable surfaces. The angle of the droplet on a smooth surface in a gaseous vapor atmosphere is thus defined by Young's equation:

$$\cos(\theta) = \frac{\gamma_{VS} - \gamma_{LS}}{\gamma_{VL}} \quad \textbf{(25)}$$

where $\theta =$ contact angle of the liquid ($\theta > 90°$ = non-wettable and $\theta < 90°$ = wettable) , γ_{VS} = vapor-solid interfacial tension, γ_{LS} = liquid-solid interfacial tension, and γ_{VL} = vapor-liquid interfacial tension. [41] The direction of positive definition for each of these values may be seen in **Error! Reference source not found.**.

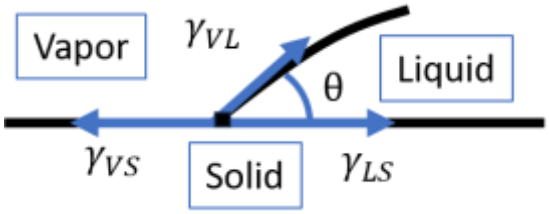

Figure 2. Definition of positive direction for each of the components in Young's equation. The vapor-liquid tension is defined along the tangent to the liquid-vapor surface at the liquid-vapor-solid interface point.

The surface roughness alters wettability significantly. To simply describe the relationship between the smooth surface and rough surface contact angle, Wenzel or Cassie-Baxter models are frequently used [41]. The Wenzel model, as shown in equation 26, is simplest and assumes that for a wettable material, roughness increases wettability, while for a non-wettable material, roughness increases the contact angle further.

$$\cos(\theta_{rough}) = r\ cos(\theta_{smooth}) \tag{26}$$

where $r =$ the ratio of actual area of the surface to the projected area. The Cassie-Baxter model describes the circumstance where the roughened surface captures air, causing a composite surface effect as characterized by equation 27.

$$\cos(\theta_{rough}) = f_1 \cos(\theta_{smooth}) - f_2 \tag{27}$$

where $f_1 =$ the total area of the solid under the drop per unit of projected area under the drop, and $f_2 =$ the total area of the trapped air under the drop per unit of projected area under the drop [41]. However, these one-dimensional simplifications to surface features are insufficient to capture the variations in wettability affected by surface morphology [42]. It is therefore required to more sophisticatedly model the surface-liquid contact behavior. The liquid-solid-air system at equilibrium stabilizes at the minimum potential energy of the liquid subject to the constraint of the surface geometry. The energy of the liquid is computed as follows:

$$E_{Pot_L} = E_{I_L} + E_{G_L} + E_{R_L} \quad \textbf{(28)}$$

if $E_{I_L} =$ the surface tension energy of the liquid, $E_{G_L} =$ gravitational energy of the liquid, and $E_{R_L} =$ the rotational kinetic energy of the liquid. Each of these components is computed with equations 29-*31*. The surface tension energy (E_{I_L}) is shown in equation 29. Variables define the 2-dimensional area of the total solid surface (A_S) and vapor-liquid interface (A_{VL}) and the liquid-solid interface (A_{LS}) [43].

$$E_{I_L} = \gamma_{VS}A_S + \gamma_{VL}A_{VL} + (\gamma_{LS} - \gamma_{VS})A_{LS} \quad \textbf{(29)}$$

The gravitational energy of the liquid (E_{G_L}) is found using:

$$E_{G_L} = \rho_L V_L \vec{g} \cdot \vec{C}_L + \rho_V V_V \vec{g} \cdot \overrightarrow{C}_V \quad \textbf{(30)}$$

with V denoting volume, ρ denoting density, and $\vec{C}$ denoting the fluid center of mass displacement vector for the liquid and vapor subscripts respectively. The rotational kinetic energy of the liquid is simply defined as:

$$E_R = \frac{1}{2}\omega^T \boldsymbol{I}\omega \quad \textbf{(31)}$$

where $\omega =$ angular velocity and $\boldsymbol{I} =$ is the moment of inertia tensor [43]. With the known smooth-surface contact angle, the precise surface geometry of a material may be calculated by solving for minimization of the potential energy of the liquid subject to a surface geometry constraint.

4.2.3 Laser Shock Peening (LSP) for Corrosion Mitigation

LSP is mainly known to mitigate stress corrosion cracking (SCC) but dissolutive type of corrosion could be co-present [10, 13, 17]. LSP has been identified as a tool for improving corrosion resistance in stainless steel, specifically by increasing pitting potential and reducing corrosion current density [13]. This effect may be attributed in part to the shock-induced surface

penetrating compressive residual stress which is shown to improve corrosion resistance. Compressive residual stress is attributed with increasing the energy required to exchange charge in aqueous environments [17]. However, too much plastic deformation on the metal surface is shown to encourage dissolution due to surface disruptions and dense dislocations which raise current density. Therefore, the control of surface morphology modification is crucial for passivated film stability when applying LSP for corrosion performance. More than a single layer of LSP application was shown to produce less favorable film stability due to heightened surface defects [44]. Optimization of LSP processing may be used to create as uniform a surface as possible. Overlap of individual peens is shown to improve corrosion resistance in comparison to no overlap [45]. In rough surfaces characterized by periodic surface features, ideal LSP parameters both neutralize initial surface roughness without causing high-frequency kurtosis [29]. These surface morphology nuances interact to alter wettability, passive film stability and therefore corrosion behavior. In the investigation of LSP corrosion enhancement of LPBF aluminum, Maleki et al [22] shows that using higher energy and higher surface overlap in LSP processing increasingly reduces surface roughness and improves corrosion resistance in comparison to the as-built condition. Maleki et al [22] does not investigate how the surface wettability is affected by these structural changes nor its interaction with corrosion. These conclusions are also limited to the aluminum material response and the as-built wall surface, which has very different surface morphology than the top surface. Alternatively for wire arc additively manufactured 308L stainless steel, LSP caused heightened surface roughness while still simultaneously improving corrosion behavior and passive stability [23]. It is clear that further exposition of surface roughness, wettability, and surface chemistry is needed to identify how LSP may be applied to LPBF stainless steel for corrosion resistance improvement.

4.3 Methods

To investigate the surface energy and electrochemical properties of additively manufactured stainless steel, both wall and top surfaces of the LPBF process are studied. Samples are made from 316L stainless steel with 40 µm layer thickness, bulk energy density of 57.7 J/mm^3 and a hatch rotation angle of 67°. The powder chemical composition is shown in **Error! Reference source not found.**. The powder particle size is given by the cumulative d istribution values d90 = 50.43 µm, d50 = 33.44 µm, and d10 = 21.71 µm. From this particle size distribution, the median is thus 33.44 µm with a span of 0.86. Two samples are made with the test surface on the top surface of the LPBF build (the X-Y plane) and two are made with the test surface on the wall of the build (the X-Z plane). These two sample types will be referred to as XY and XZ respectively and are detailed in **Error! Reference source not found.**. LSP is applied to one sample of each build orientation. The other two samples serve as reference. The laser used for LSP is a Q-switched Nd:YAG Spectra Physics laser with 10 ns pulse width and 100 Hz. LSP is applied with a 700 µm diameter spot, 10 GW/cm^2, and 50% overlap. These LSP parameters are the result of previously studied optimization.

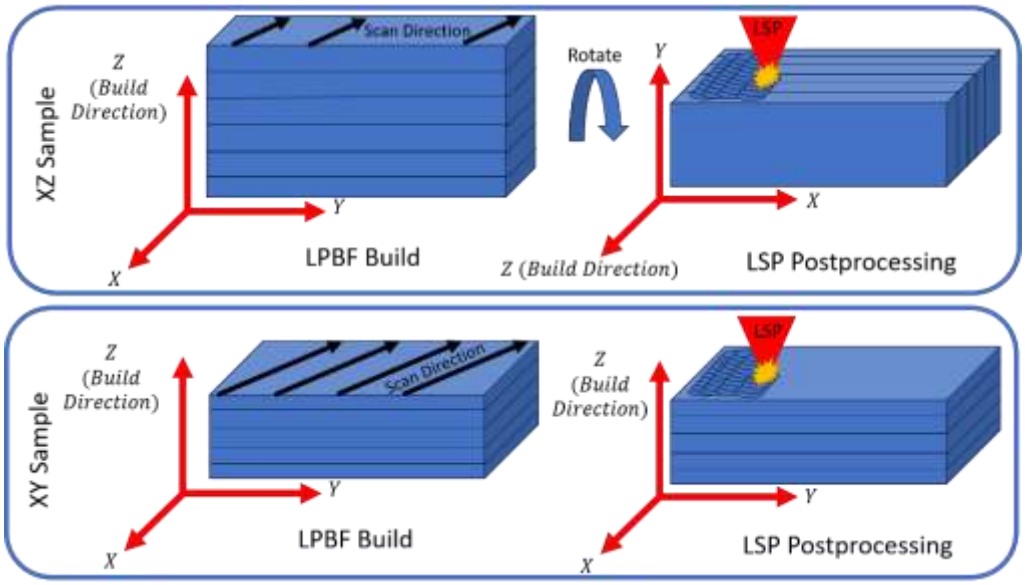

Figure 3. Identification of build and LSP post processing directions for XY and XZ samples. The LPBF scan direction and layers demonstrate the orientation of the surface scan texture.

Table 1. 316L stainless steel powder chemical composition.

	Fe	Cr	Ni	Mo	Mn	Si	N	O	Other
Weight %	64.68	17.96	12.90	2.41	1.44	0.45	0.08	0.05	<0.1%

To compare the impedance of the XY and XZ test surfaces and the LSPed and non-LSPed surfaces, EIS was performed for each sample in 3% NaCl solution. The potential was held at -842 mV vs the reference electrode and the oscillation frequency swept from 100 kHz to 100 mHz. Teflon tape covered the surfaces not of interest. Further potentiokinetic testing was performed in 3.5% NaCl solution to determine pitting potential by sweeping the reference potential from -750 mV to 1.5 V. The Tafel approximation determines corrosion current using both anodic and cathodic slopes to find the corrosion rate (β_{An} and β_{Cath}) [46].

Dynamic wettability testing with 10µL droplets of both distilled water and ethylene glycol measures contact angle. Five contact angle measurements are taken per sample and per fluid to verify repeatability. The use of two fluids and hysteresis testing allows calculation of

surface free energy from the contact angle measurements. Using the Owens-Wend-Rabel-Kaeble model, the surface free energy may be calculated with equation 32, where the total surface free energy is the sum of both the polar (p) and dispersive (d) energy components and the equilibrium contact angle (θ) is defined at the end of the advancing (or beginning of the receding) testing regime [11].

$$\frac{\gamma_L(1+\cos(\theta))}{2\sqrt{\gamma_L^d}} = \sqrt{\gamma_S^p} * \sqrt{\frac{\gamma_L^p}{\gamma_L^d}} + \sqrt{\gamma_S^d} \quad \textbf{(32)}$$

The polarized and dispersive components of water are $\gamma_L^d = 21.8$ mN/m and $\gamma_L^p = 51.0$ mN/m and for ethylene glycol are $\gamma_L^d = 29$ mN/m and $\gamma_L^p = 19$ mN/m respectively [26]. The hysteresis measurements may be used for surface free energy calculations using equation 33 where receding (r) and advancing (a) contact angles are defined for the same droplet volume [47].

$$\gamma_S = \gamma_L \cos(\theta_r) - \cos(\theta_a) + \cos^2(\theta_a) + \cos^2(\theta_r) - 1 + \cos^2(\theta_a) \quad \textbf{(33)}$$

Using both hysteresis and two-liquid methods to calculate surface free energy verifies surface trends and isolates the surface's wetting behavior from chemical liquid dependencies.

The contact angles of the surface are then simulated in the surface energy optimization finite element software SE-FIT [35]with equations 25-31, using approximate surface topology. Observing the differences in modelled wettability due to different approximate surface geometry isolates the effect of morphology from chemical changes. A Keyence laser profilometer is used to produce three-dimensional scans. Each surface shape is modelled by a Fourier-series equation fit. Surface profiles are taken across and along the scan tracks in the XY samples and along the build direction (Z direction) and along the scan direction (X direction) in the XZ samples. An eight-term Fourier series equation fits each surface profile. High-frequency surface profiles (defined as texture above a 0.2 Hz frequency) are fit separately and added to the low-frequency

Fourier series to isolate the high-frequency effects of each surface. This two-dimensional surface is then input into SE-FIT which is further used to minimize system energy of a 10 µL water droplet. The surface chemistry is studied with EDS to identify composition of both build orientation surfaces before and after LSP processing.

The effect of compressive residual stress on wettability and electrochemical behavior is investigated using XRD. The $sin\psi^2$ method extracts the surface level residual strains, which are then evaluated to find the residual stress. The reduction of residual stress due to LSP is modelled with finite element analysis in ABAQUS and compared with the measured change. A kinematic hardening model as used in Over et al [21] for LPBF-built 316L describes the plastic response and the experimentally measured residual stress is input as the initial condition for the simulation. The LSP is applied with a user subroutine and is modelled as a time-dependent gaussian-distributed pressure on the top surface of the material mesh with a 10 ns ramped pulse, 1 mm diameter spot, 50% overlap and 6 GPa peak pressure. Quarter-symmetry conditions are applied to the mesh to reduce simulation time. 50 total peens are applied to the quarter mesh with dimensions 3 mm × 6 mm × 3 mm.

4.4 Results and Discussion

4.4.1 Electrochemical Characterization

The EIS measurements for each surface are shown in **Error! Reference source not found.** and their complex response is fit using the equivalent circuit modelled by equation 24. The modelled circuit values are shown in **Error! Reference source not found.**. As seen in the response, the XZ and XY built surfaces display inherently different electrochemical responses and are also differently affected by LSP. It can be seen from both the equivalent circuit values and the plotted impedance response that LSP has a greater effect on the XY-built surface than the

XZ surface. In the XY build orientation, LSP has a primary effect upon the low frequency electrochemistry of the surface as shown by the bode plot in **Error! Reference source not found.** a) and the significant change to the polarization resistance value (R_p). The rise in the Z_{im} vs Z_{re} curve shown after LSP in **Error! Reference source not found.** b) results from this increased resistance. The dominance of the low-frequency response change indicates that LSP has a large effect on material diffusion. In the XZ build orientation the electrochemical response change is less pronounced. Only a moderate rise in the complex impedance plot is shown and the polarization resistance is not increased after LSP. However, the CPE value is increased after LSP indicating an increase to the capacitance and increased impedance to charge transfer reactions.

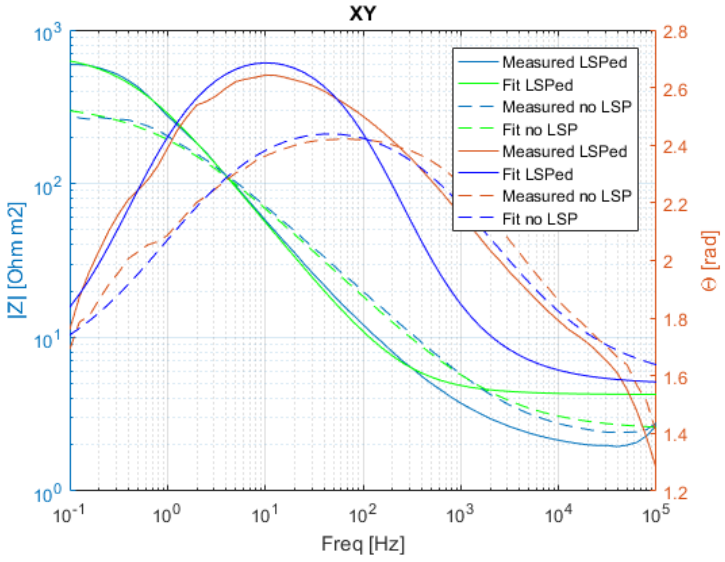

a)

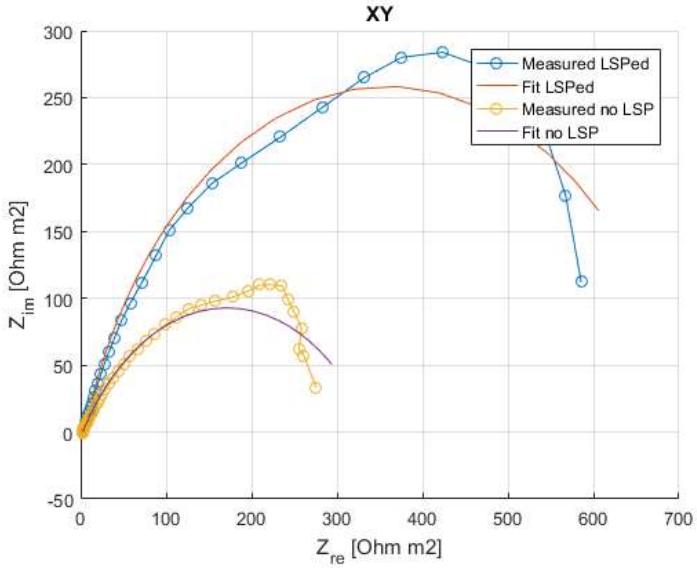

b)

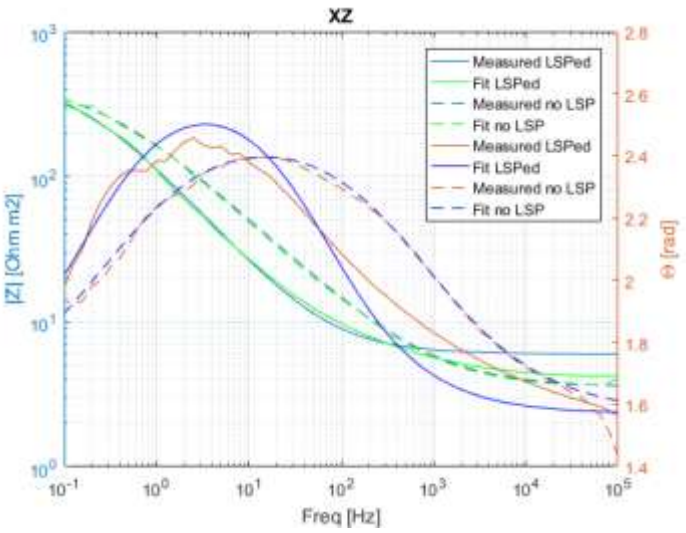

c)

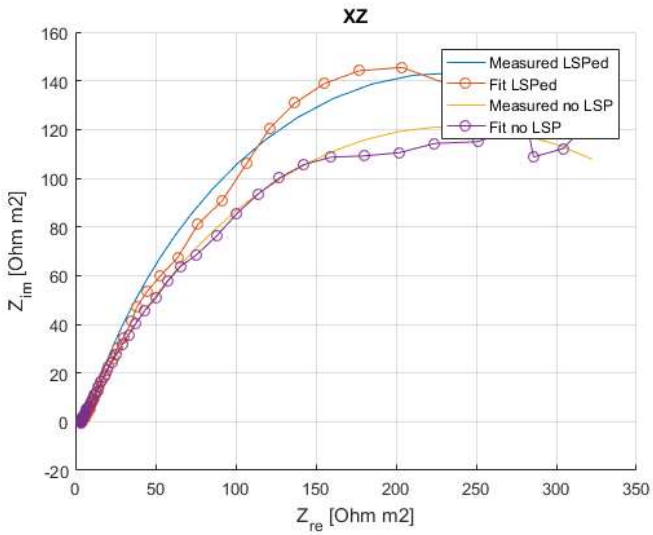

d)

Figure 4. The EIS measurements for as-built and LSPed sample surfaces for the XY a)-b) and the XZ c)-d) build orientations. Bode plots are shown in a) and c) while b) and d) plot the real and imaginary impedances.

Table 2. The equivalent circuit parameters for equation 1 as fit from EIS measurement data shown in Figure 4. The 95% confidence interval for each parameter is in brackets.

	R_s	R_p	Q	α
XY As Built	$24.88\ [1.23, 48.5]\ \Omega cm^2$	$33.73\ [32.5, 35.0]\ k\Omega cm^2$	$2.83\ [2.80, 2.90]\ \mu F cm^{-2}$	$0.64\ [0.62, 0.67]$
XY LSPed	$42.44\ [16.5, 68.4]\ \Omega cm^2$	$71.05\ [69.4, 72.7]\ k\Omega cm^2$	$3.00\ [2.90, 3.10]\ \mu F cm^{-2}$	$0.80\ [0.78, 0.82]$
XZ As Built	$35.14\ [25.1, 45.2]\ \Omega cm^2$	$46.49\ [45.4, 57.6]\ k\Omega cm^2$	$4.75\ [4.70, 4.80]\ \mu F cm^{-2}$	$0.71\ [0.71, 0.73]$
XZ LSPed	$59.83\ [50.9, 68.8]\ \Omega cm^2$	$45.36\ [44.1, 46.7]\ k\Omega cm^2$	$8.06\ [7.90, 8.20]\ \mu F cm^{-2}$	$0.61\ [0.60, 0.62]$

The potentiokinematic results, as shown in **Error! Reference source not found.** a) and b), reveal that LSP improves corrosion behavior especially in the XY sample. An example of the Tafel approximation used is shown in **Error! Reference source not found.** c). The calculated p itting potential and corrosion rate for each sample is shown in **Error! Reference source not found.**. Similar to the results described in Melia et al [34], the XZ samples are shown to have higher pitting potential than the XY samples. LSP increases pitting potential by 52 mV in the XY

samples and 106 mV in the XZ samples. In XY samples the corrosion current is shown to reduce by 30 mA/m^2 after peening. However, in the XZ samples the corrosion current increases after LSP. This phenomenon is studied and explained in subsequent sections by chemical and morphological measurements. The differences in corrosion behavior may in part be attributed to surface wettability, increased contact angle causing reduced charge transfer in the corrosive species.

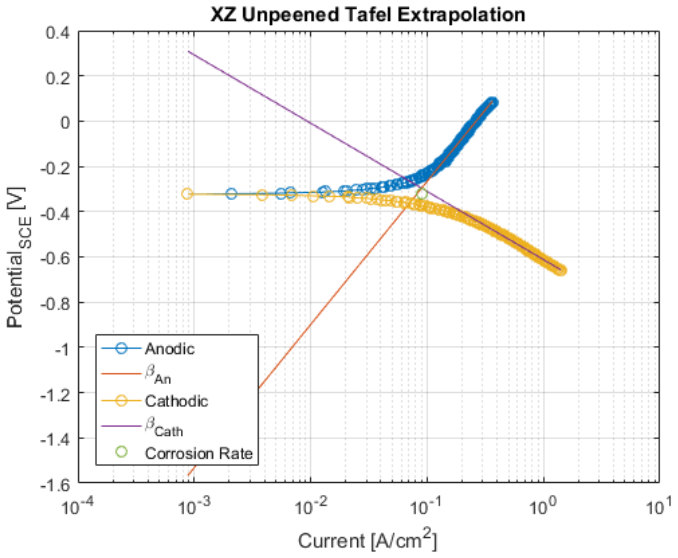

Figure 5. Potentiokinematic testing results in 3.5% NaCl solution shown for the XY a) and XZ b) build orientations. An example of the Tafel approximation calculation is shown in c).

Table 3. Corrosion potential and corrosion rate as calculated from potentiokinematic testing. The pitting potential measurement error is 2.249 mV. The corrosion rate 95% confidence interval is in brackets.

	Potential (E_{Corr} (SCE) $[mV]$)	Corrosion Rate (I_{Corr} $\left[\frac{mA}{m^2}\right]$)
XY As-Built	-588	60.6 [59.2, 61.9]
XY LSPed	-536	30.6 [29.0, 32.1]
XZ As-Built	-429	41.5 [40.8, 42.3]
XZ LSPed	-323	89.7 [89.7, 89.6]

4.4.2 Wettability and Morphology

Contact angle measurements of both build orientation surfaces show that the XY and XZ surfaces have distinctly different wettability behaviors and respond differently to LSP. These measurements are shown in **Error! Reference source not found.** a) and **Error! Reference so urce not found.**.The as-built XZ surface contact angles have larger variance than the XY surface. Both surfaces exhibit different wettability behavior along different profiles of the surface. These surface profiles are measured and studied with profilometry. In the XY surface the droplets have higher contact angle across the laser scan tracks than along the scan tracks and the XZ surface has higher contact angles along the build direction (Z direction) than along the scan direction (X direction). After LSP both surfaces exhibit reduced wettability. Furthermore, LSP reduced the variance of the XZ surface contact angles significantly.

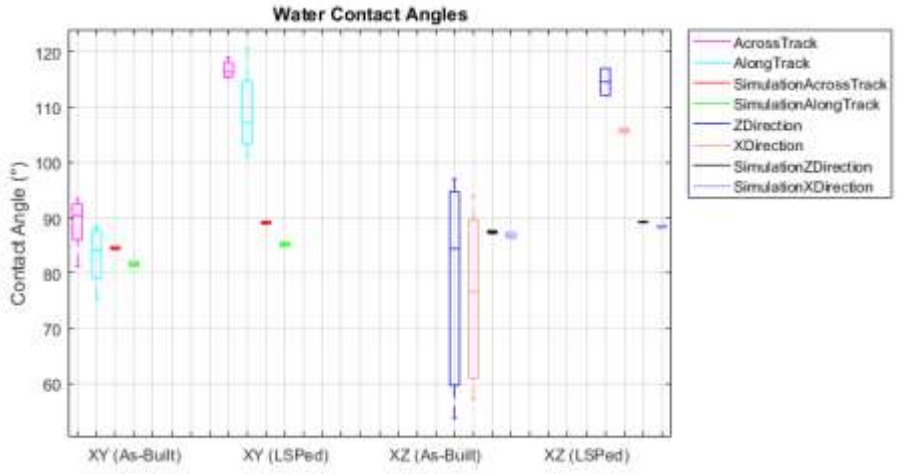

a)

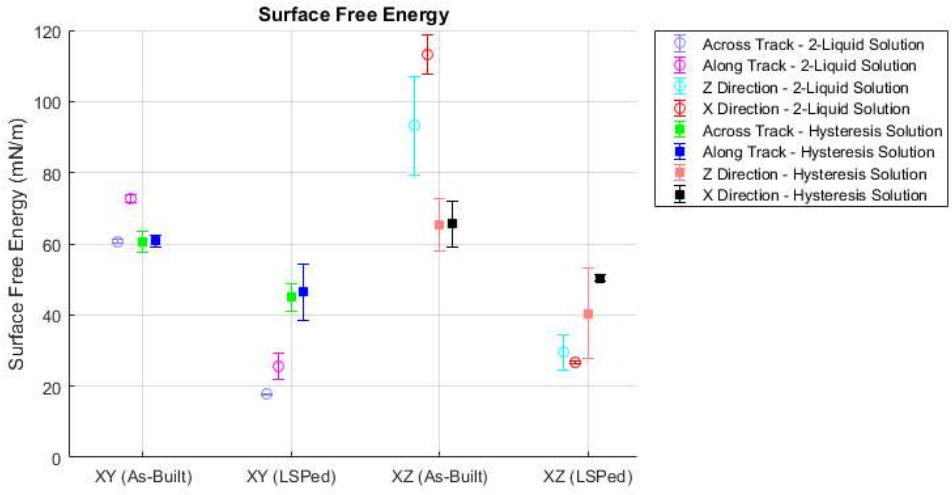

b)

Figure 6. a) Wettability measurements showing the contact angle for both XY and XZ build orientations before and after LSP in comparison with simulated values. The box denotes the interquartile interval, the line marks the median and the whiskers identify maximum and minimum values. b) Surface free energy calculations for each surface using both hysteresis and two-liquid calculation methods. The marker identifies the mean value and the error bar shows the standard deviation.

Table 4. Average measurement and simulation (SE-FIT) contact angles with standard deviations. The wettability simulation is averaged between left and right values mesh values on the modelled uneven surface, thus there is a standard deviation associated with it.

Wettability Measurements					
XY			XZ		
	As-Built	LSPed		As-Built	LSPed
Across Track	88.98 (±4.90)°	116.74 (±1.72)°	Z Direction	78.14 (±19.46)°	106.57 (±9.69)°
Along Track	83.13 (±5.40)°	109.02 (±8.41)°	X Direction	75.60 (±15.91)°	104.95 (±2.56)°
Wettability Simulation					
XY			XZ		
	As-Built	LSPed		As-Built	LSPed
Across Track	84.47 (±0.34)°	89.10 (±0.33)°	Z Direction	87.40 (±0.34)°	89.21 (±0.14)°
Along Track	81.63 (±0.64)°	85.18 (±0.56)°	X Direction	86.79 (±0.68)°	88.37 (±0.35)°

The nuanced effect of morphology on contact angle may be investigated through surface modelling and contact angle simulation. Surface morphology measurements are shown in **Error! R eference source not found.**. XY samples demonstrate periodic texture corresponding to melt pools along the scanning direction with some spatter and balling that disrupts the regular structure. The XZ surface exhibits more spatter and balling phenomenon overlaying a low-profile periodic terrain corresponding to the layer height. The periodic channel structure produced by the laser melt pools causes a capillary effect in liquid droplets along the scan tracks. This effect explains why, as shown in in **Error! Reference source not found.** and **Error! Re ference source not found.**, contact angles observed along the scan direction are less than those measured across build layers or across scan tracks. The arithmetic mean surface roughness (Sa) measurements given in **Error! Reference source not found.** show that for both as-built and LSPed conditions, the XZ samples exhibit a higher surface roughness than XY surfaces. The large number of spatter and balling features on the XZ surface may in part explain the increased variance in the measured surface contact angles. The droplet contact line experiences a "sticking" effect or pinning when encountering a large obstacle, causing the contact angle to remain high while the volume of the droplet expands [48]. When the droplet's internal pressure becomes high enough, the barrier is overcome and the contact line advances rapidly causing the contact angle to then significantly reduce. The high occurrence of these obstacles on the XZ surface, leads the contact angle measurements to vary greatly between observations. As in Siddaiah et al [29], LSP is shown to reduce surface roughness, which is a very different behavior to the effect of LSP on polished or even more regular rough surfaces [27]. This is due to LSP flattening of some pinning barriers which also results in the observed reduction to the variance of XZ contact angles. Fast Fourier transforms of the scanned surface topology, as shown in **Error! R**

eference source not found. shows that LSP also reduces the high frequency noise of the surface. This high-frequency noise reduction contributes to the contact angle change as is evidenced by modelling and simulation.

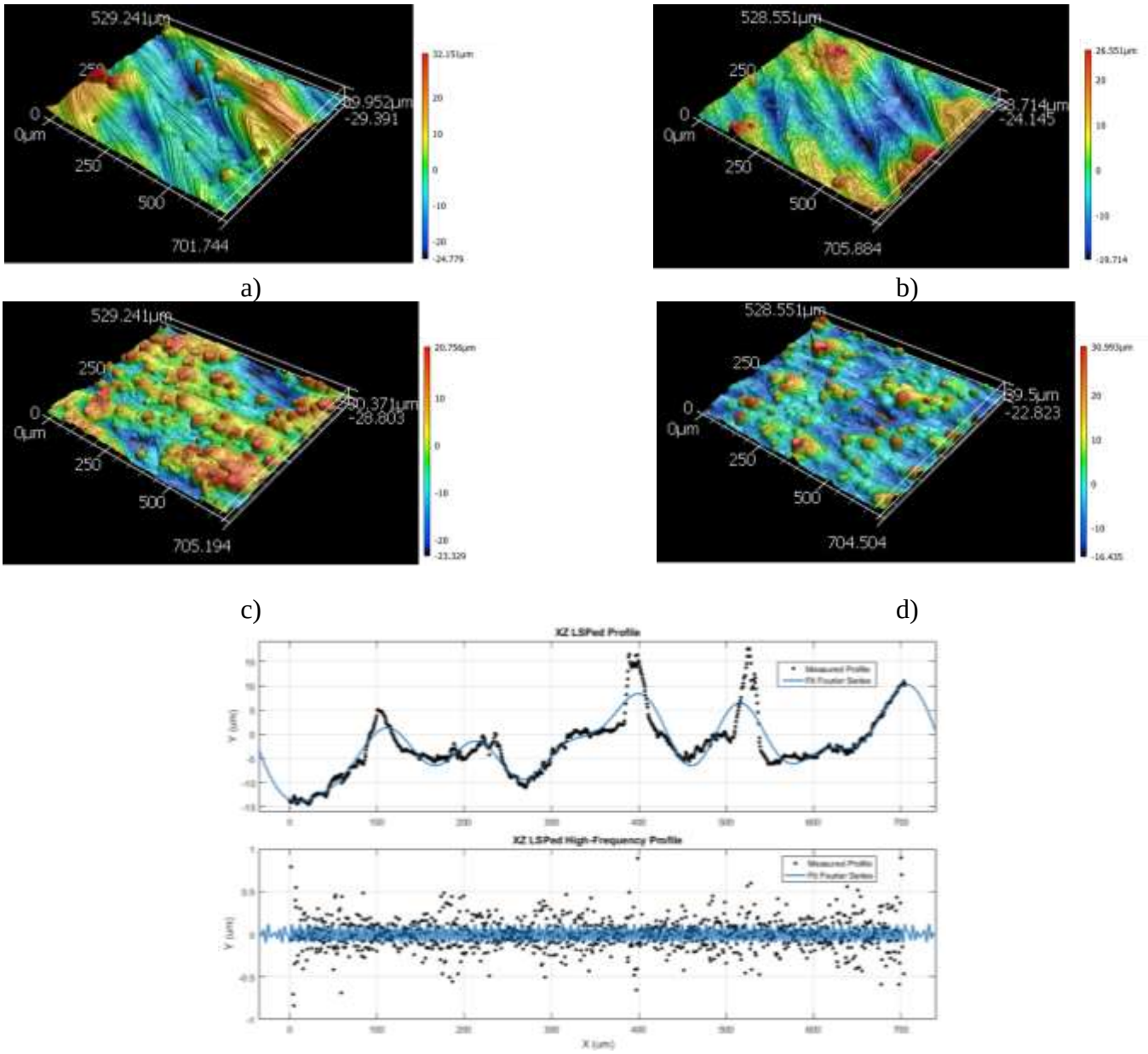

Figure 7. Surface morphology measurement for XY (a-b) and XZ (c-d) build orientations in as-built (a & c) and LSPed (b & d) conditions. A sample profile with Fourier series fit is shown in e).

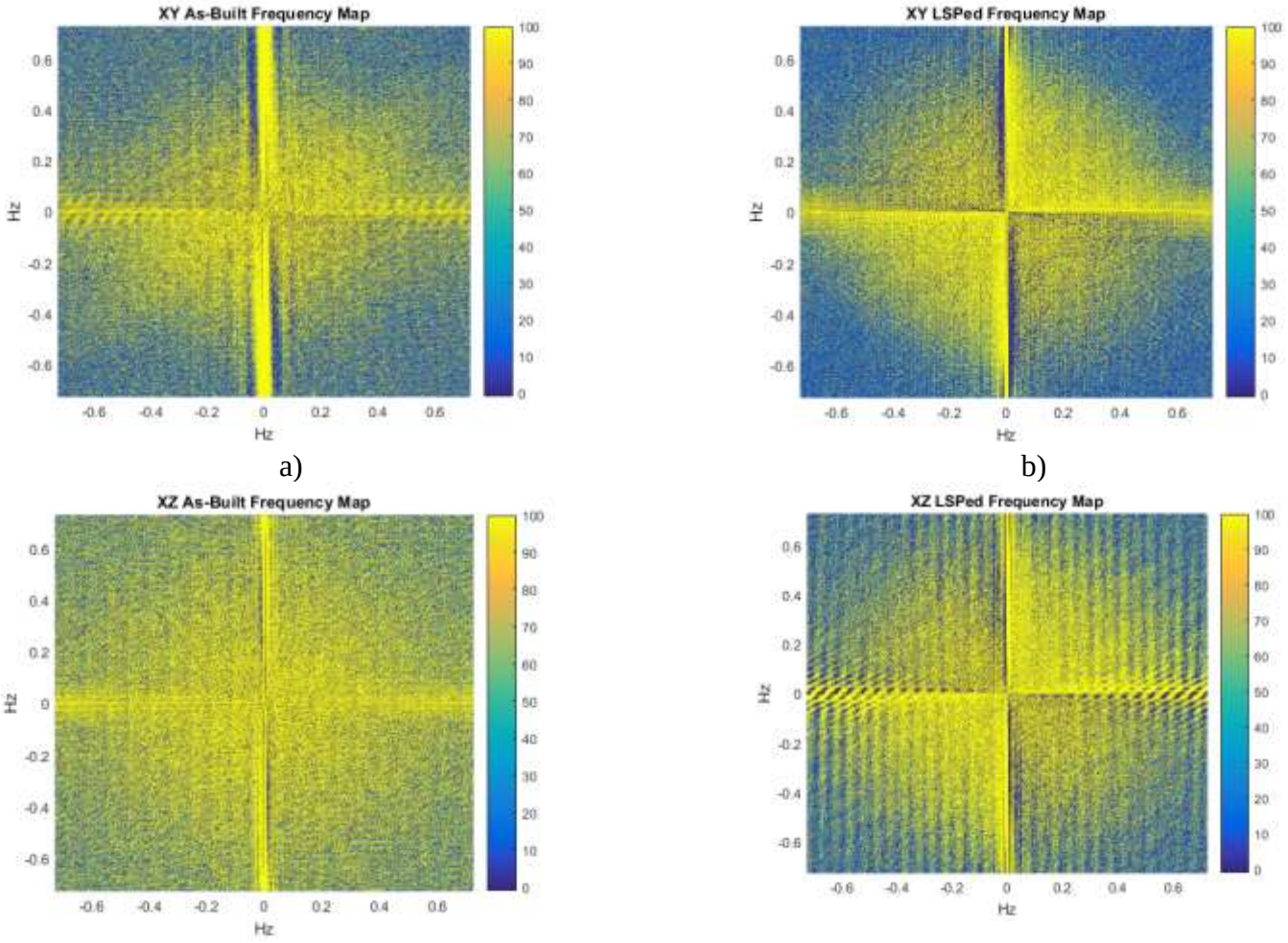

Figure 8. Fast Fourier transform frequency map for XY as-built (a), XY LSPed (b), XZ as-built (c), and XZ LSPed (d) surfaces.

Table 5. The surface roughness arithmetical mean height (Sa) measurements from each surface for both XY and XZ build orientations and LSPed and as-built samples. Height measurement resolution is 1 nm and the profile step size is 0.69µm.

	As-Built	LSPed
XY	1.29 µm	1.06 µm
XZ	2.33 µm	2.20 µm

The surface energy of each surface may be seen in **Error! Reference source not found.** b), calculated using both hysteresis and two-liquid methods which are described by equations 32

and 33 respectively. The two methods of surface energy calculation show that LSP significantly reduces surface free energy, leading to the tendency for higher contact angle when in contact with a liquid. The two-liquid calculation method also identifies that the droplets of either liquid have a tendency to spread along the scan direction. The agreement in energy trends between these methods supports the rationale that build direction is crucial for additively manufactures parts in aqueous environment and LSP postprocessing unilaterally improves wettability for corrosive applications.

The SE-FIT modelled contact angles along each direction as seen in **Error! Reference s ource not found.** a) are found to demonstrate similar trends to the experimental measurements. The left and right contact angles at the edge of the droplet mesh confined to the modelled surface are averaged for each surface and values are given in **Error! Reference source not found.**. The a cross-track contact angles are higher than the along-track contact angles in the XY sample and the XZ surface also shows a higher contact angle along the build direction than along the scan direction. Furthermore, the XZ samples are modelled to be less wettable than the XY samples just as is seen experimentally. The LSPed surfaces were modelled to have higher average angles for both the XY and XZ surfaces, a trend that is also reflected in the experimental measurements. However, while the modelled as-built contact angles are within one standard deviation of the experimentally measured values, the modelled LSPed samples do not closely match the contact angles of the real samples, experimental contact angles exceeding their modelled counterparts. This indicates that LSP alters the surfaces by more than just morphologically and therefore chemical investigation is also crucial to understand the modification.

4.4.3 Residual Stress Measurements and Simulation

XRD measurement reveals the residual stress in the as-built sample surface. The stress eigenvalues are found for each sample and input into the ABAQUS simulation as an initial condition. These measurements show that the surface of both XZ and XY samples have tensile residual stress and after LSP exhibit compressive residual stress. The values are shown in **Error! R eference source not found.**.

Table 6. Residual stress as measured by XRD with the $sin\psi^2$ method as displayed with 95% confidence intervals. Results are shown for two orthogonal in-plane directions.

Residual Stress Measurement (In-Plane Stress)					
XY			XZ		
	As-Built	LSPed		As-Built	LSPed
X Direction (σ_{xx})	334 [592, 353] MPa	-168 [-197, -140] MPa	X Direction (σ_{xx})	223 [601, -154] MPa	-25.2 [28.5, -78.9] MPa
Y Direction (σ_{yy})	80.0 [193, 2.54] MPa	-338 [-1740, -11.2] MPa	Z Direction (σ_{zz})	1.13 [222, -149] MPa	-1.06 [16.56, -6.40] MPa

The simulation calculates a surface level of compressive residual stress in both XY and XZ specimens after LSP. Planar stress distribution in the mesh may be seen in **Error! Reference s ource not found.**. The compressive residual stress is simulated to penetrate up to 0.4 mm into the sample surface. According to this simulation, the residual stress after LSP is similar in magnitude for both sample surfaces, though the initial stress conditions differ. However, experimental analysis shows that the XY sample exhibits greater compressive residual stress after LSP in comparison to XZ samples. The XY build orientation has been previously shown to be more susceptible to mechanical change due to LSP which is attributed to differences in grain orientation and morphology [21]. These factors are not ably captured in the bulk mesh simulation. However, the simulation is capable of capturing the overall mechanical response which thus matches the XY sample response well.

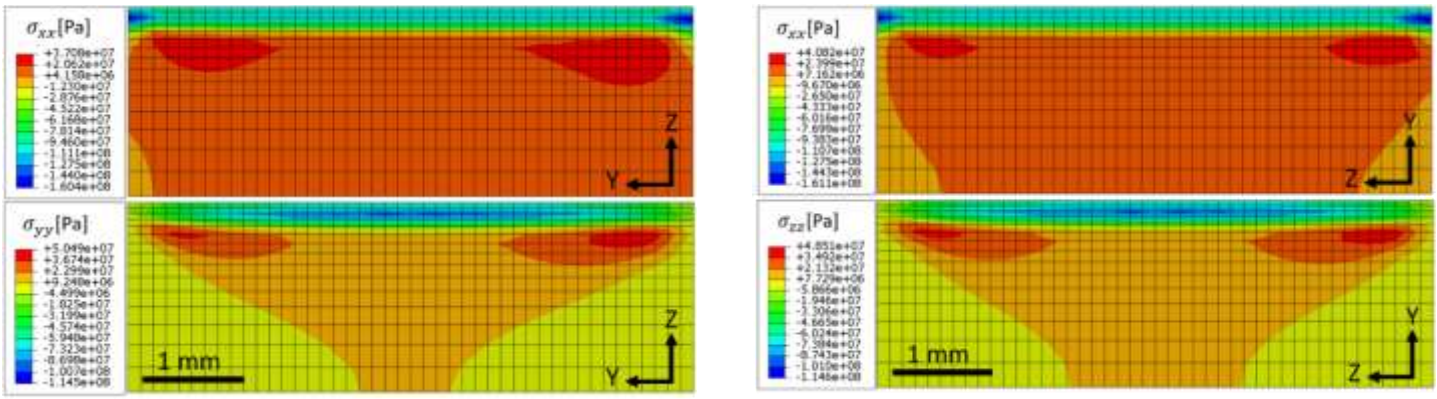

a) b)

Figure 9. Stress simulation of LSPed samples for a) XY and b) XZ build orientations.

The experimentally measured differences in residual stress response across each build orientation can explain differences in pitting potential, corrosion rate and electrochemical resistance. XZ samples do not develop significant levels of compressive residual stress after LSP and thus, while the surface's pitting potential increases which is likely the result of surface-free energy changes, the corrosion rate is not improved. Conversely, the XY samples demonstrate significant increase in resistance to charge transfer and reduced corrosion rate in addition to pitting potential improvement. As is discussed in the next section, these effects are reinforced by the surface chemistry in both build-orientation surfaces before and after LSP.

4.4.4 Surface Chemical Measurements

EDS measurements show that the build strategy affects the as-built surface chemistry, which is further altered by LSP post processing. As shown in **Error! Reference source not f ound.** a) and b), the edges of the scan tracks in the XY surface show precipitation of silicon and oxygen. In the XZ surface, silicon and oxygen precipitate along the edges of the layers. The prevalence of these elements alludes to the presence of silicon oxides. After LSP, as shown in **Error! Reference source not found.** c) and d), these silicon oxides are more evenly dispersed o ver the surface of the material. The line profile scans in **Error! Reference source not found.**

exhibit that the oxide compounds are no longer periodically distributed along the scan tracks after LSP. However, after LSP the overall silicon content is increased by 10.2% in the XY sample and by 6.85% in the XZ sample. The XY surface also shows a 1.77% increase in oxygen content after LSP indicating an increase in oxides, though the XZ surface decreases by 1.22% in oxygen content. These oxides likely affect the surface's wetting characteristics as well as electrochemistry. The periodicity of the oxides contributes to the wetting characteristics by creating periodic hydrophobicity. This exacerbates the effects of the periodic morphology in the as-built samples causing differences in contact angle along and across scan tracks. Removing this periodicity and also increasing the silicon content contributes to reduced wettability beyond the change predicted by solely the morphological simulation. The overall increase in silicon and oxides contributes to change in electrochemistry by increasing resistance to charge transfer by introducing an additional semiconductive layer. The oxide increase in the XY samples after LSP likely contributes to the reduction in corrosion rate and the decrease in the XZ sample after LSP may explain the increase in corrosion rate as observed by EIS.

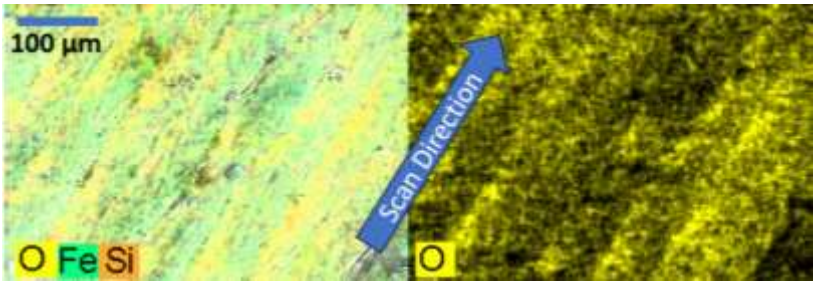

a)

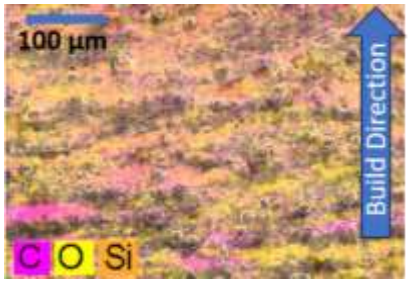

b)

c)

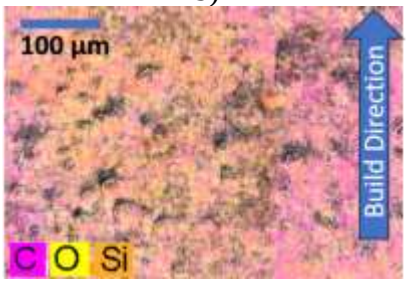

d)

Figure 10. EDS scans of the as-built a) XY and b) XZ surfaces and the LSPed c) XY and d) XZ surfaces. These images demonstrate precipitation of silicon and oxygen along the scan tracks.

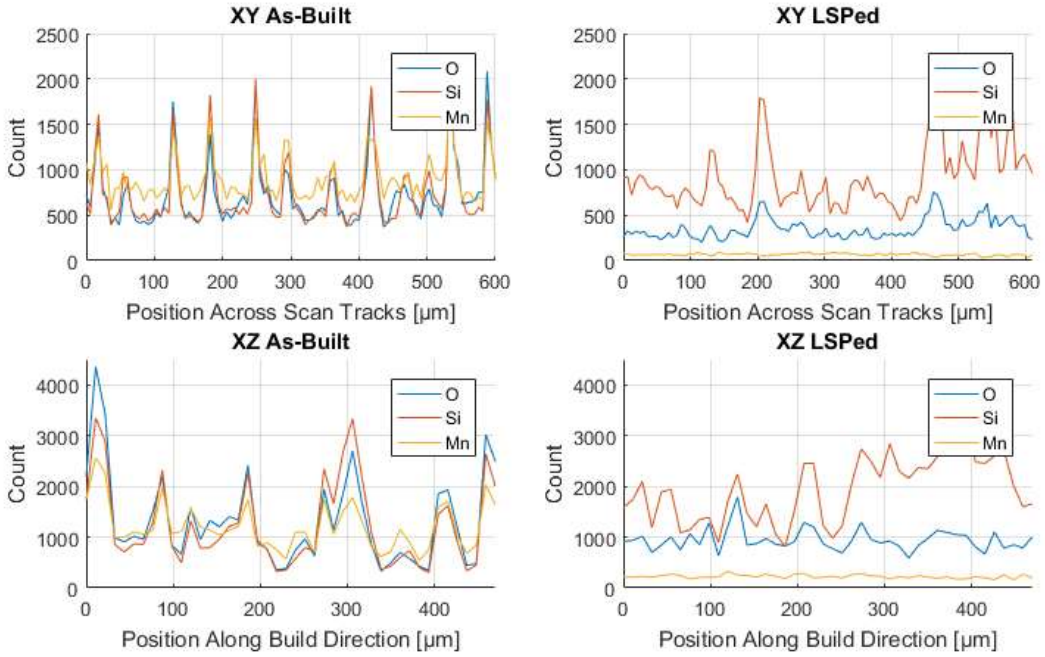

Figure 11. EDS line scans of surface chemistry in the the XY as-built (Top Left), XY LSPed (Top Right), XZ as-built (Bottom Left) and XZ LSPed (Bottom Right) sample surfaces.

4.5 Conclusion

The corrosion properties of stainless steel built with LPBF is shown to be improved by LSP post-processing. However, these properties before and after LSP are also dependent upon which surface of the LPBF part is exposed to the corrosive environment. Both the top surface perpendicular to the build direction (XY) and the wall surface parallel to the build direction (XZ) are investigated showing differing results. In EIS investigations, the XY surface shows an increase in polarization resistance after LSP while the XZ surface exhibit an increase in CPE capacitance. Potentiokinematic analysis shows the pitting potential increases for both build directions after LSP. Conversely, the corrosion rate is reduced in the XY surface after LSP while

it is increased in the XZ surface. These results show that build strategy greatly affects the surface interaction of LSP with the work piece. Surface contact angle measurement and simulation demonstrates that wetting is altered significantly by LSP for both surfaces, increasing hydrophobicity for both XZ and XY surfaces. The as-built surface morphology also greatly impacts surface-free energy. The swells that occur along scan tracks and surface layers interact with spatter surface aberrations to produce preferential wetting along the scan line. Residual stress measurements explain the electrochemical trends. The surface compressive stress in the XY samples after LSP is shown to be much larger in magnitude than in the XZ surface. Compressive residual stress is shown to reduce corrosion rate which may explain why the XY samples show such a distinct corrosion rate reduction while the XZ samples do not. The surface chemistry as observed by EDS of as-built samples identifies silicon oxides at the edge of scan tracks and layers in the XY and XZ surfaces respectively. These silicon oxides are dispersed more evenly over the surface after LSP which simultaneously decreases the surface-free energy of the sample and increases charge flow resistance, thereby resulting in improved corrosion behavior.

Chapter 5: Mitigation of Stress Corrosion Cracking in Additive Manufactured Stainless Steel by Laser Shock Peening

5.1 Introduction

Application of laser powder-bed fusion (LPBF) for manufacturing of fluid mechanical parts offers significant industry opportunities. LPBF's ability to achieve high-resolution fluidic features broadens design potential and it is already being used to produce low-volume batches of complex parts used in nuclear reactor cells [3] [4]. Minimizing corrosive failure of LPBF parts is key for this application to reach its full potential. Stainless steel alloys, in particular 316L, are chosen for such environments due to their inherent corrosion resistance. The face centered cubic (FCC) lattice structure and the thermodynamic stability of this alloy make it particularly resistant to hydrogen embrittlement. However, 316L is still susceptible to failure by stress corrosion cracking (SCC) when combined with a tensile load in a corrosive environment.

Studies show that LPBF stainless steel experiences heightened SCC crack growth rate in comparison to wrought [5]. This vulnerability may be explained due to many mechanisms and material properties specific to additively manufactured metal. Perhaps the most critical feature that places additively manufactured metal at risk of SCC is the surface-level tensile residual stress that arises in parts due to the complex thermal cycling of the build process [6]. This residual stress results in continual static loading that exacerbates the stress state of loaded parts. The anisotropic microstructure in LPBF metal also aggravates concerns and leads to anisotropic crack resistance, causing preferred directions for crack growth. SCC crack growth in LPBF samples is more than twice as fast when they are loaded transversely to the build direction, the cracks opening along the elongated grains that result from epitaxial grain growth [5]. The role of SCC mechanisms in developing these differences between build directions have not yet been

deeply investigated. This causes complications for designers that must also consider build direction when designing critical parts. Unlike in wrought samples, additively manufactured stainless steel exhibits nonuniform internal structure with ferrite phase separation along melt-pool boundaries that are revealed with etching [7]. These phases are especially prone to sensitization and intergranular corrosion. 316L stainless steel built with LPBF is shown to sensitize more readily than wrought samples [7]. Furthermore, the high density of dislocations surrounding the melt-pool boundaries cause localized dissolution and failure [8] [9]. Increased porosity and pore size also impacts SCC failure, causing elevated crack growth rate [5]. Pores cause crack tunneling by increasing the stress intensity factor ahead of the cracks, allowing for more rapid crack propagation. Pores in the surface exposed to the corrosive environment can also contribute to SCC by creating pockets of localized acidity which encourage anodic exchange between the metal surface and the environment, thereby accelerating SCC mechanisms. Exacerbating this effect, the grooved surface morphology of additively manufactured metals is host to many exposed crack initiation sites and contributes to acidification. The high density of dislocations in as-built LPBF samples may also introduce dislocation mobility thus inducing cleavage fracture. Cleavage fracture is heightened in 316L LPBF samples due to both defects and strong texture which introduces favorable slip directions [8]. Combatting these effects by creating a robust passive bilayer are the protective chromium and silicon-rich oxides which form at the perimeter of melt pools and around pores. However, when these oxides leach the surrounding material of chromium, they heighten sensitization and thus further contribute to SCC [9]. Hydrogen embrittlement is a key factor in causing SCC and Bertsch et al [10] found that both direct energy deposition (DED) and LPBF additively manufactured specimens were more susceptible to hydrogen uptake than wrought samples. Miller et al [11] recorded that LPBF

316L steel was also more prone to hydrogen embrittlement as compared with traditionally manufactured 316L. With such complex and non-uniform concerns, a solution that fortifies LPBF stainless steels against SCC in corrosive environments is of great interest.

Reduction of residual stress, environmental control, surface coatings, crevice-free design, and incorporation of corrosion inhibitors are all methods of controlling SCC in stainless steel [12]. Many of these solutions may not match a specific design intent. Environmental controls are only achievable in closed systems, surface coatings degrade, and corrosion inhibitors complicate system chemistry. Furthermore, crevices may be required to optimize fluidic geometries. Reducing residual stress in LPBF 316L steel through heat treatment or adjusting sample thickness has shown subsequent reduction in SCC susceptibility and vulnerability to hydrogen embrittlement [13] [10]. However, tensile residual stress relief through in-situ heating, annealing, and hot isostatic pressing cause softening and complicate manufacturing which may be undesirable [14] [15]. Laser shock peening (LSP) post-processing relieves tensile residual stress and also imparts deeply penetrating beneficial compressive residual stress that improves corrosion and SCC behavior without the above drawbacks.

LSP has been found to improve both SCC and dissolutive corrosion behavior in metal [1] [16]. LSP alters the surface electrochemical impedance by improving hydrophobicity and reducing ion exchange with the corrosive environments. These alterations are achieved by imparting compressive residual stress that increases the energy required to eject electrons from the surface and tightens the surface lattice preventing adsorption of corrosive elements [17] [18]. Testing of wrought 304 samples with and without LSP after cathodic charging imply that hydrogen embrittlement is significantly mitigated by LSP [1]. Martensitic transformation due to hydrogen adsorption, which leads to fracture and corrosion vulnerability, is similarly

demonstrated to be reduced by LSP [17]. The shockwaves produced by LSP are hypothesized to induce dislocations that arrest hydrogen uptake in the metal lattice thereby preventing detrimental hardening and embrittlement. While LSP has been applied to LPBF metal beneficially reducing residual stress [19], increasing fatigue life [20], tailoring microstructure [21], and improving mechanical properties such as back stress [2], it has not yet been studied in application to SCC.

This paper demonstrates that LSP improves SCC behavior in additively manufactured 316L stainless steel and identifies key mechanisms by which this improvement is actualized. Furthermore, studying samples built in two different build orientations reveals how LSP interacts with the anisotropy of additively built material to produce differences in SCC improvement. X-ray diffraction (XRD) is also used to identify residual stress disparities before and after LSP and orientation imaging microscopy (OIM) identifies augmentation to dislocation distribution. Sub-surface hardness testing allows verification of degrees of hydrogen embrittlement before and after SCC testing. SEM and electron backscatter diffraction (EBSD) imaging of crack morphologies further elucidates cracking mechanisms while crack dynamics are also considered through phase-field FEA modelling. Parameter search with this phase-field modelling also isolates causality.

5.2 Background

The interaction between LPBF stainless steel, SCC, and LSP is a new field of study, motivating brief review of the individual mechanisms at play. SCC is critically linked to hydrogen interactions within the targeted metal. In particular, infiltration of the metal lattice with hydrogen from the corrosive environment induces hydrogen embrittlement, resulting in failure via four primary causes: 1) hydrogen-enhanced localized plasticity, 2) hydrogen-enhanced

decohesion, 3) dislocation emission, and 4) hydride formation and cleavage [22]. Above the critical hydrogen density and/or above the critical stress level, hydrogen enhanced decohesion and hydride induced cleavage are the most prevalent modes of failure, while below these thresholds the material is prone to hydrogen enhanced localized plasticity and dislocation emission. In stainless steels, hydrogen enhanced decohesion and hydrogen-enhanced localized plasticity are most relevant. These processes present a unique challenge to the complex structure and mechanical properties of additively manufactured parts.

5.2.1 Stress Corrosion Cracking (SCC) of Additively Manufactured Metal

The dislocation structure within additively manufactured metals has a convoluted influence upon the material's SCC and dissolutive corrosion behavior, however hydrogen response is posited to be linked to initial dislocation structures [10]. Dislocations are shown to be highly prevalent in as-built LPBF structures and contribute significantly to mechanical properties [23] [2]. Given that dislocations are also critically relevant in hydrogen embrittlement, it is intuitive that their unique distribution in LPBF steel will affect the material's hydrogen embrittlement behavior. Dislocations, grain boundaries, and dendrite boundaries act as hydrogen trapping sites and can encourage hydrogen uptake in the surface of metal [22]. Meanwhile, subsurface dislocation tangles may also act to reduce the hydrogen diffusion coefficient by halting the transport of hydrogen into the metal's interior [1]. This interplay is relevant especially with respect to build orientation. In the study of SCC in two differently built samples of additively manufactured Ti-6Al-4V, the exposure of columnar dendrite boundaries to the corrosive medium is proposed to be the cause for the enhanced susceptibility of the horizontally built samples in comparison with those built vertically [24]. Similarly, Cruz et al [25] and Lou et al [5] found that specimens loaded along the build direction in corrosive medium had improved

ductility and reduced crack growth rate respectively when compared with specimens loaded perpendicularly to the build direction. The inference of these studies is that the exposure of the long axis of the elongated grains to the corrosive medium creates a barrier to the infiltration of hydrogen and also arrests crack growth by introducing an increased number of grain boundaries into the crack path. A similar argument emphasizing the effect of the elongated grain morphology in crack growth is used to rationalize why additively manufactured metal is prone to crack along the build direction in fatigue loading conditions [26]. This explanation is complicated by the findings of Shoemaker et al [27] who studied an additional alternate orientation in 17-4H where loading occurs transverse to the build direction but with the exposed surface oriented so that the elongated grain surface is the cracking surface. This loading condition is shown to also have higher crack growth rates than the samples loaded along the build direction though the same elongated grain boundaries are exposed to the corrosive medium. Hydrogen transport along dendrite and grain boundaries may therefore not be the only mechanism impacting SCC in additively manufactured metal. Hydrogen enhanced localized plasticity (HELP) has been identified by many studies as being a critical cause in additively manufactured metal for hydrogen embrittlement due to the complexity of dislocation distribution [22]. In Bertsch et al [10], 316L made with direct energy deposition showed reduced dislocation cell size after hydrogen charging presumably due to dislocation mobility phenomenon. If HELP is indeed partially responsible for hydrogen embrittlement in additively manufactured steel, augmentation of dislocations may significantly improve SCC behavior. In heat treated metals with lower overall dislocation density, it is found to be less susceptibility to hydrogen embrittlement, though this may be a result of reduction in residual stress [10].

The relationship between hydrogen embrittlement and residual stress in steel has been experimentally investigated and computationally modelled [28]. The concentration of absorbed hydrogen in the surface of the material is exponentially related to hydrostatic stress ($\sigma = \sigma_{ii}/3$) by:

$$c_0^* = c_0 \exp\left(\frac{V^*\sigma}{RT}\right) . \quad \textbf{(34)}$$

Where c_0 is the equilibrium concentration of hydrogen in the entire solid, σ_{ij} are elements of the Cauchy stress tensor, V^* is the molar partial volume of hydrogen, R is the ideal gas constant, and T is absolute temperature [28]. This equation serves as the boundary condition for the subsequent diffusion problem. The hydrostatic stress in equation (34) is directly impacted by both the applied stress and residual stress. Thus, in pre-strained materials or those with residual stress fields where dislocations are present, decoupling the separate effects of dislocation structure and residual stress is challenging. LPBF stainless steel is prone to both high levels of residual stress as well as significant dislocation density [23] [29]. Posing a promising solution, LSP addresses both of these mechanisms for improved SCC behavior.

5.2.2 Laser Shock Peening (LSP) Mitigation of Stress Corrosion Cracking (SCC) in Additively Manufactured Metal

LSP postprocessing has demonstrated improvement to SCC behavior in traditionally manufactured stainless steel. LSP is performed by directing a pulsed laser of very high fluence at a metal target covered in an ablative layer through a transparent confining medium. The laser energy is absorbed by the ablative layer which is transformed into plasma. The confining medium restricts the plasma expansion causing a high-pressure impact on the surface of the metal creating elastic and plastic shock waves in the target. These shock waves leave behind a compressive residual stress which is attributed with improving mechanical properties such as

fatigue life in processed parts [30]. Such mechanical improvement has been shown to also enhance SCC resistance. LSP applied to the surface of 304L u-bend samples tested for SCC in boiling $MgCl_2$ solution shows simultaneous reduction of crack growth rate and increase in crack initiation time in comparison to non-peened counterparts [31]. The same study positively correlated the average grain size and residual stress with crack growth rate of all tested specimens. These effects reaffirm the outcome of equation (34), showing that hydrogen uptake is reduced with reduction of tensile residual stress. Hardness is often used as a metric after cathodic charging to demonstrate hydrogen embrittlement in metals vulnerable to SCC. LSP is shown to produce dislocation cell structures near the peened surface that increase surface hardness [32]. However, LSP also reduces the hardening due to hydrogen exposure because the created dislocation tangles trap hydrogen and reduce the hydrogen diffusion coefficient, preventing deeper hydrogen penetration [1] [17]. Therefore, when spatially resolved hardness is tested in samples that undergo hydrogen cathodic charging, the LSPed samples, while harder than non-charged non-peened samples, exhibit less of a hardness increase after hydrogen cathodic charging [1]. LSP also reduces hydrogen susceptibility by arresting martensite transformation due to HELP [17]. Not only is martensite more brittle than austenite, but also the lattice structure of martensite has a higher hydrogen solubility which further reduces toughness. It is noted that martensite transformation due to high surface deformation is a concern in stainless steels processed by LSP [33]. However, martensite transformation does not necessarily occur after LSP processing and significant SCC improvement can be achieved [17] [1].

The interaction of LSP with dislocations is of primary importance for as-built additively manufactured metal given the relevance of dislocation distribution for its mechanical properties as discussed above. As in traditionally manufactured metals, LSP is shown to impart increased

dislocation density, dislocation cells, and dislocation tangles in additively manufactured metals [34] [35]. LSP can also induce grain refinement [33]. Furthermore, LSP interacts with the anisotropy and non-uniformity of the dislocation distribution in additively manufactured 316L. As observed in Over et al [2], LSP increases both the level and density gradient of geometrically necessary dislocations (GNDs) near grain boundaries in additively manufactured metal. This increase is more pronounced in samples LSPed along the build direction than in those LSPed transverse to the build direction due to both textural and morphological interactions [2]. The orientation of FCC crystals with respect to the LSP direction is revealed to modify the amount and distribution of the GNDs generated by LSP [36]. OIM shows that texture is present in additively manufactured metal [23] [2]. Therefore, how this texture is oriented with respect to the peening direction influences the degree to which plastic flow may occur. This results in measurable differences in mechanical behavior depending on how LSP is applied to the additively manufactured microstructure, affecting a greater mechanical change when LSP is applied along the build direction [2]. These changes are crucial for failure mechanisms in SCC.

LSP demonstrates a distinctive effect on failure and cracking modes in fatigue loading and SCC conditions. In fatigue loading regimes, optimized LSP processing retards crack growth and reduces crack initiation at the surface [37] [30]. When cracking does occur, it tends to initiate beneath the peened surface [38]. Additionally, application of LSP to a preexisting crack can slow crack expansion [37]. However, if energy density of the laser processing technique is above the optimal level, then there can be detrimental effects. Microcracks may appear in the compressive stress volume and significant surface roughness increase may encourage surface crack initiation [37]. LSP as applied to SCC shows that crack initiation tends to take place the non-peened exposed surfaces [1]. It has been observed that without LSP, wrought stainless steel

exhibits both intergranular and transgranular SCC modes while LSPed samples only exhibit intergranular cracking [1]. This effect is attributed to the increase in hydrogen in non-LSPed samples which reduces fracture toughness by hydrogen-enhanced decohesion (HEDE) thus allowing crack growth through weakened grains. This conclusion is supported by the framework that separates the HELP and HEDE mechanisms between low hydrogen concentration/low applied stress and high hydrogen concentration/high applied stress. However, transgranular fracture does not necessarily evidence HEDE and may occur with HELP as well [39]. It has been shown that fracture toughness alters with LSP surface processing though different papers report different results. In a study of 6061-T6 aluminum alloy LSP was shown to increase fracture toughness by 15.4% [40]. Another study of 6082-T651 aluminum alloy demonstrated a reduction to fracture toughness by 28-33% [41]. Further study of LSP's effect on fracture toughness is needed. Improvement of fracture toughness is another mechanism by which LSP may affect SCC resistance improvement.

5.2.3 Dynamic Crack Growth Modelling of Hydrogen Embrittlement

Crack growth morphologies may be used to identify mechanisms at work in SCC. The presence or absence of crack branching is a telling symptom of the interplay between material properties, geometry, and the applied stress field that caused failure. Cracking occurs when the energy available for crack growth exceeds the resistance energy of the material causing a new crack surface to be formed and work to be done. Crack branching is a lesser understood phenomenon, though it is commonly observed in SCC of stainless steel and also notably in additively manufactured 316L [5]. Lou et al [5] found that macroscopic crack branching occurred in SCC of LPBF 316L when cracks grew perpendicularly to the build direction, while cracks that followed the elongated grain boundaries did not display macroscopic branching.

Microscopic crack branching is posited to coincide with high-energy release, when additional energy is available to develop a fracture surface and thus the material must both create a new crack branch and advance the existing crack to dissipate the energy [42]. Branching also indicates cracking instability. The link between microscopic and macroscopic crack branching modes was established such that the crack branching length scales exponentially with stress [43]. Thus, a higher stress leads to larger crack branching. Crack models may be taxonomized into discrete models (featuring element deletion, cohesive zone models, etc.) and continuous "smeared" models with governing continuous damage functions [42]. A 2D phase-field smeared model proposed by Molnár et al [44] demonstrates good morphological coherence with experimental results. Miehe et al [45] introduced a crack surface function based on a continuous damage factor (d) defined such that $d \in [0,1]$ where $d = 1$ is completely cracked and $d = 0$ is not cracked. The crack topology function that may be solved via Euler discretization is defined over the volume (Ω) as:

$$\Gamma = \int_{\Omega} \frac{1}{2l_c} d^2 + \frac{l_c}{2} |\nabla d|^2 d\Omega \tag{35}$$

where l_c is the length scale used to scale the solution, $l_c = 2h$ where h is the element size. Molnár et al [44] solves this equation via numerical minimization of the phase-field lagrangian:

$$\mathcal{L} = D(\dot{\boldsymbol{u}}) - \Pi(\boldsymbol{u}, d) \tag{36}$$

where $D(\dot{\boldsymbol{u}})$ is the kinetic energy, $\Pi(\boldsymbol{u}, d)$ is the potential energy dependent on the damage factor, and $\boldsymbol{u}$ is the displacement field. The potential energy is broken down into the elastic strain energy ($E(\boldsymbol{u}, d)$), plastic strain energy ($P(\boldsymbol{u}, d)$), and fracture energy ($W(d)$):

$$\Pi(\boldsymbol{u}, d) = E(\boldsymbol{u}, d) + P(\boldsymbol{u}, d) + W(d). \tag{37}$$

The fracture energy ($W(d)$) is then defined in terms of the critical energy release rate (G_c) such that:

$$W(d) = \int_{\Gamma} G_c d\Gamma. \quad \textbf{(38)}$$

This formulation, within the framework of a linearly elastic material followed by perfect plasticity after yield, allows simplified modelling of dynamic crack growth with built-in sensitivity to crucial material properties such as flow stress (σ_f) and critical energy release rate.

To model the material's SCC behavior, it is necessary to identify how different hydrogen embrittlement mechanisms impact the relevant material properties. The HELP hydrogen embrittlement mode may be modelled by adjusting the material's plastic response. HELP involves the attraction of dislocations to adsorbed hydrogen causing increased dislocation mobility and plasticity. Eventually the plastic strain is so great that locking of the plastic flow occurs and the metal fractures locally. This mechanism may be modelled as a softening of local flow stress causing plastic hardening to occur:

$$\sigma_f(c) = \sigma_{mises}(1 - \frac{\xi c}{c_{atm}}) \quad (39)$$

where $\sigma_{mises}$is the local von Mises stress, c is the local hydrogen concentration measured in atoms per solvent lattice atom, $c_{atm}$is the lattice hydrogen concentration of a stress-free solid corresponding to 0.1 MPa hydrogen pressure (taken as 0.3) , and $\xi = 0.1$ is a model parameter describing hydrogen susceptibility [46]. Meanwhile, HEDE is modelled by a change in critical energy release rate:

$$G_c(\theta) = (1 - \chi\theta)G_c(0) \quad \textbf{(40)}$$

where θ is the hydrogen coverage, χ is the damage factor, and $G_c(0)$ is the critical energy release rate without hydrogen [47]. The hydrogen coverage is defined as $\theta = \frac{C}{C+\exp\left(-\frac{\Delta G_g^0}{RT}\right)}$ such that $\Delta G_g^0 = 30\ kJ/mol$ which is the Gibbs free energy of α-Fe phase, $R = 8314\ N \cdot mm/mol \cdot$

K or the ideal constant of gas, and T is the absolute temperature [47]. The critical energy release rate is related to fracture toughness by:

$$G_c = K_{IC}^2/E \quad \textbf{(41)}$$

where K_{IC} is the material fracture toughness and E is Young's modulus. Equation (*40*) models an adjustment to the energy required to fracture the lattice as affected by hydrogen. For iron, $\chi = 0.89$ [47]. LSP may be modelled as the reduction to applied stress and an increase in both flow stress, due to local hardening, and fracture toughness.

5.3 Methods

Experimental testing and FEA simulation of LSPed and non-LSPed additively built 316L stainless steel were performed to investigate SCC behavior. Samples with dimensions 55 mm x 6.35 mm x 2.5 mm were cut with wire EDM from a bar built using LPBF in an EOS M290 3d printer. The build parameters used were 40 µm layer thickness, bulk energy density of 57.7 J/mm^3 and a hatch rotation angle of 67°. The median particle size was 33.44 µm with a span of 0.86 µm. The chemical properties of the powder are given by **Error! Reference source not found.**. After building, the bar was stress relieved at 899°C for 60 minutes.

Table 1. 316L stainless steel powder chemical composition.

	Fe	Cr	Ni	Mo	Mn	Si	N	O	Other
Weight %	64.68	17.96	12.90	2.41	1.44	0.45	0.08	0.05	<0.1%

Twelve samples total were cut from the bar, using two different build orientations as seen in

Figure . The "XY" build orientation refers to the sample type that was built such that the build plane was the cracking surface and the test samples were LSPed along the build direction. The

"XZ" orientation was built such that the wall surface was the cracking surface and test samples were LSPed transverse to the build direction. Six samples were built in the XY orientation and six were built in the XZ orientation. Half of each sample type were LSPed and half were left as controls. The LSPed area is 6.35 mm wide and 40 mm long. The LSP was performed using a Spectra Physics Q-switched laser with a 700-µm diameter spot size set at 9.5 GW/cm^2 with a 75% overlap and 100 Hz repetition rate. The pulse width was 10 ns. An ablative layer of 3M polyester tape was used and the confining medium was transparent 0.25-inch-thick acrylic. A KLA stylus profilometer quantified surface morphology of samples before and after LSP processing. A light 100-grit polish smoothed the surface of the material after cutting. XRD measurements were performed using a Panalytical Xpert3 machine using a Cu long fine focus. The residual stress was extrapolated using the sin-psi-squared method, the 222-plane peak fit with the Pearson VII method. A 2-theta sweep of the XRD signature was performed from 60-120° to glean textural differences between samples and identify if any phase transformations occurred at each of the stages of sample processing. Clearance holes for 4-40 screws were drilled in both ends of each sample which were then bent using a mechanical press and die to achieve a u-bend shape with a curvature radius of 6.25 mm. The sample ends were bolted together and the resulting u-bends were immersed in boiling 37% $MgCl_2$ solution at 155°C and removed periodically to inspect for cracks. The $MgCl_2$ solution was maintained at temperature with a hot plate and prevented from evaporating by using a condenser as seen in Figure 2. Stress corrosion cracking testing apparatus with hot-plate and condenser.

. After cracks initiated, the samples were re-immersed until the last sample had cracked. The samples were then cross-sectioned with a diamond saw and polished with mechanical polish

and electropolishing. A Zeiss Sigma VP Scanning Electron Microscope (SEM) was used to take EBSD of the initial microstructure and also of the cracked cross-sections. Dendrite separation was observed after etching in 10% oxalic acid solution with both optical microscope and SEM backscattered electrons. Cracked cross-sections were then mounted in acrylic and polished to 0.5 µm-surface roughness and microhardness tests were performed on a LECO LM310AT hardness testing machine with 50 N of indentation force and a pyramidal HV indenter.

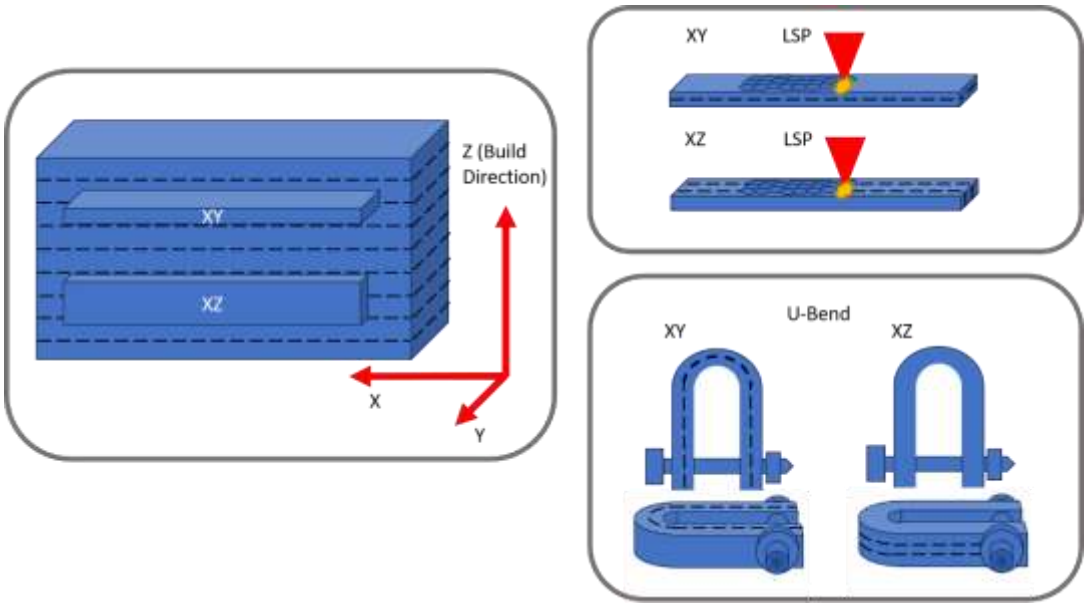

Figure 1. Build strategy demonstrating the two different sample orientations (XY and XZ) with respect to the LSP and u-bend loading direction. The dashed lines indicate layer separations.

Figure 2. Stress corrosion cracking testing apparatus with hot-plate and condenser.

Simulation of the stress applied by LSP and u-bending was performed in ABAQUS. Sixty-two LSP pulses were simulated using a DLOAD user subroutine to apply pressure to the surface of the mesh with the same spot size and pulse width as the experimental process parameters. The pulses are assumed to have gaussian spatial distribution and approximated with a triangle wave in time. The peak pressure applied was 6 GPa, chosen by plasma modelling with simplified coupled-differential equations as discussed in Over et al [48]. The stress profile was then input and an initial predefined field into a bending simulation that used symmetrically applied pressure and a die to recreate the bending process. Cracking simulation was also performed in ABAQUS applying the open-source UEL subroutine [44]. A 2D mesh was used and applied stress, critical energy release rate, and flow stress were varied to match experimental conditions using equations (39) and (*40*) to extrapolate hydrogen embrittlement levels and thereby identifying benchmark values for the observed results.

5.4 Results and Discussion

5.4.1 Stress Corrosion Cracking (SCC) Performance Analysis

SCC testing revealed LSP significantly lengthened time to crack initiation in processed u-bend samples as compared with their non-LSPed counterparts. These results are pictured in Figure . Furthermore, the XY samples cracked after a longer time of immersion than the XZ samples. The XZ non-LSPed samples on average cracked after 49.9±6.75 hours in solution while the XZ LSPed samples cracked after 78.1±4.50 hours in solution. The XY non-LSPed samples cracked after 67.1±3.05 hours in solution while the XY LSPed samples cracked after 81.8±5.75 hours in solution. LSP processing increased the crack initiation times in XZ samples by 28.2±2.25 hours and increased crack initiation times in XY samples by 14.7±2.70 hours. These results show that there are significant differences in the SCC behavior of samples built with different build orientations and LSP also interacts differently with these build orientations.

It is noted that while the improvement to SCC behavior by LSP is synchronous with the existing literature, the lack of crack growth preference for the build direction is somewhat at conflict with past investigations. However, this picture is augmented by the differences reported in cracking behavior and cracking direction between studies such as Lou et al [5], Shoemaker et al [27], and Cruz et al [25]. In each of these studies, comparison of crack growth behavior was performed between samples loaded along the build direction and those loaded transverse to the build direction. However, additively manufactured metals are reported to have a higher toughness when loaded along the build direction even when they are not immersed in corrosive medium [49]. Furthermore, in Shoemaker et al [27], the sample orientation that is loaded transverse to the build orientation but also without the build plane (XY plane) exposed also showed increased SCC rate in comparison with the sample loaded along the build direction. This

nuance in these studies shows that it may in fact be the loading direction and not the crack propagation orientation that is most relevant to crack growth rate. Thus, because none of the studied samples are loaded along the build direction, there is no distinct conflict between literature and the reported results. Investigating crack dynamics for each sample type identifies further differences in cracking behavior.

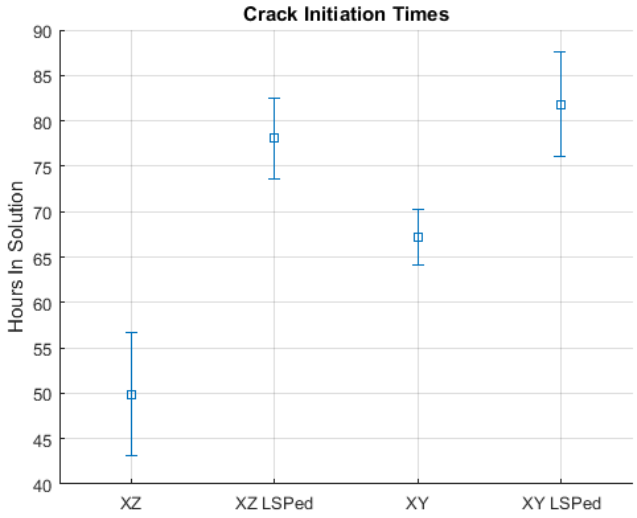

Figure 3. Average crack initiation times in number of hours in solution with standard error for each sample type.

Distinct differences in cracking morphologies between LSPed and non-LSPed specimens reflects differences in SCC susceptibility. Figure shows examples of cracks for each sample type after cross-sectioning, polishing, and etching. These etched samples show ferrite-phase separation at the perimeter of the build's melt pools. The melt pool is shown to be approximately 40 µm deep and 40 µm wide. The non-LSPed samples show larger and longer cracks than the LSPed samples for both build orientations and also show distinctive macro-level crack branching early in the crack. The crack in the XY non-LSPed sample has a macrobranch near the crack initiation site. The right leg of the crack opened more significantly than the left macrobranch and begins to branch again approximately 1 mm into the crack growth penetration. By contrast, the

XZ non-LSPed sample only macrobranches after 200 µm of crack extension and shows more even crack opening between each of the two macrobranches. However, the XZ crack penetrates more deeply into the cross-section than the XY crack. In comparison with the LSPed samples of both XY and XZ types, there is a significant difference in both crack size and behavior. The LSPed samples do not show macrocrack branching, with only some micro cracks that are arrested rapidly. Furthermore, the cracks are significantly smaller in the LSPed samples, especially the XY LSPed sample. The XY LSPed sample does, however, show that the crack turned toward the X direction at approximately a 500 µm depth. Given that crack branching and wider crack opening corresponds to increased crack propagation energy, these differences show that LSP not only increases time to crack initiation, but it also reduces the crack rate once SCC has initiated. Further investigation of the residual stress, microstructure and hydrogen embrittlement mechanisms identifies the causes of these differences in performance.

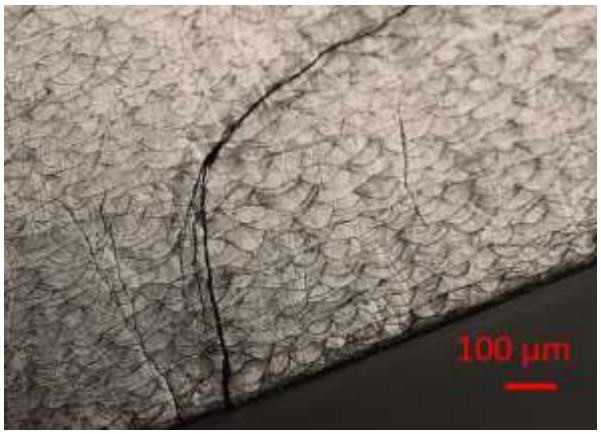

a)

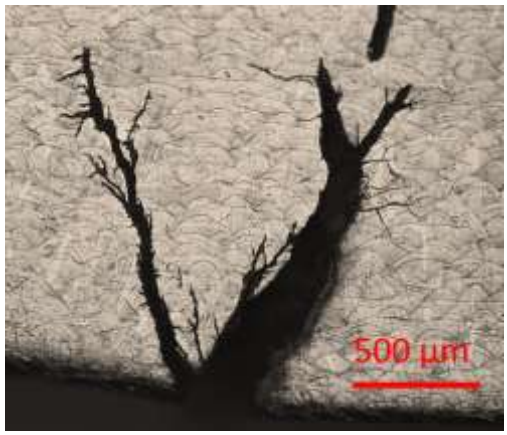

b)

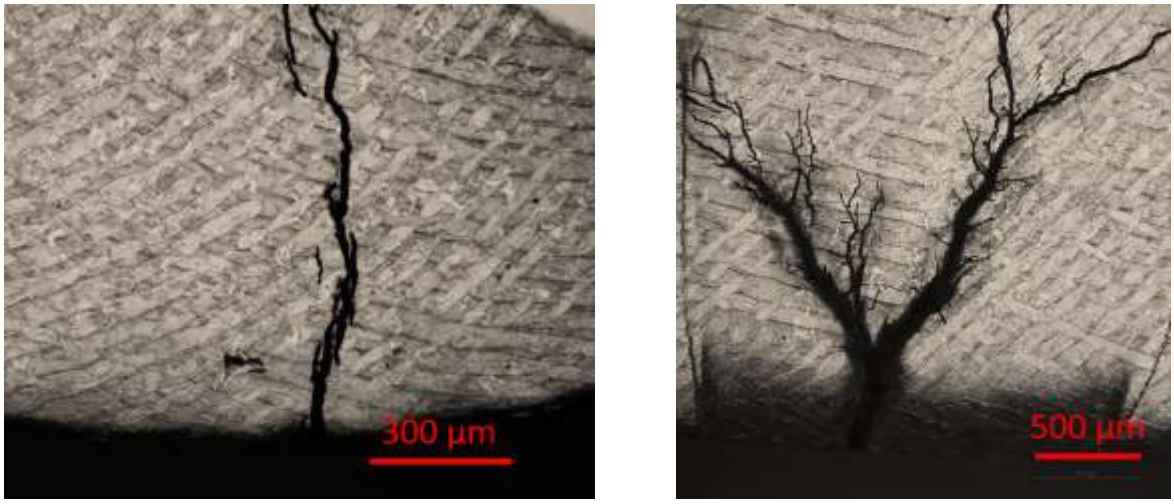

c) d)

Figure 4. Etched crack cross-sections for a) XY LSPed, b) XY non-LSPed, c) XZ LSPed, and d) XZ non-LSPed samples.

5.4.2 Investigation of Hydrogen Embrittlement Mechanisms

The degree of hydrogen invasion of each of the specimen types is reflected be subsurface hardness testing of the cracked cross-sections. Although LSP also leads to hardness increase, the increase caused by hydrogen invasion is significantly higher. Control hardness tests of LSPed and non-LSPed samples without SCC testing were also performed. As seen in Figure b), the XY and XZ samples exhibited similar hardness profiles after LSP without SCC testing. The hardness increase due to LSP is shown to penetrate until approximately 220 µm beneath the peened surface. The maximum hardness for the measured LSPed XY sample, achieved at a 59 µm-depth, is shown to be 255 HV and the maximum hardness for the LSPed XZ counterpart is 252 HV at 60 µm. As-received XY and XZ samples are measured to have hardness values of 219 HV and 226 HV respectively. Samples that are exposed to SCC testing have distinctively different hardness profiles amongst the different sample types. Hydrogen embrittlement causes the hardness to be highest near the surface. The SCC-tested non-LSPed XY and XZ samples have maximum hardnesses of 331 HV and 322 HV respectively and decline to a minimum of 272 HV

and 270 HV towards the center of the cross-section. Notably, the hardness measurements in the XY sample declines steeply and plateaus at a 191 µm-depth while the XZ sample continues to show decline until a 574 µm-depth. This indicates that hydrogen penetration extends more deeply into the XZ metal part while the XY sample arrests hydrogen absorption near the surface of the material. The hydrogen embrittlement response in LSPed specimens is also significantly different between these two build directions. The LSPed XZ sample showed an increase in hardness after immersion in $MgCl_2$, however the hardness increase near the surface was significantly less pronounced than in the non-LSPed samples and thus the slope of the hardness profile is reduced. The maximum hardness, measured at 64 µm depth, is 289 HV and the minimum hardness was 283 HV, thereby showing a decline of only 6 HV in comparison with the decrease of 51 HV in the non-LSPed sample. The LSPed XY sample showed a dramatically different hardness behavior after SCC testing and sub-surface indenting shows almost no change to the hardness profile in comparison with the non-SCC tested LSPed sample. This is a striking result as it implies that the SCC mechanism by which this sample fractured did not penetrate as deeply into the surrounding material. This sample is instead dominated by localized embrittlement limited to the volume near the crack tip, thus resulting in extended crack initiation time and also significantly lower hardness in the neighboring metal.

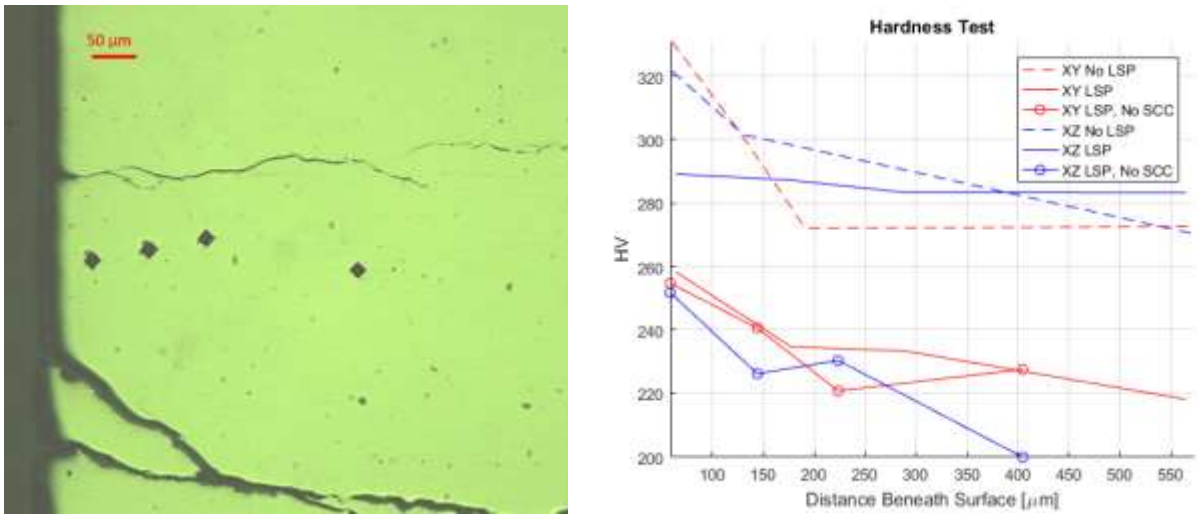

a) b)

Figure 5. Subsurface hardness measurement of cracked and uncracked cross-section specimens in HV showing a) a sample hardness test of an LSPed XY sample and b) hardness measurements.

Stress state directly impacts the absorption of hydrogen in the material's surface shown by equation (34). Therefore, the applied stress is critical to SCC behavior and is modified significantly by pre-existing residual stress. Before SCC testing and u-bending, residual stress as measured by XRD revealed LSP to have a significant effect on the stress state of each sample type. **Error! Reference source not found.** shows XRD-measured residual stress values. R esidual stress was found to be similar for both the as-received XY and XZ samples and highest in the direction of tension; 246 MPa and 228 MPa respectively. In both sample types the direction of tension is identified as the X direction as seen in Figure . The build direction or Z direction also had higher residual stress than the Y direction; 193 MPa as opposed to 53 MPa. These results are consistent with past measurements [2]. After LSP, the surface level residual stress was reduced to be compressive, achieving a greater reduction along the tensile direction in each sample type. The LSP-induced compressive surface stress achieved along X in the XY orientation is -325 MPa versus -311 MPa in the XZ orientation. The transversely induced compressive stress is -138 MPa in the Y direction of the XY sample and -91.0 MPa in the Z

direction of the XZ sample. Such a reduction is almost twice as much as the reduction found in past studies and may be attributed to the softening of the material due to heat treatment [2]. The slightly more compressive residual stress produced in the X direction of XY samples shows that, as in previous investigations, greater mechanical effect was induced when LSP was applied along the build direction. However, this result is not as pronounced as previously reported, potentially also due to some reduction of anisotropy that occurred during stress relief. The residual stress of each sample type is then added to an applied tensile stress in the u-bend process to create susceptibility to SCC. It is apparent that the degree of residual stress directly correlates with the crack initiation times in different testing condition as well as hydrogen embrittlement as measured by hardness testing. Compounding this effect, texture and anisotropic material properties are also shown to be highly relevant.

Table 2. Residual stress as measured using XRD and the sin-psi-squared method displayed with 95% confidence intervals. Residual stress is shown for XY and XZ along the tensile direction and transverse to the tensile direction.

Residual Stress Measurement (In-Plane Stress)					
XY			XZ		
	As-Built	LSPed		As-Built	LSPed
X Direction (σ_{xx})	246 [62.9, 429] MPa	-325 [-1191, 540] MPa	X Direction (σ_{xx})	228 [-19.1, 494] MPa	-311 [-591, -30.7] MPa
Y Direction (σ_{yy})	53.4 [2.83, 373] MPa	-138 [-513, 327] MPa	Z Direction (σ_{zz})	193 [6.99, 303] MPa	-91.0 [-556, 643] MPa

XRD goniometer-sweep measurements, shown in Figure , identify notable differences in textures between the XY and XZ sample surfaces with implied consequences for SCC behavior. The (222) plane is much less prominent in the XY samples both before and after LSP as compared with the XZ samples. This indicates that there is a prevailing texture such that a disproportional surface area fraction of the (222)-planes in the material's microstructure are

oriented with their normal vectors rotated away from the build direction. This result is impactful because a primary form of SCC occurs due to the locking of dislocations at Lormer-Cottrell barriers causing microcracking of (111) planes [50]. Therefore, if the (111) planes are not oriented such that their normal coincides with the cracking direction, as in the XY orientation, this cracking mechanism is less prevalent and results in a higher resistance to SCC. This is a significant factor in producing the increased SCC resistance of the XY samples. XRD measurement also revealed that after SCC testing, there is no shown change to these XRD profiles, notably lacking in the appearance of martensite phases. It may therefore by concluded that martensite transformation does not play a significant role. EBSD and OIM further examine the role of microstructure on SCC behavior.

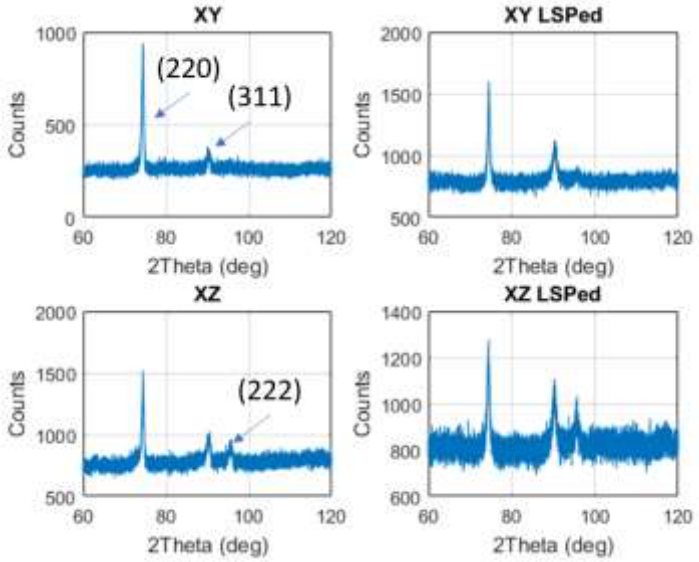

Figure 6. The XRD sweep identifying lattice planes and texture across each sample type before u-bending and stress corrosion cracking testing.

The as-received microstructure, as shown in Figure , shows anisotropic dislocation and grain structure which is linked to anisotropic SCC behavior. EBSD reveals the received samples are characterized by grains elongated along the build direction resulting from epitaxial growth

and a checkerboard grain structure in the build plane. The dislocation density in each plane is calculated from OIM lattice curvature as described in Over et al [48]. In the build-plane (XY plane), the average GND density is $21.2\pm12.6\times10^{12}/m^2$ and in the wall surface (XZ plane) the average GND density is $18.1\pm12.2\times10^{12}/m^2$. The GND density is thus higher in the XY plane which also corresponds to the increased number of exposed grain boundaries. The average grain size by diameter for XY and XZ surfaces are 17.7±18.0 μm and 22.7±28.3 μm respectively. The average aspect ratio for XY and XZ surfaces are 0.425±0.145 and 0.362±0.180. The XZ surface is thus characterized by longer grains with lower aspect ratios. These microstructural artefacts are characteristic for LPBF metals created with 90° rotation between layers during the build. Each scan causes a remelt of the previous layer at the periphery of the melt pool and epitaxial grain growth occurs. Dendrites grow from the outside of the melt pool to the center, following the highest thermal gradient [51]. The center of the melt pool solidifies last, forming micro-grains. The dislocations are shown to align along these dendrite structures. This non-uniform dislocation distribution also contributes to anisotropic plastic response or back stress and is also found to affect SCC resistance [48]. Heat treatment at 899°C contributes to some reduction to dislocation density but does not cause significant recrystallization [52]. The difference in exposed dislocations between XZ and XY surfaces results in differences in SCC behavior as demonstrated by EBSD imaging of the cracked cross sections.

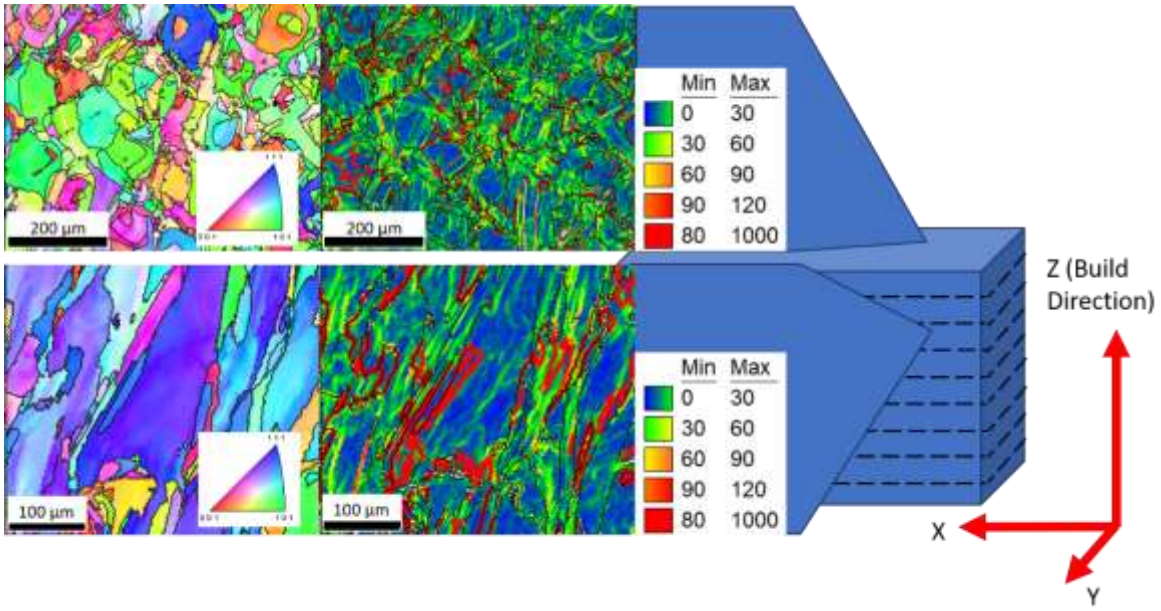

Figure 7. The texture and GND density distribution (1012/m2) of the as-received specimen as measured by EBSD and OIM.

The grain structure and dislocation density distribution in the cracked cross section, shown in Figure as measured by EBSD and OIM, evidences the prevalence of HELP and HEDE mechanisms in each specimen group. The cracking across all specimens is shown to be primarily transgranular which indicates intragranular embrittlement. Notably absent is the intergranular cracking behavior along the build direction that was observed in Lou et al [5]. This behavior is also in contrast to wrought stainless steel samples that are shown to crack intergranularly and transgranularly with a preference for intergranular cracking after LSP [1]. Transgranular cracking is caused by intragranular embrittlement by either dislocation emission, HELP, or HEDE. HELP and HEDE are the predominant modes of embrittlement in stainless steel, thus these are the two considered mechanisms. Because the transgranular mode of cracking is here preferred, the elongated grain boundaries do not provide lower-energy crack pathing and thus there was also no reduced susceptibility to SCC along the build direction. Instead, the dislocation distribution in the XY surface provided a significant barrier to hydrogen penetration which

reduced crack growth susceptibility along the build direction. Lattice misorientation clustered around crack edges is especially identifiable in XY samples, showing lattice strain and potential HELP local softening. The average misorientation and GND density is found to be higher in the LSPed crack cross sections. The average misorientation of the LSPed XZ specimen cracked cross-section is 2.46±0.88 degrees while the average misorientation of the non-LSPed XZ specimen is 1.54±0.88 degrees. Thus, the LSPed XZ sample exhibits a statistically significant mean difference of 0.92±0.2 degrees from the non-LSPed cross-section. The average misorientation of the XY LSPed specimen is 1.48±0.69 degrees while the average misorientation of the XY non-LSPed sample is 1.30±0.63 degrees. These misorientation differences correlate with GND distribution and LSPed samples exhibit an increase in the pile-ups of GNDs at grain boundaries and other barriers as shown in Figure . As can be seen in the LSPed XZ specimen (see Figure c)), the high occurrence of GND density in the specimen caused the crack to microbranch, arrest, and reinitiate repeatedly. No macrobranching occurs despite repeated microbranching. Meanwhile, in the LSPed XY sample, the crack penetrates through the grain structures without these patterns. These differences provide deep insight into the discrepancies between the hydrogen embrittlement mechanisms in the XY and XZ specimens with and without LSP. LSP is known to create mobile and sessile dislocations beneath the peened surface. These dislocations not only create hydrogen trapping sites that arrest hydrogen penetration into the interior, but they may also enhance dislocation motion towards adsorbed hydrogen. The presence of dislocations indicates the increased role of dislocation mobility and HELP in the embrittlement of the material as opposed to HEDE, which instead reduces the energy required to rupture the lattice. In both build orientations, heightened dislocation density implies LSP enhances the HELP mode of fracture over HEDE which allows for slower cracking that is rate-

limited by plastic deformation and dislocation movement. For XZ samples this effect is particularly pronounced. The increased exposure of dislocations and dendrite cell boundaries in the XY sample cracking surfaces reduces the hydrogen diffusion coefficient and therefore prevents deep infiltration of hydrogen within the surface. Thus, the LSPed XY samples only exhibit slightly more evidence of HELP as compared with their non-processed counterpart due to the relative resistance of this build orientation, processed or not, to hydrogen penetration.

Dislocation distribution and crack morphology are shown to coincide with the previously discussed hardness differences. The hardest and most embrittled sample, which is the XZ non-LSPed sample, is shown to have the lowest kernel averaged misorientation and GND density corresponding to reduced plasticity. Thus, this sample is dominated by HEDE transgranular brittle fracture. After elevated hydrogen absorption, the HELP mode of embrittlement transitions to delamination and HEDE becomes the dominant cause of failure, resulting in less evidence of plastic response in the form of GNDs. The LSPed samples demonstrate a reduced hardness after SCC testing and increased GND density and kernel average misorientation, thereby demonstrating HELP SCC mechanisms. GND density is most increased in the LSPed XZ samples. The hardness study shows that there is an increase in hydrogen absorption in these samples after SCC testing, thus the raised GND density is due to LSP enhancing the HELP mode of embrittlement. Meanwhile, the LSPed XY sample experiences less hydrogen absorption overall and thus exhibits a correspondingly lower hardness and lower level of HELP-induced GND density. The brittle fracture response of the XZ samples and plastic failure of the XY samples is further exemplified by examining the SCC crack surfaces.

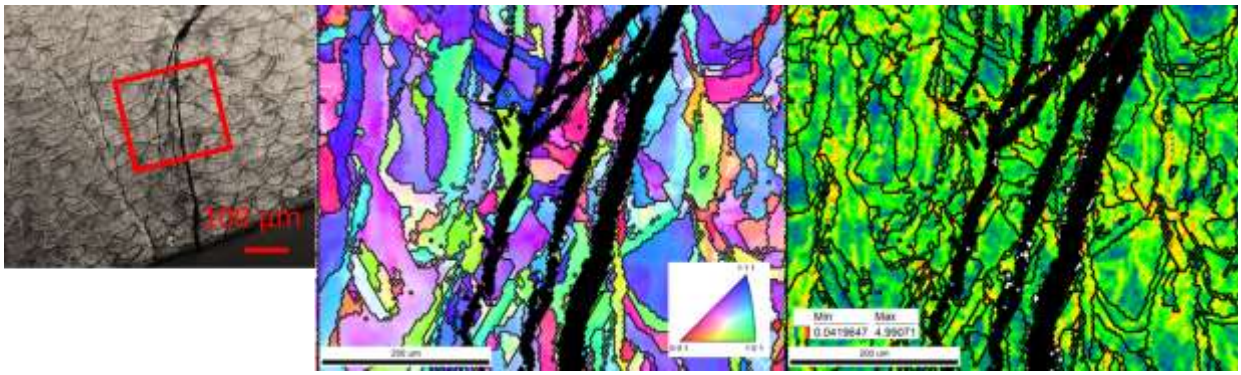

a)

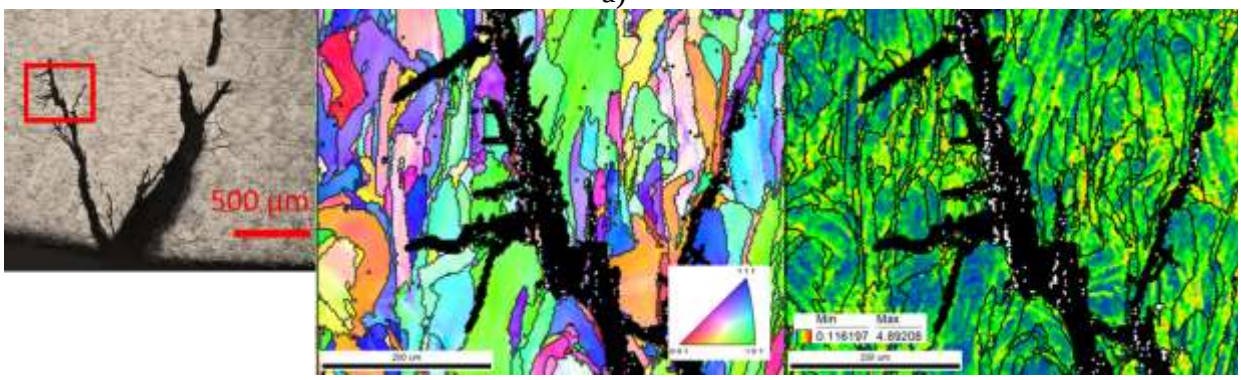

b)

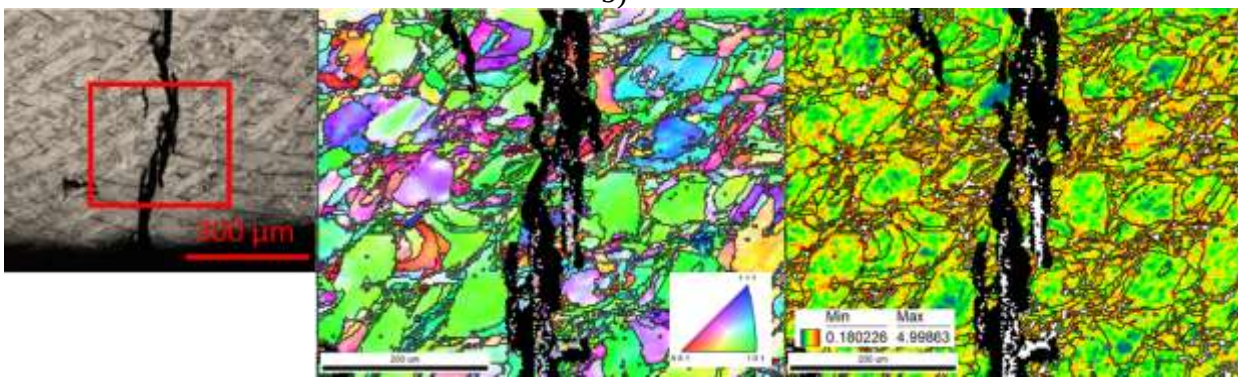

c)

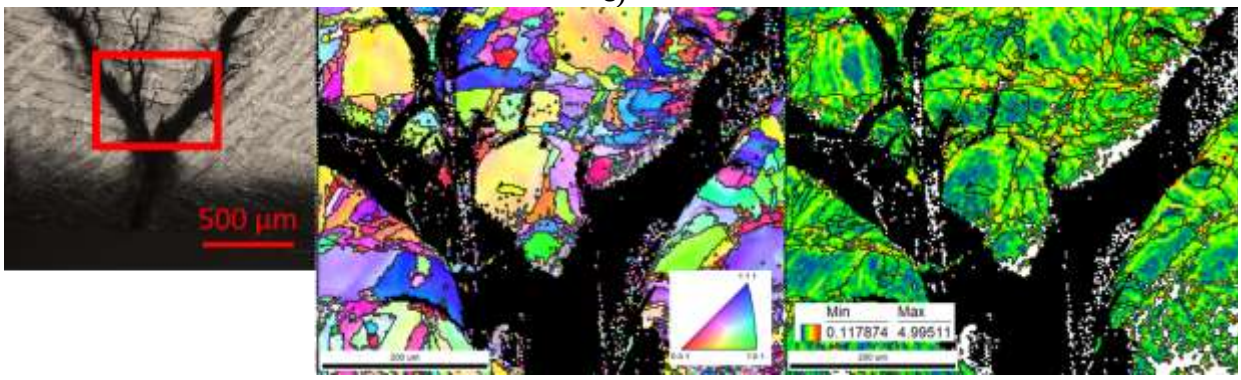

d)

Figure 8. EBSD and OIM images of microstructure and GND distribution (as denoted by kernel average misorientation) within the crack cross-sections of a) XY LSPed, b) XY non-

LSPed, c) XZ LSPed, and d) XZ non-LSPed samples. The left-most images identify where on the cracked cross section each EBSD image is taken.

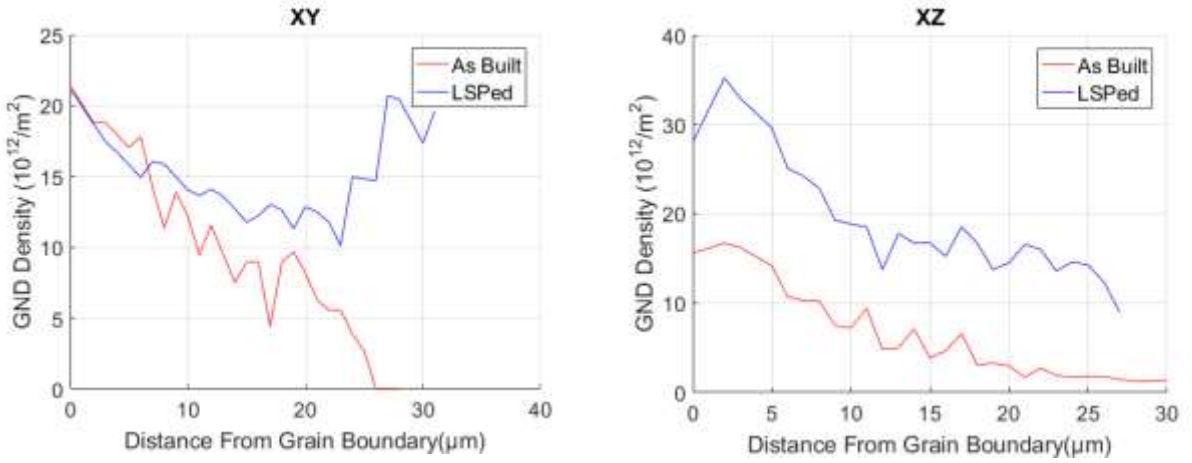

a) b)

Figure 9. GND density plotted against the distance from grain boundary for a) XY (LSPed and non-LSPed) and b) XZ (LSPed and non-LSPed) sample cross-sections after SCC testing.

Fracture surfaces of the two different build orientations, as seen in Figure , support identification of different hydrogen embrittlement modes in XY and XZ samples. From the optical image of the XY sample, two crack fronts are immediately identifiable, transitioning between slow and fast crack growth with the evolution trajectory from the upper right-hand corner across the sample to the bottom left. SEM imaging of the XY sample shows the crack advances with smooth cracking faces, exhibiting river patterns that merge after extended crack growth (up to ~400 μm of crack extension). This pattern indicates extended cleavage propagation along different crystallographic cleavage planes and it also implies slower crack tip opening with plastic deformation that proceeds ahead of the crack tip. The XZ sample meanwhile shows significantly rougher crack surfaces. In the optical image, crack fronts are less uniformly defined. The SEM image displays rough short river patterns that merge after only up to 100 μm. This indicates faster crack growth than in XY samples and the presence of brittle failure. The discussed crack-face features support the evidence that HEDE brittle fracture is more prevalent

in the XZ samples while the XY fracture exhibits a higher incidence of HELP induced cracking. Investigation of crack initiation sites help to identify how hydrogen was transported into the interior of the samples to produce cracking.

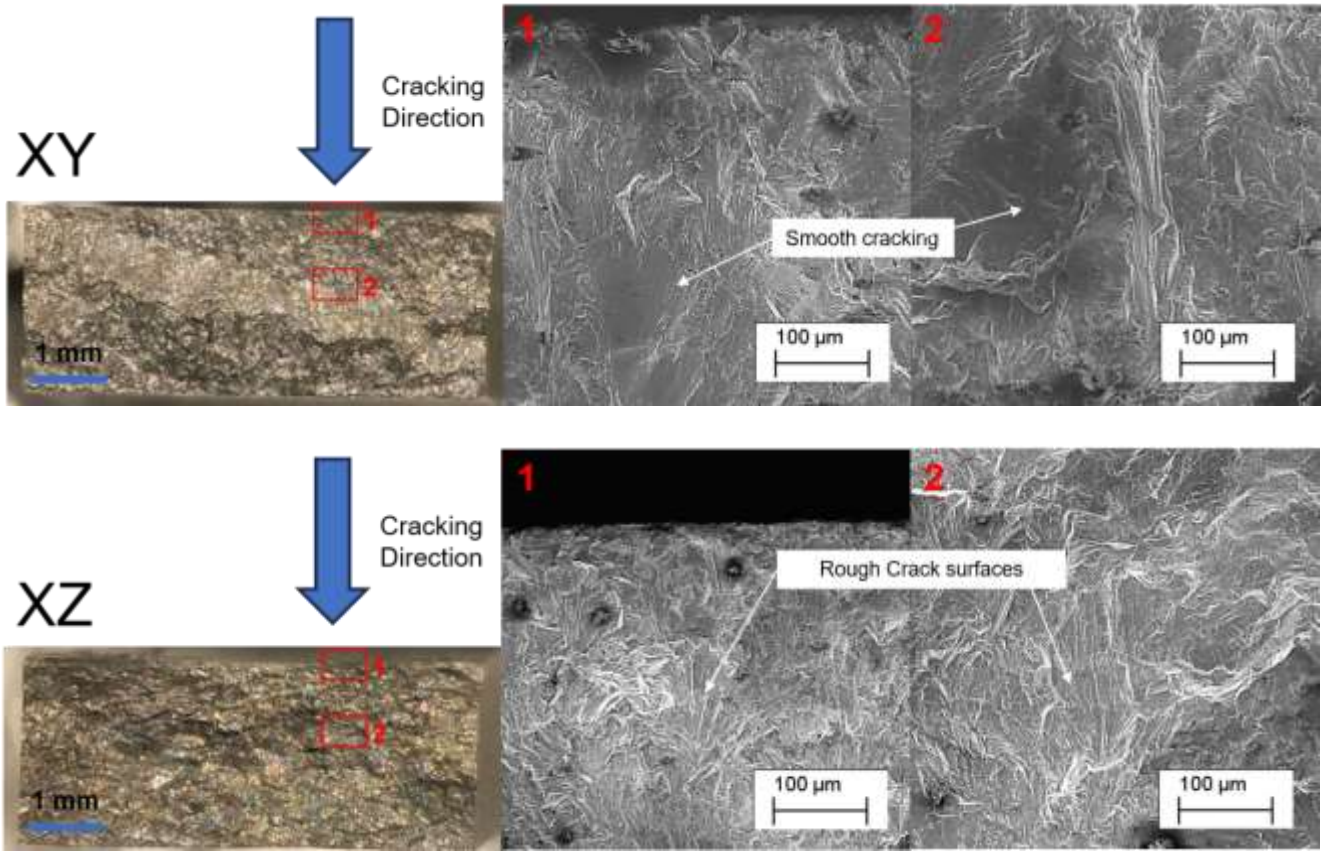

Figure 10. Crack surfaces for XY sample (top) and XZ sample (bottom) as observed with optical and SEM imaging. Image 1) indicates the crack initiation edge and image 2) is the center of the cracked face.

Magnified back-scattered electron (BSE) images of the crack initiation sites (shown in Figure) help to identify how SCC begins for each sample type. Cracks are shown to initiate along the dendrite growth direction for all samples and do not originate from a corrosion pits. Therefore, though profilometry finds LSP altered the cracking surface morphology, it did not do so significantly enough to damage film creation. The LSPed surface showed a characteristic periodic structure with 10-µm-deep indentations approximately 250-µm apart. A comparison of

the sample surface structures with and without LSP prior to u-bending is shown in Figure . The raised features surrounding each indentation may serve as surface film disruptions and cause opportunities for crack initiation. However, this effect is evidently outweighed by the beneficial mechanical effects as evidenced by examination of crack initiation sites. The initiation site occurrence along dendrite boundaries may be attributed to the preference of hydrogen to travel along such boundaries and also may coincide with surface film interruptions that occur at the perimeter of dendrite cells. At a critical hydrogen concentration, the hydrogen trapped within the dendrite boundary causes local decohesion, initiating cracking which then expands through the embrittled microstructure. The degree of hydrogen embrittlement may be estimated through simulation parameter investigation.

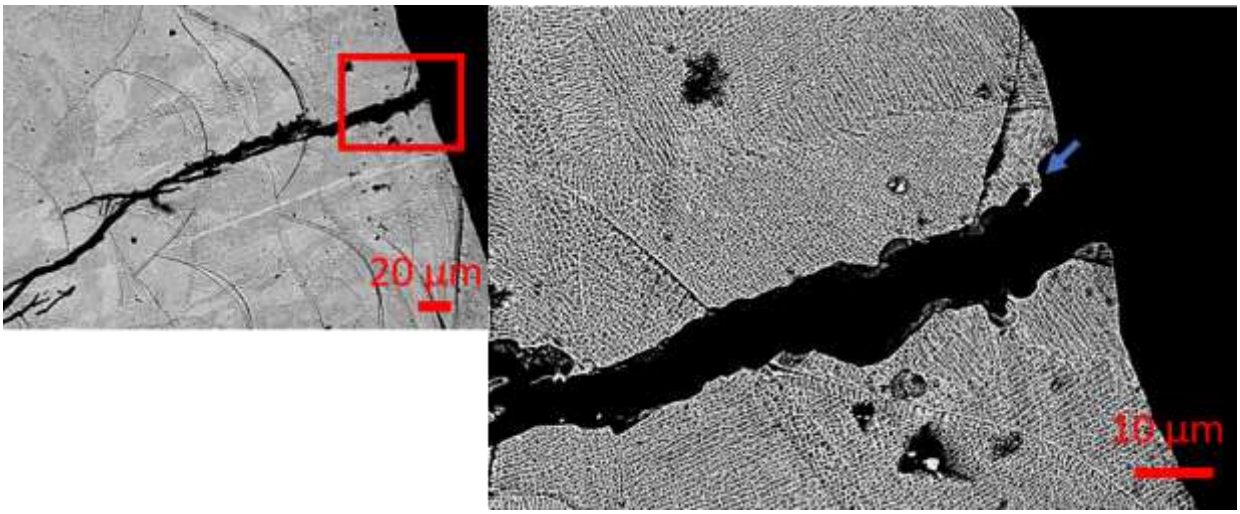

a)

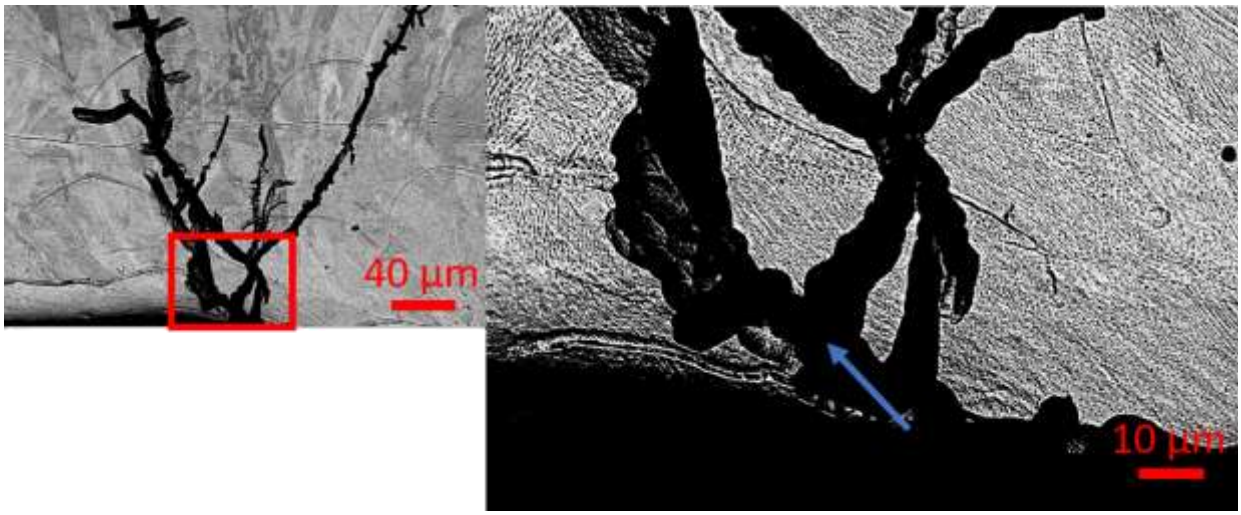

b)

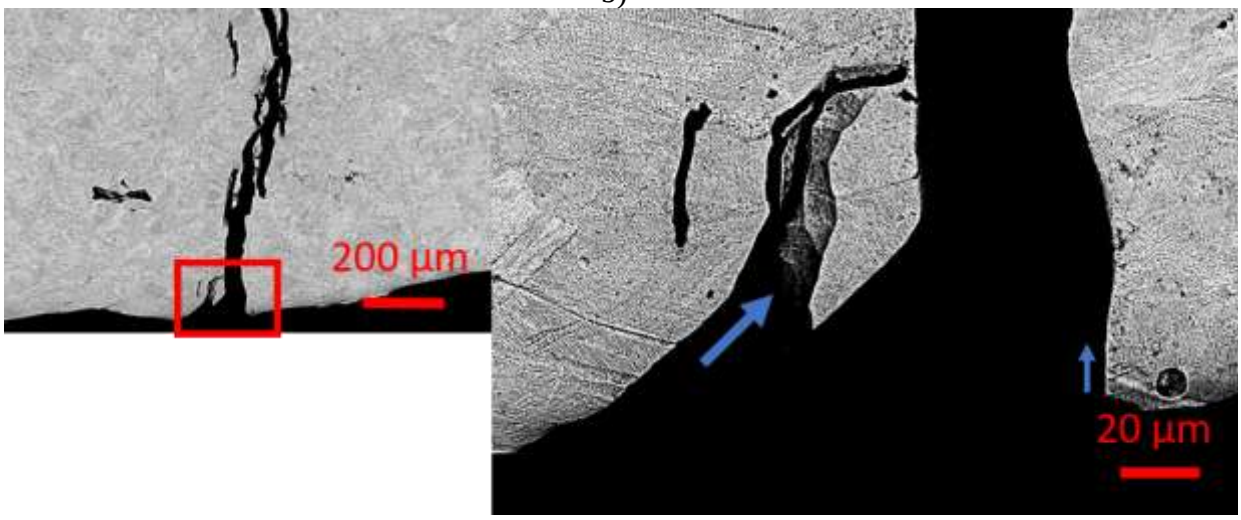

c)

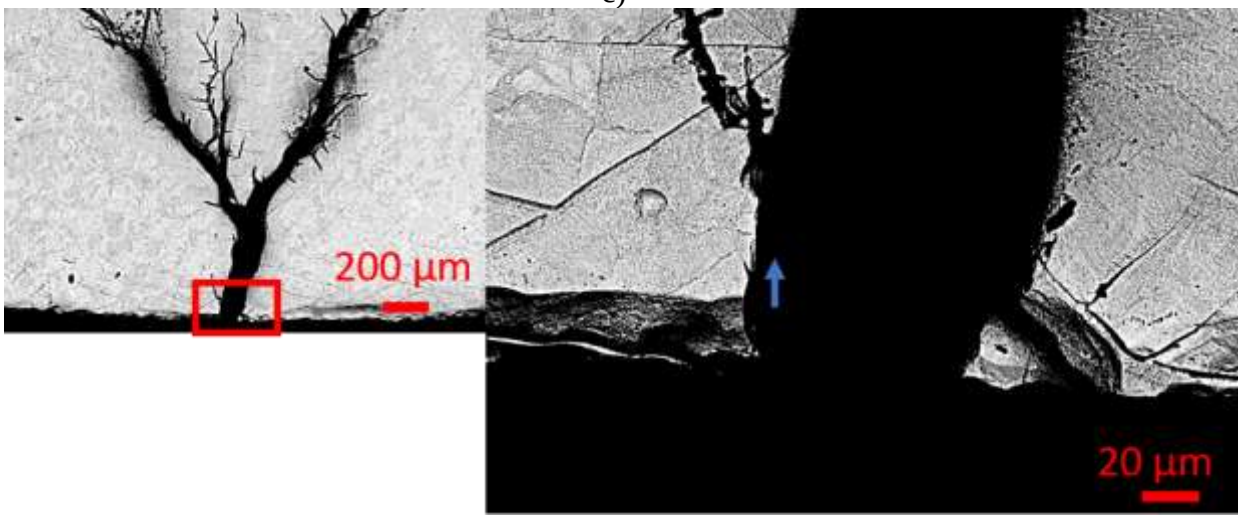

d)

Figure 11. Etched crack cross-sections imaged with SEM & BSE. Crack initiation points are shown for a) XY LSPed, b) XY non-LSPed, c) XZ LSPed, and d) XZ non-LSPed

samples. Blue arrows indicate the crack initiation direction and dendrite growth orientation (shown to be coincident).

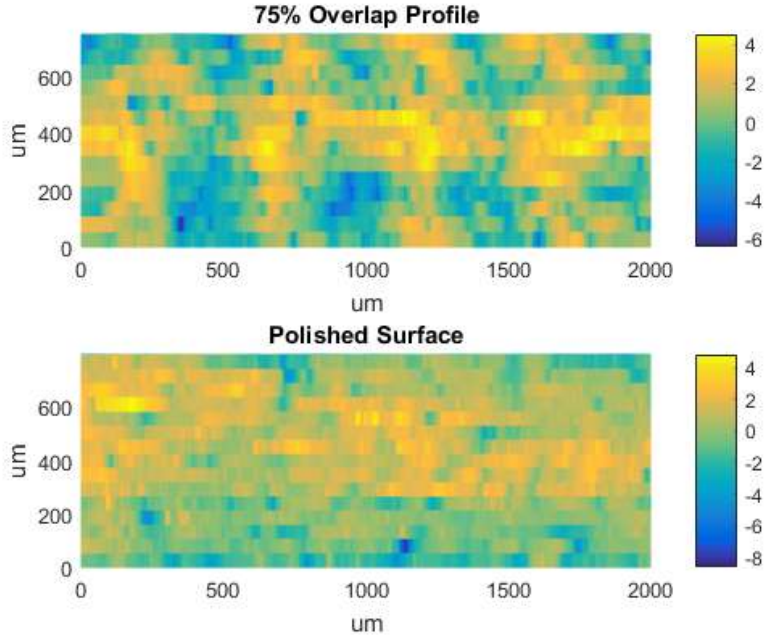

Figure 12. The surface profilometry of the polished surface of the control samples and LSPed samples before u-bending and SCC testing.

5.4.3 Simulation Results

Parameter search using simulation in ABAQUS allows comparison of the potency of residual stress, hydrogen diffusion coefficient, and HEDE versus HELP effects on SCC behavior. The analysis of the u-bend applied stress (see Figure) shows peak stress to occur on the surface near the legs of the u-bend which the prevalence of non-centered crack initiation in the tested samples confirms. The tangent normal stress is evaluated for the entire curvature of each u-bend simulation and the peak applied stress is reduced by ~50 MPa in the LSPed samples as compared to wrought. With this reduction as an input into the dynamic cracking simulation cracking morphologies can be associated with specific parameters.

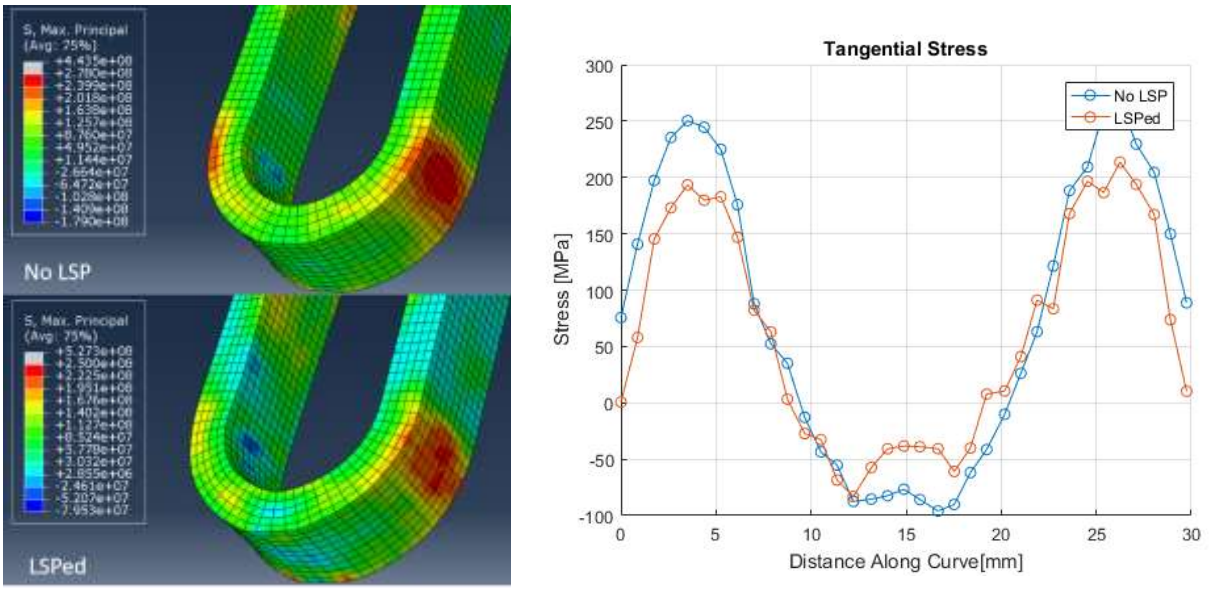

a) b)

Figure 13. Simulation results showing a) maximum principal stress after bending for non-LSPed (top) and LSPed (bottom) samples and b) tangential stress plotted along the u-bend curvature.

The dynamic crack simulation identifies the applied stress and prevalence of HEDE to have the largest impact on crack morphology. Critical energy release rates are reported for 316L LPBF steel, with estimates ranging from 260-550 kJ/m^2 [52]. Fracture toughness is shown to increase by heat treatment and also to differ depending on build orientation [52]. Crack dynamic simulation is therefore aimed at reproducing the crack morphologies to glean the correct fracture toughness and yield strength for each cracking condition and sample type. The stress state produced in simulation, as seen in Figure , allows estimates of applied surface stress for LSPed and non-LSPed conditions. The critical energy release rate chosen as a reference condition is 350 kJ/m^2 based on the heat treatment conditions of our sample and J-integral measurements of similarly built LPBF 316L samples by de Sonis et al [52]. Equations (39) and (40) input hydrogen embrittlement levels in mole fraction and produce critical energy release rate and yield strength. The temperature is input as the boiling temperature of 37% MgCl2 which is 155°C. By

varying the hydrogen content levels we may reproduce the observed crack morphologies and estimate reduction of strength variables. The non-LSPed simulation applies 250 MPa of stress on the crack tip mesh. As seen in Figure a), at baseline fracture toughness, cracking occurs but no crack branching develops. As hydrogen embrittlement is increased to 1000 ppm corresponding to a critical energy release rate of $G_c = 89{,}199$ J/m^2, branching begins to develop after some initial straight cracking. Increased hydrogen absorption leads to earlier branching and a wider angle of bifurcation. This morphological transition ends at 2000 ppm and $G_c = 69{,}204$ J/m^2 after which the crack rate increases but no morphological change is observed. These levels of hydrogen embrittlement minimally affected yield strength and thus yield strength was held at 400 MPa and Young's modulus was likewise held at 200 GPa. This parameter search shows that for macro-branching to occur, especially as seen un-peened samples, hydrogen absorption must reach at least 2000 ppm. To simulate the LSPed scenario, 200 MPa is applied to the mesh producing a noticeably different cracking behavior (shown in Figure). At baseline toughness ($G_c =$ 350 kJ/m^2) no cracking occurs. At 1000 ppm ($G_c = 94{,}399$ J/m^2) straight cracking is observed and crack branching begins to be noticeable at 3375 ppm ($G_c = 57457$ J/m^2). The final branching morphology is shown to occur at 4000 ppm of hydrogen ($G_c = 54648$ J/m^2). Given that crack branching occurs for both build orientations, simulation identifies that hydrogen absorption is less than 3375 ppm after LSP. Notably, the applied stress had a dramatic effect on the influence of fracture toughness and hydrogen embrittlement upon crack morphology. Just a 50 MPa reduction in applied stress resulted in requiring a 238% increase in fracture toughness to produce the same crack morphology. Furthermore, this is a conservative estimate that does not take into account the potential improvement to fracture toughness affected by LSP which would then require even more elevated levels of hydrogen absorption to produce the same effect. It is

shown that HELP at the tested hydrogen solubility levels minimally impacts material properties. Therefore, the application of LSP for residual stress reduction and limitation of HEDE is key to limiting cracking energy in SCC-susceptible design cases.

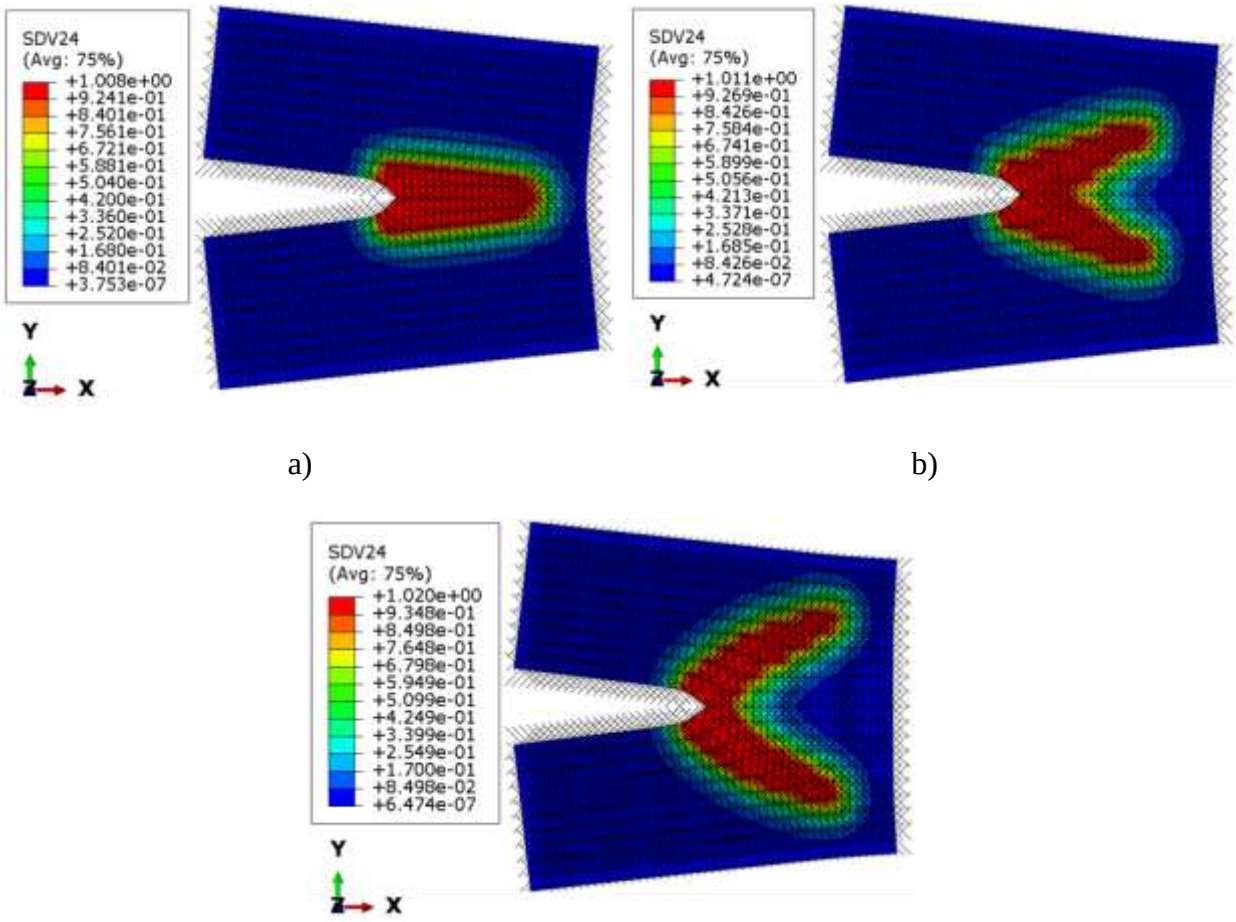

Figure 14. Crack dynamic ABAQUS model showing the evaluated field of damage variable (d) with 250 MPa of applied stress and a) $G_c = 350000\ J/m^2$, b) $G_c = 89199\ J/m^2$ (1000 ppm), and c) $G_c = 69204\ J/m^2$ (2000 ppm).

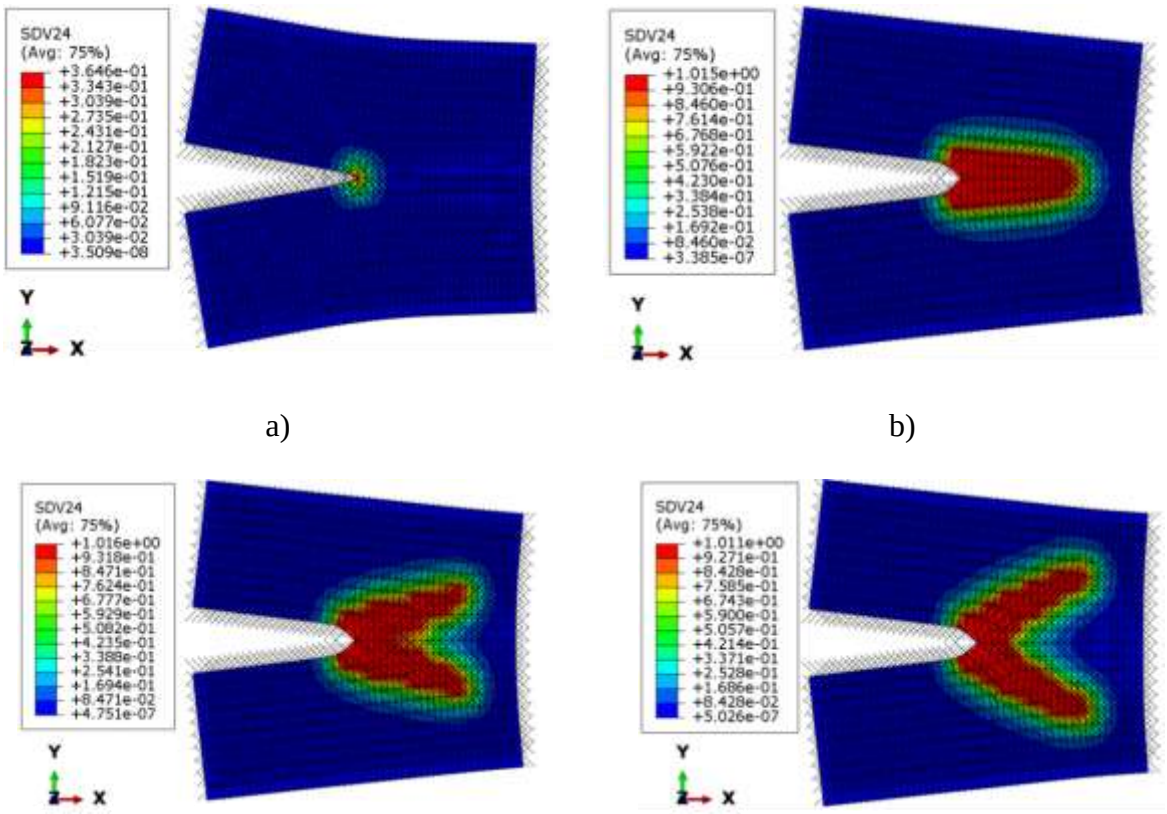

Figure 15. Crack dynamic ABAQUS model showing the evaluated field of damage variable (d) for 200 MPa of applied stress and a) $G_c = 350000\ J/m^2$, b) $G_c = 94399\ J/m^2$ (1000 ppm), c) $G_c = 57457\ J/m^2$ (3375 ppm), and e) $G_c = 54648\ J/m^2$ (4000 ppm).

5.5 Conclusion

The preceding results demonstrate that LSP surface processing improves SCC behavior in LPBF 316L stainless steel. Improvements are achieved irrespective of build direction, however LSP increases time to crack initiation more when applied to an XZ cracking surface than to an XY cracking surface. LSP increases time to crack initiation in XZ samples by 28.2±2.25 hours and XY samples by 14.7±2.70 hours, as measured from accelerated u-bend testing. The greater improvement to XZ crack resistance is shown to result from the inherent resistance to SCC in the as-received XY cracking surface such that LSP is only capable of imparting a smaller improvement to SCC behavior.

EBSD and OIM demonstrate that there is an increased number of exposed dislocations and grain boundaries in the XY surface as compared with the XZ surface which act as trapping sites for hydrogen. As a result, the hydrogen diffusion coefficient is reduced and hydrogen does not penetrate as deeply into the XY sample surface, indicated by hardness testing and the increased time to crack initiation. The XY texture is also oriented in such a way as to reduce typical modes of hydrogen embrittlement in austenite. Furthermore, SCC in XY samples is more dominated by HELP which causes cracking to be rate-limited by dislocation slip. This is evidenced by plastic strain near crack tip edges as well as by the smooth crack faces observable in the XY samples' fracture surface. LSP is shown to reduce hydrogen penetration and residual stress as well as enhance the HELP fracture mode in XY samples by imparting increased dislocations. This result is corroborated by hardness testing, showing significant reduction of hydrogen embrittlement, and observation of crack morphology, demonstrating a reduction in crack propagation rate due to LSP in the XY sample surface.

XZ sample cracking surfaces meanwhile expose fewer hydrogen trapping sites in the form of grain boundaries and dislocations to the corrosive environment. This results in deeper penetration of hydrogen into the XZ sample surface, as evidenced by steep hardness gradients near the cracked exterior. Furthermore, the XZ samples are more dominated by brittle fracture illustrative of HEDE. This is chiefly shown by SEM imaging of the XZ sample roughened crack surfaces. Mitigating this effect, LSP increases the prevalence of the HELP mode of hydrogen embrittlement in XZ samples, thereby imparting crack-rate limiting mechanisms. This improvement may be identified by observed characteristic increases in dislocation density, changes in crack morphology, and lengthening of crack initiation times.

The comparison of XY, XZ, LSPed, and non-LSPed sample types are corroborated by crack morphology simulations in ABAQUS. Crack dynamic models demonstrate that the presence of HEDE-induced intragranular embrittlement and residual stress most strongly influences cracking energy in the presence of hydrogen absorption. The mitigation by LSP to both HEDE and residual stress in LPBF metal is therefore extremely potent in improving SCC resistance. Investigation of crack initiation sites and surface morphology further shows that despite the application of LSP to the surface, no significant surface film disruption occurred and thus there is no sacrifice to dissolutive corrosion performance. This is exemplified by the lack of evidence of material loss or pitting in the sample surfaces. Instead, cracks initiated at dendrite cell boundaries which are likely channels for hydrogen transport into the metal interior and therefore sites of localized decohesion.

Chapter 6: Conclusion

In conclusion, the use of LSP for improving material properties in additively manufactured metal has been broadened beyond those typically investigated, namely for lengthening of fatigue life. This investigation has been carried out both experimentally, with mechanical, surface, and material testing and imaging, as well as with simulation techniques. It is evident that LSP improves anisotropic hardening behavior, electrochemical corrosive properties, and stress corrosion cracking behavior in LPBF 316L. It is also shown that LSP interacts with build orientation significantly to produce differences of affect depending on alignment with the part. The findings of each study of this thesis are summarized below.

6.1 LSP induced back stress reduction in rolled stainless steel

Developing a precedent of LSP influence on anisotropic plastic behavior, Chapter 2 shows LSP causes reduction in back stress in rolled stainless steel. This reduction is quantified and investigated through experimental testing, numerical simulation, and microstructural analysis. Tensile testing of both as-received and LSP-treated specimens revealed a reduction in back stress in the LSP-treated samples. Back stress was derived from stress-strain hysteresis, with LSP-treated samples showing a notable decrease compared to the as-received ones. Numerical simulation of the bulk material using a kinematic hardening model confirmed this reduction, although it underestimated the extent observed experimentally. Microstructural analysis through EBSD revealed changes in grain morphology and dislocation distribution due to LSP, including recrystallization and reduction in dislocation pile-ups. These changes contributed to the observed reduction in back stress, further supported by a shift towards equiaxed grains and increased aspect ratio. LSP demonstrates effectiveness in mitigating yield asymmetry in rolled stainless

steel by inducing compressive residual stress, compressive back stress, and promoting recrystallization.

6.2 The effect of LSP upon back stress in 316L stainless steel

Building upon the findings of Chapter 2, Chapter 3 investigates the effect of LSP on the back stress of additively manufactured stainless steel parts, considering different build orientations. Results show that LSP significantly reduces back stress in XY-built samples, with a mean difference of -247.61 MPa compared to non-LSPed samples. However, this reduction is not observed consistently in XZ-built samples. Statistical analysis reveals a significant interaction between build orientation and LSP. The difference in response is attributed to microstructural differences between orientations, particularly in grain morphology and texture. Applying LSP along the build direction in the XY-built samples causes greater compressive hardening due to the yielding of [400]/[200] and [222]/[111] planes, thereby effectively reducing tensile back stress by more than in the XZ-built counterparts. In contrast, the texture of XZ-built samples favors tensile hardening, negating the effect of LSP on back stress reduction after tensile loading and therefore rendering unobservable any initial back stress reduction due to LSP. This effect is shown to be due to rapid tensile hardening of [400]/[200] and [222]/[111] grain families in the XZ sample type. CPFE simulations corroborate experimental findings, demonstrating the role of grain families in determining the response to LSP. Build orientation and texture are found to be important in influencing the efficacy of LSP in reducing back stress in additively manufactured stainless steel parts, a nuance that provides insights for optimizing manufacturing processes to achieve desired mechanical properties.

6.3 The effect of LSP upon electrochemical and wettability characteristics in LPBF stainless steel

In Chapter 4, LSP is shown to affect improvement on the electrochemical behavior and corrosion properties of stainless steel fabricated using LPBF. The study compares two as-built surfaces, the build surface perpendicular (XY) to the build direction and the wall surface parallel to the build direction (XZ). EIS measurements reveal that LSP affects the surfaces differently, with XY surfaces showing increased polarization resistance and XZ surfaces exhibiting increased capacitance. Potentiokinetic analysis indicates that LSP raises the pitting potential for both orientations but reduces the corrosion rate only in XY surfaces. Surface wettability measurements and simulations demonstrate significant changes post-LSP, increasing hydrophobicity for both surfaces. Surface morphology, characterized by periodic textures and spatter, influences surface energy and wetting behavior. Residual stress measurements show a shift from tensile to compressive stress after LSP, with XY surfaces exhibiting greater compressive stress after surface processing. This stress alteration correlates with electrochemical trends, as compressive stress reduces corrosion rates. Additionally, surface chemistry analysis made with EDS reveals changes in silicon oxide distribution after LSP, contributing to altered surface energy and improved corrosion resistance. LSP is shown to have great effect on surface properties and corrosion behavior, with a highlighted importance of as-built surface orientation and morphology in LPBF parts. The study of mechanical response to corrosive environments is continued in Chapter 5.

6.4 Mitigation of stress corrosion cracking in LPBF 316L stainless steel

The SCC performance analysis reveals significant findings regarding the effects of LSP on processed u-bend samples compared to their non-LSPed counterparts. Testing shows that LSP

notably extends the time to crack initiation in u-bend samples, particularly in the XZ orientation, with a 28.2±2.25 hour increase, and in the XY orientation, with a 14.7±2.70 hour increase, compared to non-LSPed samples. These results indicate that LSP has a beneficial impact on SCC behavior, with differences observed in crack initiation times between different build orientations. Examination of cracking morphologies highlights distinct differences between LSPed and non-LSPed specimens. Non-LSPed samples exhibit larger and longer cracks with macro-level branching, while LSPed samples show smaller cracks with no macrobranching, indicating reduced crack propagation rates after SCC initiation. Additionally, investigation into hydrogen embrittlement mechanisms reveals differences in hardness profiles between LSPed and non-LSPed samples, with LSP significantly reducing hardness increases caused by hydrogen invasion. Residual stress measurements, texture analysis, and microstructure examination further elucidate the role of LSP in altering material properties and enhancing SCC resistance. Simulation results support these findings, demonstrating the potency of LSP in reducing cracking energy by mitigating both hydrogen embrittlement and residual stress. LSP surface processing is thus demonstrated to improve SCC behavior by reducing crack initiation times and enhancing resistance to crack propagation, with notable differences observed between different build orientations and LSP treatments.

6.5 Future Work

Overall, this thesis presents significant advancement in developing knowledge towards application of LSP as a useful tool for post-processing of LPBF metal. Furthermore, interactions between LSP and stainless-steel material properties that have not been explored are examined and quantified. However, while the scope of this research holistically examines these effects, it also lays the foundation for abundant work to expand upon these findings.

Back stress and dislocation distribution within additively manufactured parts is discussed in literature as being characteristic of LPBF manufacturing processes, however a complete investigation of yield surface and kinematic hardening has yet to be performed. The application of axial-torsion testing to plot the yield criterion would develop fruitful contribution to material understanding. While this thesis identifies yield points in the dynamic hardening surface, a complete understanding of the anisotropic plastic response is warranted. This form of mechanical testing would also confirm findings that LSP applies surface level compressive back stress but would additionally reveal other modes of yield surface change and help to establish the material's yield stability. Further investigation of dislocation dynamics may also be performed using transmission electron microscopy (TEM) with in-situ testing to observe more directly mechanisms such as the interaction of plastic slip with the presence of dislocation tangles, twinning, and nanograins induced by LSP. It is also desirable to expand the simulation of these effects to be more accurate, incorporating the elongated grain morphology of additively manufactured metal, which is shown in Chapter 3 to affect back stress. The simulation may also be supported by additional in-situ tensile sXRD testing of different grain families to corroborate LSPed adjustments to stress-strain relationships.

There are also opportunities to identify how the specific build of additively manufactured parts may affect how LSP improves back stress. This may be explored by varying build parameters such as volumetric energy density and build quality metrics such as porosity. Given that residual stress is known to change from the build plate to the last-built layer, the back stress is likely to change also and so will the interaction with LSP. Furthermore, residual stress is also exacerbated in more finely printed features and thus investigation of LSP's interaction with back stress in those features is likely different than with thickly printed geometries.

Further dissolutive corrosion testing may also contribute to the evaluation of LSP's effect on wetted additively manufactured surfaces. While a complete surface wettability and electrochemical comparison is presented here, additional volume-loss testing will help to identify unstudied effects such as re-passivation behavior and also support current findings such as corrosion rate. The impact of LSP upon corrosion properties of various printed surface textures may also be investigated. For example, changing hatch spacing and surface finishing parameters may produce significant alternations to the interaction between LSP and the printed surface. Furthermore, LSP may interact differently with down skin textures printed on structures angled from the build direction by varying degrees. The interaction of LSP with the electrochemical properties of hybrid-manufactured metal is also of interest. Polished and EDM cut surfaces exhibit different wettability and, given the interaction of the stiffness of the LSPed interface with surface roughness, it is also desirous to identify which hybrid-manufacturing process flow is best for LPBF parts. Understanding of LSP's interaction with SCC in LPBF metal may also be further examined with additional testing such as tensile testing in corrosive environment and quantitative study of crack propagation rate. Alternative hydrogen embrittlement measurement methods may be used to confirm the results this thesis presents such as hydrogen desorption testing. Again, build parameters may also affect the mechanisms explored above and it may be of interest to also investigate differently built geometries.

As of this thesis completion, there still remains unexamined uses of LSP in hybrid processing of additive materials. As briefly discussed in Chapter 1, the promising use of femtosecond LSP may allow integration of LSP within the build to create deeply penetrating beneficial compressive stress while also eliminating the need to introduce added manufacturing error by removing the part from the powder bed to apply hybrid processing. Given the

revelations with respect to ceramic LSP and brittle materials, there may also be additional opportunity to apply LSP to additively built ceramics. Some metals such as aluminum are more prone to in-build cracking due to the high residual stress, and thus application of in-situ LSP may offer a potential solution for reducing these stresses. Finally, these investigations are not complete without side-by-side comparison with other forms of hybrid processing and thus numerous studies may be populated by examining the disparity in effect between LSP and other hybrid processing techniques.

References

Chapter 1: Introduction

[1] A. Singh and H. Singh, 2021, “Metal Additive Manufacturing: From History to Applications,” in *Innovations in Additive Manufacturing*, Springer Nature Switzerland AG, pp. 3-32, ISBN: 978-3-030-89401-6.

[2] N. Haghdadi, M. Laleh, M. Moyle and S. Primig, 2021, " Additive manufacturing of steels: a review of achievements and challenges," J. Mater. Sci., **56**, pp. 67-75, DOI: 10.1007/s10853-020-05109-0.

[3] R. Baker, 1925, “Method of Making Decorative Articles,” U.S. Patent No. 423647, issued April 14.

[4] H. Fayazfar, M. Salarian, A. Rogalsky, D. Sarker, P. Russo, V. Paserin and E. Toyserkani, 2020, "A critical review of powder-based additive manufacturing of ferrous alloys: Process parameters, microstructure and mechanical properties," Mat. and Des., **144**, pp.98-128, DOI: 10.1016/j.matdes.2018.02.018.

[5] E. M. Sullivan, S. S. Hedas, M. J. Engstrom and G. Lindwall, 2023, “Effect of powder particle size distribution and contouring on build quality in electron beam powder bed fusion of a medium-C hot-work tool steel,” The Int. J. of Adv. Man. Tech., **128**, pp. 2953-2967, DOI: 10.1007/s00170-023-11944-7.

[6] J. L. Bartlett and X. Li, 2019, “An overview of residual stresses in metal powder bed fusion,” Addit. Manuf., **27**, pp.131-149 DOI: 10.1016/j.addma.2019.02.020.

[7] W. E. Frazier, 2014, “Metal Additive Manufacturing: A Review,” ASM International, **23**(6), DOI: 10.1007/s11665-014-0958-z.

[8] P. Bajaj, A. Hariharan, A. Kini, P. Kurnsteiner, D. Raabe and E. A. Jagle, 2020, “Study on the effect of tension-compression asymmetry on the cylindrical cup forming of an AA2090-T3 alloy,” Mat. Sci. Eng. A, **772**, pp. 138633, DOI: 10.1016/j.msea.2019.138633.

[9] W. Chen, T. Voisin, Y. Zhang, J. Florien, C. M. Spadaccini, D. L. McDowell, T. Zhu, and Y. M. Wang, 2019, “Microscale Residual Stresses in Additively Manufactured Stainless Steel,” Nat. Commun., **10**(4338), DOI: 10.1038/s41467-019-12265-8.

[10] M. Y. Wang, T. Voisin, J. T. McKeown, J. Ye, N. P. Calta, Z. Li, Z. Zeng, Y. Zhang, W. Chen, T. T. Roehling, R. T. Ott, M. K. Santala, P. J. Depond, M. J. Matthews, A. V. Hamza and T. Zhu, 2017 “Additively manufactured hierarchical stainless steels with high strength and ductility,” Nat. Mater., **17**, pp. 63–71, DOI: 10.1038/nmat5021.

[11] W. M. Steen and J. Mazumder, 2010, *Laser Material Processing, 4th Edition*, Springer, Heidelberg, NY, ISBN: 978-1849960618.

[12] C.-Y. Tsai, C.-W. Cheng, A.-C. Lee and M.-C. Tsai, 2019, “Synchronized multi-spot scanning strategies for the laser powder bed fusion process,” Addit. Manuf., **27**, pp.1-7, DOI: 10.1016/j.addma.2019.02.009.

[13] X. Peng, L. Kong, J. Y. H. Fuh and H. Wang, 2021, “A Review of Post-Processing Technologies in Additive Manufacturing,” J. Manuf. Mater. Process., **5** (8), 38, DOI: 10.3390/jmmp5020038.

[14] M. Sealy, G. Madireddy, R. Williams, P. Rao and M. Toursangsaraki, 2018, “Hybrid Processes in Additive Manufacturing,” J. Manuf. Sci. Eng., **140**(6), 060801, DOI: 10.1115/1.4038644.

[15] Z. Yu, Y. Zheng, J. Chen, C. Wu, J. Xu, H. Lu and C. Yu, 2020, “Effect of laser remelting processing on microstructure and mechanical properties of 17-4 PH stainless steel during laser direct metal deposition," J. of Mat. Proc. Tech., **284**, pp. 116738, DOI: 10.1016/j.jmatprotec.2020.116738.

[16] P. Peyre and R. Fabbro, 1995, “Laser shock processing: a review of the physics and applications,” Opt Quantum Electron, **27**, pp. 1213-1229, DOI: 10.1007/BF00326477

[17] N. Kalentics, E. Boillat, S. Ciric-Kostic, N. Bogojevic and R. E. Loge, 2017, "Tailoring residual stress profile of Selective Laser Melted parts by Laser Shock Peening," Addit. Manuf., **16**, pp. 90-97, DOI: 10.1016/j.addma.2017.05.008.

[18] A. H. Clauer and J. H. Holbrook, “Effects of laser induced shock waves on metals,” *Shock Waves and High-Strain-Rate Phenomena in Metals*, Plenum Publishing Corporation, New York (1981): pp. 675-703.

[19] R. Fabbro, J. Fournier, P. Ballard, D. Devaux and J. Virmont, 1990, “Physical study of laser-produced plasma in confined geometry,” J. Appl. Phys., **68**(2), DOI: 10.1063/1.346783.

[20] Y. Fan Y. Wang, S. Vukelic and Y. L. Yao, 2005, “Wave-solid interactions in laser-shock-induced deformation processes,” J. Appl. Phys., **98**(10), DOI: 10.1063/1.2134882.

[21] H. Chen, J. Kysar and Y. L. Yao, 2004, “Characterization of Plastic Deformation Induced by Microscale Laser Shock Peening,” J. Appl. Mech., **71**(5), pp. 713-723, DOI: 10.1115/1.1782914.

[22] W. Zhang, Y. L. Yao, and I.C. Noyan, 2004, “Micro Scale Laser Shock Peening of Thin Films, Part 1: Experiment, Modeling and Simulation,” J. Manuf. Sci. E., **126**(1), pp. 10-17, DOI: 1.1645878.

[23] G. J. Cheng, M. Cai, D. Pirzada, M. J.-F. Guinel and M. G. Norton, 2008, “Plastic Deformation in Silicon Crystal Induced by Heat-Assisted Laser Shock Peening,” J. Manuf. Sci. Eng., **130** (1), pp. 011008 DOI: 10.1115/1.2815343.

[24] P. P. Shukla, P. T. Swanson and C. J. Page, 2013, “Laser shock peening and mechanical shot peening processes applicable for the surface treatment of technical grade ceramics: A review,” J. Eng. Manuf., **228**(5), pp. 639-652, DOI: 10.1177/0954405413507250.

[25] S. Jang, S. Park and C.-j. Bae, " Development of ceramic additive manufacturing: process and materials technology," Biomed. Eng. Lett., **10**, pp. 493-503 DOI: 10.1007/s13534-020-00175-4.

[26] Y. Cao, X. Xie, J. Antonaglia, B. Winiarzki, G. Wang, Y. C. Shin, P. J. Withers, K. A. Dahmen and P. K. Liaw, 2015, “Laser Shock Peening on Zr-based Bulk Metallic Glass and Its Effect on Plasticity: Experiment and Modeling,” Sci. Rep., **5**, pp. 10789, DOI: 10.1038/srep10789.

[27] C. Ye, Y. Liao and G. J. Cheng, 2010, " Warm Laser Shock Peening Driven Nanostructures and Their Effects on Fatigue Performance in Aluminum Alloy 6160," Adv. Eng. Mat. , **12**(4), pp. 291-297, DOI: 10.1002/adem.200900290.

[28] Y. Li, Z. Ren, X. Jia, W. Yang, N. Nassreddin, Y. Dong, C. Ye, A. Fortunato and X. Zhao, 2021, “The effects of the confining medium and protective layer during femtosecond laser shock peening,” Manuf. Lett., **27**, pp. 26-30, DOI: 10.1016/j.mfglet.2020.11.006.

[29] Y. Zhang, T. Besshi, M. Tsuyama, M. Heya and H. Nakano, 2023, “Pliable solid medium as a plasma confinement layer for laser peening,” J. Las. App., **35**, pp. 012014, DOI: 10.2351/7.0000753.

[30] M. Ayeb, M. Frija and F. Raouf, 2024," Laser Peening: A Review of the Factors, Efects, Applications, Comparison with Shot Peening and State-of-the-Art," Met. And Mat. Int., **30**, pp. 259-283, DOI: 10.1007/s12540-023-01517-4

[31] A. D. Evans, A. King, T. Pirling, G. Bruno and P. J. Withers, 2005, “The effect of incidence angle on residual stress state in laser peened Ti-6Al-4V plate,” in *ICSP-9*, Paris, France.

[32] D. Dye and H. J. Stone, 2001, “Intergranular and Interphase Microstresses,” Curr. Opin. Solid State Mater. Sci., **5**(1), pp. 31-37, DOI: 10.1016/S1359-0286(00)00019-X.

[33] G. Burns and M. Glazer, 2013, *Space Groups for Solid State Scientists, Third Edition*, Academic Press, Waltham, MA, ISBN: 978-0128100615.

[34] W. Bollman, 1956, “ Interference Effects in the Electron Microscopy of Thin Crystal Foils,” Phil. Mag., **86**(6),pp. 29-31, DOI: 10.1080/14786430600779524.

[35] EDAX, 2018, *OIM Analysis*, Amtek Inc., Materials Analysis Division.

[36] SAE HS-784, 2003, “Residual stress measurement by X-ray diffraction”, SAE International, Warrendale, Pa, ISBN: 978-0-7680-1069-5.

[37] V. I. Monine, J. d. C. P. Filho, R. S. Gonzaga, E. K. D. Passos and T. J. de Assis, 2018, " X-ray diffraction technique for residual stress measurement in NiCrMo alloy weld metal," Adv. In Mat. Sci. and Eng., **2018**, 8986423, DOI: 10.1155/2018/8986423.

[38] J. Lin, N. Ma, Y. Lei and H. Murakawa, 2017, “Measurement of residual stress in arc welded lap joints by cosa X-ray diffraction method,” J. of Mat. Proc. Tech., **243**, pp. 387-394, DOI: 10.1016/j.jmatprotec.2016.12.021.

[39] J. D. Eshelby, 1957, “The determination of the elastic field of an ellipsoidal inclusion, and related problems,” Proc. R. Soc. Lond., **241**(1226), pp. 376-396, DOI: 10.1098/rspa.1957.0133.

[40] J. Lubliner, 2008, *Plasticity Theory*, Dover Publications, Mineola, NY, ISBN: 9780486462905.

[41] G. Hu, K. Zhang, S. Huang and J. W. Wu, 2012, "Yield surfaces and plastic flow of 45 steel under tension-torsion loading paths," Acta. Mec. Solida, Sin., **25**(4), DOI: 10.106/S0894-9166(12)60032-9.

[42] K. G. Budinski, 1979, Engineering Materials: Properties & Selection, Third Edition, Academic Press, Englewood Cliffs, NJ, ISBN: 978-0132779975.

[43] X. Zhou, C. Liao, Y. Wang and Y. Zhu, 2021, “Constructing the Pourbaix diagram of Fe-Cl−-H2O ternary system under supercritical water conditions,” Electrochemica Acta, **377**, pp. 138075, DOI: 10.1016/j.electacta.2021.138075.

[44] J. Davis, 2000, Corrosion: Understanding the Basics, ASM Internationa, Materials Park, OH, ISBN: 978-0-87170-641-6.

Chapter 2: Laser Shock Peening Induced Back Stress Mitigation in Rolled Stainless Steel

[1] Battelle Memorial Institute, 2020, *Metallic Materials Properties Development and Standardization (MMPDS-15)*, Battelle Memorial Institute, Chap. 2

[2] Shintani, T., and Murata, Y., 2011, "Evaluation of the dislocation density and dislocation character in colled rolled type 304 steel determined by profile analasys of X-ray diffraction," Acta Mater., **59**(11), pp. 4314-4322, DOI: 10.1016/j.actamat.2011.03.055.

[3] Charpentier, P.L., 2015, "Post-forming monotonic and cyclic behavior in HSLA steel sheet after large deformations in-plane compression," Int. J. Fatigue, **79**, pp. 54-64, DOI: 10.1016/j.ijfatigue.2015.04.003

[4] Charpentier, P.L., 2019, "Post-forming room temperature brittle fracture in a high-strength low alloy steel sheet after various forming modes," J. Mater. Eng. Perform., **28**, pp. 7119-7140, DOI: 10.1007/S11665-019-04445-W

[5] Mehrabi, H., Yang, R. C. and Wang, B., 2020, "Effects of Tension-Compression Asymmetry on Bending of Steels," Appl. Sci., **10**(9), DOI :10.3390/app10093339

[6] Barros, P.D., Alves, J. L., Oliveira, M. C., and Menezes, L. F. , 2018, "Study on the effect of tension-compression asymmetry on the cylindrical cup forming of an AA2090-T3 alloy," Int. J. Solids Struct., **151**, DOI: 10.1016/j.ijsolstr.2017.06.034

[7] Garud, C., Benedyk, J., Mostovoy, S., and Nash, P., 2005, "Evaluating the Bauschinger effect in heavily cold worked 301 austenitic stainless steel used in multi-layer head gaskets," SAE 2005 World Congress & Exhibition, Detroit.

[8] Chen, J., Yao, W., and Gao, D., 2020, "Fatigue life evaluation of tension-compression asymmetric material using local stress-strain method," FFEMS, **43**(9), pp. 1994-2005, DOI: 10.1111/ffe.13279

[9] Meininger, J. M., Dickerson, S. L., and Gibeling, J. C., 1996, " Observations of tension/compression asymmetry in the cyclic defomration of aluminum alloy 7075," FFEMS, **19**(1), pp. 85-97, DOI : 10.1111/j.1460-2695.1996.tb00934.x.

[10] Li, X., Cheng, C., Le, Q., Zhou, X., Liao, Q., Chen, X., and Jia, Y., 2019, "Ex-situ EBSD Analysis of Yield Asymmetry, Texture and Twinning Development in Mg—5Li—3Al—2Zn Alloy During Tensile and Compressive Deformation," J. Alloys Compd., **805**, pp. 947-956, DOI: 10.1016/j.jallcom.2019.07.099

[11] P. Lin, Y. Hao, B. Zhang, S. Zhang, C. Chi, and J. Shen, 2017, "Tension-compression asymmetry in yielding and strain hardening behavior of CP-Ti at room temperature," Mater. Sci. Eng. A, **707**, pp. 172-180, DOI: 10.1016/j.msea.2017.09.042

[12] Gall, K., and Sehitoglu, H., 1999, "The role of texture in tension-compression asymmetry in polycrystalline NiTi," Int. J. Plast., **15**, pp. 69-92, DOI: 10.1016/S0749-6419(98)00060-6

[13] Davis, A. E., Robson, J. D., and Turski, M., 2019, "Reducing yield asymmetry and anisotropy in wrought magnesium alloys—A comparative study," Mater. Sci. Eng. A, **744**, pp. 525-537, DOI: 10.1016/j.msea.2018.12.060

[14] Wang, J., Li, X., Jin, P., Li, S., Ma, G., and Zhao, L., 2019 “Reducing the tension-compression yield asymmetry in an extruded ZK60 alloy by ultrafine grains,” Mater. Res. Express, **5**, DOI: 10.1088/2053-1591/aadd6b

[15] Tong, L. B., Zheng, M. Y., Kamado, S., Zhang, D. P., Meng, J., Cheng, L.R., and Zhang, H. J., 2015, “Reducing the tension-compression yield asymmetry of extruded Mg-Zn-Ca alloy via equal channel angular pressing” J. Magnes. Alloy, **3**(4), pp. 302-308, DOI: 10.1016/j.jma.2015.08.007

[16] Wei, J., You, J., Zhang, D., Jiang, S., Chen, Z., and Liu, C., 2020 “Reducing yield asymmetry in wrought Mg-9Al alloy by randomized texture achieved via multi-directional forging,” Mater. Sci. Eng. A, **796**, DOI: 10.1016/j.msea.2020.140003

[17] Chen, H. B., Liu, T. M., Zhang, Y., Zhai, Y. B., and He, J. J., 2016, “Reducing tension-compression yield asymmetry by free end torsion in extruded Mg alloy,” Mater. Sci. Tech., **32**(2), pp. 111-118, DOI: 10.1179/1743284715Y.0000000058

[18] Ellermann, A., and Scholtes, B., 2011, “The Bauschinger effect in different heat treatment conditions of 42CrMo4,” Int. J. Solids Struct., **3**(1), pp. 1-13.

[19] Clauer, A. H., 1996, “Laser shock peening for fatigue resistance,” *Surface Performance of Titanium*, Cincinnati, Ohio.

[20] Wang, C., Wang, L., Wang, C.-L., Li, K., and Wang, X.-G., 2019 “Dislocation density-based study of grain refinement induced by laser shock peening,” Opt. Laser Technol., **121**, DOI: 10.1016/j.optlastec.2019.105827

[21] Pan, X., Wang, X., Tian, Z., He, W., Shi, X., Chen, P., and Zhou, L., 2021, “Effect of dynamic recrystallization on texture orientation and grain refinement of Ti6Al4V titanium alloy subjected to laser shock peening,” J. Alloy Compd., **850**, DOI: 10.1016/j.jallcom.2020.156672

[22] Peyre, P., and Fabbro, R., 1995, “Laser shock processing: a review of the physics and applications,” Opt Quantum Electron, **27**, pp. 1213-1229, DOI: 10.1007/BF00326477

[23] Long, J., Pan, Q., Tao, N., and Lu, L., 2018, “Residual stress induced tension-compression asymmetry of gradient,” Mater. Res. Lett., **6**(8), pp.456-461, DOI: 10.1080/21663831.2018.1478898

[24] Hill, R., 1950, *The Mathematical Theory of Plasticity*, Clarendon Press, Oxford, UK, Chap. 2. ISBN: 978-0198503675

[25] Cottrell, A. H., 1953, *Dislocations and Plastic Flow in Crystals*, Oxford University Press, London, UK, Chap. 9. ISBN: 0198512066

[26] Sowerby, R., Uko, D. K., and Tomita, Y., 1979, "A review of certain aspects of the Bauschinger effect in metals," Mat. Sci. Eng., **41**(1), pp. 43-58, DOI: 10.1016/0025-5416(79)90043-0

[27] Yang, M., Pan, Y., Yuan, F., Zhu, Y., and Wu, X., 2016, "Back stress strengthening and strain hardening in gradient structure," Mat. Res. Lett., **4**(3), pp. 145-151, DOI: 10.1080/21663831.2016.1153004

[28] Ashby, M. F., 1970, “The deformation of plastically non-homogeneous materials,” Philos. Mag. Lett., **21**(170), DOI: 10.1080/14786437008238426

[29] Field, D. P., Trivedi, P. B., Wright, S. I., and Kumar, M., 2005, “Analysis of local orientation gradients in deformed single crystals,” Ultramicroscopy, **103**(1), DOI: 10.1016/j.ultramic.2004.11.016

[30] El-Dasher, B. S., Adams, B. L., and Rollett, A. D., 2003, “Viewpoint: experimental recovery of geometrically necessary dislocation density in polycrystals,” Scr. Mater., **48**(2), pp. 141-145, DOI: 10.1016/S1359-6462(02)00340-8

[31] Hansen, L. T., Fullwood, D. T., Homer, E. R., Wagoner, R. H., Lim, H., Carroll, J. D., Zhou, G., and Bong, H. J., 2019, "An investigation of geometrically necessary dislocations and back stress in large grained tantalum via EBSD and CPFE," Mater. Sci. Eng. A, **777**, DOI: 10.1016/j.msea.2019.138704.

[32] Sikhamov, R., Fomin, F., Klusemann, B., and Kashaev, N., 2020, “The influence of laser shock peening on fatigue properties of AA2024-T3 alloy with a fastener hole,” Metals, **10**(495), DOI: 10.3390/met10040495

[33] Lu, J. Z., Deng, W. W., Luo, K. Y., Wu, L. J., and Lu, H. F., 2017, “Surface EBSD analysis and strengthening mechanism of AISI 304 stainless steel subjected to massive LSP treatment with different pulse energies,” Materials Characterization, **125**, pp.99-107, DOI: 10.1016/j.matchar.2017.01.036

[34] Clauer, A. H., and Holbrook, J. H., 1981, “Effects of laser induced shock waves on metals,” *Shock Waves and High-Strain-Rate Phenomena in Metals,* Plenum Publishing Corporation, New York, Plenum, Chap. 38., pp. 675-703

[35] Brandal, G., and Yao, Y. L., 2017, “Material influence on mitigation of stress corrosion cracking via laser shock peening,” J. Manuf. Sci. E.-T. ASME, **139**(1), DOI: 10.1115/1.4034283

[36] Shadangi, Y., Chattopadhyay, K., Rai, S. B., and Singh, V., 2015, “Effect of laser shock peening on microstructure, mechanical properties and corrosion behavior of interstitial free steel,” Surface & Coatings Technology, **280**, pp. 216-224, DOI: 10.1016/j.surfcoat.2015.09.014

[37] Kalentics, N., Huang, K., Ortega Varela de Seijas, M., Burn, A., Romano, V., and Loge, R. E., 2019, "Laser shock peening: a promising tool for tailoring metallic microstructures in selective laser melting," J. Mater. Process. Technol., **266**, pp. 612-618, DOI: 10.1016/j.jmatprotec.2018.11.024

[38] Lin, C. C., and Hu, C. C., 2008, “Electropolishing of 304 stainless steel: Surface roughnessontrol using experimental design strategies and summarized electropolishing model,” Electrochim. Acta, **53**, pp. 3356-3363, DOI: 10.1016/j.electacta.2007.11.075

[39] Zhang, W., and Yao, Y. L., 2002, “Micro Scale Laser Shock Processing of Metallic Components,” J. Manuf. Sci. E.-T. ASME, **124**(2), pp. 369-378, DOI: 10.1115/1.1445149

[40] Fabbro, R., Fournier, J., Ballard, P., Devaux, D., and Virmont, J., 1990, “Physical study of laser-produced plasma in confined geometry,” J. Appl. Phys., **68**(2), DOI: 10.1063/1.346783

[41] 2019, *Abaqus 6.19 Theory Manual*, Dassault Systemes, Providence, RI.

[42] H. Bjørn, 2019, “Bauschinger effect modelled by yield surface distortions,” Int. J. Plast., **123**, pp. 86-100 DOI: 10.1016/j.ijplas.2019.07.009

[43] Jin, H., Sanborn, B., Lu, W. Y., and Song, B., 2021, "Mechanical characterization of 34L-VAR stainless steel in tension with coverate of low, intermediate and high strain rates," Mech. Mater. **152**, DOI: 10.1016/j.mechmat.2020.103654

[44] Fan, Y., Wang, Y., Vukelic, S., and Yao, Y. L., 2005, "Wave-solid interactions in laser-shock-induced deformation processes," J. Appl. Phys., **98**(10), DOI: 10.1063/1.2134882

[45] Cahn, R.W., 1996, "Recovery and recrystallization," *Physical Metallurgy (Fourth, Revised and Enhanced Edition)*, Department of Materials Science and Metallurgy, University of Cambridge, Cambridge, UK, Chap. 28., pp. 2399-2500

[46] Salehi, M. S., Anjabin, N., and Kim, H. S., 2019, "Study of geometrically necessary dislocations of a partially recrystallized aluminum alloy using 2D EBSD," Microsc. Microanal., **25**(3), pp. 656-663, DOI: 10.1017/S1431927619000382

[47] Hasegawa, T., Yakou, T., and Karashima, S., 1975, "Deformation behaviour and dislocation structures upon stress reversal in polycrystalline aluminum," Mater. Sci. Eng. A, **20**, pp. 267-276 DOI: 10.1016/0025-5416(75)90159-7

[48] Hasegawa, T., and Yakou, T., 1986, "Forward and reverse rearrangements of dislocations in tangled walls," Mater. Sci. Eng. A, **81**, pp. 189-199 DOI: 10.1016/0025-5416(86)90262-4

[49] Ghosh, A. K., 1980, "A physically-based constitutive model for metal deformation," Acta Metall. Mater., **28**, pp. 1443-1465, DOI: 10.1016/0001-6160(80)90046-2

[50] Cleveland, R. M., and Ghosh, A. K., "Inelastic effects on springback in metals," Int. J. Plast., **18**(5-6), DOI: 10.1016/S0749-6419(01)00054-7

[51] Valeyev, I., Kaibyshev, R., Sitdikov, O., and Sokolov, B., 1990, "The formation of high angle grain boundaries during the plastic deformation of magnesium and magnesium alloys" J. Phys. Colloq., **51**(C1), pp. C1-673-C1-677, DOI: 10.1051/jphyscol:19901107

[52] EDAX, 2018, *OIM Analysis*, Amtek Inc., Materials Analysis Division

[53] Mura, T., 1925, *Micromechanics of Defects in Solids*, Kluwer Academic Publishers, Dordrecht.

Chapter 3: Effect of Laser Shock Peening on Back Stress of Additively Manufactured Stainless Steel Parts

[1] A. H. Clauer, Oct. 7 1996, "Laser shock peening for fatigue resistance," *Surface Performance of Titanium*, Cincinnati, Ohio.

[2] G. Brandal and Y. L. Yao, 2017, " Laser shock peening for suppression of hydrogen-induced martensitic transformation in stress corrosion cracking," J. Manuf. Sci. E.-T. ASME, **139**(8), DOI: 10.1115/1.403 6530.

[3] W. Zhang and Y. L. Yao, 2002, "Micro Scale Laser Shock Processing of Metallic Components," J. Manuf. Sci. E.-T. ASME, **124**(2), pp. 369-378, DOI: 10.1115/1.1445149.

[4] J. Z. Lu, W. W. Deng, K. Y. Luo, L. J. Wu and H. F. Lu, 2017, "Surface EBSD analysis and strengthening mechanism of AISI 304 stainless steel subjected to massive LSP

treatment with different pulse energies," Materials Characterization, **125**, pp.99-107, DOI: 10.1016/j.matchar.2017.01.036 .

[5] A. H. Clauer and J. H. Holbrook, "Effects of laser induced shock waves on metals," *Shock Waves and High-Strain-Rate Phenomena in Metals,* Plenum Publishing Corporation, New York (1981): pp. 675-703.

[6] G. Brandal and Y. L. Yao, 2017, "Material influence on mitigation of stress corrosion cracking via laser shock peening," J. Manuf. Sci. E.-T. ASME, **139**(1), DOI: 10.1115/1.4034283 .

[7] Y. Shadangi, K. Chattopadhyay, S. B. Rai, and V. Singh, 2015, "Effect of laser shock peening on microstructure, mechanical properties and corrosion behavior of interstitial free steel," Surface & Coatings Technology, **280**, pp. 216-224, DOI: 10.1016/j.surfcoat.2015.09.014 .

[8] V. Over and Y. L. Yao, 2021, " Laser shock peening induced back stress mitigation in rolled stainless steel,"ASME J. Manuf. Sci. Eng., **144** (6), 061010, DOI: 10.1115/1.4052909.

[9] N. Kalentics, E. Boillat, S. Ciric-Kostic, N. Bogojevic and R. E. Loge, 2017, "Tailoring residual stress profile of Selective Laser Melted parts by Laser Shock Peening," Addit. Manuf., **16**, pp. 90-97, DOI: 10.1016/j.addma.2017.05.008.

[10] X. He, Y. P. Ye and B. B. He, 2022, " A review on the science of plastic deformation in laser-based additively manufactured steel," J. Meter. Sci., **57**, 10803–10835 DOI: 10.1007/s10853-022-07197-6.

[11] B. Pommier, 2000, Bauschinger effect of alloys and plasticity-induced crack closure: a finite element analysis," FFEMS, **23**, pp. 129-139, DOI:10.1046/j.1460-2695.2000.00259.x.

[12] F. S. Silva 2007, "Fatigue crack propagation after overloading and underloading at negative stress ratios," Int. J. Fatigue, **29**(9-11), DOI: 10.1016/j.ijfatigue.2007.03.012.

[13] P.D. Barros, J. L. Alves, M. C. Oliveira and L. F. Menezes, 2018, "Study on the effect of tension-compression asymmetry on the cylindrical cup forming of an AA2090-T3 alloy," Int. J. Solids Struct., **151**, DOI: 10.1016/j.ijsolstr.2017.06.034.

[14] P.L. Charpentier, 2015, "Post-forming monotonic and cyclic behavior in HSLA steel sheet after large deformations in-plane compression," Int. J. Fatigue, **79**, pp. 54-64, DOI: 10.1016/j.ijfatigue.2015.04.003.

[15] J. Chen, W. Yao, and D. Gao, 2020, "Fatigue life evaluation of tension-compression asymmetric material using local stress-strain method," FFEMS, 43(9), pp. 1994-2005, DOI: 10.1111/ffe.13279.

[16] Grand View Research, 2019, *3D Printing Metal Market Size, Share & Trends Analysis Report By Product (Titanium, Nickel), By Form (Filament, Powder), By Application (Aerospace & Defense, Medical & Dental), By Region, And Segment Forecasts, 2021 - 2028.*

[17] W. E. Frazier, 2014, "Metal Additive Manufacturing: A Review," ASM International, **23**(6), DOI: 10.1007/s11665-014-0958-z.

[18] C. Y. Yap, C. K. Chua, Z. L. Dong, Z. H. Liu, D. Q. Zhang, L. E. Loh and S. L. Sing, 2019, " Review of selective laser melting: Materials and applications," *App. Phys. Rev.*, **2**, 041101, DOI: 10.1063/1.4935926 .

[19] K.M. Bertsch, G. Meric de Bellefon, B. Kuehl, and D.J. Thoma, 2020, "Origin of dislocation structures in an additively manufactured austenitic stainless steel 316L," Acta Mater., **199**, pp. 19-33, DOI: 10.1016/j.actamat.2020.07.063.

[20] G. Wang, H. Ouyang, C. Fan, Q. Guo, Z. Li and W. Yan, 2020, "The origin of high-density dislocations in additively manufactured metals," Mater. Res. Lett., **4**(3), pp. 283-290, DOI: 10.1080/21663831.2020.1751739.

[21] W. Chen, T. Voisin, Y. Zhang, J. Florien, C. M. Spadaccini, D. L. McDowell, T. Zhu, and Y. M. Wang, 2019, "Microscale Residual Stresses in Additively Manufactured Stainless Steel," Nat. Commun., **10**(4338), DOI: 10.1038/s41467-019-12265-8.

[22] Z. Sun, X. Tan, S. B. Tor and C. K. Chua, 2018, "Simultaneously enhanced strength and ductility for 3D-printed stainless steel 316L by selective laser melting," NPG Asia Mater., **10**, pp. 127-136, DOI: 10.1038/s41427-018-0018-5.

[23] M. Yang, Y. Pan, F. Yuan, Y. Zhu and X. Wu, 2016, "Back stress strengthening and strain hardening in gradient structure," Mat. Res. Lett., **4**(3), pp. 145-151, DOI: 10.1080/21663831.2016.1153004.

[24] S. Paul, J. Liu, S. T. Strayer, Y. Zhao, S. Sridar, M. A. Klecka, W. Xiong and C. A. To, 2017, "A Discrete Dendrite Dynamics Model for Epitaxial Columnar Grain Growth in Metal Additive Manufacturing with Application to Inconel," Addit. Manuf., **36**, 101611, DOI: 10.1016/j.addma.2020.101611.

[25] S. Gorsse, C. Hutchinson, M. Goune and R. Banerjee, 2017, "Additive manufacturing of metals: a brief review of the characteristic microstructures and properties of steels, Ti-6Al-4V and high-entropy alloys," Sci. Technol. Adv. Mater., **18**(1), pp. 1443-1465, DOI: 10.1080/14686996.2017.1361305.

[26] J. G. Pauza, W. A. Tayon and A. D. Rollett, 2021, "Computer simulation of microstructure development in powder-bed additive manufacturing with crystallographic texture," Modelling Simul. Mater. Sci. Eng., **29**(5), 055019, DOI: 10.1088/1361-651X/ac03a6.

[27] M. S. Moyle, N. Haghdadi, X. Z. Liao, S. P. Ringer and S. Primig,, 2022, " On the microstructure and texture evolution in 17-4 PH stainless steel during laser powder bed fusion: Towards textural design," J. Mater. Sci. Technol., **117**, pp. 183-195, DOI: 10.1016/j.jmst.2021.12.015.

[28] K. Saeidi, L. Kevetkova, F. Lofaj, and Z. Shen, 2016, " Novel ferritic stainless steel formed by laser melting from duplex stainless steel powder with advanced mechanical properties and high ductility, " Mater. Sci. Eng. A, **665**, pp. 59-65, DOI: 10.1016/j.msea.2016.04.027.

[29] C. Y. Liu, J. D. Tong, M. G. Jiang, Z. W. Chen, G. Xu, H. B. Liao, P. Wang, X. Y. Wang, M. Xu and C. S. Lao, 2019, "Effect of scanning strategy on microstructure and mechanical properties of selective laser melted reduced activation ferritic/martensitic steel," Mater. Sci. Eng. A, **766**, 138364, DOI: 10.1016/j.msea.2019.138364.

[30] M. Y. Wang, T. Voisin, J. T. McKeown, J. Ye, N. P. Calta, Z. Li, Z. Zeng, Y. Zhang, W. Chen, T. T. Roehling, R. T. Ott, M. K. Santala, P. J. Depond, M. J. Matthews, A. V. Hamza and T. Zhu, 2017 “Additively manufactured hierarchical stainless steels with high strength and ductility,” Nat. Mater., **17**, pp. 63–71, DOI: 10.1038/nmat5021.

[31] X. X. Zhang, H. Andra, S. Harjo, W. Gong, T. Kawasaki, A. Lutz and M. Lahres, 2021, “Quantifying internal strains, stresses, and dislocation density in additively manufactured AlSi10Mg during loading-unloading-reloading deformation,” Mater. & Des., **198**, 109339, DOI: 10.1016/j.matdes.2020.109339.

[32] Y. Kok, X. P. Tan, P. Wang, M. L. S. Nai, N. H. Loh, E. Liu, and S. B. Tor, 2018, "Anisotropy and heterogeneity of microstructure and mechanical properties in metal additive manufacturing: A critical review," Mater. Des., **139**, pp.565-586 DOI: 10.1016/j.matdes.2017.11.021.

[33] M.-S. Pham, B. Dvgyy, P. A. Hooper, C. M. Gourlay and A. Piglione, 2020, “The role of side-branching in microstructure development in laser powder-bed fusion,” Nat. Commun., **11**(749), DOI: 10.1038/s41467-020-14453-3.

[34] Y. D. Im, K. H. Kim, K. H. Jung, Y. K. Lee and K. H. Song, 2019, "Anisotropic Mechanical Behavior of Additive Manufactured AISI 316L Steel," Metall. Mater. Trans. A Phys. Metall. Mater. Sci., **50**, pp. 2014-2021, DOI: 10.1007/s11661-019-05139-7.

[35] M. Higashi and T. Ozaki, 2020, " Selective laser melting of pure molybdenum: Evolution of defect and crystallographic texture with process parameters," Mater. Des, **191**, 108588 DOI:10.1016/j.matdes.2020.108588.

[36] C. Li, Z. Y. Liu, X. Y. Fang and Y. B. Guo, 2018, “Residual Stress in Metal Additive Manufacturing,” Procedia CIRP, **71**, pp. 348-353, DOI: 10.1016/j.procir.2018.05.039.

[37] L. Parry, I. A. Ashcroft and R. D. Wildman, 2016, “Understanding the effect of laser scan strategy on residual stress in selective laser melting through thermo-mechanical simulation,” Addit. Manuf., **12**(A), DOI: 10.1016/j.addma.2016.05.014.

[38] P. Mercelis and J.-P. Kruth, 2006, " Residual stresses in selective laser sintering," Rapid Prototyp. J., **12**(5), pp. 254-265, DOI: 10.1108/13552540610707013.

[39] H. T. Tran, Q. Chen, J. Mohan and A. C. To, 2020, A new method for predicting cracking at the interface between solid and lattice support during laser powder bed fusion additive manufacturing,” Addit. Manuf., **32**, 101050, DOI: 10.1016/j.addma.2020.101050.

[40] S.-g. Chen, H.-j. Gao, Y.-d. Zhang, Q. Wu, Z.-h. Gao and X. Zhou, 2022, “Review on residual stresses in metal additive manufacturing: formation mechanisms, parameter dependencies, prediction and control approaches,” J. Mater. Res. Technol., **17**, pp. 2950-2974, DOI: 10.1016/j.jmrt.2022.02.054.

[41] Z.-C. Fang, Z.-L. Wu, C.-G. Huang and C.-W. Wu,, 2020, “Review on residual stress in selective laser melting additive manufacturing of alloy parts,” Opt. Laser Technol., **129**, 106283, DOI: 10.1016/j.optlastec.2020.106283.

[42] N. Kalentics, E. Boillat, P. Peyre, C. Gorny, C. Kenel, C. Leinenbach, J. Jhabvala and R. E. Loge, 2017, "3D Laser Shock Peening - A new method for the 3D control of residual stresses in Selective Laser Melting ," Mater. & Des., **130**, pp. 350-356, DOI: 10.1016/j.matdes.2017.05.083.

H. T. Tran, Q. Chen, J. Mohan and A. C. To, 2020, A new method for predicting cracking at the interface between solid and lattice support during laser powder bed fusion additive manufacturing," Addit. Manuf., **32**, 101050, DOI: 10.1016/j.addma.2020.101050.

[43] M. Sealy, G. Madireddy, R. Williams, P. Rao and M. Toursangsaraki, 2018, "Hybrid Processes in Additive Manufacturing," J. Manuf. Sci. Eng., **140**(6), 060801, DOI: 10.1115/1.4038644.

[44] X. Peng, L. Kong, J. Y. H. Fuh and H. Wang, 2021, "A Review of Post-Processing Technologies in Additive Manufacturing," J. Manuf. Mater. Process., **5** (8), 38, DOI: 10.3390/jmmp5020038.

[45] L. Hackel, J. R. Rankin, A. Rubenchik, W. E. King and M. Matthews, 2018, "Laser peening: A tool for additive manufacturing post-processing," Addit. Manuf., **24**, pp. 67-75, DOI: 10.1016/j.addma.2018.09.013.

[46] M. Munther, T. Martin, A. Tajyar, L. Hackel, A. Beheshti and K. Davami, 2020, "Laser shock peening and its effects on microstructure and properties of additively manufactured metal alloys: a review," *Eng. Res. Express*, **2**(2), 022001, DOI: 10.1088/2631-8695/ab9b16.

[47] M. P. Sealy, G. Madireddy, C. Li and Y. B. Guo, 2016, "Finite Element Modeling of Hybrid Additive manufacturing by Laser Shock Peening," in *Proceedings of the 27th Annual International Solid Freeform Fabrication Symposium*, Austin.

[48] N. Kalentics, N. Sohrabi, H. G. Tabasi, S. Griffiths, J. Jamasp, C. Leinenbach, A. Burn and R. E. Loge, 2019, " Healing cracks in selective laser melting by 3D laser shock peening," Addit. Manuf., **30**, 100881, DOI: 10.1016/j.addma.2019.100881.

[49] A. d. Plessis, D. Glaser, H. Moller, N. Mathe, L. Tshabalala, B. Mfusi and R. Mostert, 2019, "Pore closure effect of laser shock peening of additively manufactured AlSi10Mg," 3D Print. Addit. Manuf., **6**(5), pp. 245-252, DOI: 10.1089/3dp.2019.0064.

[50] W. Guo, R. Sun, B. Song, Y. Zhu, F. Li, Z. Che, B. Li, C. Guo, L. Liu and P. Peng, 2018, "Laser Shock Peening of Laser Additive Manufactured Ti6Al4V Titanium Alloy," Surf. Coat. Technol., **349**, pp. 503-510, DOI: 10.1016/j.surfcoat.2018.06.020.

[51] S. Luo, W. He, K. Chen, X. Nie, L. Zhou and Y. Li, 2018, "Regain the Fatigue Strength of Laser Additive Manufactured Ti Alloy via Laser Shock Peening," J. Alloys Compd., **750**, pp.626-635, DOI:10.1016/j.jallcom.2018.04.029.

[52] M. Busi, N. Kalentics, M. Morgano, S. Griffiths, A. S. Tremsin, T. Shinohara, R. Loge, C. Leinenbach and M. Strobl, 2021, " A parametric neutron Bragg edge imaging study of additively manufactured samples treated by laser shock peening," Sci. Rep.,**11**, DOI: 10.1038/s41598-021-94455-3.

[53] J. Lu, H. Lu, X. Xu, J. Yao, J. Cai and K. Luo, 2020, "High-performance integrated additive manufacturing with laser shock peening-induced microstructural evolution and improvement in mechanical properties of Ti6Al4V alloy components," Int. J. Mach. Tools Manuf., **148**, 103475, DOI: 10.1016/j.ijmachtools.2019.103475.

[54] N. Kalentics, K. Huang, M. Ortega Varela de Seijas, A. Burn, V. Romano and R. E. Loge, 2019, "Laser shock peening: a promising tool for tailoring metallic microstructures in selective laser melting," J. Mater. Process. Technol., **266**, pp. 612-618, DOI: 10.1016/j.jmatprotec.2018.11.024.

[55] M. J. Uddin, E. Ramirez-Cedillo, R. A. Mirshams and H. R. Siller, 2021, "Nanoindentation and electron backscatter diffraction mapping in laser powder bed fusion of stainless steel 316L," Mater. Charact., **174**, 111047, DOI: 10.1016/j.matchar.2021.111047.

[56] A. Mostafaei, C. Zhao, Y. He, S. R. Ghiaasiaan, B. Shi, S. Shao, N. Shamsaei, Z. Wu, N. Kouraytem, T. Sun, J. Pauza, J. V. Gordon, B. Webler, N. D. Parab, M. Asherloo, Q. Guo, L. Chen and A. D. Rollett, 2022, " Defects and anomalies in powder bed fusion metal additive manufacturing," Curr Opin Solid State Mater Sci, **26**(2), 100974, DOI: 10.1016/j.cossms.2021.100974.

[57] B. Zhang, Y. Li and Q. Bai, 2017, "Defect Formation Mechanisms in Selective Laser Melting: A Review," Chin. J. Mech. Eng., **30**, pp. 515-527, DOI: 10.1007/s10033-017-0121-5.

[58] D. Pal and B. Stucker, 2013, "A study of subgrain formation in Al 3003 H-18 foils undergoing ultrasonic additive manufacturing using a dislocation density based crystal plasticity finite element framework," J. Appl. Phys., **113**, 203517, DOI: 10.1063/1.4807831.

[59] M. M. Francois, A. Sun, W. E. King, N. Henson, D. Tourret, C. Bronkhorst, N. N. Carlson, C. Newman, T. Haut, J. Bakosi, J. W. Gibbs, V. Livescu, S. VanderWiel, A. J. Clarke, M. Schraad, T. Blacker, H. Lim, T. Rodgers, S. Owen, F. Abdeljawad, J. Madison, A. T. Anderson, J.-L. Fattebert, R. M. Ferencz, N. E. Hodge, S. A. Khairallah and O. Walton, 2017, "Modeling of Additive Manufacturing Processes for Metals: Challenges and Opportunities," Curr. Opin. Solid State Mater. Sci., **21**(4), DOI: 10.1016/j.cossms.2016.12.001.

[60] K. Kapoor, Y. S. J. Yoo, T. A. Book, J. P. Kacher and M. D. Sangid, 2019, " Incorporating grain-level residual stresses and validating a crystal plasticity model of a two-phase Ti-6Al-4 V alloy produced via additive manufacturing," J. Mech. Phys. Solids, **121**, pp. 447-462, DOI: 10.1016/j.jmps.2018.07.025.

[61] A. Lakshmanan, M. Yaghoobi, K. S. Stopka and V. Sundararaghavan, 2022, "Crystal plasticity finite element modeling of grain size and morphology effects on yield strength and extreme value fatigue response," J. Mater. Res. Technol., **19**, pp. 3337-3354, DOI: 10.1016/j.jmrt.2022.06.075.

[62] S. S. Acar, O. Bulut and T. Yalcinkaya, 2022, "Crystal plasticity modeling of Additively manufactured metallic microstructures," Procedia Struct. Integr., **35**, pp. 219-227 DOI: 10.1016/j.prostr.2021.12.068.

[63] J. Zhang, J. Li, S. Wu, W. Zhang, J. Sun and G. Qian, 2022, "High-cycle and very-high-cycle fatigue lifetime prediction of additively manufactured AlSi10Mg via crystal plasticity finite element method," Int. J. Fatigue, **155**, 106577, DOI: 10.1016/j.ijfatigue.2021.106577.

[64] S. R. Kalidindi, C. A. Bronkhorst and L. Anand, 1992, " Crystallographic Texture Evolution in Bulk Deformation Processing of FCC Metals," *J. Mech. Phys. Solids,* **40**(3), pp. 537-569, DOI:10.1016/0022-5096(92)80003-9.

[65] R. J. Asaro and A. Needleman,1985, "Texture Development and Strain Hardening In Rate Dependent Polycrystals," Acta metall., **33**(6), pp. 923-953, DOI: 10.1016/0001-6160(85)90188-9.

[66] J. D. Eshelby, 1957, “The determination of the elastic field of an ellipsoidal inclusion, and related problems,” Proc. R. Soc. Lond., **241**(1226), pp. 376-396, DOI: 10.1098/rspa.1957.0133.

[67] H. D. Espinosa, M. Panico, S. Berbenni and K. W. Schwarz, 2006, “Discrete dislocation dynamics simulations to interpret plasticity size and surface effects in freestanding FCC thin films,” Int. J. Plast., **22**(11), pp. 2091-2117, DOI: 10.1016/j.ijplas.2006.01.007.

[68] G. I. Taylor, 1938, “Plastic strain in metals,” *J. Inst. Metals,* **62**, pp. 307-324.

[69] W. F. Hosford, 2010, *Mechanical Behavior of Materials*, Cambridge University Press, Cambridge, UK, Chap. 7. ISBN: 978-0-511-65836-5.

[70] H. Chen, J. Kysar and Y. L. Yao, 2004, “Characterization of Plastic Deformation Induced by Microscale Laser Shock Peening,” J. Appl. Mech., **71**(5), pp. 713-723, DOI: 10.1115/1.1782914.

Chapter 4: Effect of Laser Shock Peening on Electrochemistry and Wettability of Additively Manufactured Stainless Steel

[1] S. Patel, “Nuclear First: 3D-Printed Safety-Related Components Installed at Browns Ferry,” Power: News & Technology for the Global Energy Industry, 10 August, 2021.

[2] S. A. Anderson and C. Uriarte, 2015, “Final Technical Report on Laser Direct Manufacturing (LDM) for Nuclear Power Components,” Lockheed Martin.

[3] K. Geenen, A. Rottger and W. Theisen, 2016, “Corrosion behavior of 316L austenitic steel processed by selective laser melting, hot-isostatic pressing, and casting,” *Mater. and Corros.,* **68**, pp. 764-775, DOI: 10.1002/maco.201609210.

[4] R. Schaller, . M. Taylor, J. Rodelas and E. J. Shindelholz, 2017, "Corrosion Properties of Powder Bed Fusion Additively Manufactured 17-4 PH Stainless Steel," *Corrosion ,* **73**(7), pp. 796-807, DOI: 10.5006/2365.

[5] V. B. Vukkum and R. K. Gupta, 2022, “Review on corrosion performance of laser powder-bed fusion printed 316L stainless steel: Effect of processing parameters, manufacturing defects, post-processing, feedstock, and microstructure” Mater. & Des., **221**(110874), DOI: 10.1016/j.matdes.2022.110874.

[6] D. A. Macatangay, S. Thomas, N. Birbilis and R. G. Kelly, 2018, " Unexpected Interface Corrosion and Sensitization Susceptibility in Additively Manufactured Austenitic Stainless Steel," Corros. Commun., **74**(2), pp. 153-157, DOI: 10.5006/2723.

[7] M. Laleh, A. E. Hughes, W. Xu, N. Haghdadi, K. Wang, P. Cizek, I. Gibson and M. Y. Tan, 2019, “On the unusual intergranular corrosion resistance of 316L stainless steel additively manufactured by selective laser melting,” Corros. Sci., **161**(108189), DOI: 10.1016/j.corsci.2019.108189.

[8] R. H. Jones, 1992, Stress-Corrosion Cracking: Materials Performance and Evaluations, ASM International, Materials Park, Ohio, ISBN: 978-1-62708-118-4.

[9] P. Mercelis and J.-P. Kruth, 2006, " Residual stresses in selective laser sintering," Rapid Prototyp. J., **12**(5), pp. 254-265, DOI : 10.1108/13552540610707013.

[10] G. Brandal and Y. L. Yao, 2017, “Material influence on mitigation of stress corrosion cracking via laser shock peening,” J. Manuf. Sci. E.-T. ASME, **139**(1), DOI: 10.1115/1.4034283.

[11] V. Cruz, Q. Chao, N. Birbilis, D. Fabijanic, P. D. Hodgson and S. Thomas, 2020, "Electrochemical studies on the effect of residual stress on the corrosion of 316L manufactured by selective laser melting," Corros. Sci., **164**(108314), DOI: 10.1016/j.corsci.2019.108314.

[12] O. Takakuwa and H. Soyama, 2014, “Effect of Residual Stress on the Corrosion Behavior of Austenitic Stainless Steel,” Adv. Chem. Engineer. Sci., **5** pp. 62-71, DOI: 10.4236/aces.2015.51007.

[13] P. Peyre, X. Scherpereel, L. Berthe, C. Carboni, R. Fabbro, G. Beranger and C. Lemaitre, 2000, “Surface modifications induced in 316L steel by laser peening and shot-peening. Influence on pitting corrosion resistance,” Mater. Sci. Eng. A, **280**(2), pp. 294-302, DOI: 10.1016/S0921-5093(99)00698-X.

[14] X. Liu and G. S. Frankel, 2006, “Effects of compressive stress on localized corrosion in AA2024-T3,” Corros. Sci., **48**, pp. 3309-3329, DOI: 10.1016/j.corsci.2005.12.003.

[15] C. Wang, H. Bian, K. Luo, I. V. Alexandrov, Y. Su, Q. Zhang, X. Bu and J. Lu, 2022, “Laser shock peening-induced carbide evolution and remarkable improvement in electrochemical and long-term immersion corrosion resistance of 2Cr12NiMoWV martensitic stainless steel,” Surf. Coat. Technol., **451**, 129034, DOI:10.1016/j.surfcoat.2022.129034.

[16] H. Krawiec, V. Vignal, H. Amar and P. Peyre, 2011, " Local electrochemical impedance spectroscopy study of the influence of ageing in air and laser shock processing on the micro-electrochemical behaviour of AA2050-T8 aluminium alloy," Electrochemica Acta., **56**, pp.9581-9587 DOI:10.1016/j.electacta.2011.01.091.

[17] G. Brandal and Y. L. Yao, 2017, “Laser shock peening for suppression of hydrogen-induced martensitic transformation in stress corrosion cracking,” J. Manuf. Sci. E.-T. ASME, **139**(8), DOI: 10.1115/1.403 6530.

[18] Q. Chao, V. Cruz, S. Thomas, N. Birbilis, P. Collins, A. Taylor, P. D. Hodgson and D. Fabijanic, 2017, “On the enhanced corrosion resistance of a selective laser melted austenitic stainless steel,” Scr. Mater., **141**, pp. 94-98, DOI: 10.1016/j.scriptamat.2017.07.037.

[19] P. Peyre and R. Fabbro, 1995, “Laser shock processing: a review of the physics and applications,” Opt Quantum Electron, **27**, pp. 1213-1229, DOI: 10.1007/BF00326477

[20] N. Kalentics, E. Boillat, S. Ciric-Kostic, N. Bogojevic and R. E. Loge, 2017, "Tailoring residual stress profile of Selective Laser Melted parts by Laser Shock Peening," Addit. Manuf., **16**, pp. 90-97, DOI: 10.1016/j.addma.2017.05.008.

[21] V. Over, J. Donovan, and Y. L. Yao, 2023, " The effect of laser shock peening on back stress of additively manufactured stainless steel parts,"ASME J. Manuf. Sci. Eng., **145** (4), 041005, DOI: 10.1115/1.4056571.

[22] E. Maleki, O. Unal, S. Shao and N. Shamsaei, 2023, " Effects of Laser Shock Peening on Corrosion Resistance of Additive Manufactured AlSi10Mg," Coat., **13**, pp. 153-157, DOI: 10.3390/coatings13050874.

[23] G. Thangmani, P. I. A., M. K. Singh, D. K. Rai, V. G. S. Priyan and S. K. Subbu, 2023, “Post-processing of Wire Arc Additive Manufactured Stainless Steel 308L to Enhance Compression and Corrosion Behavior using Laser Shock Peening Process,” *J. of Materi Eng and Perform*, pp. 1059-9495, DOI: 10.1007/s11665-023-08592-z.

[24] V. A. Annakodi, A. R. Singh, S. Jaylakshmi, Y. Zhang, M. A. Khan, K. S. Rao and R. Shabadi, 2022, “Patterning SS304 Surface at Microscale to Reduce Wettability and Corrosion in Saline Water,” Metals, **12**(7), 1137, DOI: 10.3390/met12071137.

[25] D. Holder, F. Hetzel and T. Graf, 2022, " Surface treatment of additively manufactured metal parts for any arbitrary wetting state between superhydrophilic and super hydrophobic," *Procedia CIRP*, **111**, pp. 715-720, DOI: 10.1016/j.procir.2022.08.014.

[26] X. Shen, P. Shukla, P. Swanson, Z. An, S. Prabhakarn, D. Waugh, X. Nie, C. Mee, S. Nakhodchi and J. Lawrence, 2019, “Altering the wetting properties of orthopaedic titanium alloy (Tie6Ale7Nb) using laser shock peening,” J. Alloys Compd., **801**, pp. 327-342, DOI: 10.1016/j.jallcom.2019.06.104.

[27] A. K. Gujba and M. Medraj, 2014, “Laser peening process and its impact on materials properties in comparison with shot peening and ultrasonic impact peening,” Mtl, **7**, pp. 7925-7974, DOI: 10.3390/ma7127925.

[28] F. Dai, J. Zhou, J. Lu and X. Luo, 2016, “A technique to decrease surface roughness in overlapping laser shock peening,” Appl. Surf. Sci., **370**, pp. 501-507, DOI: 10.1016/j.apsusc.2016.02.138.

[29] A. Siddaiah, B. Mao, Y. Liao and P. L. Menezes, 2018, “Surface characterization and tribological performance of laser shock peened steel surfaces,” Surf. Coat. And Technol., **351**, pp. 188-197 DOI: 10.1016/j.surfcoat.2018.07.087.

[30] J. J. Kim and Y. M. Young, 2013, " Study on the passive film of type 316 stainless steel," *Int. J. Electrochem. Sci*, **8**, pp. 11847-11859, DOI: 10.1016/S1452-3981(23)13227-5.

[31] D. D. Macdonald, 2011, " The history of the Point Defect Model for the passive state: A brief review of film growth aspects," Electrochimica Acta, **56**(4), pp. 1761-1772, DOI: 10.1016/j.electacta.2010.11.005.

[32] H. S. Magar, R. Y. A. Hassan and A. Mulchandani, 2021, "Electrochemical Impedance Spectroscopy (EIS): Principles, Construction, and Biosensing Applications," Sensors, **21**(19), pp. 6578, DOI: 10.3390/s21196578.

[33] X. Yang, F. Tang, X. Hao and Z. Li, 2021, " Oxide Evolution During the Solidification of 316L Stainless Steel from Additive Manufacturing Powders with Different Oxygen Contents," Metall. Mater. Trans. B., **52**, pp. 2253-2253, DOI: 10.1007/s11663-021-02191-w.

[34] M. A. Melia, J. G. Duran, J. R. Koepke, D. J. Saiz, B. H. Jared and E. J. Schindelholz, 2020, " How build angle and post-processing impact roughness and corrosion of additively manufactured 316L stainless steel," npj Mater Degrad, **4**(21), DOI: 10.1038/s41529-020-00126-5.

[35] "I. Puigdomenech, Medusa software, Chemical equilibrium diagrams," 2010. [Online]. Available: http://www.kemi.kth.se/medusa/.

[36] M. J. K. Lodhi, K. M. Deen and W. Haider, 2018, “Corrosion behavior of additively manufactured 316L stainless steel in acidic media,” Materiala, **2**, pp. 111-121, DOI: 10.1016/j.mtla.2018.06.015

[37] B. Laurent, N. Gruet, B. Gwinner, F. Miserque, K. Rousseau and K. Ogle, 2019, "Dissolution and Passivation of a Silicon-Rich Austenitic Stainless Steel during Active-Passive Cycles in Sulfuric and Nitric Acid," J. Electrochem. Soc.**, 164**(13), C892, DOI: 10.1149/2.1531713jes.

[38] D. D. Macdonald, 1999, "Passivity - the key to our metals-based civilization," Pure Appl. Chem., **71**(6), pp. 951-978, DOI: 10.1351/pac199971060951.

[39] G. Sander, S. Thomas, V. Cruz, M. Jurg, N. Birbilis, X. Gao, M. Brameld and C. R. Hutchinson, 2017, " On The Corrosion and Metastable Pitting Characteristics of 316L Stainless Steel Produced by Selective Laser Melting," J. Electrochem. Soc., **164** (6), pp. C250-C257, DOI: 10.1149/2.0551706jes.

[40] A. d. Plessis, D. Glaser, H. Moller, N. Mathe, L. Tshabalala, B. Mfusi and R. Mostert, 2019, “Pore closure effect of laser shock peening of additively manufactured AlSi10Mg,” 3D Print. Addit. Manuf., **6**(5), pp. 245-252, DOI: 10.1089/3dp.2019.0064.

[41] A. W. Adamson and A. P. Gast, 1997, *Physical Chemistry of Surfaces*, John Wiley & Sons, Inc., New York, ISBN: 0-471-14873-3.

[42] M. Sedlacek, B. Podgornik and J. Vizintin, 2016, “Correlation between standard roughness parameters skewness and kurtosis and tribological behaviour of contact surfaces,” Tribol. Int., **48**, pp. 102-112, DOI: 10.1016/j.triboint.2011.11.008.

[43] Y. Chen, B. M. Schaeffer, R. Jenson, M. M. Weislogel, 2012, *Surface Evolver – Fluid Interface Tool: Version 1.112 User’s Manual*, Department of Mechanical and Materials Engineering, Portland State University.

[44] X. Wei, C. Zhang and X. Ling, 2017 “Effects of laser shock processing on corrosion resistance of AISI 304 stainless steel in acid chloride solution,” J. Alloys Compd., **723**, pp. 237-243, DOI: 10.1016/j.jallcom.2017.06.283.

[45] V. K. Caralapatti and S. Narayanswamy, 2017, “Effect of high repetition laser shock peening on biocompatibility and corrosion resistance of magnesium,” Opt. Laser Technol., **88**, pp. 75-84, DOI: 10.1016/j.optlastec.2016.09.003.

[46] G. Rocchini, 1995 " The determination of Tafel slopes by the successive approximation method," Corros. Sci, **37**(6), pp. 987-1003, DOI: 10.1016/0010-938X(95)00009-9 .

[47] E. Chibowski, 2003, " Surface free energy of a solid from contact angle hysteresis," Adv. Colloid Interface Sci., **103**, pp.149-172, DOI: 10.1016/S0001-8686(02)00093-3.

[48] Q. Li, P. Zhou, and H. J. Yan, 2016, “Pinning−Depinning Mechanism of the Contact Line during Evaporation on Chemically Patterned Surfaces: A Lattice Boltzmann Study,” Langmuir, **32**(37), pp.9389 - 9396, DOI: 10.1021/acs.langmuir.6b01490.

Chapter 5: Mitigation of Stress Corrosion Cracking in Additively Manufactured Stainless Steel by Laser Shock Peening

[1] G. Brandal and Y. L. Yao, 2017, “Material influence on mitigation of stress corrosion cracking via laser shock peening,” J. Manuf. Sci. Eng. ASME, **139**(1), 011002, DOI: 10.1115/1.4034283.

[2] V. Over, J. Donovan, and Y. L. Yao, 2023, " The effect of laser shock peening on back stress of additively manufactured stainless steel parts,"ASME J. Manuf. Sci. Eng., **145** (4), 041005, DOI: 10.1115/1.4056571.

[3] S. Patel, “Nuclear First: 3D-Printed Safety-Related Components Installed at Browns Ferry,” Power: News & Technology for the Global Energy Industry, 10 August, 2021.

[4] S. A. Anderson and C. Uriarte, "Final Technical Report on Laser Direct Manufacturing (LDM) for Nuclear Power Components," Lockeed Martin, 2015.

[5] X. Lou, M. Song, P. W. Emigh, M. A. Othon, and P. L. Andresen, 2017, “On the stress corrosion crack growth behaviour in high temperature water of 316L stainless steel made by laser powder bed fusion additive manufacturing,” Corros. Sci., **128**, pp.140-153, DOI: 10.1016/j.corsci.2017.09.017.

[6] P. Mercelis and J.-P. Kruth, 2006, " Residual stresses in selective laser sintering," Rapid Prototyp. J., **12**(5), pp. 254-265, DOI : 10.1108/13552540610707013.

[7] D. A. Macatangay, S. Thomas, N. Birbilis and R. G. Kelly, 2018, " Unexpected Interface Corrosion and Sensitization Susceptibility in Additively Manufactured Austenitic Stainless Steel," Corros. Commun., **74**(2), pp. 153-157, DOI: 10.5006/2723.

[8] V. Cruz, Q. Chao, N. Birbilis, D. Fabijanic, P. D. Hodgson and S. Thomas, 2020, "Electrochemical studies on the effect of residual stress on the corrosion of 316L manufactured by selective laser melting," Corros. Sci., **164**(108314), DOI: 10.1016/j.corsci.2019.108314.

[9] X. Yang, F. Tang, X. Hao and Z. Li, 2021, " Oxide Evolution During the Solidification of 316L Stainless Steel from Additive Manufacturing Powders with Different Oxygen Contents," Metall. Mater. Trans. B., **52**, pp. 2253-2253, DOI: 10.1007/s11663-021-02191-w.

[10] K.M. Bertsch, A. Nagao, B. Rankouhi, B. Kuehl and D. J. Thoma, 2021, “Hydrogen embrittlement of additively manufactured austenitic stainless steel 316L,” Corros. Sci., **192**, pp. 109790, DOI: 10.1016/j.corsci.2021.109790.

[11] J. T. Miller, J. H. Martin and E. Cudjoe, 2021, "Comparison of the effects of a sulfuric acid environment on traditionally manufactured and additive manufactured stainless steel 316L alloy," Addit. Manuf., **23**, pp. 272-282, DOI : 10.1016/j.addma.2018.08.023.

[12] B. F. Brown, 1976, “ Stress corrosion cracking control measures,” Washington: U.S. Dept. of Commerce, National Bureau of Standards : for sale by the Supt. of Docs., U.S. Govt. Print. Off.

[13] E. K. Karasz, J. Taylor, D. M. Autenrieth, P. Reu, K. Johnson, M. Melia and P. Noell, 2022, "Measuring the Residual Stress and Stress Corrosion Cracking Susceptibility of

Additively Manufactured 316L by ASTM G36-94," Corros., **78**(1), pp. 3-12, DOI: 10.5006/3894.

[14] X. Peng, L. Kong, J. Y. H. Fuh and H. Wang, 2021, “A Review of Post-Processing Technologies in Additive Manufacturing,” J. Manuf. Mater. Process., **5** (8), 38, DOI: 10.3390/jmmp5020038.

[15] M. Sealy, G. Madireddy, R. Williams, P. Rao and M. Toursangsaraki, 2018, “Hybrid Processes in Additive Manufacturing,” J. Manuf. Sci. Eng., **140**(6), 060801, DOI: 10.1115/1.4038644.

[16] P. Peyre, X. Scherpereel, L. Berthe, C. Carboni, R. Fabbro, G. Beranger and C. Lemaitre, 2000, “Surface modifications induced in 316L steel by laser peening and shot-peening. Influence on pitting corrosion resistance,” Mater. Sci. Eng. A, **280**(2), pp. 294-302, DOI: 10.1016/S0921-5093(99)00698-X.

[17] G. Brandal and Y. L. Yao, 2017, “ Laser shock peening for suppression of hydrogen-induced martensitic transformation in stress corrosion cracking,” J. Manuf. Sci. E.-T. ASME, **139**(8), DOI: 10.1115/1.4036530.

[18] H. Krawiec, V. Vignal, H. Amar and P. Peyre, 2011, " Local electrochemical impedance spectroscopy study of the influence of ageing in air and laser shock processing on the micro-electrochemical behaviour of AA2050-T8 aluminium alloy," Electrochemica Acta., **56**, pp.9581-9587 DOI: /10.1016/j.electacta.2011.01.091.

[19] N. Kalentics, E. Boillat, P. Peyre, C. Gorny, C. Kenel, C. Leinenbach, J. Jhabvala and R. E. Loge, 2017, "3D Laser Shock Peening - A new method for the 3D control of residual stresses in Selective Laser Melting ," Mater. & Des., **130**, pp. 350-356, DOI: 10.1016/j.matdes.2017.05.083.

[20] S. Luo, W. He, K. Chen, X. Nie, L. Zhou and Y. Li, 2018, “Regain the Fatigue Strength of Laser Additive Manufactured Ti Alloy via Laser Shock Peening,” J. Alloys Compd., **750**, pp.626-635, DOI: 10.1016/j.jallcom.2018.04.029.

[21] N. Kalentics, K. Huang, M. Ortega Varela de Seijas, A. Burn, V. Romano and R. E. Loge, 2019, "Laser shock peening: a promising tool for tailoring metallic microstructures in selective laser melting," J. Mater. Process. Technol., **266**, pp. 612-618, DOI: 10.1016/j.jmatprotec.2018.11.024.

[22] J. Y. Yao, J. Venezuela, A. Aterns and Z. Ming-Xing, 2023, " Recent research progress in hydrogen embrittlement of additively manufactured metals – A review," Curr. Opin. Solid State Mater. Sci., **27**(5), pp. 101106, DOI: 10.1016/j.cossms.2023.101106.

[23] W. Chen, T. Voisin, Y. Zhang, J. Florien, C. M. Spadaccini, D. L. McDowell, T. Zhu, and Y. M. Wang, 2019, “Microscale Residual Stresses in Additively Manufactured Stainless Steel,” Nat. Commun., **10**(4338), DOI: 10.1038/s41467-019-12265-8

[24] R. Silverstein and D. Eliezer, 2018, “Hydrogen trapping in 3D-printed (additive manufactured) Ti-6Al-4V,” Mater. Charact., **144**, pp. 297-304, DOI: 10.1016/j.matchar.2018.07.029.

[25] V. Cruz, Y. Qiu, N. Birbilis and S. Thomas, 2022, "Stress corrosion cracking of 316L manufactured by laser powder bed fusion in 6% ferric chloride solution," Corros. Sci., **207**, pp. 110535, DOI: 10.1016/j.corsci.2022.110535.

[26] A. Riemer, S. Leuders, M. Thöne, H.A. Richard, T. Tröster, and T. Niendorf, 2014 "On the fatigue crack growth behavior in 316L stainless steel manufactured by selective laser melting," Eng. Fract. Mech, **102**, pp. 15-25, DOI: 10.1016/j.engfracmech.2014.03.008

[27] T. K. Shoemaker, Z. D. Harris and J. T. Burns, 2022, "Comparing Stress Corrosion Cracking Behavior of Additively Manufactured and Wrought 17-4H Stainless Steel," Corros., **78**(6), pp. 528-546, DOI: 10.5006/4064.

[28] J. Toribio and M. Elices, 1991, "Influence of Residual Stresses on Hydrogen Embrittlement Susceptibility of Prestresing Steels," Int. J. Solids Structures, **28**(6), pp. 791-803, DOI: 10.1016/0020-7683(91)90157-B.

[29] C. Li, Z. Y. Liu, X. Y. Fang and Y. B. Guo, 2018, "Residual Stress in Metal Additive Manufacturing," Procedia CIRP, **71**, pp. 348-353, DOI: 10.1016/j.procir.2018.05.039.

[30] A. H. Clauer, Oct. 7 1996, "Laser shock peening for fatigue resistance," *Surface Performance of Titanium*, Cincinnati, Ohio.

[31] Y.-R. Yoo, S.-H. Choi and Y.-S. Kim, 2023, "Effect of Laser Shock Peening on the Stress Corrosion Cracking of 304L Stainless Steel," Metals, **13**(3), pp. 516, DOI: 10.3390/met13030516.

[32] B. N. Mordyuk, Y. V. Milman, M. O. Iefimov, G. I. Prokopenko, V. V. Silberschmidt, M. I. Danylenko and A. V. Kotko, 2008, " Characterization of ultrasonically peened and laser-shock peened surface layers of AISI 321 stainless steel," Surf. Coat. Int., **202**(19), pp. 4875-4883, DOI: 10.1016/j.surfcoat.2008.04.080.

[33] L. Zhou, W. He, S. Luo, C. Long, C. Wang, X. Nie, G. He, X. Shen and Y. Li, 2016, "Laser shock peening induced surface nanocrystallization and martensite transformation in austenitic stainless steel," Surf. Coat. Techno, **655**, pp. 66-70, DOI: 10.1016/j.jallcom.2015.06.268.

[34] W. Guo, R. Sun, B. Song, Y. Zhu, F. Li, Z. Che, B. Li, C. Guo, L. Liu and P. Peng, 2018, "Laser Shock Peening of Laser Additive Manufactured Ti6Al4V Titanium Alloy," Surf. Coat. Technol., **349**, pp. 503-510, DOI: 10.1016/j.surfcoat.2018.06.020.

[35] R. Sun, L. Li, Y. Zhu, W. Guo, P. Peng, B. Cong, J. Sun, Z. Che, B. Li, C. Guo and L. Liu, 2018, "Microstructure, Residual Stress and Tensile Properties Control of Wire-Arc Additive Manufactured 2319 Aluminum Alloy with Laser Shock Peening," J. Alloys Compd., **747**, pp. 255-265, DOI: 10.1016/j.jallcom.2018.02.353.

[36] Y. Wang, J. W. Kysar, S. Vukelic and Y. L. Yao, 2009, "Spatially resolved characterization of geometrically necessary dislocation dependant deformation in microscale laser shock peening," J. Manuf. Sci. Eng., **131**(4), pp. 041014, DOI: 10.1115/1.3160370.

[37] A. K. Gujba and M. Medraj, 2014, "Laser peening process and its impact on materials properties in comparison with shot peening and ultrasonic impact peening," Mtl, **7**, pp. 7925-7974, DOI: 10.3390/ma7127925.

[38] A. G. Sanchez, C. You, M. Leering, D. Glaser, D. Furfari, M. E. Fitzpatrick, J. Wharton and P. A. S. Reed, 2021, "Effects of laser shock peening on the mechanisms of fatigue short crack initiation and propagation of AA7075-T651," Int. J. Fatigue, **143**, pp. 106025, DOI: 10.1016/j.ijfatigue.2020.106025.

[39] S. P. Lynch, 2007, “Progress Towards Understanding Mechanisms Of Hydrogen Embrittlement And Stress Corrosion Cracking,” in *NACE International Corrosion Conference & Expo,* Nashville, Tennessee.

[40] C. Rubio-Gonzalez, J. L. Ocana, G. Gomez-Rosas, C. Molpeceres, M. Paredes, A. Banderas, J. Porro and M. Morales, "Effect of laser shock processing on fatigue crack growth and fracture toughness of 6061-T6 aluminum alloy," *Materials Science and Engineering:A,* vol. 386, no. 1-2, pp. 291-295, 2004.

[41] Z. Bergant, U. Trdan and J. Grum, 2016, “Effects of laser shock processing on high cycle fatigue crack growth rate and fracture toughness of aluminium alloy 6082-T651,” Int. J. Fatigue, **87**, pp. 444-455, DOI: 10.1016/j.ijfatigue.2016.02.027.

[42] Y. Sun, M. G. Edwards, B. Chen and C. Li, 2021, “A state-of-the-art review of crack branching,” Eng. Fract. Mech., **257**, pp. 108036, DOI: 10.1016/j.engfracmech.2021.108036.

[43] E. Sharon, S. P. Gross and J. Fineberg, 1995, “Local Crack Branching as a Mechanism for Instability in Dynamic Fracture,” Phys. Rev. Lett., **74**(25), pp. 5096-5099, DOI: 10.1103/PhysRevLett.74.5096.

[44] G. Molnár, A. Gravouil, R. Seghir and J. Réthoré, 2020, " An open-source Abaqus implementation of the phase-field method to study the effect of plasticity on the instantaneous fracture toughness in dynamic crack propagation," Comput. Methods Appl. Mech. Engrg., **365**, 113004, DOI: 10.1016/j.cma.2020.113004.

[45] C. Miehe, F. Welshinger and M. Hofacker, 2010, " Thermodynamically consistent phase-field models of fracture: variational principles and multi-field FE implementations," Internat. J. Numer. Methods Eng., **83**(10), pp. 1275-1311, DOI :10.1002/nme.2861.

[46] S. Huang and H. Hui, 2022, " Predictive environmental hydrogen embrittlement on fracture toughness of commercial ferritic steels with hydrogen-modified fracture strain model," Int. J. Hydrog. Energy, **47**(19), pp. 10777-1087, DOI: 10.1016/j.ijhydene.2021.12.128.

[47] Y. Li and K. Zhang, 2022, “Analysis of Hydrogen-Assisted Brittle Fracture Using Phase-Field Damage Modelling Considering Hydrogen Enhanced Decohesion Mechanism,” metals, **12**(6), pp. 1032, DOI: 10.3390/met12061032.

[48] V. Over and Y. L. Yao, 2021, " Laser shock peening induced back stress mitigation in rolled stainless steel,"ASME J. Manuf. Sci. Eng., **144** (6), 061010, DOI: 10.1115/1.4052909.

[49] M. Mukherjee, 2019, " Effect of build geometry and orientation on microstructure and properties of additively manufactured 316L stainless steel by laser metal deposition," Mater., **7**, 100359, DOI: 10.1016/j.mtla.2019.100359.

[50] W. F. Flanagan, P. Bastias and B. D. Lichter, 1991, “A theory of transgranular stress-corrosion cracking,” *Acta metall. mater.*, **39**(4), pp. 695-705, DOI: 10.1016/0956-7151(91)90138-Q.

[51] S. Paul, J. Liu, S. T. Strayer, Y. Zhao, S. Sridar, M. A. Klecka, W. Xiong and C. A. To, 2017, “A Discrete Dendrite Dynamics Model for Epitaxial Columnar Grain Growth in Metal Additive Manufacturing with Application to Inconel,” Addit. Manuf., **36**, 101611, DOI: 10.1016/j.addma.2020.101611.

[52] E. de Sonis, S. Depinoy, P.-F. Giroux, H. Maskrot, P. Wident, O. Hercher, F. Villaret and A.-F. Grougues-Lorenzon, 2023, “Microstructure – Toughness relationships in 316L stainless steel produced by laser powder bed fusion,” Mater. Sci. Eng. A, **877**, pp. 145179, DOI: 10.1016/j.msea.2023.145179.